

# **Lyotropic liquid crystals as templates for the synthesis of silver nanoparticles**

an der  
Fakultät für Naturwissenschaften  
Department Chemie  
der Universität Paderborn

zur Erlangung des Grades eines  
Doktors der Naturwissenschaften  
Dr. rer. nat.  
genehmigte Dissertation

von  
**Dmitry Kushnikovskiy**  
aus Kasan (Russland)

Paderborn 2017



Die vorliegende Dissertation entstand im Zeitraum von Oktober 2012 bis Juli 2017 im Fachgebiet Physikalische Chemie (Arbeitskreis Prof. Dr. Claudia Schmidt) an der Fakultät für Naturwissenschaften der Universität Paderborn.

**Promotionkommission:**

Erstgutachterin:	Prof. Dr. Claudia Schmidt
Zweitgutachter:	Prof. Dr. Heinz-Siegfried Kitzerow
3. Mitglied:	PD. Dr. Hans Egold
Vorsitzender	Prof. Dr. Jörg Lindner

Die Arbeit wurde eingereicht am: 13.07.17

Tag der mündlichen Prüfung: 14.09.17



## Acknowledgements

First and foremost, I would like to thank my supervisor, Prof. Dr. Claudia Schmidt, for giving me the opportunity to join the research group “Struktur und Dynamik” for this interesting topic and conduct an independent research. I really appreciate her scientific guidance and willingness to discuss the results. The skills I have gained in her laboratory will be invaluable in my future career.

My deep gratitude goes to Prof. Dr. Azat Bilalov from Kazan National Research Technological University for the fruitful collaboration during his two visits to Paderborn and for giving important advises both experimentally and theoretically.

Also, there are a lot of people who have contributed to this work and without them this thesis would have been impossible. I want to thank:

Kristina Duschik, Nadine Buitkamp, Prof. Dr. Jörg Lindner, Dr. Yvonne Hertle (Bielefeld University), Prof. Dr. Cosima Stubenrauch and Dr. Natalie Preisig (University of Stuttgart) for electron microscopy measurements.

Frank Lüdel (Bielefeld University), Dominik Klaus for the small angle X-ray measurements.

Karin Stolte and Dr. Hans Egold for the high-resolution NMR measurements.

Dr. Adrian Keller for his help with AFM measurements.

Matthias Siebert, Martin Siebrecht, Xiao Fu for the help with sample preparation and NMR measurements.

Deutsche Forschungsgemeinschaft (Graduate program 1464 “Micro- and Nanostructures in Optoelectronics and Photonics) for the financial support.

Anna Ezhova, Mingxue Tang, Felix Grewe, Melanie Kube, Rance Kwamen, Martin Butschies, Tiago Mendes Ferreira, Amin Ordikhani-Seyedlar, Emmanuele Ferrarotto, all past and present members of AK Schmidt and colleagues from Physical Chemistry Department for the friendly working environment.

Diliara, I am grateful to you for cheering me up and believing in me in the most difficult moments. Even though we are far apart, I feel your encouragement and inspiration.

Finally, I would like to thank my family and friends for the constant moral and emotional support along the way. I was very happy to continue our family tradition.



# Content

1 Introduction .....	4
2 Theoretical background.....	7
2.1 Surfactants .....	7
2.2 Lyotropic liquid crystals .....	8
2.3 Characterization of liquid crystalline phases .....	12
2.4 Interaction of DNA with cationic surfactants .....	23
2.5 Synthesis of metallic nanoparticles.....	27
2.6 Optical properties of metallic nanoparticles. Influence of size, shape, dielectric environment, and particle interaction. ....	29
3 Formation of silver nanoparticles in liquid crystalline phases of aqueous solution of monoolein.....	40
3.1 Introduction.....	40
3.2 Verification of the phase behavior.....	42
3.3 Mechanism of silver nanoparticle formation .....	43
3.4 Influence of the nanoparticle formation on the liquid crystalline structure.....	45
3.5 Nanoparticle formation in the cubic Ia3d phase .....	47
3.6 Effect of Ag <sup>+</sup> concentration on nanoparticle formation in the cubic Ia3d phase.....	54
3.7 Synthesis of nanoparticles in the cubic Pn3m phase. Effect of Ag <sup>+</sup> concentration and aging time .....	56
3.8 Long-term stability of the bicontinuous cubic liquid crystalline mesophases.....	60
3.9 Synthesis of nanoparticles in the inverse hexagonal phase .....	60
3.10 Summary.....	65
4 Synthesis of silver nanoparticles in DNA-containing monoolein-based liquid crystals.....	66
4.1 Introduction.....	66
4.2 Influence of nanoparticle formation on the liquid crystalline structure.....	67
4.3 Kinetics of nanoparticle formation in the DNA-containing cubic phase.....	68
4.4 Effect of Ag <sup>+</sup> concentration and UV irradiation time on nanoparticle formation.....	71

4.5 Spontaneous formation of silver nanoparticles. Effect of aging.....	75
4.6 Summary.....	78
5 Chemical and photochemical synthesis of silver nanoparticles in the DTADNA/lecithin/water ternary system .....	80
5.1 Introduction.....	80
5.2 Spontaneous formation of silver nanoparticles in the DNA-free lecithin/water binary lamellar phase. Effect of Ag <sup>+</sup> concentration and aging time .....	82
5.3 Photoinduced formation of silver nanoparticles in the DNA-containing lamellar phase .....	90
5.4 Photoinduced formation of silver nanoparticles in the DNA-containing inverse hexagonal phase.....	94
5.5 Summary.....	100
6 Photoinduced formation of silver nanoparticles in the DTADNA/2-hydroxypropyl- $\beta$ -cyclodextrin/water system.....	101
6.1 Introduction.....	101
6.2 Synthesis of silver nanoparticles in isotropic DTADNA/HP $\beta$ CD solution. Effect of Ag <sup>+</sup> concentration and UV irradiation time on the nanoparticle formation .....	103
6.3 Photochemical formation of silver nanoparticles in the hexagonal phase. Effect of composition and irradiation time .....	109
6.4 Photoinduced formation of silver nanoparticles in the tetragonal phase .....	114
6.5 Summary.....	117
7 Conclusion and outlook.....	119
Appendix .....	123
A1 Experimental procedures .....	123
A2 Synthesis of silver nanoparticles in the ternary systems sodium octanoate/octanoic acid/water and sodium octanoate/decanol/water .....	129
A3 Additional data.....	134
Abbreviations and symbols:.....	146
References.....	148



# 1 Introduction

The research of nanostructured metallic materials has received a lot of attention in the fields of colloid and material science due to their unique optical, electric and magnetic properties, compared to the corresponding bulk materials [1]. Based on their properties, extensive application of the noble metallic nanoparticles has been found in photonics, electronics, imaging and biomedical sensing. A lot of physical and chemical methods have been used to prepare nanoparticles, and most of them are based on a so-called template method, where the metal precursor is limited in nano-size domains and nanoparticles are synthesized by in situ reactions. Block copolymer films [2], charged polymeric brushes [3], mesoporous silica [4], DNA [5], single and multi-walled carbon nanotubes [6], and microemulsions [7] can be used as a template for the preparation of nanoparticles. The size, shape, and polydispersity of the nanostructures inside these templates is affected by the structure and dimensions of the domains.

Due to the broad field of potential applications, there is also a growing interest in developing new green methods for the controlled synthesis of nanostructured materials. Due to the biocompatibility and rich polymorphism, lyotropic liquid crystals formed by biologically-friendly amphiphilic molecules are particularly interesting for the synthesis of metallic nanoparticles. Such systems have an advantage because the dimensions of the nanoreactors can be varied by changing the composition and temperature which makes them suitable systems to control size and morphology of the nanoparticles [8]. Of particular interest for the preparation of nanoparticles are DNA-containing lyotropic liquid crystals. While both DNA and surfactants have been successfully used for the synthesis of silver nanoparticles, the templating properties of DNA-cationic surfactant complexes and DNA-containing lyotropic liquid crystals are almost unknown.

This thesis is focused on the synthesis of silver nanoparticles in various lyotropic liquid crystalline phases formed by biologically friendly surfactants with or without cationic surfactant-DNA complexes in aqueous solution with different additives. Two different synthetic strategies have been used. Firstly, nanoparticles were synthesized by the chemical reduction of silver ions by the nonionic or zwitterionic surfactant molecules which were used to form the liquid crystalline phase. Secondly, by using DNA-containing liquid crystals, silver nanoparticles were synthesized via photoreduction of the Ag-DNA complexes where DNA itself may act as templating and photosensitizing agent.

The effect of the formation of silver nanoparticles on the lyotropic liquid crystalline phase was investigated by  $^2\text{H}$  and  $^{31}\text{P}$  NMR spectroscopy, small angle X-ray scattering, and polarizing optical microscopy. The influence of the template mesophase on the formation rate and nanoparticle size and morphology was studied using UV-spectroscopy, transmission electron and atomic force microscopy techniques.

The present thesis consists of 7 chapters. In chapter 2, the introduction to the surfactant systems and methods used for characterization of the liquid crystalline phases is given. A brief review of the research background and work related to the synthesis and optical properties of silver nanoparticles is also provided. This will focus on optical properties, in particular on the surface plasmon resonance, and its dependence on the nanoparticle size, shape and dielectric environment. Simulation of UV-Vis absorption spectra will be provided to help understand experimental results.

Chapter 3 will focus on the synthesis of silver nanoparticles in liquid crystalline phases formed by monoolein. It is shown that monoolein can reduce  $\text{Ag}^+$  to  $\text{Ag}^0$ ; therefore, no external reducing agent is needed. The participation of the surfactant molecules in the redox reaction was investigated by FTIR and  $^1\text{H}$  NMR spectroscopy. Since no external strong reducing agent is used the reaction is slow and the formation rate and morphology of silver nanoparticles can be monitored in situ by measuring the surface plasmon resonance band in the UV-Vis region.

In chapter 4 the chemical and photochemical synthesis of silver nanoparticles in DNA containing cubic lyotropic liquid crystalline phases formed by monoolein is investigated. Nanoparticles were obtained by spontaneous formation due to the  $\text{Ag}^+$  reduction by monoolein as well as by irradiation of the Ag-DNA complex dispersed in liquid crystal.

In chapter 5 the results of the chemical and photochemical synthesis of silver nanoparticles in lamellar and inverse hexagonal liquid crystalline phases formed in the ternary system DTADNA/lecithin/water will be presented. DTADNA is the complex formed by dodecyltrimethylammonium (DTA) as cation and DNA. The influence of the template structure on nanoparticle formation and of nanoparticle formation on the liquid crystalline mesophase is discussed.

In chapter 6, the synthesis of silver nanoparticles in the isotropic and two liquid crystalline phases of the DTADNA/2-hydroxypropyl- $\beta$ -cyclodextrin/water ternary system is reported. A possible mechanism resulting in two different particle morphologies, depending on the

concentration ratio  $[\text{Ag}^+]/[\text{DNA}_{\text{base}}]$  and the type of the liquid crystalline mesophase is proposed.

Finally, chapter 7 summarizes and compares the results of this thesis, and outlines some work which can be performed in the future as an extension of this project.

## 2 Theoretical background

### 2.1 Surfactants

Surfactants (surface active agents) are amphiphilic molecules, consisting of both a lyophobic (hydrophobic) and a lyophilic (hydrophilic) group. The hydrophobic group consists of one or more long and flexible hydrocarbon chains (alkyl or alkylaryl). It may also be a siloxane or fluorocarbon chain. The hydrophilic head is polar and may be either ionic or nonionic. Depending on the nature of the head group, surfactants are classified as ionic (cationic or anionic), nonionic and zwitterionic (containing both anionic and cationic charge). Some examples of different types of surfactants which were used in the present work are shown in figure 2.1.

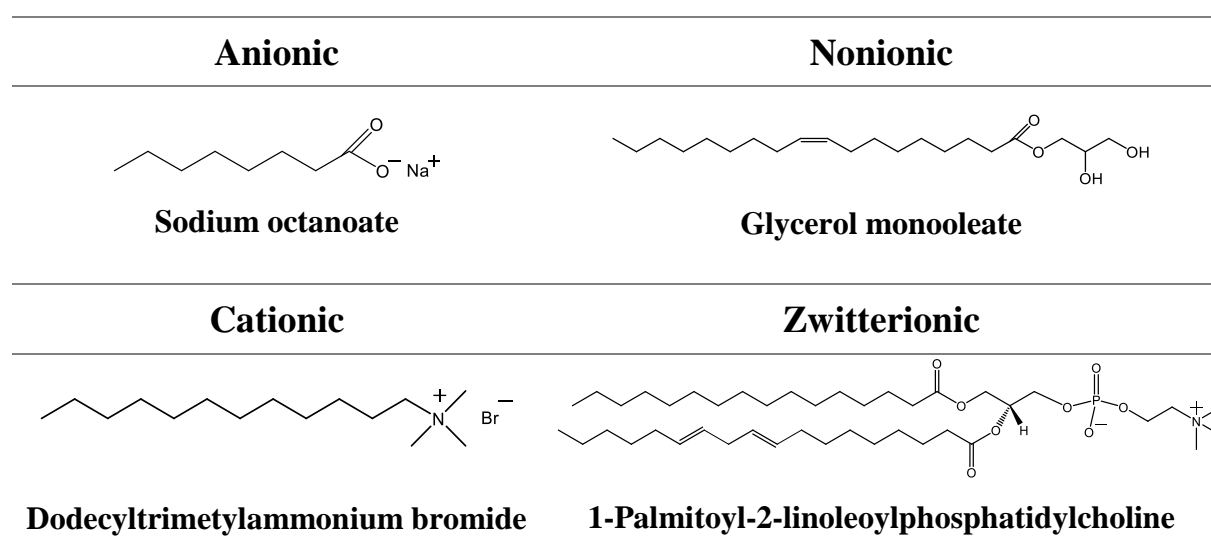


**Figure 2.1.** Some examples of the different kinds of surfactants.

Due to their amphiphilic properties, surfactant molecules tend to adsorb at surfaces and interfaces lowering the surface tension of the liquid. Another fundamental property of surfactants is their ability to form self-assembled supramolecular aggregates called micelles. The driving force for micelle formation in aqueous solution is the effective interaction between the hydrophobic parts of the surfactant molecules. The concentration when micelles start to form is called the critical micelle concentration or CMC. As the concentration increases, the size and shape of the micelles can change, from spherical to cylindrical, disklike, wormlike or branched. Depending on temperature, surfactant and solvent nature, surfactants may form normal or inverse molecular aggregates. Double-tailed surfactants, like phosphatidylcholines can form spherical bilayer aggregates called vesicles. Such aggregates can consist of a single

bilayer, as in the cell, or they can be made up of multiple bilayers. The multilamellar vesicles are often called liposomes. Typically, vesicles are thermodynamically unstable and phase separate into a lamellar liquid crystalline phase and a dilute aqueous solution.

## 2.2 Lyotropic liquid crystals

By definition, liquid crystals (LC) are intermediate states of matter. Unlike liquids but like crystals they have orientational and positional order. There are two main classes of liquid crystals: thermotropic and lyotropic ones. Thermotropic LC are formed by geometrically anisotropic molecules, and the phase behavior is controlled by a temperature variation. In contrast, lyotropic liquid crystals (LLC) are composed of at least two components: surfactant molecules and water (or any other selective solvent). The behavior of lyotropic liquid crystalline structures depends on sample composition as well as temperature.

The most widely used nomenclature of lyotropic liquid crystalline phases was proposed by Luzatti and is partly adopted in this thesis [9]. The capital letter refers to the phase morphology, e.g. H for hexagonal, L for lamellar, T for tetragonal, and Q with corresponding crystallographic space group number for cubic phases. However, in the chapters 3–7 cubic phases are named according to Hermann-Mauguin notation [10]. Subscripts I and II are used to distinguish the normal (oil in water) and inverse (water in oil) mesophase topology. Often, an additional subscript shows the chain conformation:  $c$  – crystalline,  $\beta$  – gel-like,  $\alpha$  – fluid-like. A prime symbol at this subscript indicates that the alkyl chains are tilted with respect to the bilayer surface (e.g.  $L_{\beta'}$  is the tilted gel lamellar phase).

The arrangement of the surfactant molecules in LLC phases can be explained using the critical packing parameter (CPP), describing the effective molecular shape. The dimensionless packing parameter  $P$ , introduced by Israelachvili et al. is defined as [11]:

$$P = \frac{V}{a_0 l}$$

where  $V$  is the volume of the lipophilic chain,  $a_0$  the interfacial area occupied by the hydrophilic headgroup, and  $l$  is the length of the lipophilic chain.

As a reference structure phosphatidylcholine with a cylindrical shape ( $P=1$ ), which tends to form a bilayer, is shown in figure 2.2. If the surfactant has a conical shape, like lysophosphatidylcholine ( $P=1/3$ ), or resembles a truncated cone ( $1/3 < P < 1/2$ ), the most

favorable aggregates will be spherical and cylindrical micelles, respectively. For surfactants with the shape of an inverted truncated cone ( $P > 1$ ), the preferred packings are inverse structures. The critical packing parameter allows a quite accurate prediction of the self-assembly of a surfactant molecule.

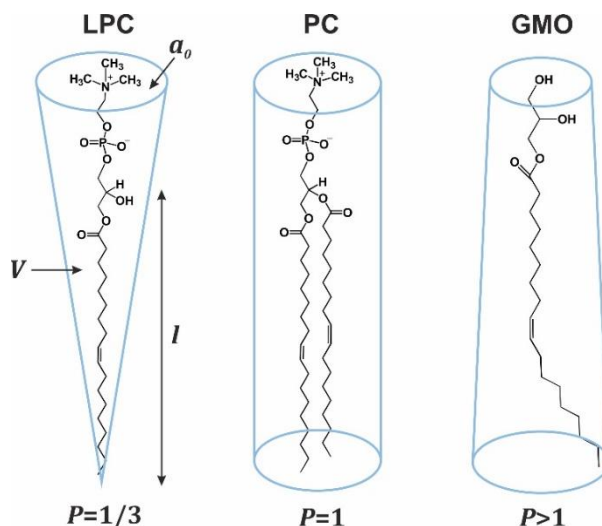


**Figure 2.2.** Critical packing parameter of lysophosphatidylcholine (LPC), phosphatidylcholine (PC) and glycerol monooleate (GMO).

Another model uses the surfactant monolayer as the basic structural unit of the surfactant aggregates. The flexible surface model considers that the surfactant layer always adopts a mean curvature that minimizes the Gibbs energy of the system, assigned as spontaneous curvature ( $H_0$ ) [12]. The packing of amphiphilic molecules is directly related to the surface curvature of the surfactant aggregates. The spontaneous monolayer curvature can be positive (towards the hydrocarbon region), zero (for a planar layer), or negative (towards water).

There are three basic liquid crystalline structures: hexagonal, lamellar and cubic. Figure 2.3 demonstrates the Fontell scheme, showing the phase sequence along with a schematic representation of different liquid crystalline phases [13]. For any known binary surfactant/water system this idealized phase sequence has not been observed in full, some phases are usually missing. However, the complete sequence has been found in the ternary Pluronic P84/p-xylene/water system [14].

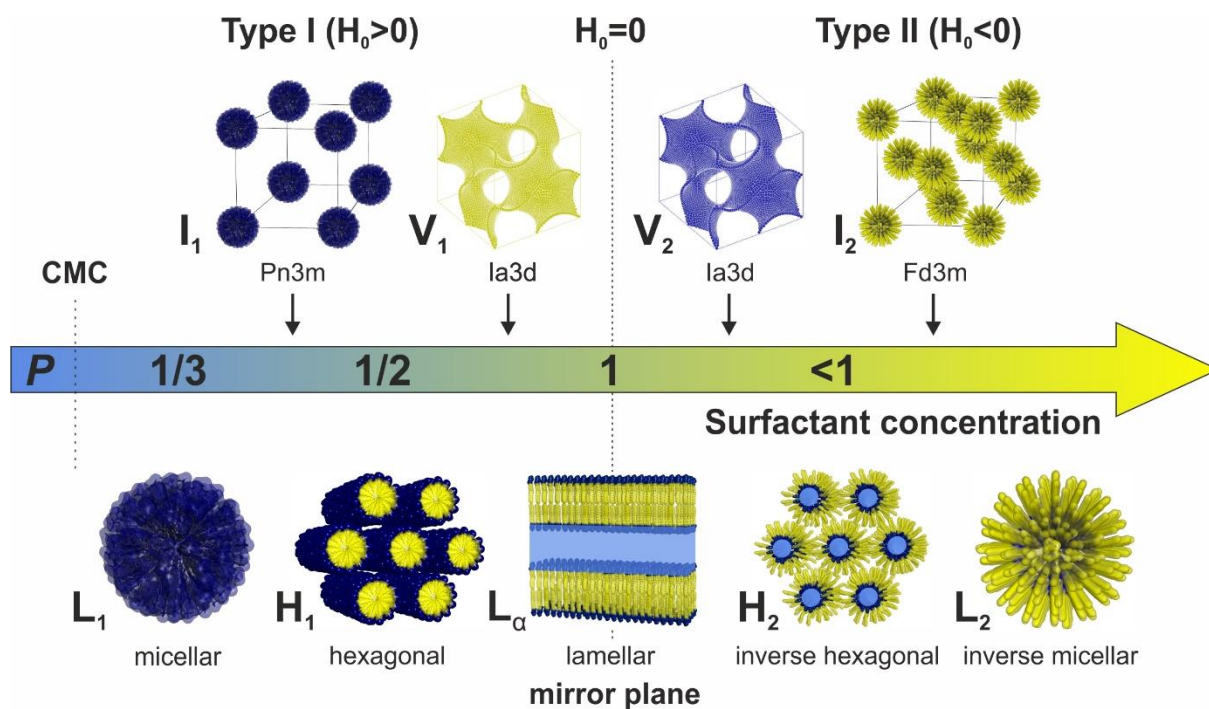


**Figure 2.3.** Schematic representation of the idealized liquid crystalline phase sequence, depending on the spontaneous curvature, critical packing parameter, and surfactant concentration. Notations for cubic phases: I is a micellar and V is a bicontinuous cubic phase.

The hexagonal phase is formed by infinitely long cylindrical micelles arranged into a two-dimensional hexagonal lattice. Hexagonal phases can be either normal or inverse. The first consists of cylindrical surfactant aggregates in a continuous water medium. The inverse hexagonal phase is formed by rod-like surfactant aggregates with a water core and aliphatic chains pointing outward. The diameter of the aqueous core is typically 20–100 Å, making the hexagonal phase a potentially attractive release matrix for hydrophilic drugs.

The lamellar phase consists of surfactant bilayers alternating with water layers. It is organized in such a way that the hydrocarbon chain of the surfactant molecule is shielded from contact with water molecules. Several types of the lamellar phase have been characterized: crystalline lamellar ( $L_c$ ), fluid lamellar ( $L_\alpha$ ) and gel lamellar ( $L_\beta$ ) phases [15].

Cubic phases are not very common in lyotropic mixtures and usually exist in narrow regions of the phase diagram. So far, seven cubic phases have been identified with six different crystallographic space groups ( $Q^{212}$ ,  $Q^{223}$ ,  $Q^{224}$ ,  $Q^{227}$ ,  $Q^{229}$ ,  $Q^{230}$ ) [16]. All of them are optically isotropic but may present shear-induced birefringence. Micellar cubic phases consist of an ordered 3D packing of micellar aggregates. The micelles are more elongated rather than spherical, allowing a better packing in the cubic cell. The most common micellar cubic phases, which have been characterized,  $Q^{223}$  (Pm3n) and  $Q^{227}$  (Fd3m), are cubic micellar phases with

normal and inverse topology.  $Q^{223}$  was observed in two-component surfactant-water mixtures, while  $Q^{227}$  requires water-miscible and water-immiscible components and a solvent. Also, two more discontinuous type I cubic phases have been reported: bcc-packed  $Q^{229}$  (Im3m) and fcc-packed  $Q^{225}$  (Fm3m) [17].

Another type of cubic phases is bicontinuous. The term “bicontinuous” indicates that these structures are continuous not only in the solvent but also in the surfactant. For a bicontinuous cubic phase the arrangement of the surfactant bilayer in the cubic cell is based on the so-called infinite periodic minimal surface (IPMS), having a negative Gaussian and zero mean curvature. Three different types of IPMS have been identified according to their crystallographic space group: the diamond (D) type of IPMS corresponding to the Pn3m primitive lattice ( $Q^{224}$ ); the primitive (P) type of IPMS, which corresponds to the Im3m body-centered lattice ( $Q^{229}$ ), and the gyroid (G) type of IPMS corresponding to the Ia3d body-centered lattice ( $Q^{230}$ ). Their unit cells are schematically depicted in figure 2.4. The G-type is the only bicontinuous cubic phase observed in both normal and reverse topology [18].

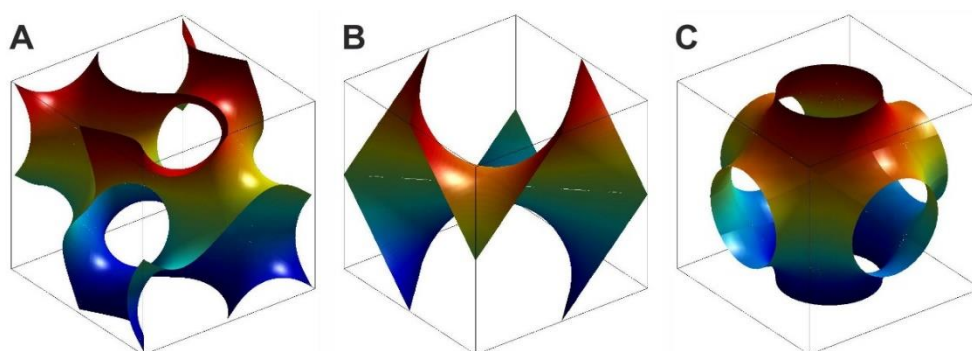


**Figure 2.4.** Schematic representation of infinite periodic minimal surfaces: (A) gyroid (Ia3d space group), (B) double diamond (Pn3m space group), (C) primitive (Im3m space group). In the case of a normal topology, water drapes the surface, while for inverse structures the surface is the midpoint of the surfactant bilayer.

The cubic phase  $Q^{212}$  shows an intermediate behavior between bicontinuous and discontinuous micellar cubic phases. It was found in the ternary system monoolein/water/cytochrome c [19]. The addition of protein modifies the original  $Q^{230}$  (Ia3d) phase by replacing one of the sets of lipid/water channels with lipid/protein inverse micelles, making the cubic phase chiral.

In addition to the above-mentioned phases tetragonal and rhombohedral [9], rectangular [20] and several intermediate mesophases, ribbon [21], mesh [22], and noncubic bicontinuous [23] phases have been reported.

## 2.3 Characterization of liquid crystalline phases

### NMR of liquid crystalline systems

Nuclear magnetic resonance is a powerful method for the investigation of lyotropic liquid crystals. Given the number of NMR active nuclei and the variety of available NMR techniques, it can provide information about chemical structure, molecular orientation and conformation, self-diffusion and molecular dynamics, phase structure and phase transition.

### Quadrupolar interaction

Quadrupolar nuclei (nuclei with a spin number  $I \geq 1$ ) can interact with an electric field gradient (EFG) at the site of the nucleus. The quadrupole coupling depends on the orientation of the electric field gradient (and therefore the molecular orientation) with respect to the external magnetic field and is expressed in terms of second-rank tensors. It is possible to choose the axis frame where the EFG is defined in such a way that the resulting tensor is diagonal [24]. Thus, it only contains  $V_{xx}$ ,  $V_{yy}$ , and  $V_{zz}$  elements of the electric field gradient. This axis frame is called principal axis frame, designated as PAF (figure 2.5). The coordinate system is often chosen in such a way that  $|V_{zz}| \geq |V_{yy}| \geq |V_{xx}|$ .

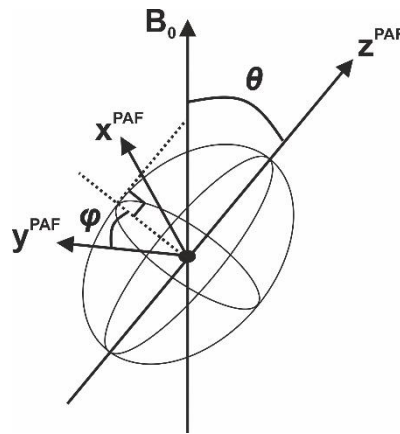


**Figure 2.5.** Schematic representation of the principal axis frame and polar and azimuthal angles describing the orientation of  $B_0$ .

For a nucleus with a spin  $\geq 1$  in a strong magnetic field, two energy terms must be considered: Zeeman and quadrupolar interaction (in first order). This leads to the following equation

$$E = -\frac{\gamma h}{2\pi} m_I B_0 + e^2 Q q \frac{3m_I^2 - I(I+1)}{8I(2I-1)} (3\cos^2\theta - 1 + \eta \sin^2\theta \cos 2\varphi) \quad (2.1)$$

where  $\gamma$  is the gyromagnetic ratio,  $B_0$  the external magnetic field,  $m_I$  the nuclear spin magnetic quantum number,  $eq$  the largest component ( $V_{zz}$ ) of the electrical field gradient, and  $eQ$  the nuclear quadrupole moment.  $\theta$  and  $\varphi$  are the polar and azimuthal angles of  $B_0$  in the principal axis frame of the EFG, and  $\eta = \frac{V_{xx}-V_{yy}}{V_{zz}}$  ( $0 \leq \eta \leq 1$ ) is the asymmetry parameter describing the deviation of the electric field gradient from axial symmetry [25].

The quadrupole interaction affects the Zeeman energy levels, as shown in figure 2.6.

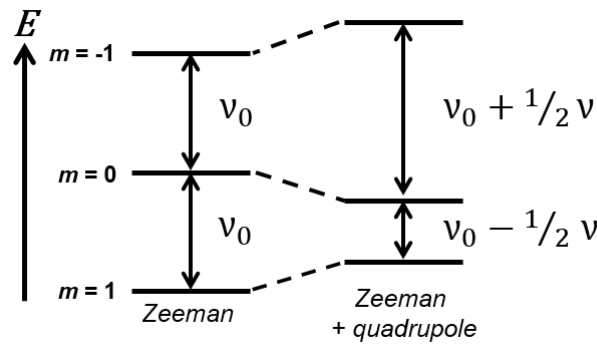


**Figure 2.6.** Splitting of the energy levels in the magnetic field for  $I=1$  spins.

For the deuterium nucleus, the spin number  $I=1$  and, in many cases, the electric field gradient is axially symmetric, so the asymmetry parameter  $\eta$  vanishes and equation (2.1) can be simplified:

$$E_{m_I} = -\frac{\gamma h}{2\pi} m_I B_0 + e^2 Qq \frac{3m_I^2 - 2}{8} (3\cos^2\theta - 1) \quad (2.2)$$

where  $\theta$  is the angle between  $B_0$  and the z-axis of the PAF of the electric field gradient.

By applying the selection rule  $\Delta m_I = \pm 1$ , the resulting  $^2\text{H}$  NMR spectrum is a doublet with the difference  $\Delta\nu$  between the two transition frequencies given by

$$\Delta\nu = \frac{\Delta\nu_q}{2} (3\cos^2\theta - 1) \quad (2.3)$$

where  $\Delta\nu_q = \frac{3e^2 Qq}{2h}$  is the quadrupole coupling constant.

The typical spectra from a sample with single orientation of  $\theta$  and from a powder sample with a spherical distribution of EFG orientations are shown in figure 2.7. The latter is also known as Pake powder pattern [26].

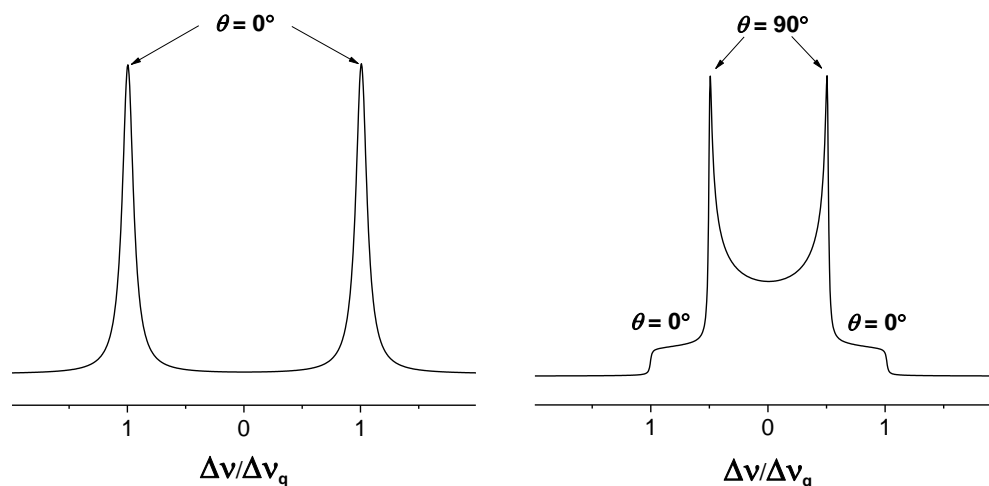


**Figure 2.7.**  $^2\text{H}$  NMR spectra of a sample oriented parallel to the external magnetic field (left), and a typical powder spectrum with a spherical distribution of orientations probability (right).

## $^2\text{H}$ NMR of surfactant systems

$^2\text{H}$  NMR is an important technique for the study of the liquid crystalline phase behavior in both single- and multiphase samples. Deuterium can be introduced to the surfactant system in two different ways: either by using the partially or fully deuterated surfactant or by replacing water with  $\text{D}_2\text{O}$  [27]. The first method can provide information about the degree of motional and orientational order of the molecule or specific groups in the surfactant. It will not be discussed further. The second method gives information about surface curvature and the orientational order of the surfactant aggregates, which can be used for the phase identification and characterization of phase transitions.

$\text{D}_2\text{O}$  molecules can be either associated with surfactants aggregates or be located as free water in the aqueous channels. The bound molecules are in dynamic exchange with free water molecules. Therefore, the quadrupole splitting is given as

$$\Delta\nu = p_f \Delta\nu_f + p_b \Delta\nu_b$$

where  $p_f$  and  $p_b$  is the fraction of free and bound water molecules, respectively. For free water  $\Delta\nu_f$  is zero due to the rapid molecular tumbling of the water molecules. Considering the fraction of bound water ( $p_b$ ) equation (2.3) can be rewritten as

$$\Delta v = \frac{1}{2} \Delta v_q p_b (3 \cos^2 \theta_q - 1) \quad (2.4)$$

For the complete understanding of the  $^2\text{H}$  NMR spectra of surfactant aggregates in aqueous solution three different reference frames should be considered, as schematically shown in figure 2.8.

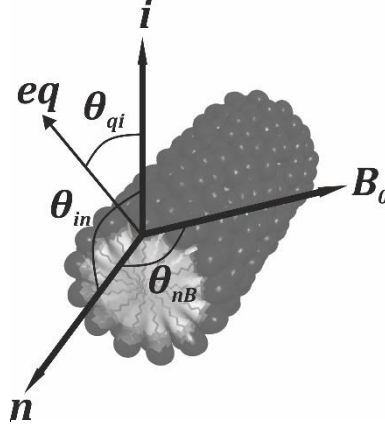


**Figure 2.8.** Reference frames and corresponding angles used to describe NMR in surfactant systems.  $\theta_{qi}$  is the angle between the z-axis of the PAF of the electric field gradient and the normal to the interface  $i$ ,  $\theta_{in}$  is the angle between the normal to the interface and the director of the liquid crystalline phase  $n$ , and  $\theta_{nB}$  is the angle between the director of the phase and the external magnetic field  $B_0$ . Redrawn from [25].

Due to the motional averaging (2.4) can be written as

$$\Delta v = \Delta v_q p_b S_{qi} \frac{1}{2} (3 \cos^2 \theta_{in} - 1) \frac{1}{2} (3 \cos^2 \theta_{nB} - 1) \quad (2.5)$$

where  $S_{qi}$  is the order parameter of the bound water describing its orientation with respect to the interface

$$S_{qi} = \frac{1}{2} (3 \cos^2 \theta_{qi} - 1) \quad (2.6)$$

Since for the lamellar phase  $\theta_{in}=0$ , eq. (2.5) becomes

$$\Delta v = \Delta v_q p_b S_{qi} \frac{1}{2} (3 \cos^2 \theta_{nB} - 1) \quad (2.7)$$

In the hexagonal phase, due to the small radius of the cylindrical micelles, lateral diffusion of the water molecules about the cylindrical axis further averages  $\Delta v$ . The director of the phase

lies perpendicular to the interface ( $\theta_{in} = 90^\circ$ ) so the observed splitting is half as big as for the lamellar phase

$$\Delta\nu = \Delta\nu_0 p_b S_{qi} \frac{1}{4} (3 \cos^2 \theta_{nB} - 1) \quad (2.8)$$

Introducing another order parameter  $S_{in} = \frac{1}{2} (3 \cos^2 \theta_{in} - 1)$  that describes the deviation from the lamellar phase, equation (2.5) becomes

$$\Delta\nu = \Delta\nu_0 p_b S_{qi} S_{in} \frac{1}{2} (3 \cos^2 \theta_{nB} - 1) \quad (2.9)$$

For a lamellar phase,  $S_{in}=1$ , for a hexagonal phase  $S_{in}= -1/2$ , and for a cubic phase  $S_{in}=0$ . Therefore, the  $^2\text{H}$  NMR spectra of all cubic phases exhibit zero splitting, producing only a single narrow peak. A comparison of the  $^2\text{H}$  NMR spectra from different liquid crystalline phases is shown in figure 2.9.

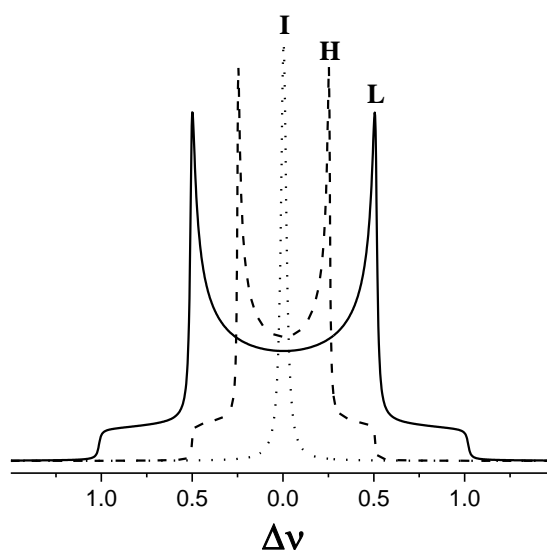


**Figure 2.9.** Schematic representation of  $^2\text{H}$  NMR spectra of different liquid crystalline phases with identical composition. I – isotropic (micellar, sponge, cubic), H – hexagonal, L – lamellar phases.

## Chemical shift anisotropy: $^{31}\text{P}$ NMR of surfactant systems

The natural abundance of the  $^{31}\text{P}$  nucleus is 100% and no synthetic labeling is needed.  $^{31}\text{P}$  has a nuclear spin  $I = 1/2$  and in an external magnetic field  $B_0$  there are two eigenstates of the spin with magnetic quantum number  $m = -1/2$  and  $m = 1/2$ . The total energy of the nuclear spin is expressed as the sum of the Zeeman and the chemical shielding interactions

$$E = -\gamma\hbar(1 - \sigma)B_0 \quad (2.10)$$

where  $\sigma$  is the chemical shielding constant.

The resonance frequency of a particular nucleus in a molecule depends on the electronic environment produced by the surrounding electrons that shield the nucleus from the external magnetic field. As a result, the nuclei at different sites in the molecule experience different shielding, and hence have a different chemical shift depending also upon the orientation of the molecule with respect to  $B_0$ . Therefore, in the solid state or in an anisotropic medium the chemical shift is not a scalar quantity like in solution NMR but must be expressed as a second-rank tensor. The principal components of the chemical shift tensor,  $\delta_{11}$ ,  $\delta_{22}$  and  $\delta_{33}$  are typically ordered from highest to lowest frequency [28]. Hence, the chemical shift  $\delta$  is expressed as

$$\delta = \delta_{iso} + \frac{1}{2} \delta_{CSA} (3 \cos^2 \theta - 1 + \eta \sin^2 \theta \cos 2\phi) \quad (2.11)$$

where  $\delta_{iso} = (\delta_{11} + \delta_{22} + \delta_{33})/3$  is the isotropic chemical shift,  $\delta_{CSA} = \delta_{11} - \delta_{iso}$  is the chemical shift anisotropy,  $\theta$  and  $\phi$  are the polar and azimuthal angles of  $B_0$  in the principal axis frame, and  $\eta = \frac{\delta_{33} - \delta_{22}}{\delta_{11}}$  is the asymmetry parameter showing the deviation from axial symmetry.

In a randomly oriented rigid sample, all angles between the principal axis frame and the external magnetic field are populated resulting in a  $^{31}\text{P}$  spectrum that is the sum of all possible orientations (figure 2.10 A). The principal values of the chemical shift anisotropy tensor can be obtained from the powder spectrum;  $\delta_{11}$  and  $\delta_{33}$  define the outermost edges and  $\delta_{22}$  is attributed to the peak. The direction of the principal axes in the molecular system can be found by studying a single crystal of known symmetry [29].

However, in membranes phospholipid molecules are not rigid and undergo different kinds of motion, as shown in figure 2.10 B and C. In the simplest case, molecular rotation occurs around the 1 axis (corresponding to  $\delta_{11}$ ), averaging the values  $\delta_{22}$  and  $\delta_{33}$ . Thus, for an axially

symmetric system the chemical shift will have the same value for the field anywhere in the 2-3 plane, labeled  $\delta_{\perp}$ , and a different value when the field is parallel to the rotation axis, labeled  $\delta_{\parallel}$ .

In the case of biological membranes, a rapid motion of limited amplitude occurs, in addition to the rotation about the 1 axis. The 1 axis now moves within a cone, resulting in partial averaging of  $\delta_{\perp}$  and  $\delta_{\parallel}$ , which yield smaller values of the chemical shift anisotropy, labeled  $\delta'_{\parallel}$  and  $\delta'_{\perp}$  (figure 2.10, C). As a consequence, the spectrum is still axially symmetric but with reduced chemical shift anisotropy (CSA). When the amplitude becomes unrestricted, the motion is effectively isotropic, so the CSA pattern disappears and only a single line with isotropic chemical shift is observed, similar to the solution NMR spectrum as shown in figure 2.10, D [30].

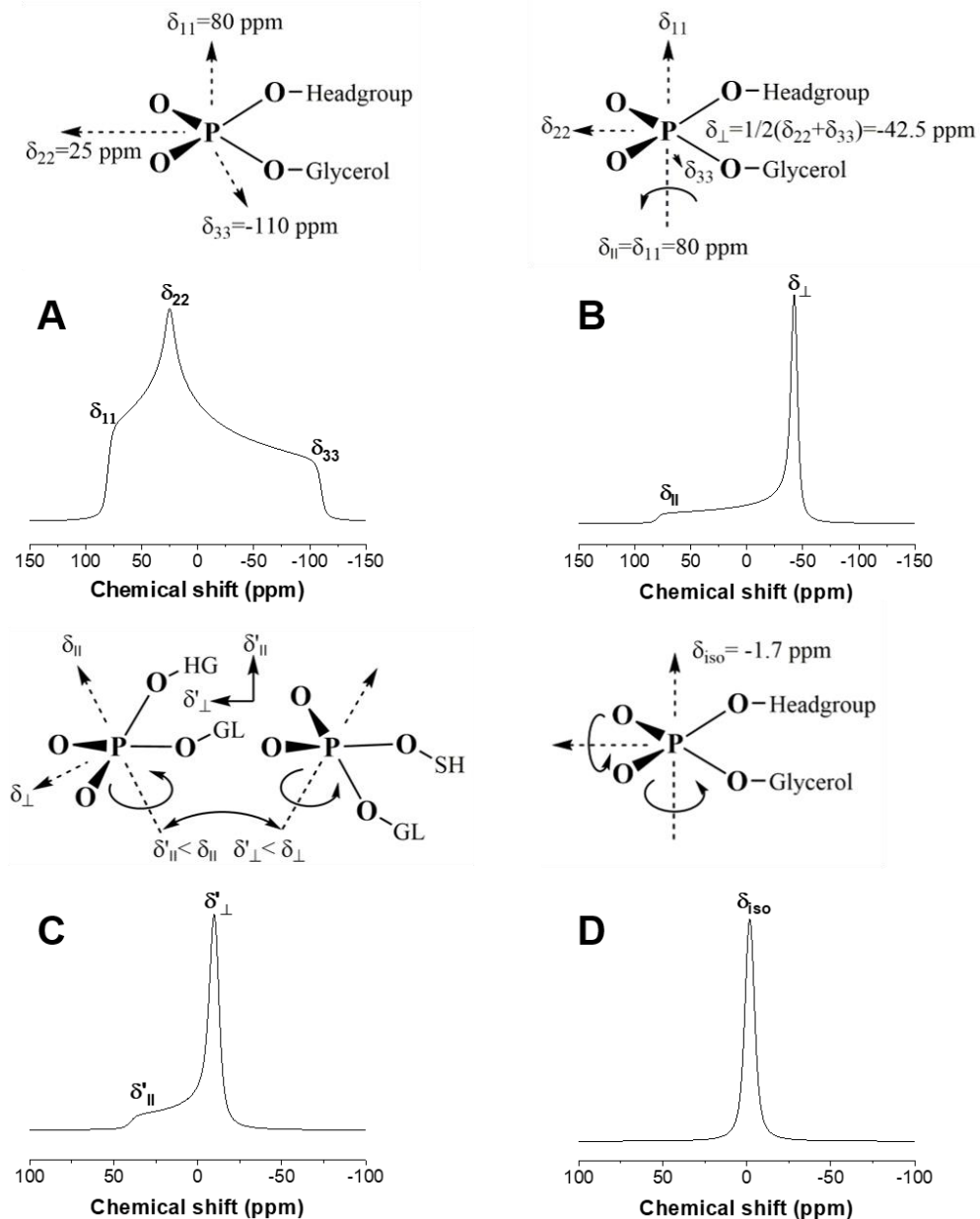


**Figure 2.10.** Different kinds of molecular motion of phospholipids, redrawn from [30].

$^{31}\text{P}$  NMR is also sensitive to lipid polymorphism. In  $^2\text{H}$  NMR  $\text{H}_{\parallel}$  and  $\text{L}_{\alpha}$  phases result in similar powder spectra and phase assignment requires additional information, such as sample orientation with respect to the magnetic field or relaxation time. In comparison, hexagonal and lamellar phase often can be identified directly from the  $^{31}\text{P}$  NMR spectrum (figure 2.11). When a transition occurs from the lamellar to the hexagonal phase, the effective chemical shift anisotropy,  $\Delta\delta$ , changes its sign and is reduced by a factor of one half. The director of the phase is along the cylinder axis of the rod-like micelles, labeled  $\delta^H_{\parallel}$ . Along this axis, the field is approximately normal to the hydrophobic group, so the expected chemical shift is roughly the same as for  $\delta^L_{\perp}$ . Due to the rapid molecular motion around the cylindrical axis of the hexagonal phase  $\delta^H_{\perp}$  is an average value of  $\delta^L_{\perp}$  and  $\delta^L_{\parallel}$ . Hence,

$$\begin{aligned}\delta^H_{\parallel} &= \delta^L_{\perp} \\ \delta^H_{\perp} &= \frac{1}{2}(\delta^L_{\perp} + \delta^L_{\parallel}) \\ \Delta\delta^H &= \frac{1}{2}\Delta\delta^L\end{aligned}\tag{2.12}$$

This allows one to monitor transitions between two phases and to assign phases with rather high certainty. However, the phase structure also should be confirmed by additional techniques, like freeze-fracture electron microscopy or small angle X-ray diffraction because the change of the headgroup conformation or the location of motional axis relative the phospholipid moiety can cause additional spectral changes, making phase assignment less certain.

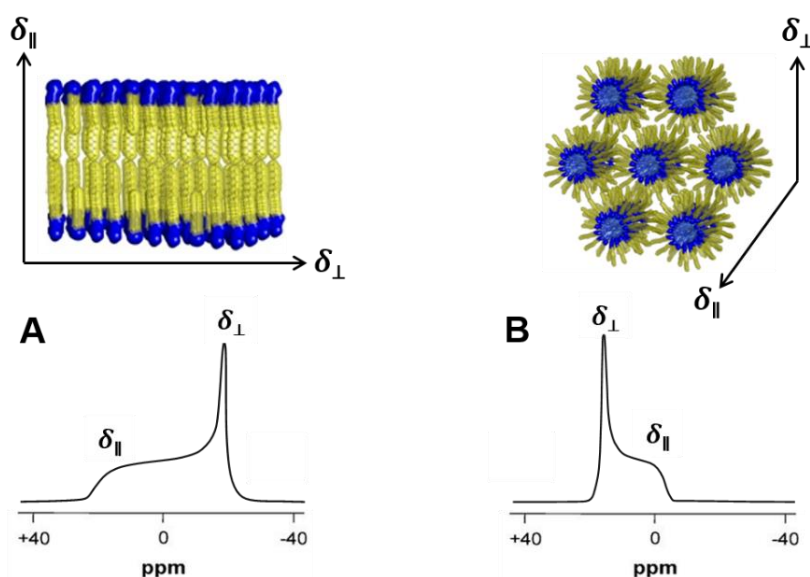


**Figure 2.11.** Static  $^{31}\text{P}$  NMR spectra of lamellar (A) and inverse hexagonal (B) liquid crystalline phases.

In the bicontinuous cubic phase the lipid lateral diffusion over the curved periodic minimal surface leads to fast molecular reorientation. Due to the phase symmetry, this molecular motion averages the CSA tensor to its isotropic value. The resulting  $^{31}\text{P}$  NMR spectrum is similar to the spectra of micelles and small vesicles.

High resolution solution NMR and MAS solid state NMR are often used to obtain information about the composition of phospholipid mixtures, both quantitatively and qualitatively. In addition to the phospholipids,  $^{31}\text{P}$  solid state NMR can be used for investigation of DNA structure and dynamics. Studies of  $^{31}\text{P}$  chemical shift anisotropy lineshapes, and relaxation times have provided information about the range of motions of the phosphate group in different forms of DNA [31]. It was found that the DNA conformational transition upon hydration is accompanied by a gradual decrease of the spectral linewidth with two plateaus in the regions corresponding to A- and B-form of DNA.

### Small angle X-ray scattering

Small angle X-ray scattering (SAXS) is a powerful method to study the structure of both disordered and ordered systems with electron density fluctuations on the length scale from 100 nm down to several Ångström. In X-ray diffraction, a parallel beam of X-rays with a wavelength comparable to atomic distances irradiates the sample and is scattered in all directions from the electrons in the sample. X-ray experiments are sensitive to electronic density contrasts in the liquid crystalline structures, coming from different electronic distributions of polar heads of the amphiphilic molecules, of the solvent, and of the hydrocarbon chains. When the X-ray beam is incident on a set of periodic points in a lattice, diffraction maxima occur in certain directions where the scattered X-rays are in phase (figure 2.12).

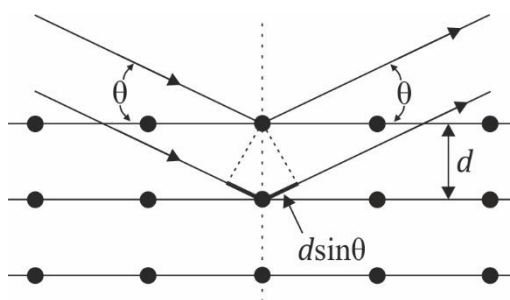


**Figure 2.12.** Schematic representation of Bragg reflection.

There are two regions of the diffraction pattern that are used to study the structure and dynamics of the liquid crystalline mesophase. Small angle X-ray scattering gives information about the phase structure and the dimensions of the unit cell in LLC [32]. Wide angle X-ray scattering (WAXS) provides information about the short-range order of the system, like the packing of the surfactant hydrocarbon chains, and can be used to distinguish between the crystal, gel and fluid lamellar phases [33]. Also, X-ray scattering can be used to study the effect of environmental conditions (temperature, pH, pressure, ionic strength), different additives, such as drug molecules, proteins or DNA, on the phase behavior of the liquid crystals [34].

According to Bragg's law, constructive interference between rays reflected by planes occur when the path difference,  $2d \sin \theta$  equals an integral number of wavelength

$$n\lambda = 2d \sin \theta \quad (2.13)$$

The scattering vector  $q$  is defined by

$$q = \left(\frac{4\pi}{\lambda}\right) \sin \theta \quad (2.14)$$

where  $2\theta$  is the scattering angle and  $\lambda$  is the wavelength of the incoming X-rays. Typically, Cu- $K_\alpha$  radiation with  $\lambda=1.542 \text{ \AA}$  is used.

The lattice spacing can be calculated according to

$$d = \frac{2\pi}{q} \quad (2.15)$$

The diffraction pattern is related to the reciprocal lattice described by the Miller indices ( $hkl$ ) of the lattice planes. Single diffracted points will be observed for diffraction from a single crystal; however, in powder diffraction, the domains of the powder liquid crystalline sample are randomly orientated and hence the reciprocal lattice is allowed to explore all possible orientations giving rise to diffraction rings rather than points. The long-range translational ordering of the surfactant aggregates and their arrangement in a 1-, 2- or 3-dimensional lattice result in Bragg reflections with characteristic ratios of the reciprocal spacings. The position of the diffraction peaks is reciprocally related to the distance between diffraction planes in the liquid crystalline phase. The lattice parameters can then be calculated from the corresponding diffraction peaks. For the cubic phase, not all reflections will be present depending on the particular symmetry and the structure factor of the electron density distribution. Table 2.1 summarizes the characteristic features of some lyotropic liquid crystalline phases that are described by a single lattice parameter ( $a$ ) or two parameters ( $a$  and  $c$ ).

**Table 2.1.** Indexing of lyotropic liquid crystalline mesophases used in this thesis.

Phase	Lattice spacing	Space group	Miller indices	Peak ratio
<b>Lamellar</b>	$d = \frac{a}{\sqrt{h^2}} \quad (2.16)$	Pm	100	1
			200	2
			300	3
			400	4
<b>Hexagonal</b>	$d = \frac{1}{\sqrt{\frac{4}{3a^2}(h^2 + k^2 + hk)}} \quad (2.17)$	P6mm	100	1
			110	$\sqrt{3}$
			200	2
			210	$\sqrt{7}$
			220	$\sqrt{12}$
<b>Bicontinuous cubic</b>	$d = \frac{a}{\sqrt{h^2 + k^2 + l^2}} \quad (2.18)$	Ia3d	211	$\sqrt{6}$
			220	$\sqrt{8}$
			321	$\sqrt{14}$
			400	4
			420	$\sqrt{20}$
			332	$\sqrt{22}$
		Pn3m	110	$\sqrt{2}$
			111	$\sqrt{3}$
			200	2
			211	$\sqrt{6}$
			220	$\sqrt{8}$
		Im3m	221	3
			110	$\sqrt{2}$
			200	2
			211	$\sqrt{6}$
220	$\sqrt{8}$			
310	$\sqrt{10}$			
222	$\sqrt{12}$			
<b>Tetragonal</b>	$d = \frac{1}{\sqrt{\frac{h^2 + k^2}{a^2} + \frac{l^2}{c^2}}} \quad (2.19)$		100	1
			001	
			110	$\sqrt{2}$
			101	
			111	$\sqrt{3}$
			200	2
210	$\sqrt{5}$			

The surfactant chain length ( $L$ ) in the bicontinuous cubic phase is determined as

$$\Phi_{lip} = 2A_0 \left(\frac{L}{a}\right) + \frac{4\pi\chi}{3} \left(\frac{L}{a}\right)^3 \quad (2.20)$$

where  $a$  is the lattice parameter obtained from the SAXS analysis,  $\Phi_{lip}$  is the surfactant volume fraction,  $A_0$  is the ratio of the minimal surface in a unit cell to the quantity (unit cell volume)<sup>2/3</sup> and  $\chi$  is the topology index of the surface (Euler-Poincaré characteristic) of the IPMS geometry [35]. Parameters for the bicontinuous cubic phases are summarized in table 2.2.

**Table 2.2.** Minimal surface and the Euler-Poincaré characteristic of the IPMS geometry.

<b>IPMS</b>	<b>Space group</b>	$\chi$	$A_0$
<b>D</b>	Pn3m	-2	1.919
<b>P</b>	Im3m	-4	2.345
<b>G</b>	Ia3d	-8	3.091

The radius of the aqueous channels in a bicontinuous cubic phase can be calculated from

$$r_w = \left( \frac{A_0}{-2\pi\chi} \right)^{\frac{1}{2}} a - L \quad (2.21)$$

For the inverse hexagonal phase  $r_w$  is given by

$$r_w = a \sqrt{\left( \frac{\sqrt{3}}{2\pi} \right) (1 - \Phi_{surf})} \quad (2.22)$$

## 2.4 Interaction of DNA with cationic surfactants

DNA (deoxyribonucleic acid) is a biopolymer responsible for storage of biological information. From the chemical point of view, DNA is a macromolecule consisting of repeated stacks of base pairs (bp) formed by either adenine and thymine (A–T) or guanine and cytosine (G–C) coupled via hydrogen bonds and organized in the double-helix structure by a deoxyribose-phosphate backbone. Due to the double helical nature, DNA is a rather stiff biopolymer. The DNA persistence length is both model and method dependent and values in the range of 300–500 Å are typically reported [36].

DNA can adopt several conformations depending on the primary sequence and environmental conditions such as counterion/ionic strength and relative humidity/hydration. A comparison between the most common forms of DNA is shown in table 2.3. A- and B-DNA are characterized by a right-handed helix. The B form of DNA is the most stable in physiological conditions, while the A form originates from the dehydration of the B form (at ca. 75% relative humidity). A third conformation of double-stranded DNA (dsDNA), known as Z-DNA, forms a left-handed double helix and has been observed at high ionic strength [37], or in modified DNA [38].

**Table 2.3.** Characteristics of A, B, and Z forms of DNA [39].

<b>Helical sense</b>	<b>A-form Right-handed</b>	<b>B-form Right-handed</b>	<b>Z-form Left-handed</b>
<b>Diameter</b>	~ 26 Å	~ 20 Å	~ 18 Å
<b>bp per helical turn</b>	11.6	10.5	11.6
<b>Helix rise per bp</b>	2.6 Å	3.4 Å	3.7 Å
<b>Charge density</b>	0.77 e <sup>-</sup> /Å	0.59 e <sup>-</sup> /Å	0.54 e <sup>-</sup> /Å

Due to the biological role, the interaction between DNA and different substances (metal ions, proteins, amphiphiles, polyelectrolytes) is an important aspect in molecular biology and biochemistry. It has been shown, that interaction between cationic surfactants and DNA molecules in aqueous solution leads to the formation of cationic surfactant-DNA complexes (CSDNA), where the surfactant molecules bind to DNA through the attractive Coulomb interaction, and the hydrophobic groups of the surfactant stabilize the complex through hydrophobic interaction [40]. The interaction between cationic surfactant and DNA is similar to other polyelectrolytes. It is proposed that complexation occurs via several stages [39]. At low surfactant concentration, the individual molecules bind to the DNA. Such association is linearly dependent on the surfactant concentration and has no effect on the conformational state of DNA. Above a certain concentration, known as critical association concentration (CAC), surfactant aggregates are formed in the vicinity of DNA, neutralizing the polyanion charge and inducing DNA compaction followed by precipitation of the CSDNA complex from the aqueous solution.

The morphology of the resulting complex depends on the surfactant nature and concentration as well as its ability to form different supramolecular aggregates. Typically, surfactant-polyelectrolyte complexes adopt the structure of the surfactant aggregates. However, unlike other polyelectrolytes which are flexible enough to wrap around spherical micelles, DNA is a stiff molecule and requires the presence of rod-like surfactant aggregates. A structure of the stoichiometric (1:1 molar ratio of positive charges of surfactant and negative charges of DNA) dodecyltrimethylammonium-DNA (DTADNA) is demonstrated in figure 2.13. The results of the SAXS measurements of DTADNA in excess water suggest a 1:2 micelle-DNA compound arranged into the square lattice with a lattice spacing  $a = 37 \text{ \AA}$  [41].

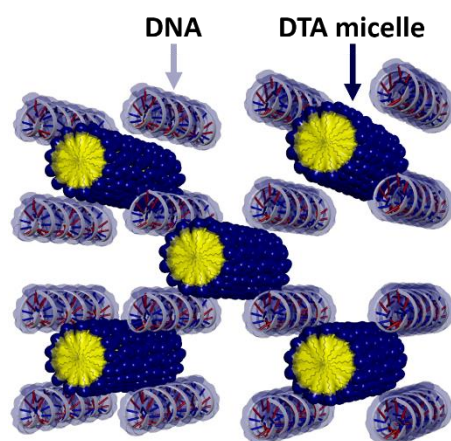


**Figure 2.13.** Schematic representation of the hydrated dodecyltrimethylammonium-DNA complex, redrawn from [41].

The structure of the surfactant-DNA aggregates is strongly affected by the counterion and the surfactant chain length. Increase of the number of carbon atoms in the surfactant chain from 12 (DTA) to 16 (cetyltrimethylammonium, CTA) results in different CSDNA packing. Leal et al. showed that hydrated CTADNA has a normal hexagonal symmetry with cylindrical surfactant micelles surrounded by six DNA helices [42]. Krivtsov et al. reported the hexagonal packing of the stoichiometric didodecyltrimethylammonium-DNA (DDADNA) complex [43]. However, since the double-tailed surfactant DDA typically does not form normal micelles, the preferred organization is an inverse hexagonal structure where the DNA is located in the aqueous cores of the inverse cylindrical micelles.

In the presence of additives that form self-assembled supramolecular architectures with the amphiphiles and enhance micellization, the CSDNA complex can take part in the formation of lyotropic liquid crystalline phases. The liquid crystalline structure is formed by the surfactant or lipid aggregates, in which DNA is tightly packed and shielded from the surroundings [41]. Several examples are demonstrated in chapters 4–6.

### **Interaction of DNA with silver ions**

Based on spectroscopic and potentiometric data, it has been reported that DNA can form at least three different complexes with Ag(I) depending on the  $[Ag^+]/[DNA_{base}]$  ratio, by embedding the silver ions inside the double helix [44]. Compared to other noble metals, silver binds exclusively to the nucleobases. No interaction with either phosphate or pentose moieties has been reported.

The type I complex is formed when  $0 < [Ag^+]/[DNA_{base}] \leq 0.2$  and is more important ( $Ag^+$  binds more strongly to DNA) for a G–C rich DNA. Complex formation is accompanied by little or no proton release and preservation of the DNA double helical structure. It is generally believed that the formation of the type I complex occurs via  $Ag(I)$  chelation between  $N_7$  and  $C_6O$  groups of guanine (figure 2.14 A) [45]. However, later spectroscopic studies suggest that type I complexation occurs via a two-step mechanism with a guanine  $N_7$  being the primary binding site at low silver content and adenine  $N_7$  the secondary target at higher  $Ag^+$  concentrations [46]. The proposed structures are shown in figure 2.14.

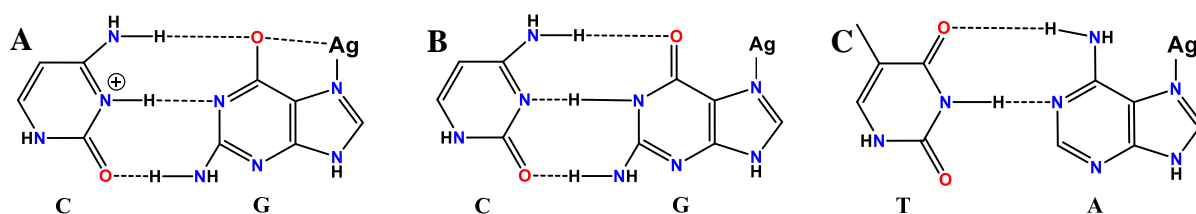


**Figure 2.14.** Proposed structures of type I  $Ag$ -DNA complex; (A) redrawn from [45], (B, C) from [46].

The type II complex is formed when  $0.2 < [Ag^+]/[DNA_{base}] \leq 0.5$  with nucleobases unaffected by the type I complex. It occurs with  $N-H \cdots N$  hydrogen bond to  $N-Ag-N$  bond conversion accompanied by a proton release, resulting in interchelation of  $Ag$  between guanine  $N_1$  and cytosine  $N_3$  atoms as well as adenine  $N_1$  and thymine  $N_3$  atoms, as schematically demonstrated in figure 2.15 [44]. Since the sum of type I and II complexes fully saturates the DNA base pairs, it is assumed that nucleobases involved into formation in the first binding cannot participate in the type II complex.

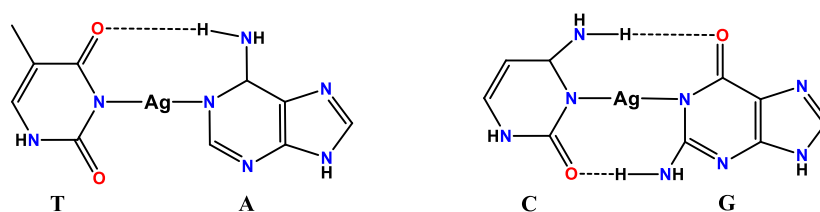


**Figure 2.15.** Proposed structures of type II  $Ag$ -DNA complex, redrawn from [44].

If  $[Ag^+]/[DNA_{base}] > 0.5$ , evidence of a type III complex formation has been reported. However, such ratio may result in  $Ag$ -DNA precipitation [46]. Therefore, this type of binding has not been extensively studied.

## 2.5 Synthesis of metallic nanoparticles

Nanoparticles of noble metals and particularly of gold and silver were one of the first nanoobjects of synthesis and study because of their potential in catalysis, photoreactions, sensors, and as components of optical and electronic devices [48]. A long time back, there were only reports on spherical or quasi-spherical particles [49]. More than twenty years ago one-dimensional nanostructures such as nanorods [50] and nanowires [51] have been synthesized. Recently, reports on nanoparticles of different shapes have grown dramatically. Until now nanocubes [52], nanoprisms [53] nanoplates [54], nanobelts [55], and many others shapes of nanoparticles have been prepared.

Many different physical and chemical methods have been used to prepare nanoparticles. In general, they can be divided into two groups: top-down and bottom-up. Top-down methods produce nanoparticles by removing a part of the material from the bulk. Top-down methods include photolithography [56], focused ion and electron beam lithography [57], laser ablation [58], sonication, milling and other mechanochemical techniques [59]. Bottom-up strategies mostly utilize wet colloidal chemical methods. Bottom-up techniques start with the solution of a silver salt precursor that is reduced in a chemical reaction and the nanoparticles are formed through nucleation and growth [60]. With the bottom-up methods, the use of templating and capping agents is crucial to control the particle size and shape, as well as to provide stability for the synthesized nanoparticles.

The so-called polyol process is one of the most established methods for the synthesis of Ag and Au nanoparticles with desired size and morphology. It is based on the reduction of the nanoparticle precursor by alcohols with more than one OH functional group, which are oxidized to carbonyl groups. In a typical synthesis, ethylene glycol is used, which acts as both solvent and a reducing agent at elevated temperatures. The formation of particles with different shapes is facilitated by adding a polymeric capping agent, like polyvinylpyrrolidone and adjusting reaction conditions [61].

Another important method for the synthesis of spherical and highly anisotropic nanoparticles is seed-mediated growth [62]. It is a typical example of heterogeneous nucleation and consists of two steps. During the first stage, small spherical nanoparticles (seeds) are formed using a strong reducing agent, like  $\text{NaBH}_4$ . The second step involves the subsequent growth of the seed particles in a growth solution containing metal precursors, mild reducing agent and shape-directing agent. Yield, aspect ratio and monodispersity of the resulting nanorods depend on the

experimental parameters, such as size and concentration of seeds, pH, temperature, reducing agent, precursor and surfactant, the use of other cosurfactants and additives [63]. Change of the experimental conditions may result in modifications of the typical cylindrical shape of nanorods and formation of nanoparticles with other shapes [64].

The synthesis of nanoparticles based on surfactant templates is another important method in nanoscience. The morphology of nanostructures inside lyotropic liquid crystalline templates will be affected by the structure of the liquid crystalline phase. Qi et al. showed that a lamellar liquid crystalline phase consisting of C<sub>12</sub>EO<sub>4</sub> surfactants and water can be used to produce silver nanoparticles with a narrow size distribution [65]. Hexagonal and cubic liquid crystalline templates are well-known templates for the synthesis of mesoporous oxides [66], but have also been used as a template for the formation and macroscopic alignment of silver nanoparticles [67].

DNA has been widely used as a template for nanoparticle synthesis as well as for particle assembly into complex nanostructures. In 1998 Braun et. al. synthesized the first DNA-templated silver nanowires [5]. Current protocols of silver nanoparticle synthesis directly on a DNA molecule include the chemical modification of DNA with aldehyde moieties followed by Tollens reaction, reduction of silver ions with reducing agents or by illumination of the Ag-DNA with UV light [68]. Recently, Berti and coworkers demonstrated that exposure of the type II complex, where silver is embedded into the DNA double helix, to UV light leads to the formation of small nanoparticles [69]. In the experiment performed Ag-DNA was irradiated using 254 nm UV light, which is specifically absorbed by the DNA bases. It gave rise to photooxidation of DNA bases and a formation of highly reactive radicals or singlet oxygen which concomitantly promoted in situ reduction of Ag<sup>+</sup> bound on the DNA. A similar photoreduction procedure was later applied for the synthesis of palladium nanoparticles [70], metallic nanorods [71] and other nanostructures [72] where DNA acts both as a template and photosensitizing agent.

UV photoreduction has been proven to be an important approach for the synthesis of monodisperse metal nanoparticles. For example, Toshima et al. prepared colloidal Pt and Pd nanoclusters in the presence of surfactants [73]. Gold nanoparticles were synthesized by UV-induced reduction in the presence of double hydrophilic block copolymers with different functional groups [74]. The particle size could be controlled by variation of the functional group of the block copolymers or surfactants and UV irradiation power. It has been demonstrated that it is also possible to produce shaped metal nanomaterials using UV photoreduction. Esumi et

al. successfully obtained rodlike Au nanoparticles by using cylindrical hexadecyltrimethylammonium chloride micelles as soft template [75]. Moreover, illumination of nanoparticles with UV light may cause a photoconversion of nanospheres into nanoprism [76]

Huber et al. produced silver nanoparticles in long-chain sodium polyacrylates and spherical polyacrylate brushes [77]. Irradiation of the polyacrylate solution in the presence of  $\text{Ag}^+$  ions with UV light induces the formation of AgNP within the shrunken polymer. It was found that either isolated particles or particle assemblies could be obtained by varying the aging time and  $[\text{Ag}^+]/[\text{COO}^-]$  ratio. A similar approach towards the synthesis of silver nanoparticles in the lyotropic liquid crystals formed by anionic carboxylate-based surfactants was taken in the early stage of this thesis but turned out to be not very successful, as will be demonstrated in the appendix.

## 2.6 Optical properties of metallic nanoparticles. Influence of size, shape, dielectric environment, and particle interaction.

Noble metallic nanoparticles, such as Au, Ag and Cu have received a lot of attention due to their interesting geometry-dependent optical properties, determined by surface plasmons. When a spherical nanoparticle with  $d \ll \lambda$  (known as quasi-static limit) is irradiated with light, the oscillating electromagnetic wave causes the conductive electrons to oscillate coherently. A restoring force arises from the Coulomb attractive interaction between electron and nuclei, which results in the displacement of the electron cloud relative to the nuclear framework (figure 2.16) [78]. This effect is called localized surface plasmon resonance (SPR).

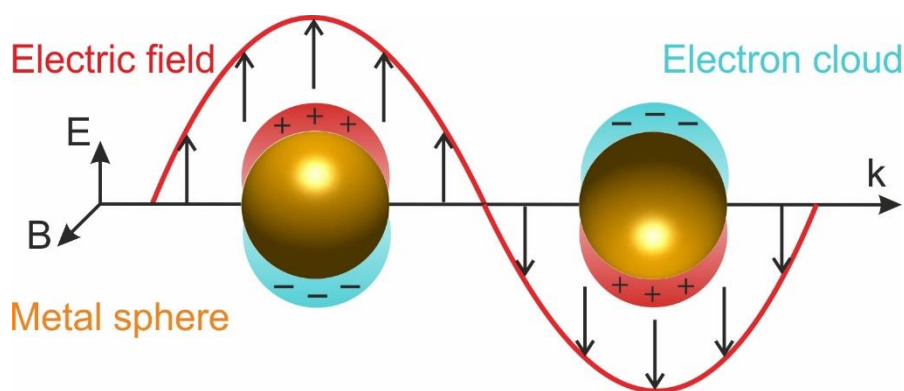


**Figure 2.16.** Schematic representation of the surface plasmon resonance.

First attempts to explain the unusual optical properties of metallic nanoparticles were performed in the beginning of the 20<sup>th</sup> century, when Gustav Mie found an analytical solution of the Maxwell equation for spherical nanoparticles [79]. However, Mie theory is applicable only for spherical nanoparticles and infinitely long nanowires. For more complex shapes no analytical solution has been found so far. Several numerical techniques have been developed, such as discrete dipole approximation (DDA), finite difference time domain (FDTD), boundary element method (BEM) and many others [80].

According to Mie theory, the total extinction cross-section is expressed by:

$$C_{ext} = \frac{24\pi^2 r \varepsilon_M^{3/2}}{\lambda} \frac{\varepsilon_2}{(\varepsilon_1 + 2\varepsilon_M)^2 + \varepsilon_2^2} \quad (2.23)$$

where  $r$  is the particle radius,  $\varepsilon_M$  the dielectric constant of the medium (its real part; imaginary part can be neglected),  $\lambda$  the incident light wavelength,  $\varepsilon_1$  the real and  $\varepsilon_2$  the imaginary part of the dielectric constant of silver [81].

The extinction efficiency  $Q_{ext}$  is determined as

$$Q_{ext} = \frac{C_{ext}}{\pi r^2} \quad (2.24)$$

The optical properties depend on both free electron oscillation and electron interband transition contributions to the metal's dielectric function. Figure 2.17 shows a comparison of the dielectric functions of Ag, Au, and Cu together with simulated extinction spectra of a single 25 nm nanosphere. The onset of the electronic interband transition from the valence band to the Fermi level causes a sharp increase in the imaginary part and a change in the slope of the real part of the dielectric function. The spectral locations of the interband transition and the plasmon resonance result in significant differences between noble metallic nanoparticles. Of the three metals (Ag, Au, Cu) that show plasmon resonance in the visible spectrum, silver exhibits the highest efficiency of plasmon excitation because of the highest energy of the interband transition (~3.8 eV). The large energy difference between interband transition and plasmon resonance results in the minimal damping of the plasmon. An extinction cross-section can be about 10 times larger than the geometric cross-section, which means that the particles can capture more light than is incident on them. Moreover, the optical excitation of the plasmon resonance in nanosized silver is one of the most efficient mechanisms of light interacting with matter. A single silver nanoparticle interacts with light more efficiently than any known organic and inorganic chromophore of the same dimensions [82]. The position of the surface plasmon

resonance band of silver nanoparticles can be selectively tuned the wide wavelength range in the UV-Vis and near-IR spectral range by varying the nanoparticle size or shape and dielectric environment.

Au nanospheres display a well-defined resonance peak at ca. 520 nm which is closer to the interband transition region ( $\sim 2.5$  eV), resulting in a SPR band with lower intensity in comparison to Ag. For Cu nanospheres plasmon oscillations are resonant with the interband transition ( $\sim 2.1$  eV), resulting in a surface plasmon resonance band at ca. 560 nm that is much weaker than in the case of Ag and Au. The interband transitions are also responsible for a strong damping of the surface plasmons and strong absorbance in the UV-Vis region of the spectra [83].

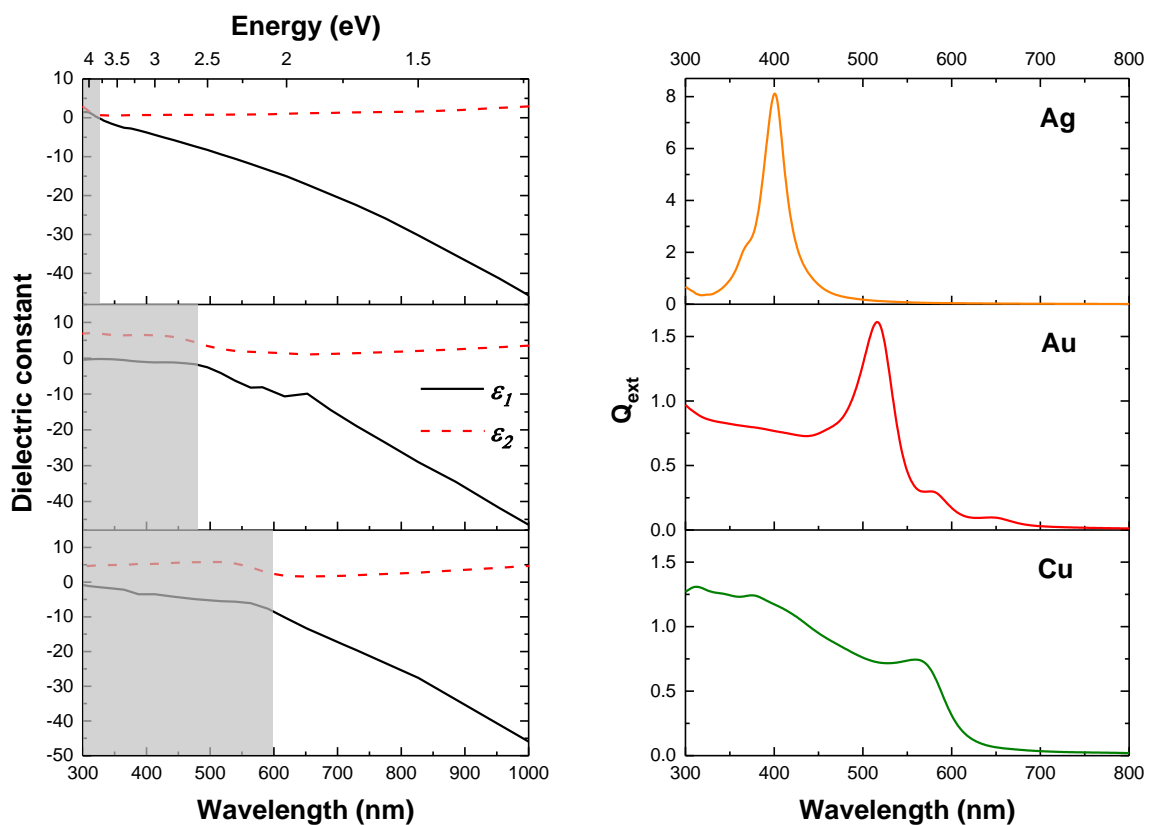


**Figure 2.17.** Dielectric function (left) and simulated extinction spectra (right) of a single Ag, Au and Cu nanosphere with a diameter of 25 nm (in water). Spectral regions where interband transitions occur are shaded in gray. Reproduced from [83].

## Effect of the particle size

For a small spherical particle, the displacement of the electron cloud is homogeneous, yielding a dipolar charge distribution on the surface. Such a dipole oscillation gives rise to a single resonance mode, independent on the direction of the incident light. As the size increases, the resonance wavelength of the surface plasmon band increases and shifts towards longer wavelength due to the decrease in the restoring force between the opposite charges. Figure 2.18 shows the UV-Vis spectra of silver nanospheres with a diameter of 10, 50 and 100 nm.

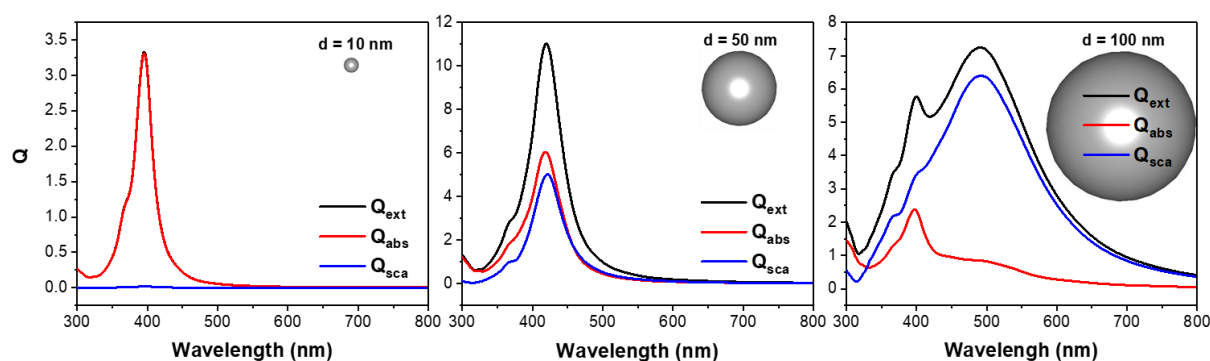


**Figure 2.18.** Simulated extinction spectra of single silver nanospheres with a variable diameter (in water). Reproduced from [84].

The relative contribution of absorption and scattering strongly depends on the particle size. Small particles ( $d < 30$  nm) exhibit only absorption of the dipole resonance mode (figure 2.18 A). When the size of the nanoparticle increases, the scattering effect becomes more important. For a particle with a size of 50 nm the scattering and absorption contributions become nearly equal, but their peak maxima are slightly shifted relative to each other, as shown in figure 2.18 B. As the nanoparticle size is further increased, the scattering dominates over the absorption due to the limited penetration depth of the incident light. Also, extinction is dominated by scattering resulting from free-electron oscillations, whereas the absorption requires interaction of electrons with lattice phonons [82].

For nanoparticles with a size  $> 50$  nm the displacement of the electronic cloud is no longer homogeneous so the extinction originates from both dipolar and multipolar modes. The dipole and quadrupole contribution become nearly equal for spherical particle with a diameter of 75 nm. The quadrupolar and octupolar surface plasmon resonance modes are always located at shorter wavelength with respect to the dipolar mode, which is always red-shifted in comparison to small particles (figure 2.18 C).

## Effect of particle shape

The surface plasmon resonance strongly depends on the shape of the nanoparticle. For anisotropic particles, like nanorods, dipole oscillations induced by electromagnetic wave across and along the cylinder are not uniform, which results in two different surface plasmon resonances, as schematically shown in figure 2.19. The electron oscillation along the short axis induces a plasmon band similar to the one of a nanosphere, called transverse band. The excitation of the electron oscillation along the long axes results in a much stronger plasmon resonance, which is shifted towards longer wavelength.

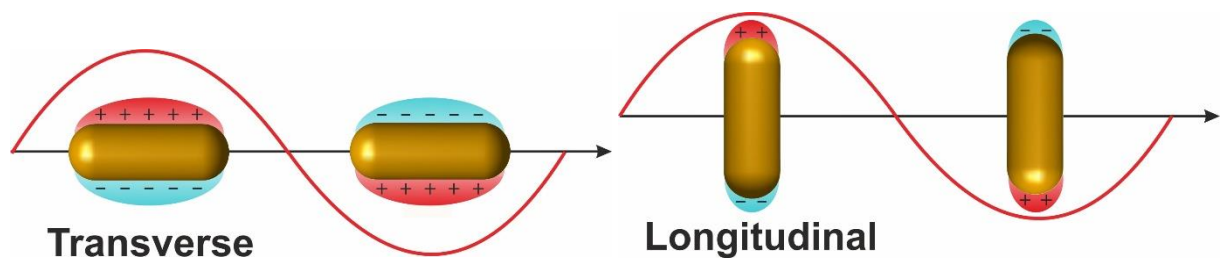


**Figure 2.19.** Schematic representation of two different plasmon resonance modes of a rod-like nanoparticle.

The transverse SPR mode is almost insensitive to the size of nanorods, but the longitudinal band is significantly red-shifted with increasing aspect ratio (AR), as can be seen in figure 2.20 [85].

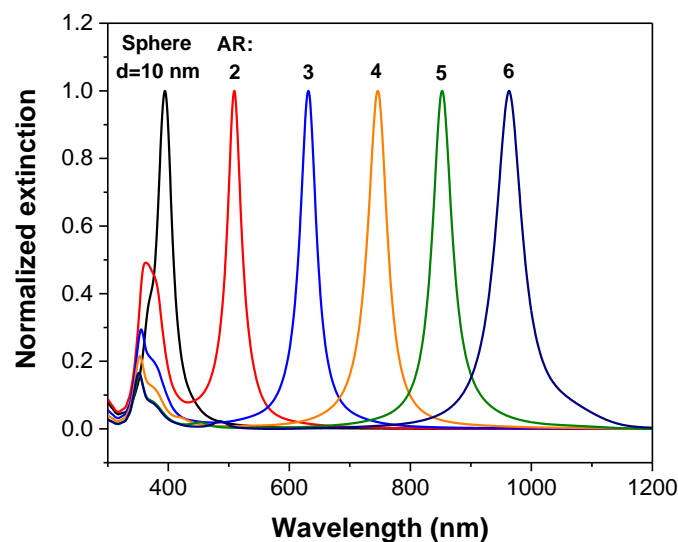


**Figure 2.20.** Simulated extinction spectra of silver nanorods with different aspect ratio in water in comparison to a single silver nanosphere ( $d=10$  nm).

Gans applied Mie theory to describe extinction spectra of ellipsoidal particles and nanorods [86]. The extinction cross-section for elongated ellipsoids is defined by the following equation:

$$C_{ext} = \frac{8\pi^2 r^3 \varepsilon_M^{\frac{3}{2}}}{3\lambda} \sum_j \frac{\left(\frac{1}{P_j^2}\right) \varepsilon}{\left(\varepsilon_1 + \frac{1 - P_j}{P_j} \varepsilon_M\right)^2 + \varepsilon_2^2} \quad (2.25)$$

where  $P_j$  represents the depolarization factors for the nanorod axes ( $a > b = c$ ) defined as

$$P_a = \frac{1 - r^2}{r^2} \left[ \frac{1}{2r} \ln \left( \frac{1 + r}{1 - r} \right) - 1 \right] \quad (2.26)$$

$$P_b = P_c = \frac{1 - P_a}{2} \quad (2.27)$$

and the parameter  $r = \sqrt{1 - (b/a)^2}$  is related to the nanorod aspect ratio.

Figure 2.21 (A) demonstrates the extinction spectrum of a single silver nanoprism with an edge length of 35 nm and a thickness of 12 nm (similar particles were produced by chemical synthesis of nanoparticles in monoolein-based liquid crystals, as shown in chapter 3). The spectrum consists of three different plasmon excitation modes, shown in figure 2.21 (B) as an electron energy loss spectroscopy (EELS) map. The intense peak at 615 nm is attributed to the in-plane dipole resonance, while the much weaker in-plane quadrupole resonance mode is located at 437 nm. A third peak at 344 nm is assigned to the out-of-plane quadrupole resonance. The out-of-plane dipole peak at 395 nm often is evident experimentally only as a small shoulder.

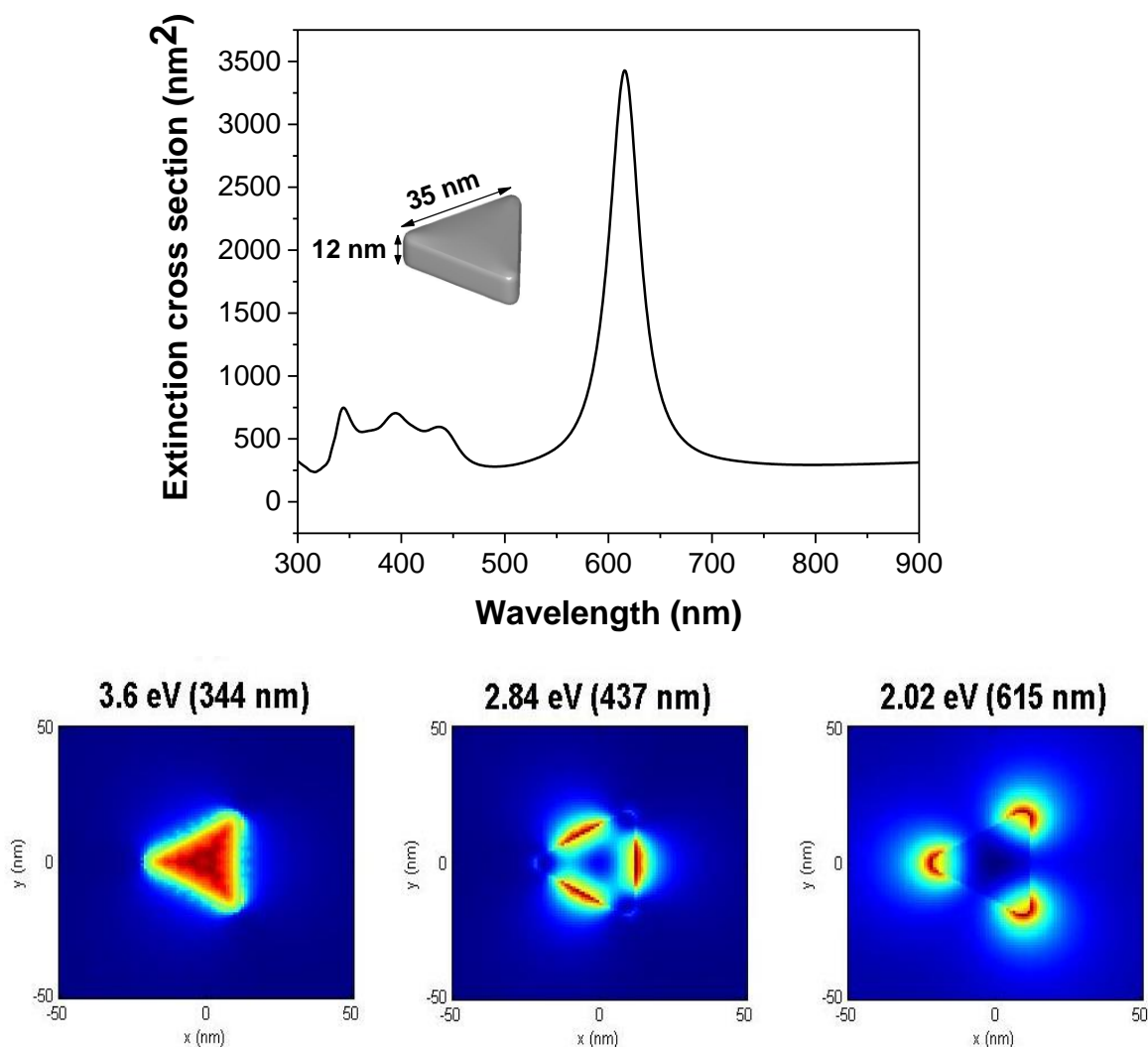


**Figure 2.21.** (A) BEM simulation of the orientation averaged extinction spectra of a single silver equilateral nanoprism (35 nm edge length, 12 nm thickness), in glycerol monooleate. (B) Simulated EELS amplitude map showing three different resonance modes, from left to right: out-of-plane quadrupole resonance mode, in-plane quadrupole resonance mode, in-plane dipole resonance mode.

The extinction spectra and in particular the position of the surface plasmon resonance band strongly depend on the shape of the plate-like particles [87]. Figure 2.22 shows the effect of the tip sharpness of the triangular nanoprisms in comparison to the nanodisk of the same dimensions. The dipole resonance is extremely sensitive to the height, edge length and tip sharpness of the nanoprism, while both in- and out-of-plane quadrupole resonances are not strongly affected by the morphological change. As the tips of a nanoprism become more rounded, the dipole resonance is blue-shifted, due to the redistribution of electron density across

the surface. An increase of the particle height and edge length results in the respective blue and red shift of the surface plasmon resonance band.

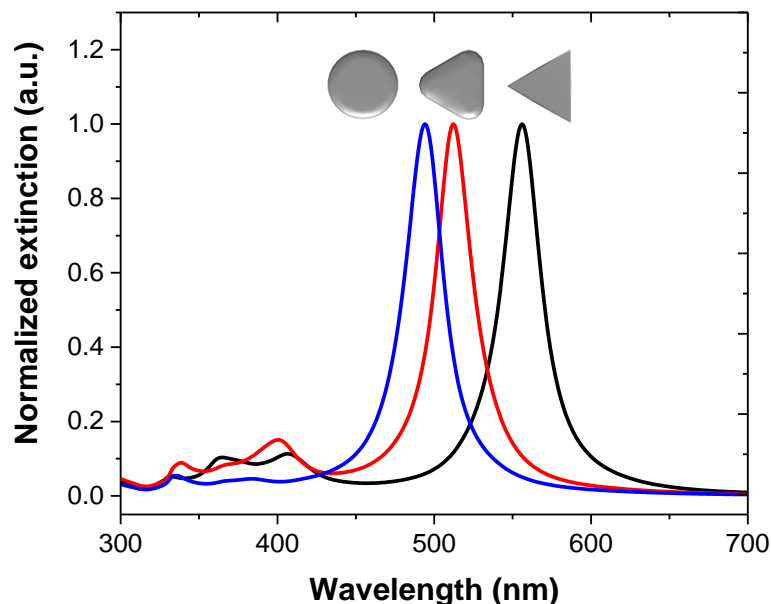


**Figure 2.22.** Simulated extinction spectra of plate-like silver nanoparticles with different shapes (edge length 50 nm, thickness 15 nm) in water.

### Effect of the refractive index of the medium

The refractive index of the surrounding medium also has an influence on the optical properties of metallic nanomaterials. The position of the surface plasmon resonance band can be tuned by variation of the refraction index of the solvent or by coating the nanoparticles with different polymers or silica [78]. Mie theory for a spherical silver nanoparticle predicts a linear relationship between the dielectric function of the medium and the wavelength of the plasmon absorption band. Increasing the value of the dielectric function of the surroundings changes the resonance condition and results in a reduction of the Coulomb restoring force of the conducting electrons. Hence the resonance occurs at lower frequency.

Figure 2.23 shows the effect of the refractive index of the solvent on the surface plasmon resonance band in the absorption spectrum of a single 50 nm silver spherical nanoparticle. Indeed, the position of the absorption band shifts almost linearly towards higher wavelength with an increase of the refractive index (compared to the vacuum).

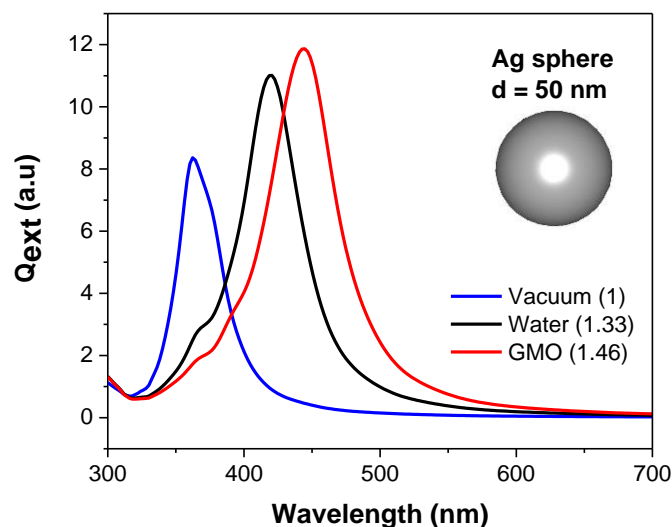


**Figure 2.23.** Simulated extinction cross section of a single 50 nm silver nanosphere, showing the dependence on the refractive index of the surrounding medium.

### Effect of nanoparticle coupling

Neighboring nanoparticles can interact with each other via their optical near and far field. The plasmonic interaction between nanoparticles generates additional low-energy plasmon resonances. The resonance frequency of the surface plasmon resonance of coupled nanoparticles depends on the cluster configuration and interparticle distance, typically showing a red-shift as compared to the one from isolated particles.

In addition, the local electric fields can be enormously enhanced in the gap between closely-spaced nanoparticles, providing so-called “hotspots” for surface-enhanced spectroscopy. The enhancement of a particle cluster is much stronger than the added contributions of individual particles [84].

Figure 2.24 demonstrates simulated extinction spectra and E-field enhancement maps generated around a single silver nanosphere ( $d = 25$  nm) in comparison to those from a dimer of silver nanoparticles separated by 5 nm. The type of the shift of the plasmon resonance band typically depends on the polarization state of the incident light.

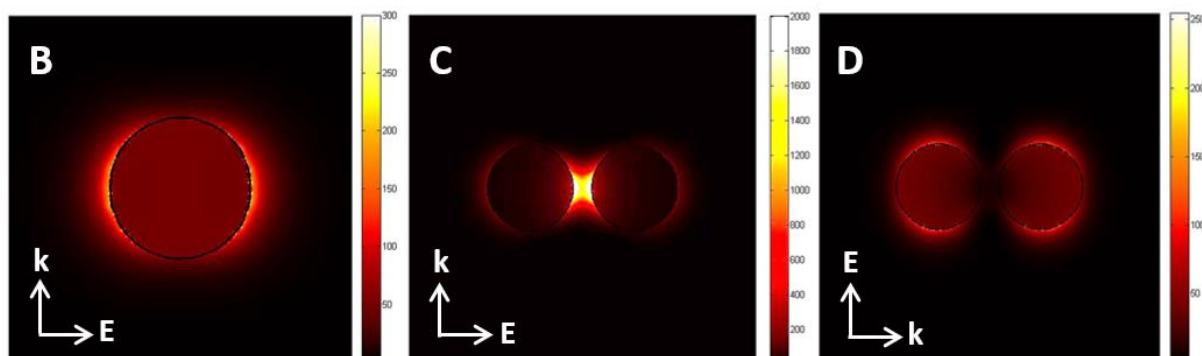
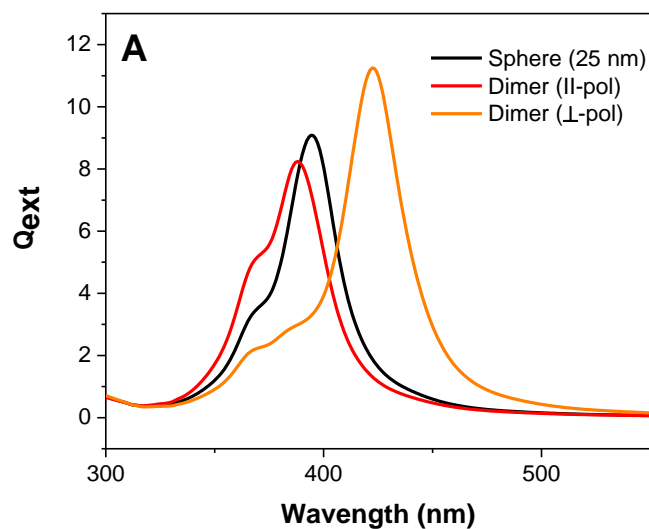


**Figure 2.24.** A: simulated extinction spectra of two silver nanospheres ( $d = 30$  nm) separated by 5 nm, depending on the polarization of the incident light in comparison to a single nanoparticle. Bottom: E-field enhancement of single nanoparticle (B), dimer, when light is polarized parallel to the dimer axis (C), dimer, when light is polarized perpendicular to the dimer axis (D).

As it was already mentioned, the extinction spectra of nanoparticle dimers are very sensitive to the separation distance. As the nanoparticles approach each other, the dipole resonance shifts towards longer wavelength and the quadrupole resonance becomes more intense as shown in figure 2.25.

Such a dependence of the surface plasmon resonance on the interparticle spacing has been used as a “plasmonic ruler” to measure distances in biological systems [88]. Apart from this, the effect of the strong electric field enhancement was used for SERS single molecule detection [89]. By optimizing the size and shape of the nanoparticles and assemblies as well as the interparticle distance, enhancement factors of  $10^{10}$ - $10^{11}$  can be reached [90].

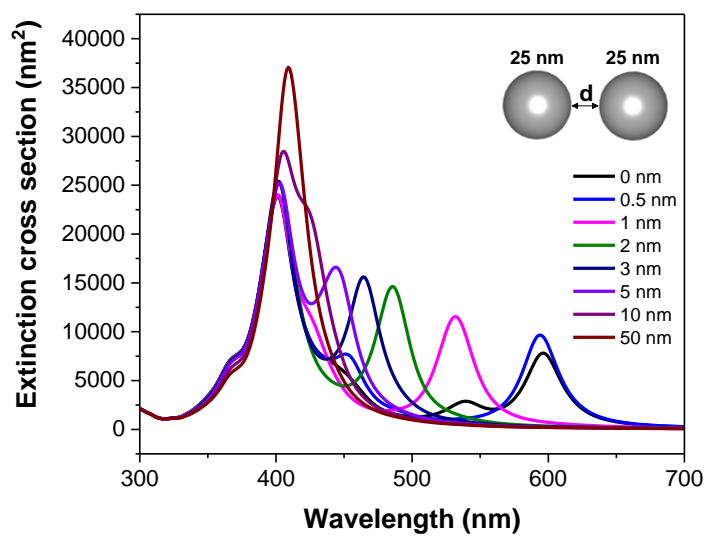


**Figure 2.25.** Simulated extinction spectra of two silver nanospheres with different interparticle spacing (in glycerol monooleate).

## **3 Formation of silver nanoparticles in liquid crystalline phases of aqueous solution of monoolein**

### **3.1 Introduction**

Monoolein/water was chosen as a first system for the synthesis of silver nanoparticles. The aqueous monoolein (GMO) system has been extensively studied during the last twenty years and phase diagrams were reported in a number of studies [91].

Monoolein, (1-(*cis*-9-octadecenoyl)-*rac*-glycerol) is a polar nonionic amphiphilic molecule, consisting of the hydrocarbon chain which is attached to the glycerol backbone by an ester bond. It is a nontoxic, biocompatible and biodegradable material classified as GRAS (generally recognized as safe), included in the Inactive Ingredient Guide from the U.S. Food and Drug Administration [92] and approved by the European Food Safety Authority [93] as a food additive (E471).

Monoolein swells in water giving rise to several liquid crystalline phases, as shown in figure 3.1. A lamellar liquid crystalline phase exists at low water content. In the presence of ca. 20–40 wt.% water, monoolein forms an extensive region of cubic liquid crystalline phases. On heating, both the cubic and lamellar phases are destabilized, and an inverse hexagonal phase is formed. The cubic phases formed in the GMO/water system are bicontinuous and consist of curved bilayers organized to form two unconnected systems of water channels. Two microstructures have been identified in the binary system. The curved bilayer of the first phase can be described by the diamond type infinite periodic minimal surface (IPMS), and the gyroid IPMS describes the second cubic phase. These structures correspond to a primitive lattice (space group Pn3m) and body-centered lattice (space group Ia3d), respectively. Cubic phases are stable in excess of water and can be dispersed into submicron-sized particles with surface active agents as stabilizers [94] which makes them potentially interesting for the use as drug delivery vehicles [95].

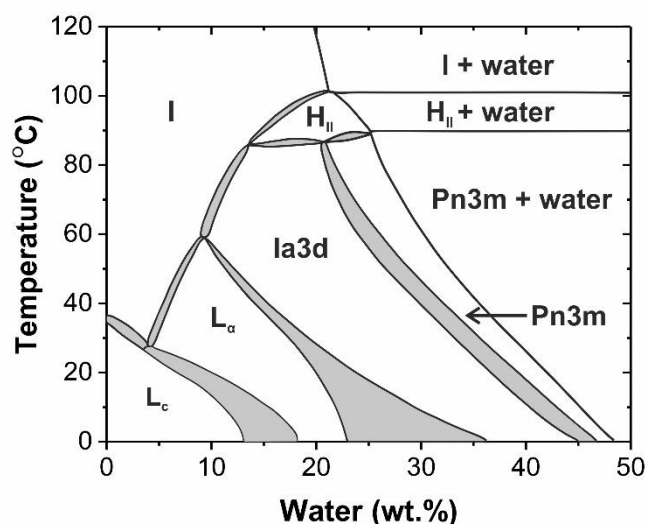


**Figure 3.1.** Monoolein/water binary phase diagram, redrawn from [91]. Grey areas indicate two-phase regions.

In the case of the GMO/water binary system, the inverse hexagonal phase exists only at relatively high temperature, as measured by  $^2\text{H}$  NMR spectroscopy (figure A.8). However, Garti et al showed that addition of triacylglycerol (TAG) with medium-chain fatty acids causes an increase of the critical packing parameter due to the incorporation of TAG in the lipophilic part of monoolein layer and transforms the lamellar or cubic phase into the inverse hexagonal phase [96]. The ternary phase diagram of GMO/TAG/water is shown in figure 3.2.

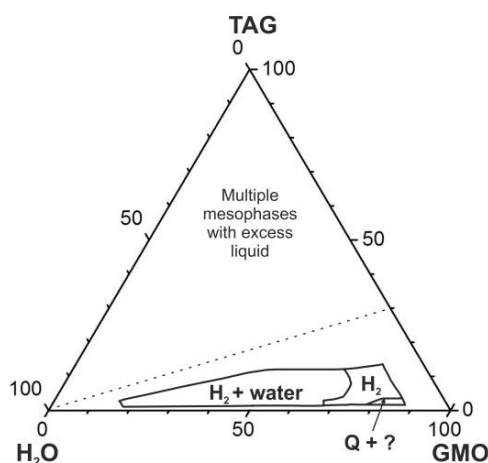


**Figure 3.2.** Ternary GMO/TAG/water phase diagram at 25°C, redrawn from [96].

The spontaneous (i.e. without any additional reductants) reduction of  $\text{Ag}^+$ ,  $\text{Au}^{3+}$ , and other noble metals has been reported in a number of studies. Barnickel et. al reported the reduction of noble metals in microemulsions based on cationic and nonionic surfactants [97]. Esumi and coworkers proposed that reduction occurs through oxidation of alcohol groups to carbonyl

groups [98]. Puvvada et al. showed that reduction of the palladium salt by monoolein in cubic phase occurs through oxidation of the alcohol groups to carbonyl one [99]. Regev et al. [100] and Meyre et al. [101] reported the oxidation of the terminal alcohol group to a carboxylic group upon reduction of Au(III) to Au(0) in multilamellar phosphatidylcholine/monoolein vesicles.

### 3.2 Verification of the phase behavior

Since in this study not pure monoolein, but the commercially available Rylo MG-19 was used, due to impurities the phase diagram may differ from the ones reported in the literature. In addition, heavy water was used because it is required for the  $^2\text{H}$  NMR measurements. To verify the phase behavior, several samples from both cubic and inverse hexagonal regions of the phase diagram were prepared. A combination of  $^2\text{H}$  NMR spectroscopy, polarizing optical microscopy (POM) and small angle X-ray scattering techniques have been used to reexamine the phase diagram. In our case, several deviations from the phase diagram were found (at  $25^\circ\text{C}$ ), in particular, a shift of the phase boundaries ( $L_c$ :  $\leq 4$  wt.%,  $L_d$ : 7–13 wt.%, cubic Ia3d: 16–32 wt.%, cubic Pn3m: 33–38 wt.%), in agreement with previously reported data for GMO of the same purity [102].

Samples of both types of cubic phases as well as the inverse hexagonal phase have been prepared. The composition of the prepared samples is shown in table 3.1. For all experiments in this chapter, two different sets of samples were prepared, with  $\text{D}_2\text{O}$  and with  $\text{AgNO}_3$  solution in  $\text{D}_2\text{O}$  (0.01–0.1 M).

**Table 3.1.** Composition and phase behavior of prepared samples.

Phase	Composition, wt.%		
	GMO	TAG	$\text{D}_2\text{O}$
Cubic Ia3d	70	0	30
Cubic Pn3m	63	0	37
Inverse hexagonal	70	5	25

### 3.3 Mechanism of silver nanoparticle formation

For the synthesis of silver nanoparticles, D<sub>2</sub>O was replaced by silver nitrate solutions of various concentrations. Sample preparation was performed in a lipid mixer, similar to the one reported by Caffey et. al. [103]. After mixing was finished the color of the samples turned to slightly yellow-orange and after three days into different colors, as shown in figure 3.3. This color change is indicative of the formation of nanoparticles.

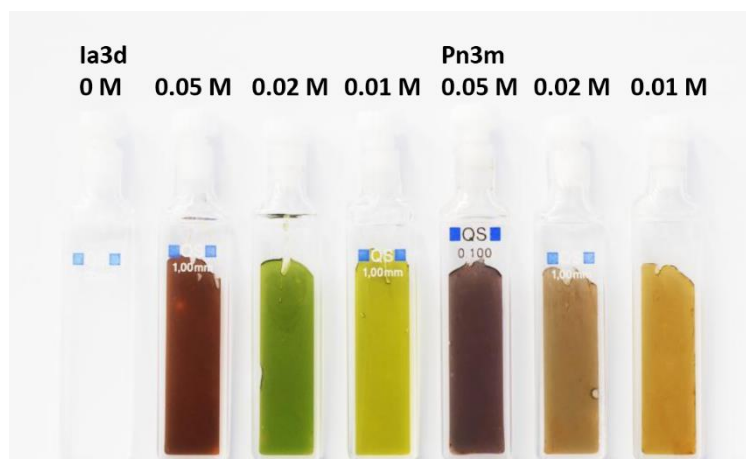


**Figure 3.3.** Cubic Ia3d and Pn3m samples with various Ag<sup>+</sup> concentration 1 week after preparation.

To verify the proposed mechanism of silver reduction in the monoolein-based liquid crystals <sup>1</sup>H and <sup>13</sup>C NMR and ATR-FTIR spectroscopy were used. Figure 3.4 shows the <sup>1</sup>H NMR spectra of the lyophilized monoolein from the cubic Ia3d phase, dissolved in CDCl<sub>3</sub>. A peak appearing at 9.75 ppm may indicate the formation of aldehyde due to the silver reduction and concomitant oxidation of the  $\gamma$ -alcohol group of monoolein. However, the origin of the peak splitting into a triplet is not yet fully understood. The concentration of the detected aldehyde is low because monoolein is in large excess (GMO/Ag ratio is 73 for 0.1 M AgNO<sub>3</sub> solution).

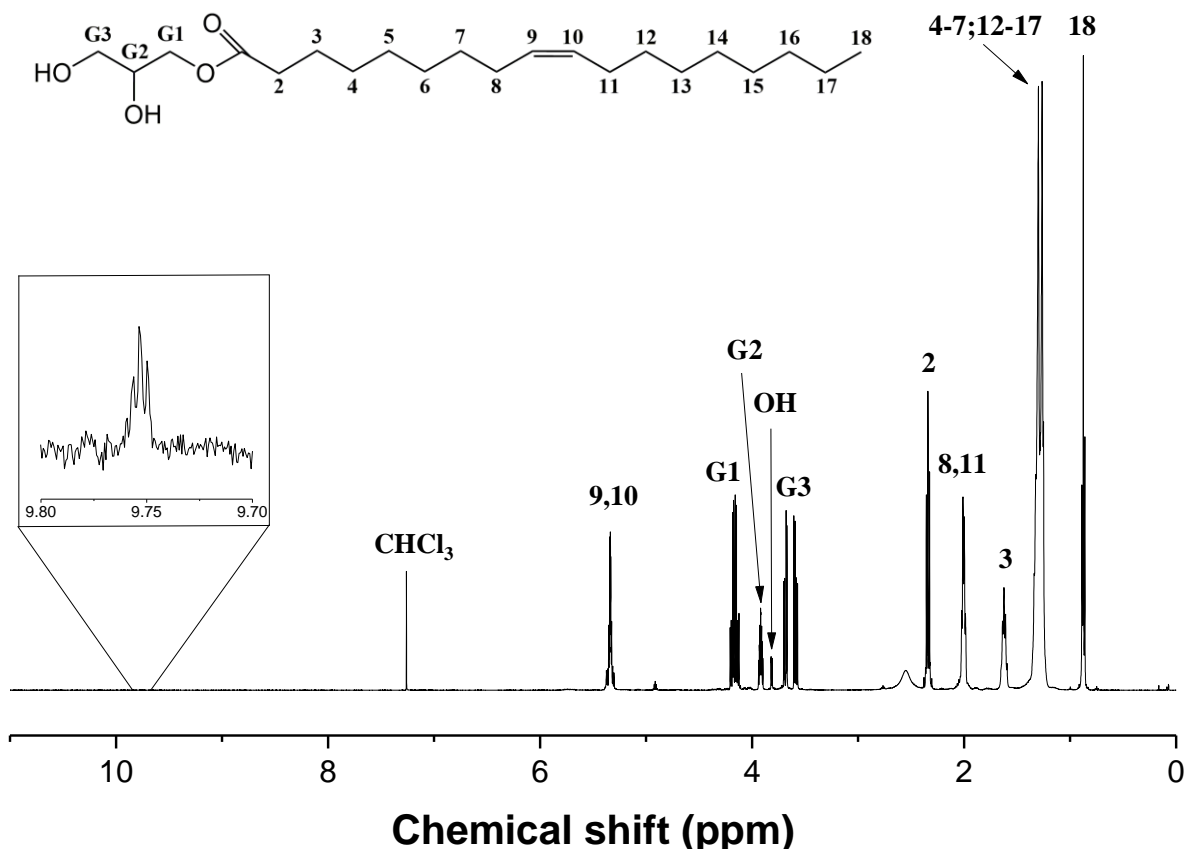
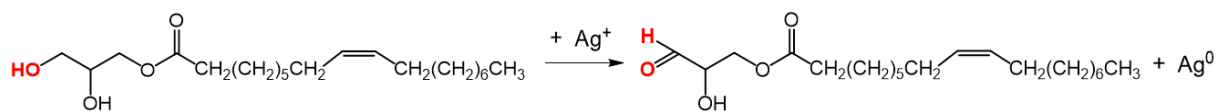


**Figure 3.4.**  $^1\text{H}$  NMR spectrum of GMO after formation of nanoparticles in the cubic Ia3d phase (70 wt.% GMO/30 wt.% 0.1 M  $\text{AgNO}_3$ ), showing in the inset the aldehyde peak due to the oxidation of monoolein.

The analysis of the NMR and infrared (figure A.9) spectra shows that monoolein is directly involved in the formation of nanoparticles. GMO can take part in the polyol-like reaction where the reduction of silver ions occurs through the oxidation of the  $\gamma$ -alcohol group of the surfactant to an aldehyde, as shown in scheme 3.1. The obtained results are in agreement with data reported by Puvvada et al. [99].



**Scheme 3.1.** Schematic representation of the oxidation of the monoolein due to the reduction of silver ions.

### 3.4 Influence of the nanoparticle formation on the liquid crystalline structure

The ability of the liquid crystalline phase to act as a template for the nanoparticle synthesis was examined for the two bicontinuous cubic mesophases composed of GMO/water and GMO/TAG/water in the case of the inverse hexagonal phase. It should be noted, that preparation of nanoparticles in the lamellar phase resulted in a fast particle formation. Most of them existed as aggregated sub- and micrometer-sized particles, visible with the naked eye, indicating fast nanoparticle formation. Thus, the results of the particle synthesis in the  $L_{\alpha}$  phase have not been investigated further and will not be reported in this thesis. One week after mixing, liquid crystals were characterized by small angle X-ray scattering, polarizing optical microscopy, and  $^2\text{H}$  NMR spectroscopy. Results for the cubic Ia3d and Pn3m phases are shown in figure 3.5. For comparison, similar measurements were performed for the corresponding reference samples containing pure  $\text{D}_2\text{O}$ .

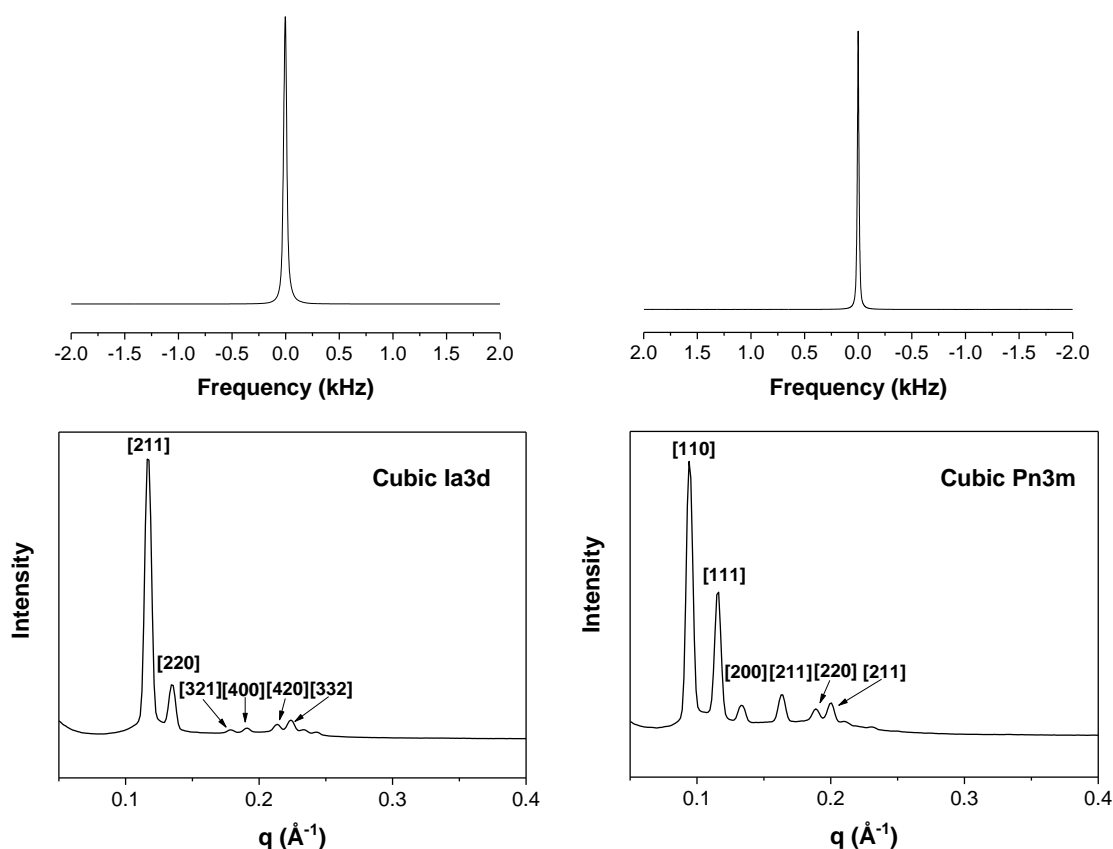


**Figure 3.5.**  $^2\text{H}$  NMR spectra (top) and small angle X-ray scattering patterns (bottom) of left: cubic Ia3d (70 wt.% GMO/30 wt.% 0.01 M  $\text{AgNO}_3$ ) and right: Pn3m (63 wt.% GMO/37 wt.% 0.01 M  $\text{AgNO}_3$ ) phase aged for one week after particle preparation (different NMR line width are due to shimming).

Samples from both cubic liquid crystalline phases are highly viscous and optically isotropic. The SAXS diffractograms display at least six distinctive Bragg reflections with a ratio of  $\sqrt{6}:\sqrt{8}:\sqrt{14}:\sqrt{16}:\sqrt{20}:\sqrt{22}$  for the cubic Ia3d and  $\sqrt{2}:\sqrt{3}:2:\sqrt{6}:\sqrt{8}:3$  for the cubic Pn3m phase. The  $^2\text{H}$  NMR spectra of both cubic liquid crystalline phases show a single peak characteristic for an isotropic phase.

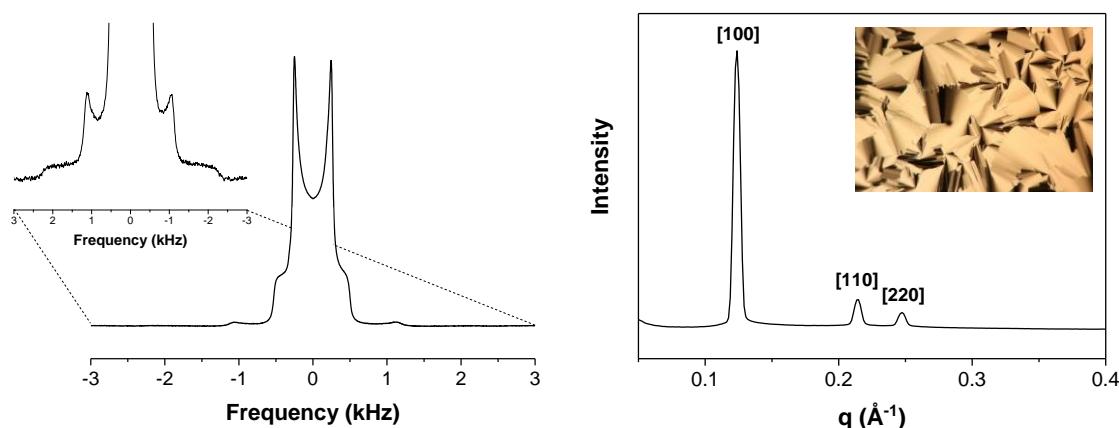


**Figure 3.6.**  $^2\text{H}$  NMR spectrum (left) and SAXS pattern (right) of the inverse hexagonal phase (70 wt. % GMO/5 wt.% TAG/25 wt.% 0.01 M  $\text{AgNO}_3$ ) aged for 1 week at 25 °C. The inset in the right panel shows a polarizing optical microscopy image of the  $\text{H}_{\text{II}}$  phase.

The  $\text{H}_{\text{II}}$  sample of GMO/TAG/water system was turbid due to the presence of a second phase. However, no macroscopic phase separation was observed after one day. The SAXS pattern displays three distinctive Bragg reflections with a ratio of  $1:\sqrt{3}:2$ , confirming a two-dimensional hexagonal lattice, as shown in figure 3.6. A nonoriented thin sample observed between cross polarizers shows a typical fan-like texture of a hexagonal phase (figure 3.6, inset) [104]. The  $^2\text{H}$  NMR spectrum of the inverse hexagonal phase consists of two Pake powder patterns indicating a coexistence of two different phases. The morphology of the second phase, of which only a small amount is present, is not entirely clear from the deuterium spectrum and SAXS diffractogram. If the second phase would have been a lamellar phase, the recorded quadrupole splitting should have been twice as large as for the hexagonal phase. However, the quadrupole splitting measured from the separation of the inner peaks (cylinders oriented perpendicular to the magnetic field, in the case of  $\text{H}_{\text{II}}$  phase) are 488 Hz and 2138 Hz showing more than a fourfold difference. It may indicate that two phases with largely different composition coexist in the sample. They are in equilibrium in a broad range of temperatures (figure A.10). As the temperature increases, a phase transition occurs from the hexagonal to the fluid isotropic phase.

The lattice parameter and the size of the aqueous domains of the liquid crystalline phases were calculated from the SAXS diffractograms. A comparison of the structural parameters of samples with and without silver added is shown in table 3.2. As can be seen, the dimensions of liquid crystalline phase remain almost unaltered in the presence of  $\text{Ag}^+/\text{AgNP}$ . The data are in agreement with previous reports [99]. All samples maintain their original liquid crystalline mesophase after incorporation of silver nitrate solution, followed by formation of silver nanoparticles.

**Table 3.2.** Composition of samples, lattice parameter ( $a$ ) and radius of the aqueous channel ( $r_w$ ), one week after particle preparation (0.01 M  $\text{AgNO}_3$  solution) in comparison with reference samples containing  $\text{D}_2\text{O}$ .

Composition	Phase	$a$ (Å)		$r_w$ (Å)	
		0.01 M	$\text{D}_2\text{O}$	0.01 M	$\text{D}_2\text{O}$
70 wt.% GMO/30 wt. % 0.01 M $\text{AgNO}_3$	Cubic Ia3d	131.7	128.5	15.5	14.9
63 wt.% GMO/67 wt. % 0.01 M $\text{AgNO}_3$	Cubic Pn3m	94.1	93.4	19.3	19.0
70 wt. % GMO/5 wt. % TAG/ 25 wt. % 0.01 M $\text{AgNO}_3$	Inverse hexagonal	58.6	58.0	16.0	15.9

### 3.5 Nanoparticle formation in the cubic Ia3d phase

The process of nanoparticle formation in the cubic Ia3d phase with various concentrations of  $\text{AgNO}_3$  was monitored by UV-Vis spectroscopy and transmission electron microscopy. Since the cubic phase is optically isotropic, measurements can be performed in situ, without dilution and therefore without destroying the liquid crystalline structure. Samples were measured in 1 mm quartz glass cuvettes, and the cubic phase without silver nitrate was used as reference. A time-dependent UV-Vis measurement for the cubic Ia3d phase (0.01 M  $\text{AgNO}_3$ ) is shown in figure 3.7.

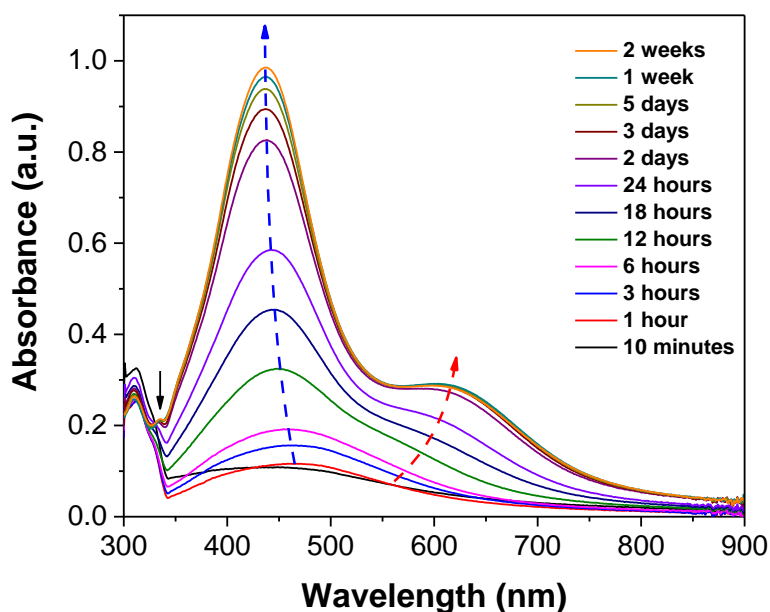


**Figure 3.7.** Time evolution of UV-Vis spectra of nanoparticles formed in the cubic Ia3d phase (70 wt.% GMO/30 wt.% 0.01 M AgNO<sub>3</sub>).

Nonionic surfactants are weak reducing agents so the process of nanoparticle formation is slow and the reaction is not yet completed after 2 weeks. Three peaks can be observed in the spectrum. The largest peak with a maximum at ca. 430–450 nm indicates the formation of spherical nanoparticles. It shows a red-shift compared to Ag nanoparticles in an aqueous medium due to the higher refractive index of the liquid crystalline phase ( $n_d^{20} = 1.46$  for pure monoolein). The change of the peak intensity shows an increase in the number of particles with reaction time. A second surface plasmon resonance band emerges at 600 nm. It can be attributed to the longitudinal plasmon resonance of nanorods or the in-plane dipole resonance mode of plate-like particles [105]. Some examples of such anisotropic particles are represented in TEM micrograph shown in figure 3.8(A). Other possible explanations for the second peak are the coupling of the surface plasmons of neighboring particles due to the formation of aggregates [106] or the formation of particles with a size larger than 100 nm. However, no evidence of sufficient number of large particles was found in TEM pictures. After 1 week, a small third peak at 335 nm was observed in the spectrum. It can be assigned to out-of-plane quadrupole resonance mode of plate-like particles [107]. This assignment is based on the BEM simulation of the different absorption modes of a single equilateral silver nanoprism, similar to the ones found in TEM micrographs (cf. figure 2.21).

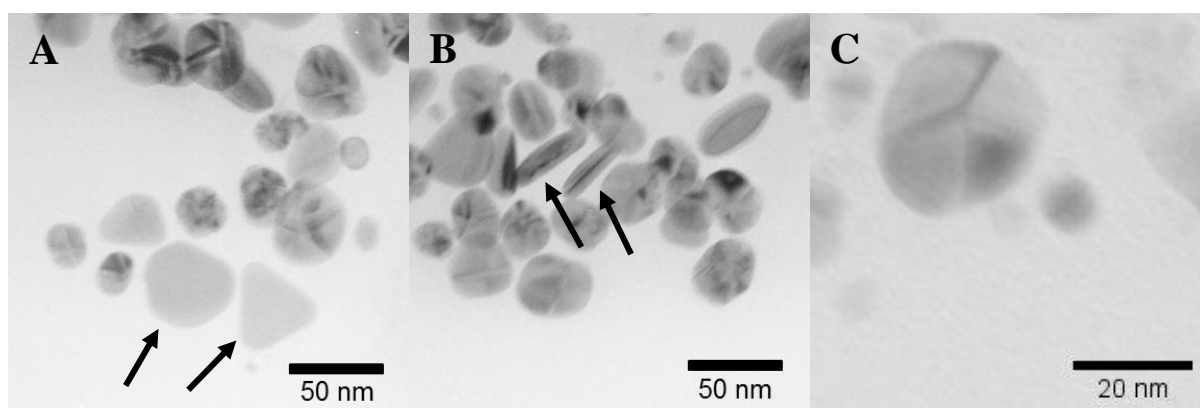


**Figure 3.8.** TEM micrographs showing some of the anisotropic particles: nanodisk and nanoprism (A), platelets standing on their edges (B); and multiple twinned nanoparticle (C) formed in the cubic Ia3d phase (70 wt.% GMO/30 wt.% 0.01 M AgNO<sub>3</sub>) after 1 month of aging.

In order to observe the evolution of size and morphology of the obtained nanoparticles with time transmission electron microscopy measurements have been performed. Because of the high surfactant content, nanoparticles cannot be measured directly in liquid crystals by conventional or cryo-TEM techniques. For the TEM measurements, 50 mg of the liquid crystal were dissolved in absolute ethanol and nanoparticles were collected by centrifugation. Figure 3.9 shows TEM images of nanoparticles formed in the cubic Ia3d phase after 12 hours, 1 day, 1 week and 1 month. At the early stage of the synthesis (12 and 24 hours), the nanoparticles are mostly spherical and ellipsoidal in shape. After one week two different sets of nanoparticles can be clearly seen. The first set consists of nearly spherical polyhedral particles which are mono- and polycrystalline with a size of 2–30 nm. The second set consists of anisotropic flat particles having a variety of shapes, from circular to triangular with a size of 30–60 nm. They can be seen in the TEM micrographs as low contrast objects. The thickness was found to be in the range of 10–15 nm, as determined from nanoplates standing edge on to the electron beam, as shown in figure 3.8 (B). Besides anisotropic plate-like particles, some of the nanoparticles exhibit multiply twinned morphology (figure 3.8 (C)).

Interestingly, the mean size of nanoparticles is nearly independent of the aging time. Based on the TEM measurements, it was observed that larger nanoparticles and anisotropic particles tend to form already during the first hours of reaction. The relative proportion of smaller nanoparticles ( $\leq 10$  nm) was increased after 1 week and remained almost unchanged after 1 month.

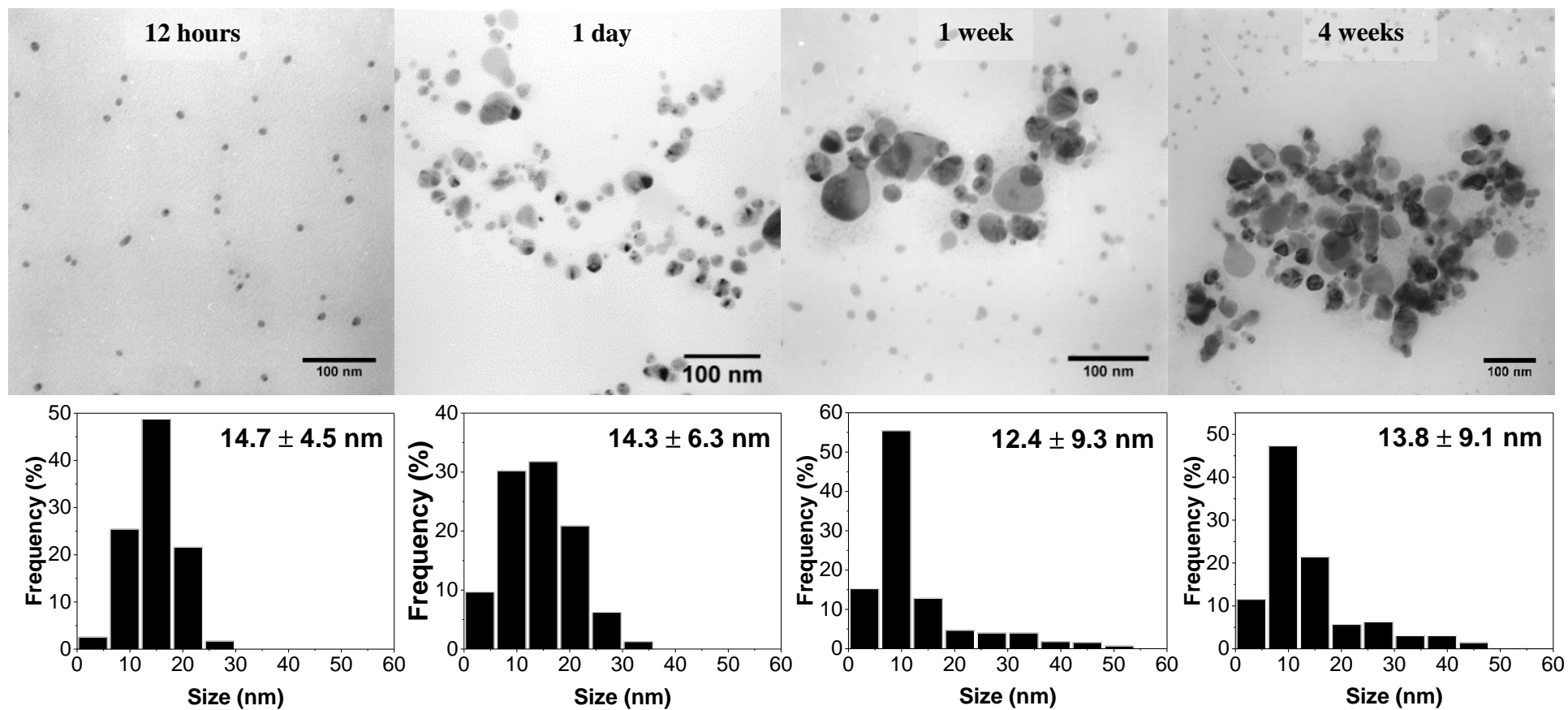


**Figure 3.9.** Time-dependent TEM micrographs (top) and corresponding size distribution (bottom) of nanoparticles prepared in the cubic Ia3d phase (70 wt.% GMO/30 wt.% 0.01 M AgNO<sub>3</sub>). Results are presented as a mean size ± standard deviation.

It has been reported that flat anisotropic nanoparticles with a size below the electrostatic limit are unstable in solution and tend to reorganize into the spherical particles via several reformation processes, like internal reorganization, Ostwald ripening and aggregation/agglomeration [108]. In our case, the high viscosity of the liquid crystalline phase and adsorption of the surfactant molecules on the nanoparticle surface stabilize the particles and prevent them from growth and shape reformation. When platelets reached a mature stage after 1 week, their size remained almost unchanged for at least one month, as was confirmed by transmission electron microscopy and UV spectroscopy. Further spectroscopic characterization was not conducted because after 4–5 weeks particle sedimentation was observed.

To study the kinetics of nanoparticle formation, the absorption spectra from figure 3.7. were fitted to obtain the position and intensity of the dipolar surface plasmon resonance peaks. The results are presented in figure 3.10. As can be seen from the kinetic curves, the formation process of anisotropic particles is faster compared to small spherical nanoparticles. Position and intensity at  $\lambda_{\max}$  of the long-wavelength absorption band levels off after 2–3 days in comparison to 1 week for isolated AgNP, indicating that anisotropic particles grow faster to the mature state.

The first peak (figure 3.10 A) shows a blue shift of the maximum absorption peak position during the first two days of the reaction. Andersson and coworkers reported a blue shift and dependence of the final SPR position on the initial silver concentration as well as a change in the size, size distribution and morphology of nanoparticles [7]. In our case the peak around 435 nm arises not only from spherical particles but also from the in-plane quadrupole plasmon resonance whose position is shifted when the aspect ratio of the anisotropic nanoparticle changes; furthermore, the number of the small particles increases over time. The position of the second plasmon resonance band shows a more significant change – from ca. 540 to nearly 600 nm (figure 3.10 B). Such a strong red shift of the SPR position is indicative of a morphological change of anisotropic nanoparticles while keeping the same thickness. These results are also in agreement with those reported in literature [109].

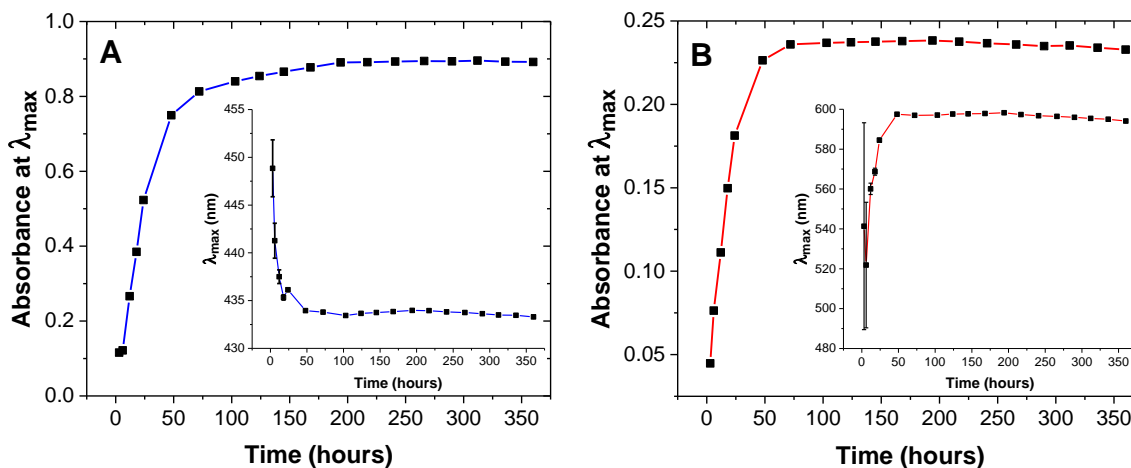


**Figure 3.10.** Change of the maximum absorbance at  $\lambda_{max}$  and SPR position (shown in the inset) of dipolar surface plasmon resonance of spherical (A) and anisotropic (B) particles as a function of time.

In order to distinguish whether the additional peaks observed are due to the presence of anisotropic particles but not particle aggregates or large particles, freeze-fracture electron microscopy (FFEM) of the cubic Ia3d phase and UV-Vis spectroscopy of ethanolic LC solution were performed.

Figure 3.11 shows UV-Vis spectra of liquid crystalline samples dissolved in absolute ethanol 1 day and 1 week after mixing. Optical glass cuvettes with a path length of 10 mm were used. Samples were diluted tenfold and sonicated for one minute to destroy possible agglomerates. In comparison to the spectra of the undiluted sample (cf. figure 3.7) both peaks show an unexpected shift to higher wavelength. It has been suggested that such a shift can be caused by adsorption of the surfactant molecules and silver ions on the nanoparticle surface [110]. Therefore, dilution in ethanol, which should remove adsorbed species, should result in a shift to lower wavelength. Hence, there must be another mechanism that explains the red shift. Most probably, the observed red shift is caused by aggregation of particles in solution. This phenomenon has also been observed in the literature [111]. Indeed, the TEM results of an aged ethanol dispersion of the silver nanoparticles show mostly the presence of silver aggregates (data not shown).

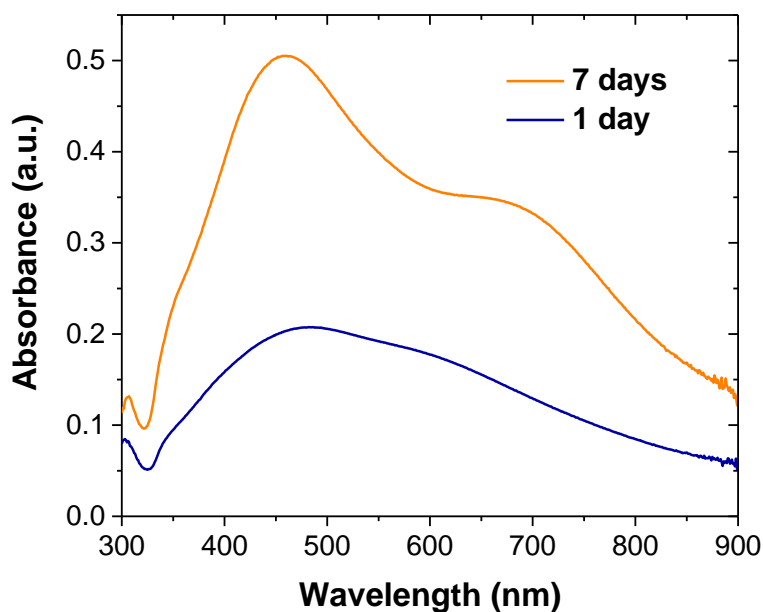


**Figure 3.11.** UV-Vis absorption spectra of 0.1 g cubic Ia3d phase (70 wt. % GMO/30 wt.% 0.01 M AgNO<sub>3</sub>) dissolved in ethanol.

In order to study the morphology of silver nanoparticles synthesized in the liquid crystalline cubic Ia3d phase (70 wt.% GMO/30 wt.% 0.01 M AgNO<sub>3</sub>), freeze-fracture electron microscopy has been employed. This method has an advantage over conventional TEM because it allows to study the whole sample (nanoparticles in the liquid crystal matrix). The results are displayed in figure A.11. FFEM micrographs show that the majority of nanoparticles are isolated with some examples of closely-spaced particles. However, due to the small number of observed AgNP a quantitative analysis of the FFEM images was not possible. Based on FFEM aggregation can be excluded to large extent and the red-shifted second peak observed mostly due to anisotropic particles that are also found by TEM.

Since the headgroup of the monoolein is directly involved in the synthesis, it is believed that nanoparticle formation takes place in the aqueous channels of the liquid crystals. Hence, the size of the nanoparticles should be about the same dimensions as the diameter of the water channels. However, the average size of the synthesized nanoparticles was approximately 4–5 times larger than the size of the aqueous pores of the liquid crystal. It is possible that some of the nanoparticles result due to the clustering and aggregation of neighboring particles. The low fraction of small particles indicates that the highly viscous bicontinuous cubic phase cannot fully prevent nanoparticles from aggregating and nanoparticles growing beyond the liquid crystalline dimensions.

### 3.6 Effect of $\text{Ag}^+$ concentration on nanoparticle formation in the cubic Ia3d phase

In order to study the influence of the silver concentration on the nanoparticle formation process, two more samples have been prepared. Figure 3.12 shows the results of the time evolution of UV-Vis spectra of cubic Ia3d samples loaded with 0.02 and 0.05 M  $\text{AgNO}_3$  solution.

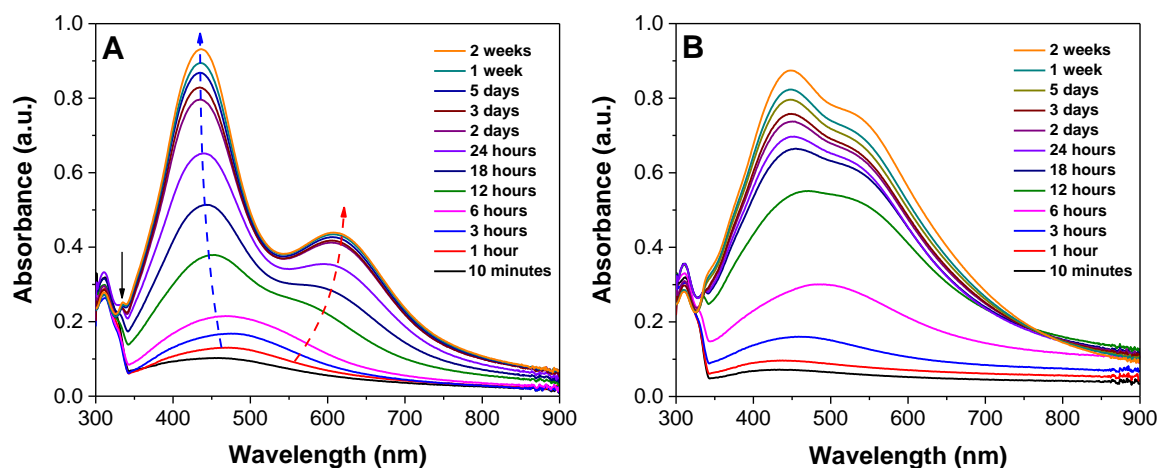


**Figure 3.12.** Time evolution UV-Vis spectra of cubic Ia3d phase (70 wt.% GMO/30 wt.%  $\text{AgNO}_3$  solution) containing (A) 0.02 M  $\text{AgNO}_3$ , (B) 0.05 M  $\text{AgNO}_3$ .

The sample with 0.02 M  $\text{AgNO}_3$  solution presents a similar behavior to the sample with lower  $\text{Ag}^+$  concentration. When compared with the 0.01 M  $\text{AgNO}_3$  sample (figure 3.7), two things are apparent: first, the surface plasmon resonance at 610 nm shows increased intensity suggesting that there is an increase in the relative population of anisotropic nanoparticles. Second, the absorption band at higher wavelength was typically blue shifted with an increase of  $\text{Ag}$  concentration indicating a more circular shape or larger thickness of anisotropic particles.

UV-Vis absorption measurements were repeated for three independent samples containing 0.02 M  $\text{AgNO}_3$  solution (figure A.12). The position of first absorption band remained almost unaffected, whereas the second peak position varied in the range of 585–606 nm (average  $593 \pm 12$  nm), indicating that the size and morphology of the flat nanoparticles was not constant. With further increase of silver nitrate concentration, the second peak shifts more towards the lower wavelength, indicating that the shape of the silver nanoparticles becomes more spherical (figure 3.12, B) [112]. It also should be noted, that increase of  $\text{Ag}^+$  concentration may result in particle aggregation and, therefore, peak broadening and an increase of the absorption intensity in the long-wavelength region. As can be seen in the figure 3.13, in addition to spherical

particles, plate-like nanoparticles are present in the sample with 0.02 M  $\text{AgNO}_3$  already after 12 hours. As the reaction proceeds, the number of anisotropic nanoparticles gradually increases. The following data are in perfect agreement with the measured UV-VIS spectra. An increase of  $\text{Ag}^+$  concentration had almost no effect on the average size of the synthesized particles, as shown in figures 3.13 and 3.14.

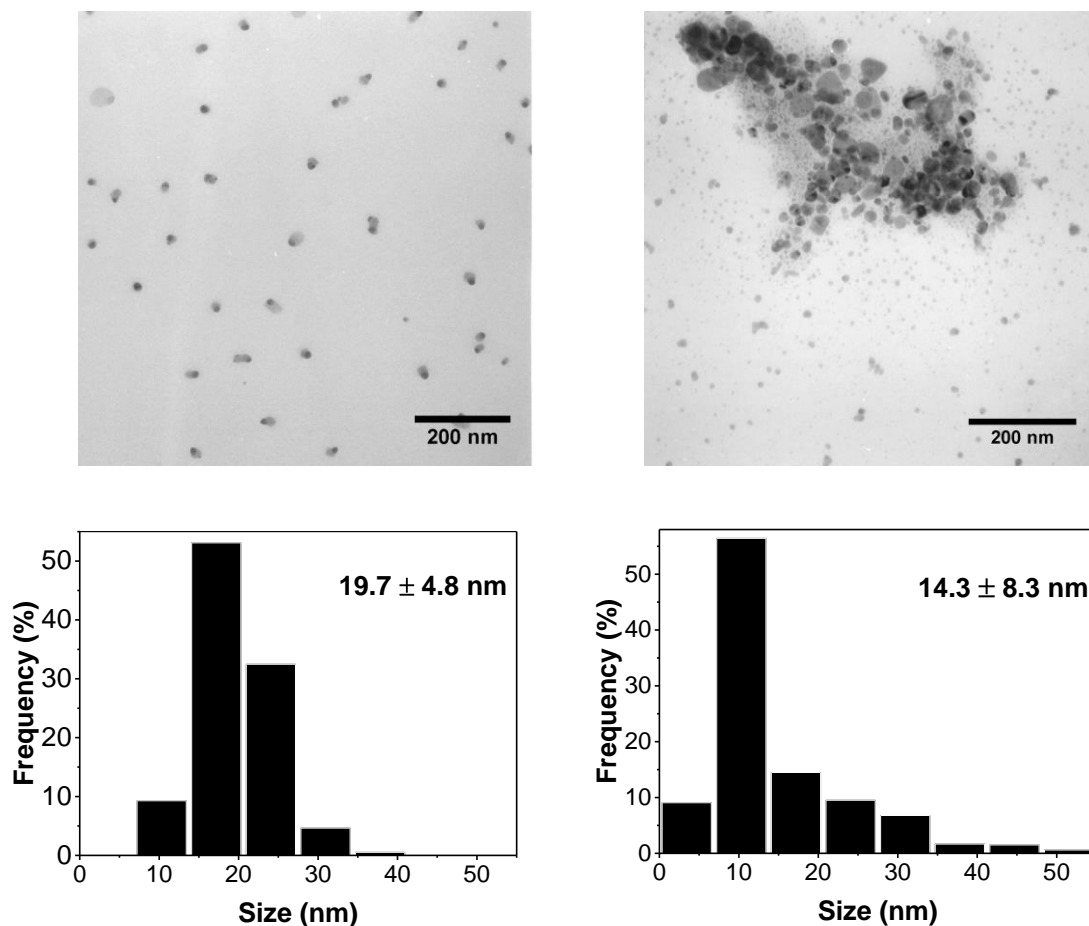


**Figure 3.13.** TEM micrographs (top) and size distribution (bottom) of nanoparticles synthesized in the cubic Ia3d phase (70 wt.% GMO/30 wt.% 0.02 M  $\text{AgNO}_3$ ) after 12 hours (left) and 1 month (right).

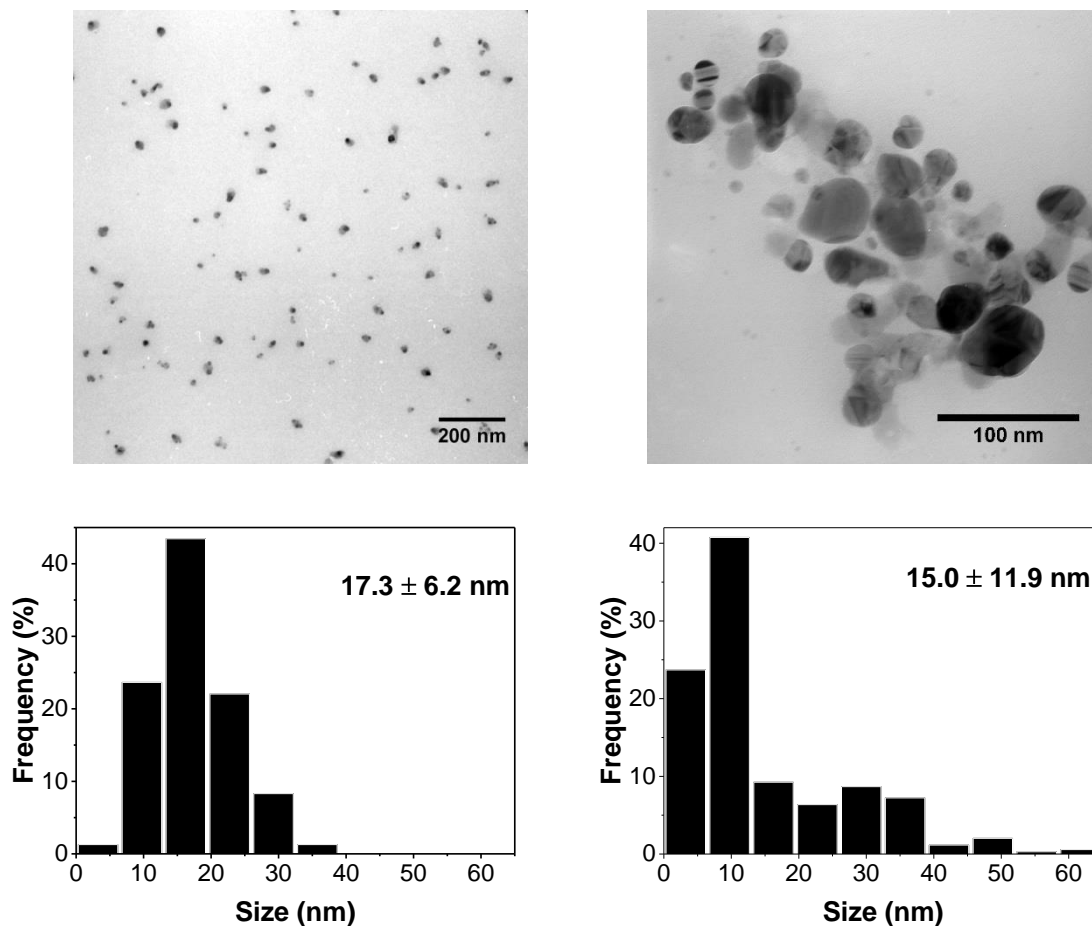


**Figure 3.14.** TEM images (top) and size distribution histogram (bottom) of nanoparticles synthesized in the cubic Ia3d phase (70 wt.% GMO/30 wt.% 0.05 M AgNO<sub>3</sub>) after 12 hours (left) and 1 month (right).

### 3.7 Synthesis of nanoparticles in the cubic Pn3m phase. Effect of Ag<sup>+</sup> concentration and aging time

To study the influence of the template structure on AgNP formation, nanoparticles also have been synthesized in cubic Pn3m and inverse hexagonal liquid crystalline phases. Figure 3.15 shows the results of the time-dependent UV-Vis spectroscopy for the cubic Pn3m phase (0.01 M AgNO<sub>3</sub>) measured during two weeks after the sample preparation. As can be seen, the results are similar to the cubic Ia3d phase (figure 3.7). At the beginning of the reaction, only one peak around 460 nm is present in the UV spectrum, showing the formation of particles. After 12 hours, a shoulder arising at 575 nm attributed to the presence of anisotropic and tabular nanoparticles. The peak is less pronounced, compared to cubic Ia3d phase with similar AgNO<sub>3</sub> concentration (figure 3.7), indicating that the anisotropic nanoparticles have a more irregular

shape. As the reaction proceeds, the first peak shows a blue shift while the second shifts towards longer wavelength. After two days of aging, the third absorption peak with low intensity was detected at 333 nm, attributed to the out-of-plane quadrupole resonance of nanoprisms and nanodisks [107].

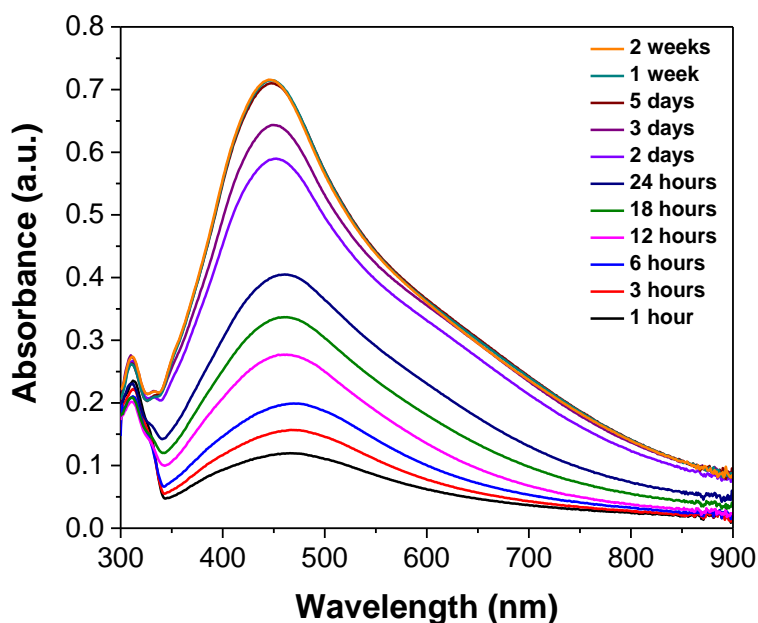


**Figure 3.15.** Time evolution UV-Vis spectra of nanoparticles generated in the cubic Pn3m phase (67 wt.% GMO/37 wt.% 0.01 M AgNO<sub>3</sub>).

The size and morphology of nanoparticles synthesized in the cubic Pn3m phase (0.01 M AgNO<sub>3</sub>) have been investigated by transmission electron microscopy after 12 hours and 1 month (figure 3.16). After 12 hours of synthesis, individual quasispherical mono- and polycrystalline nanoparticles with a size in the range of 3–50 nm were formed. After 1 month, large and anisotropic particles with a variety of shapes were found.

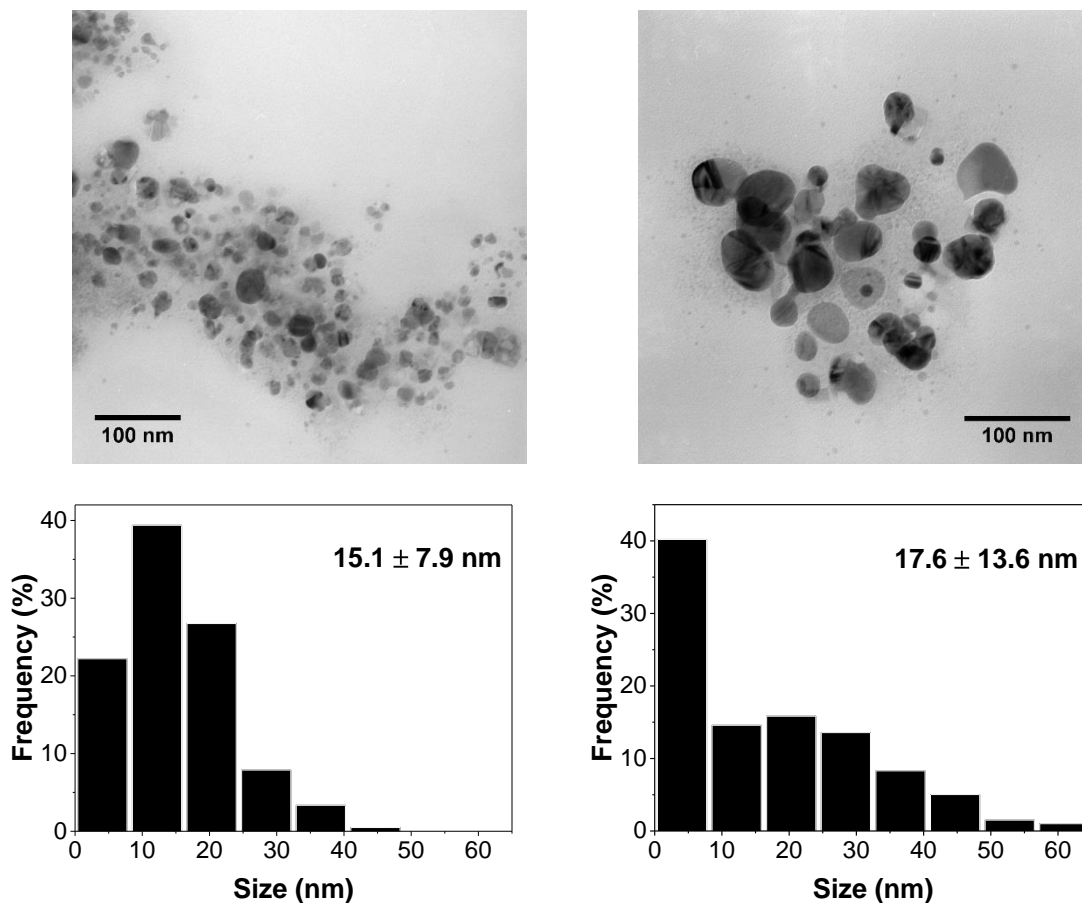


**Figure 3.16.** TEM micrographs (top) and size distribution histograms (bottom) of nanoparticles synthesized in the cubic Pn3m phase (0.01 M AgNO<sub>3</sub>) after 12 hours (left) and 1 month (right).

Analogously to the cubic Ia3d phase, two more samples with a larger AgNO<sub>3</sub> concentration have been prepared. Figure 3.17 displays UV-Vis absorption spectra of nanoparticles synthesized in the cubic Pn3m phase containing 0.02 M and 0.05 M AgNO<sub>3</sub> solution measured during 2 weeks after the preparation.

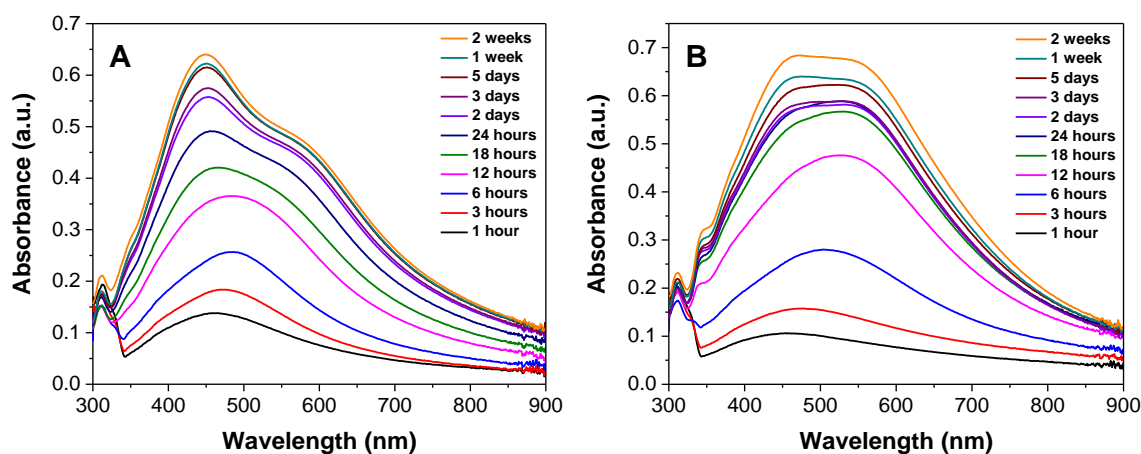


**Figure 3.17.** Time evolution UV-Vis spectra of cubic Pn3m phase (67 wt.% GMO/37 wt.% AgNO<sub>3</sub> solution) containing (A) 0.02 M AgNO<sub>3</sub>, (B) 0.05 M AgNO<sub>3</sub>.

Absorption spectra represent a similar trend as previously reported in chapter 3.5. With an increase of  $\text{AgNO}_3$  amount, the position of the dipolar resonance from anisotropic particles and aggregated structures shifts towards lower wavelength. The differences in the absorption spectra are associated with morphological changes of anisotropic particles and the decrease of the interparticle spacing in particle aggregates. For the sample with 0.05 M  $\text{AgNO}_3$  peak at a longer wavelength, assigned to the anisotropic flat particles and particle aggregates has a comparable intensity to the absorption band of spherical nanoparticles. The average size of nanoparticles synthesized in cubic Pn3m phases with various silver nitrate concentration after 12 hours and 1 month is shown in figure 3.18. As can be seen, the average size of nanoparticles is almost independent on the  $\text{Ag}^+$  concentration. After 1 month, the average size is slightly increased (1–2 nm), compared to 12 hours. However, the size distribution became broader due to the longitudinal growth of anisotropic nanostructures and an increased fraction of small particles. The TEM pictures and size distribution histograms of silver particles obtained in cubic Pn3m phase with 0.02 M and 0.05 M  $\text{AgNO}_3$  solution are represented in figures A.13 and A.14.

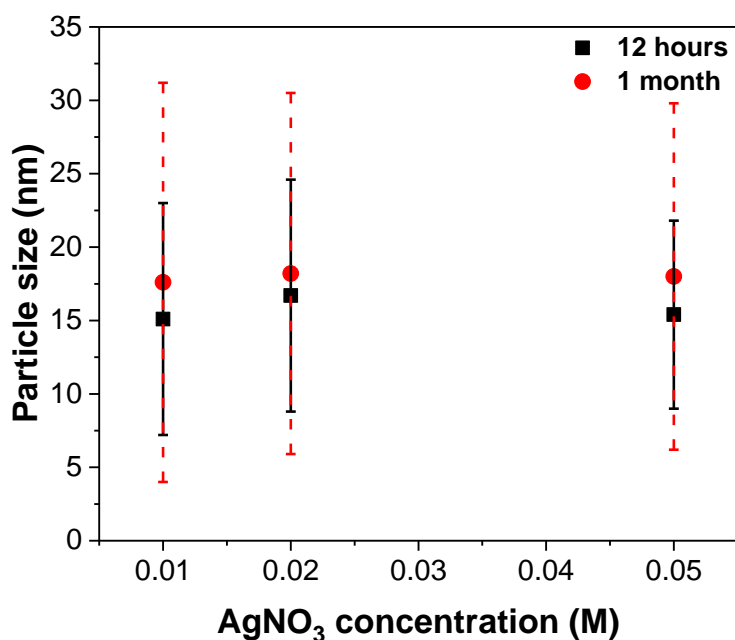


**Figure 3.18.** Average size of silver nanoparticles synthesized in the cubic Pn3m phase with various  $\text{AgNO}_3$  concentration after 12 hours and 1 month.

### 3.8 Long-term stability of the bicontinuous cubic liquid crystalline mesophases

Formation of silver nanoparticles also affects the long-term stability of the monoolein-based liquid crystals. It has been already demonstrated that hydrolysis of the monoolein leads to the formation of oleic acid and glycerol and therefore induce cubic to  $H_{II}$  phase transition [113]. Borne et. al. showed that a small content of oleic acid favors the formation of the  $H_{II}$  phase [114]. Polarizing optical microscopy images of the aged cubic Ia3d and Pn3m samples loaded with high  $Ag^+$  concentration clearly demonstrate a presence of the inverse hexagonal phase after 6–12 months, as shown in figure 3.19. In comparison, samples in the absence of  $Ag^+$  retain their structures even after a long (more than 2 years) storage. Based on that, we can assume that the formation and presence of silver nanoparticles can accelerate the hydrolysis rate of GMO and induces cubic to inverse hexagonal phase transition.



**Figure 3.19.** Polarizing optical microscopy images of initially cubic Ia3d (left) and Pn3m (right) samples containing 0.1 M  $AgNO_3$  aged for 1 year.

### 3.9 Synthesis of nanoparticles in the inverse hexagonal phase

In the inverse hexagonal phase, surfactant molecules self-assemble into two-dimensional rod-like aggregates arranged into a hexagonal cell. As in the cubic phases GMO headgroups slowly reduce  $Ag^+$  ions dissolved in the aqueous medium. An inverse hexagonal phase has an advantage due to the restriction of silver precursor and resulting silver nanoparticles in two dimensions instead of one for the lamellar phase, being a potential template for the synthesis of nanorods and nanowires. Andersson and coworkers reported the synthesis of silver nanoparticles in  $H_{II}$  formed by nonionic surfactant Pluronic P123/butyl acetate/water [67]. They were able to prepare small nanoparticles (3 nm) macroscopically aligned into fibrils which were

packed into millimeter long fibers. However, to the best of our knowledge, no successful examples of silver nanorods preparation in the  $H_{II}$  phase have been reported.

For the synthesis of nanoparticles several samples of hexagonal phase (70 wt.% GMO/5 wt.% TAG/25 wt.%  $AgNO_3$  solution of various concentrations) have been prepared. As for the cubic liquid crystalline phases, formation of particles in the inverse hexagonal phase during the reduction was observed by the color change, from colorless (before reduction) to brown-green (after reduction). The intensity of color gradually increased during one week of synthesis. Due to the strong birefringence and turbidity because of the presence of the second phase detected by  $^2H$  NMR (see section 3.4), in situ UV-Vis absorption measurement of the inverse hexagonal phase are difficult. Hence, 0.1 g of liquid crystalline material was dissolved in 0.9 ml of absolute ethanol and the resulting dispersions were sonicated to destroy possible agglomerates. Figure 3.20 shows UV-Vis absorption spectra of such dispersions of nanoparticles synthesized in the inverse hexagonal phase aged for 1 day, 3 days and 1 week.

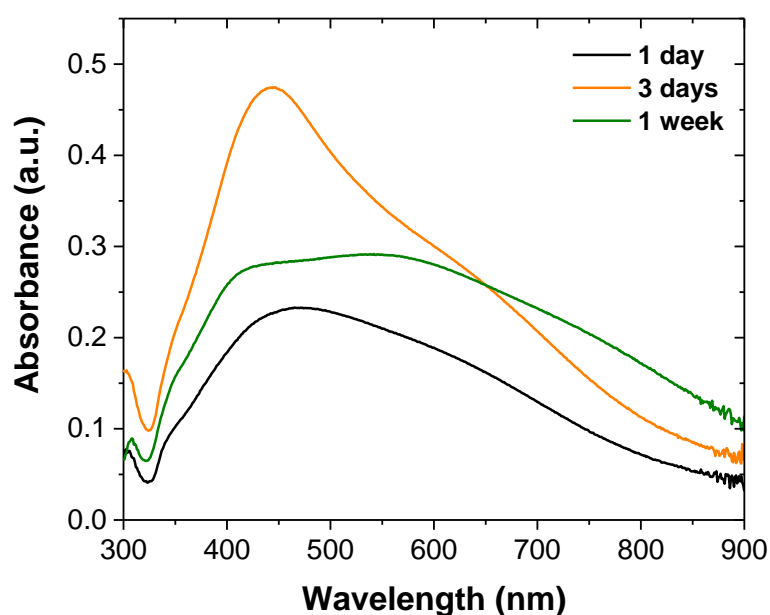


**Figure 3.20.** UV-Vis spectra of nanoparticles formed in the inverse hexagonal phase (70 wt.% GMO/5 wt.% TAG/25 wt.% 0.01 M  $AgNO_3$ ) after 1 day, 3 days and 1 week.

Spectra after 1 and 3 days of synthesis are similar to the absorption spectra for the cubic Ia3d phase in solution. The peak at 445 nm indicates the formation of the spherical particles. A shoulder at 620–650 nm arises due to the formation of anisotropic flat particles. The absorption efficiency of SPR band is decreasing with increasing aging time while the intensity in the near infrared region undergoes an increase. After 1 week particle aggregation was noticeable, resulting

in a broader and less intense spectrum. A peak splitting into short- and long-wavelength resonance was observed due to the decrease of the interparticle spacing in particle aggregates.

In order to observe the size and morphology of nanoparticles, samples have been analyzed with TEM after 1 day and 1 week. The results of the TEM measurements are shown in figure 3.21. After 1 day of synthesis, most of the individual nanoparticles are spherical with a size in the range of 3–30 nm. Some rodlike particles can be seen in the TEM picture, resulting due to the coalescence of two neighboring particles. After 1 week, the average size is bigger and the size distribution is broader, compared to the nanoparticles obtained after 1 day. In addition, more anisotropic and flat particles can be found after 1 week of aging. The average size of nanoparticles obtained after 1 day and 1 week was  $14.7 \pm 7$  and  $16.9 \pm 9.6$  nm, respectively.

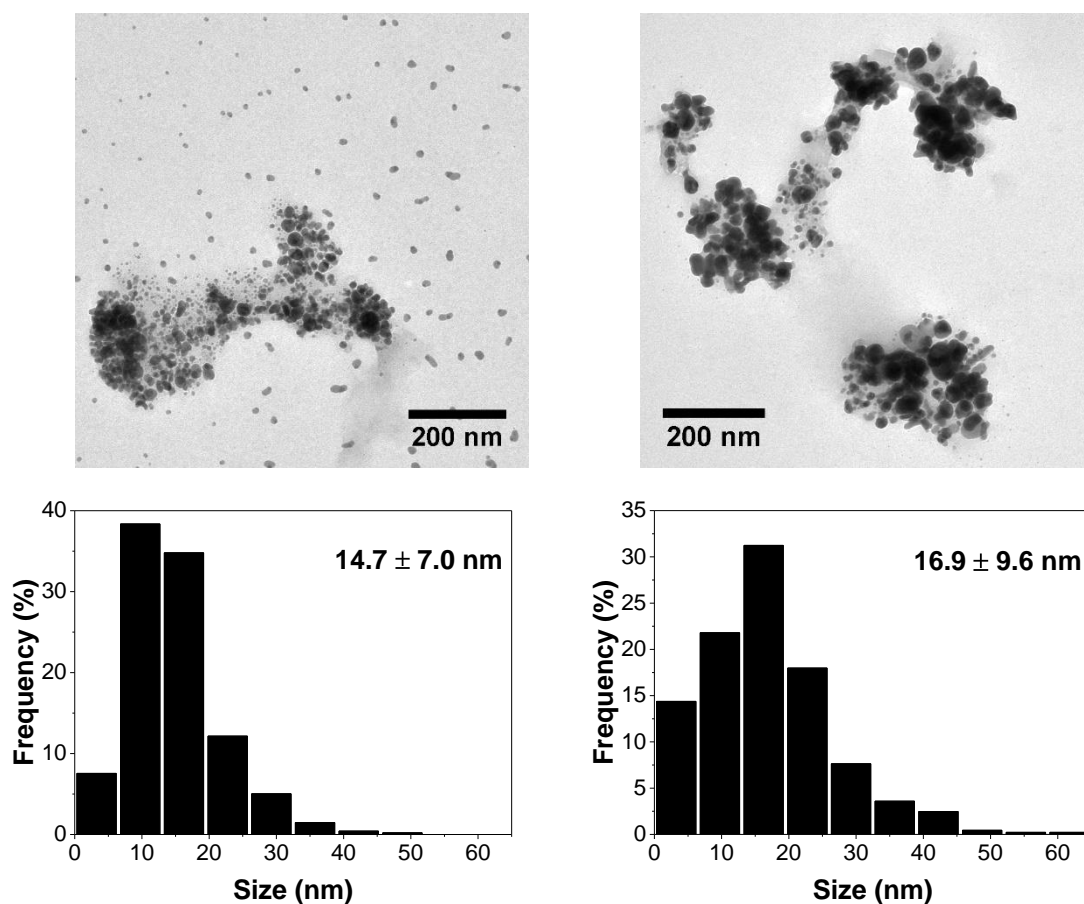


**Figure 3.21.** TEM pictures (top) and size distribution histogram of nanoparticles (bottom), formed in inverse hexagonal phase (70 wt.% GMO/5 wt.% TAG/25 wt.% 0.01 M AgNO<sub>3</sub>) after 1 day (left) and 1 week (right).

UV-Vis spectra of the inverse hexagonal phase loaded with 0.05 M AgNO<sub>3</sub>, presented in figure 3.22, shows a very broad absorption peak due to the anisotropic nanoparticles and particle aggregates. In this case, the reduction of silver ions was almost completed after 1 day. Further

aging resulted in small batho- and hyperchromic shift of the surface plasmon resonance band. Besides that, aggregation of particles was quicker and more noticeable. Lower viscosity and water content of the inverse hexagonal phase led to a faster reduction of silver ions and faster diffusion of silver precursor towards growing particles, compared to the cubic Ia3d and Pn3m phases.

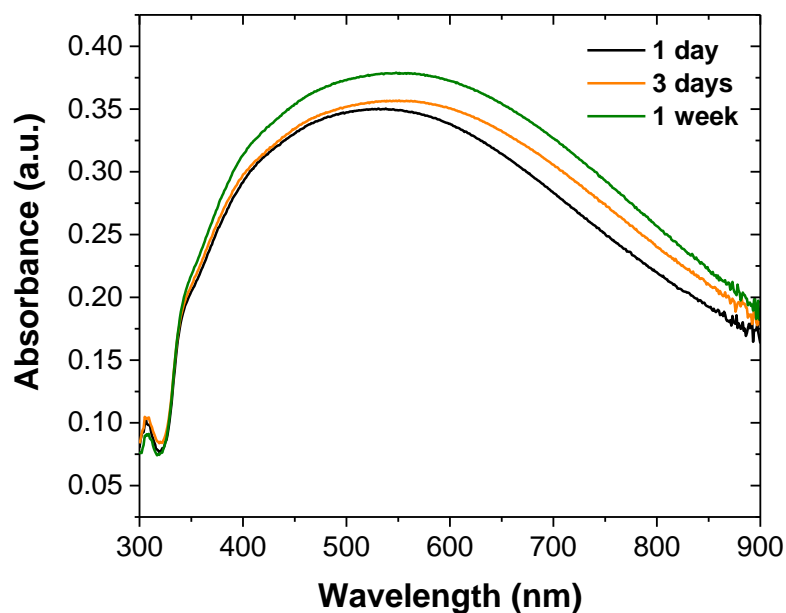


**Figure 3.22.** UV-Vis spectra of nanoparticles formed in inverse hexagonal phase (70 wt.% GMO/5 wt.% TAG/25 wt.% 0.05 M AgNO<sub>3</sub>) after 1 day, 3 days and 1 week.

TEM images of nanoparticles synthesized in the inverse hexagonal phase (0.05M AgNO<sub>3</sub>) after 1 day and 1 week are displayed in figures 3.23 and 3.24 respectively. After 1 day results are similar to the sample with lower Ag<sup>+</sup> concentration. Although the resulting nanoparticles demonstrated a range of shapes, the majority of nanoparticles were spherical in the range of 3–30 nm with an average size of  $14 \pm 7.2$  nm. Most of the AgNP with a size larger than 30 nm are flat nanoparticles with geometries ranging from triangular to circular. Furthermore, clusters of particles with different morphologies consisting of several particles were observed in the TEM pictures (figure 3.23, B). An increase of the Ag<sup>+</sup> concentration may result in the decrease of the interparticle distance and cluster formation. These structures possibly undergo internal reorganization and shape transformation into tabular particles.

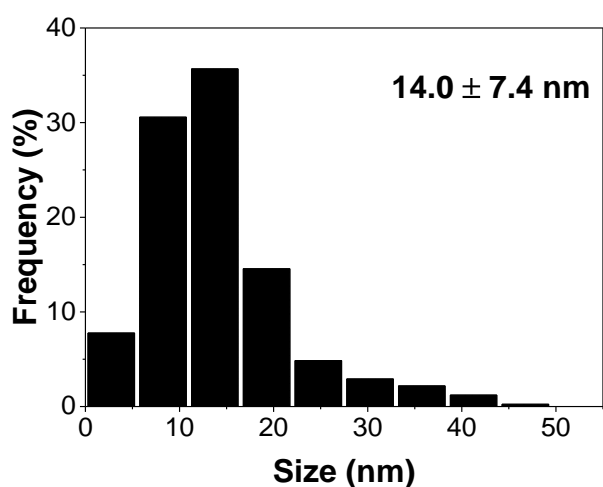
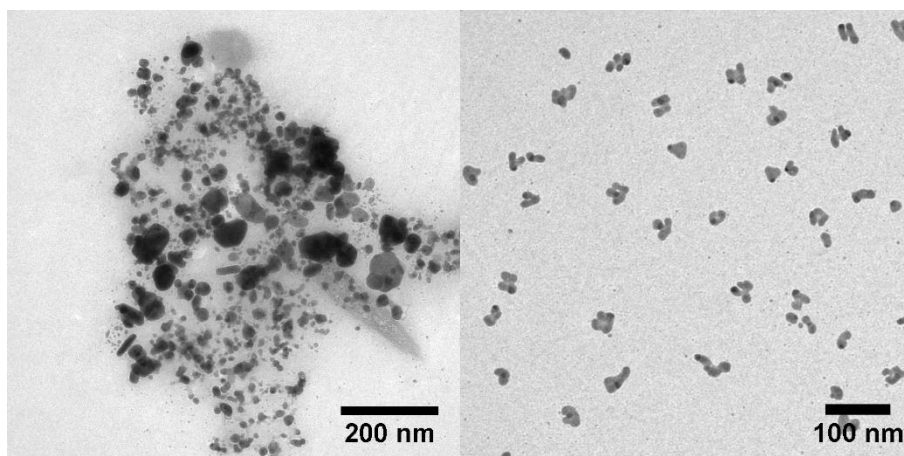


**Figure 3.23.** TEM images (top) and size distribution histogram (bottom) of nanoparticles formed in the inverse hexagonal phase (70 wt.% GMO/5 wt.% TAG/25 wt.% 0.05 M AgNO<sub>3</sub>) after 1 day.

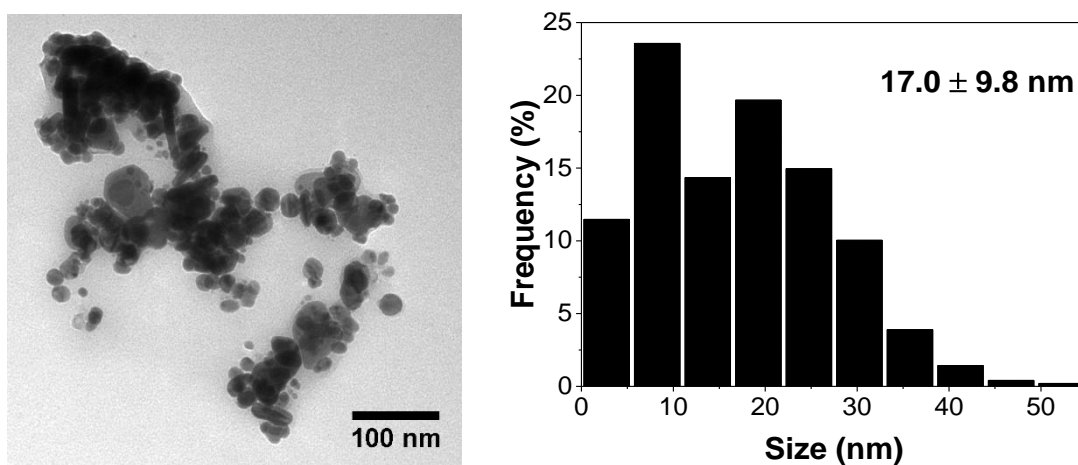


**Figure 3.24.** TEM images and size distribution histogram of nanoparticles formed in the inverse hexagonal phase (70 wt.% GMO/5 wt.% TAG/25 wt.% 0.05 M AgNO<sub>3</sub>) after 1 week.

### 3.10 Summary

The present chapter is focused on the synthesis of silver nanoparticles by the reduction of silver ions in the various lyotropic liquid crystalline phases formed by biologically friendly surfactant – monoolein with and without tricaprilyn.

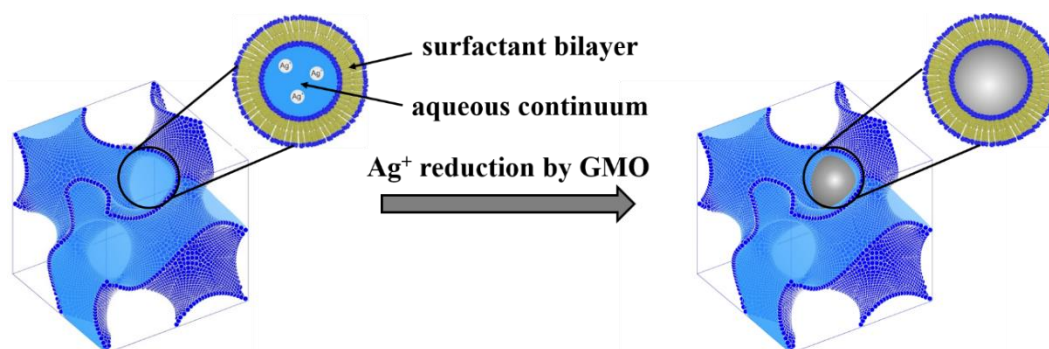


**Figure 3.25.** Schematic representation of the synthesis of silver nanoparticles in the cubic Ia3d liquid crystalline phase.

The initial focus of this work was to test the ability of the monoolein-based lyotropic liquid crystalline phases as templates for the controlled synthesis of silver nanoparticles with different size and morphology. Surfactant molecules have been used to form the liquid crystalline phases in aqueous solution as well as to reduce the silver ions to Ag<sup>0</sup> as confirmed by evidence for oxidation of the surfactant from ATR-FTIR and <sup>1</sup>H NMR spectroscopy. Monoolein takes part in polyol-type reaction by reduction of Ag<sup>+</sup> due to the oxidation of alcohol groups. Since no external strong reducing agent was used the kinetics of the silver particle formation is slow, which makes it possible to study the process in situ. The microstructure of the liquid crystals is investigated by polarizing optical microscopy, <sup>2</sup>H NMR spectroscopy, and small angle X-ray scattering. It was confirmed that the liquid crystalline phase is maintained upon nanoparticle formation. However, the synthesized nanoparticles may affect the long-term stability of the LC mesophase. The formation rate and the morphology of silver particles have been monitored by UV–visible spectroscopy and transmission electron microscopy. Variation of size and shape of particles as well as the presence of particle aggregates may explain the variation of UV-Vis spectra.

The average size of the resulting nanoparticles is ca. 15 nm which is approximately 4–5 times larger than the corresponding dimensions of the aqueous channels of the liquid crystalline phase. Two different particle structures were found: spherical and plate-like anisotropic particles with a variety of geometries, from triangular nanoprisms to nanodisks. Nanoparticle size and shapes remain almost unaltered by the increase of the concentration of silver nitrate solution.

## 4 Synthesis of silver nanoparticles in DNA-containing monoolein-based liquid crystals

### 4.1 Introduction

Both DNA and surfactants have been successfully used for the synthesis of silver nanoparticles. However, the templating properties of DNA-containing liquid crystals are almost unknown. In the present chapter, the photoinduced formation of silver nanoparticles in DNA-containing lyotropic liquid crystal formed by monoolein is reported. Photochemical methods are attractive for the synthesis of metallic nanoparticles because they allow to use time-delayed chemistry so nanoparticles can be synthesized on-demand to provide fresh samples. Reaction conditions can be controlled by variation of light intensity and exposure times.

The chosen dodecyltrimethylammonium-DNA/monoolein/water ternary phase diagram has been studied by Bilalov et al. at 25°C in comparison to the DNA-free analogue [115]. The phase diagram is shown in figure 4.1. Several liquid crystalline phases have been identified in the monoolein-rich region of the phase diagram: two bicontinuous cubic phases with Ia3d and Pn3m space groups, an inverse hexagonal phase ( $H_{II}$ ), and a lamellar liquid crystalline phase ( $L_{\alpha}$ ). The lamellar phase does not contain any DTADNA because the presence of DNA prevents swelling of the  $L_{\alpha}$  phase and an inverse hexagonal phase is formed instead. The inverse hexagonal phase consists of two-dimensional rod-like micelles arranged into the hexagonal lattice where DNA is intercalated in the aqueous interior of the surfactant aggregates.

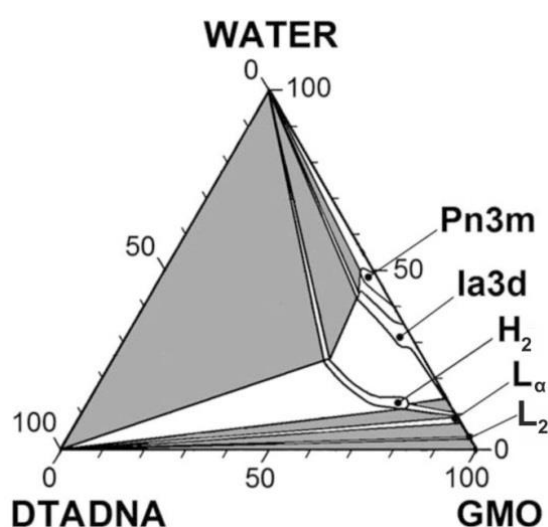


**Figure 4.1.** Phase diagram of the DTADNA/GMO/water ternary system at 25 °C [115]. Non-labeled white areas represent two-phase regions, gray – three phases.

## 4.2 Influence of nanoparticle formation on the liquid crystalline structure

Preparation of silver nanoparticles was conducted in cubic Ia3d and Pn3m phases containing 1 wt.% of the DTADNA. Due to the high content of the solid DTADNA complex and limited volume of the lipid mixer, the method used for the preparation of cubic samples could not be used to prepare samples from the inverse hexagonal phase region. Therefore, the formation of silver nanoparticles in the  $H_{II}$  phase was not investigated. For the synthesis of silver nanoparticles,  $D_2O$  was replaced with a silver nitrate solution of various concentration. The DTADNA complex was first incubated with a silver nitrate solution for 12–48 hours and then mixed with molten monoolein using the same procedure as in chapter 3.

After preparation and equilibration for 3 days, samples have been irradiated with UV-light for 1 hour to generate nanoparticles. The liquid crystalline phase after 1 hour of UV irradiation has been characterized by  $^2H$  NMR, polarizing optical microscopy, and small angle X-ray scattering techniques. Figure 4.1. shows a picture of cubic Ia3d and Pn3m samples (0.02 M  $AgNO_3$  solution) exposed to UV for 1 hour and a sample aged for 4 weeks. Freshly prepared samples were highly viscous gel-like and colorless. During the UV-irradiation samples turned yellow to orange, indicating the formation of particles.



**Figure 4.1.** Left to right: reference sample ( $D_2O$ ), cubic Ia3d after 4 weeks of aging (0.02 M), cubic Ia3d (0.02 M) after 1 hour of irradiation, cubic Pn3m (0.02 M) after 1 hour of irradiation.

It has been previously shown that inverse cubic Ia3d and Pn3m phases can contain up to 7 and 4 wt. % of DTADNA, respectively [115]. An analysis of the X-ray data indicates that incorporation of 1 wt.% of the DTADNA and silver nitrate does not have a substantial effect on the cubic structure and the liquid crystalline structure is maintained (figure 4.2). Some of the samples were slightly birefringent due to the presence of a second, most likely inverse hexagonal phase. It has been reported that a stacking of the short-stranded DNA may induce

the cubic Ia3d to inverse hexagonal phase transition [116]. However, due to the relatively small content, the second phase was not detected by  $^2\text{H}$  NMR (data not shown) and SAXS measurements.

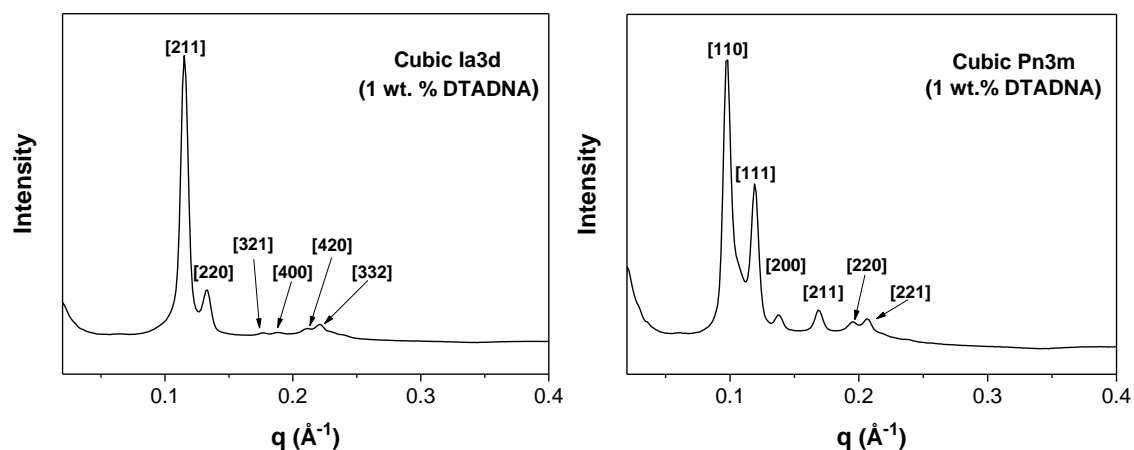


**Figure 4.2.** Small angle X-ray pattern of the cubic Ia3d (A) and Pn3m (B) samples containing 1 wt.% of DTADNA and 0.02 M  $\text{AgNO}_3$  solution.

Further structural information of different samples was extracted from the SAXS data and results are summarized in table 4.1.

**Table 4.1.** Composition of samples, lattice parameter ( $a$ ) and radius of the aqueous channel ( $r_w$ ) 3 days after preparation (0.02 M  $\text{AgNO}_3$ ) in comparison with reference samples ( $\text{D}_2\text{O}$ ).

Composition DTADNA/GMO/ $\text{D}_2\text{O}$ , wt.%	Phase	$a$ (Å)		$r_w$ (Å)	
		$\text{D}_2\text{O}$	0.02 M $\text{Ag}^+$	$\text{D}_2\text{O}$	0.02 M $\text{Ag}^+$
1/69.5/29.5	Cubic Ia3d	133.9	133.8	16.3	16.3
1/62.5/36.5	Cubic Pn3m	93.6	91.3	19.4	18.5

### 4.3 Kinetics of nanoparticle formation in the DNA-containing cubic phase.

After preparation, samples have been equilibrated for 3 days. The photochemical synthesis of silver nanoparticles was monitored by UV-Vis spectroscopy in situ in quartz glass cuvettes with a path length of 1 mm. Sample without silver added was used as a reference. Figure 4.4 displays the UV-Vis measurements of cubic Ia3d and Pn3m phases repeatedly measured during 60 minutes of ultraviolet irradiation.

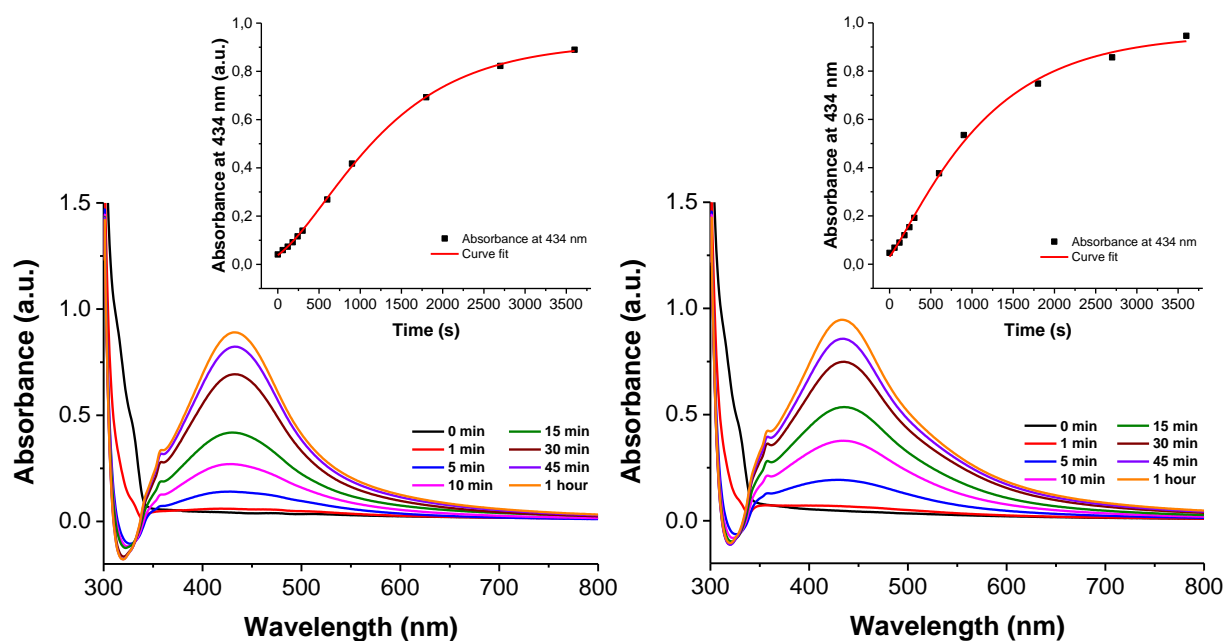


**Figure 4.4.** Absorption spectra at various irradiation times for DNA-containing cubic Ia3d phase (left) and cubic Pn3m phase (right) with 0.02 M AgNO<sub>3</sub> solution. Kinetics of silver nanoparticle formation, measured by the absorption intensity at 434 nm as a function of the irradiation time is shown in the insets.

The absorption spectra of silver nanoparticles synthesized in cubic Ia3d and Pn3m were almost equivalent indicating that the size and shape of the resulting AgNP are nearly independent of the liquid crystalline phase. Nanoparticles were not formed after the sample mixing was completed (spectra are not shown) and after 3 days of aging in the dark. After illumination to UV light for 1 minute, an absorption peak with low intensity can be detected at ca. 430–440 nm. As the reaction proceeded, a continuous increase of the intensity is observed, which is attributed to an increasing amount of silver nanoparticles. The position of the surface plasmon resonance shows a red shift at the beginning of the reaction until it reaches a constant position of 433 nm after 30 minutes. Further irradiation does not shift the plasmon absorption band only increasing the peak intensity. In comparison to the DNA-free binary system, additional surface plasmon resonance peaks from anisotropic particles were not present in the absorption spectra.

After 1 hour of irradiation, nanoparticles have been separated from the liquid crystalline phase and analyzed with TEM. The morphology and size distribution of the obtained particles are shown in figure 4.5.

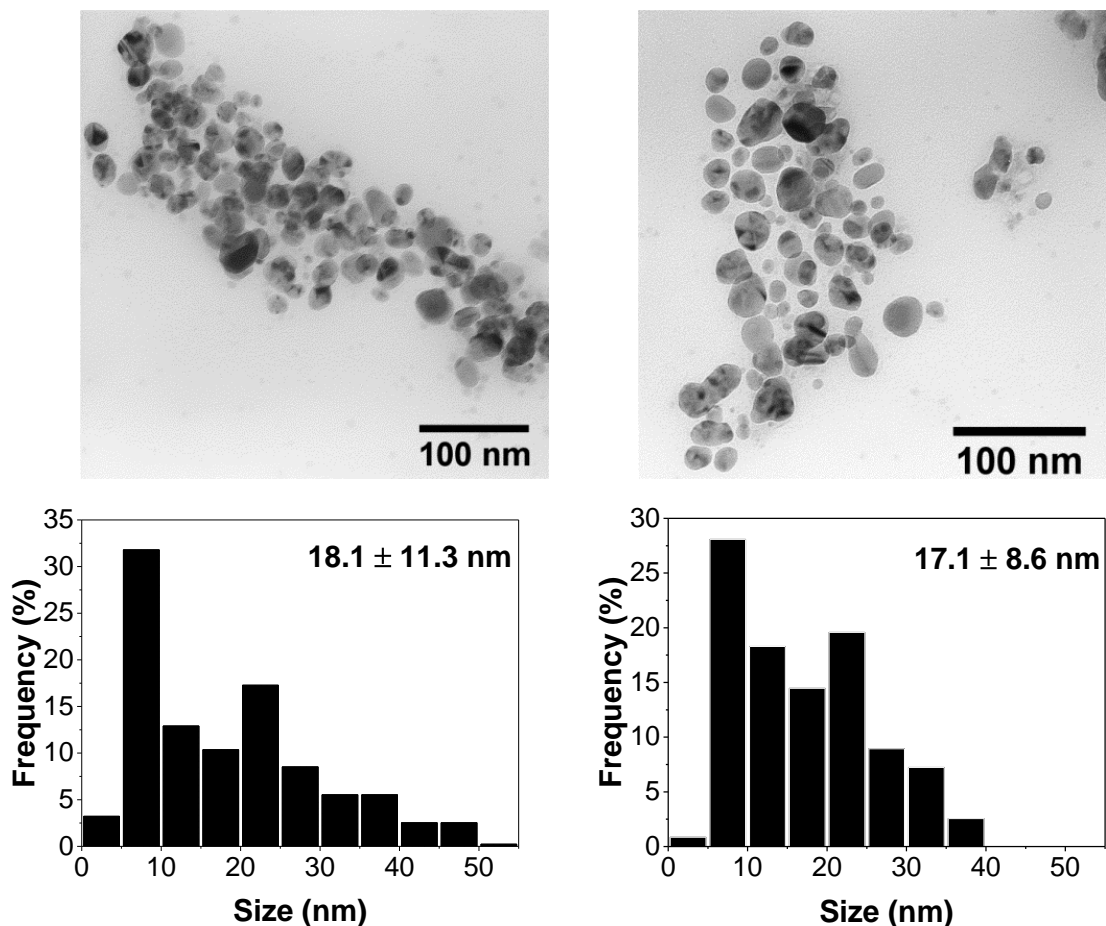


**Figure 4.5.** TEM pictures and size distribution histogram of nanoparticles synthesized in DNA-containing cubic Ia3d (left) and Pn3m (right) after 1 hour of UV irradiation.

An analysis of the TEM pictures shows results almost similar to the nanoparticles synthesized in DNA-free cubic Ia3d and Pn3m phases. Nanoparticles are single and polycrystalline with a size in the range of 3–50 nm. In comparison to the binary GMO/water system, no anisotropic particles and nanoplates have been found.

In order to verify, whether negative absorption in the region of lower wavelength and appearance of two additional peaks are not caused by the nanoparticle formation, a reference cubic Ia3d sample containing only D<sub>2</sub>O was illuminated with UV light. The absorption spectra depending on the exposure time are shown in figure 4.6. On irradiation with UV light, the absorption in the region of 300–350 nm decreases and two peaks with low intensity at 340 and 357 nm developed with irradiation time. The significant absorption reduction occurs within the first five minutes of irradiation with UV light. It could not result from the denaturation and photodegradation of DNA because the DNA absorption peak is located at 240–320 nm with  $\lambda_{\text{max}}$  at 260 nm. Due to the high DNA concentration in the liquid crystalline phase (10 mg/ml) and instrumental limitation, the DNA absorption peak cannot be measured in situ. The influence

of the UV irradiation and DNA-silver complexation followed by nanoparticle formation on the DNA will be demonstrated in chapter 6.2.

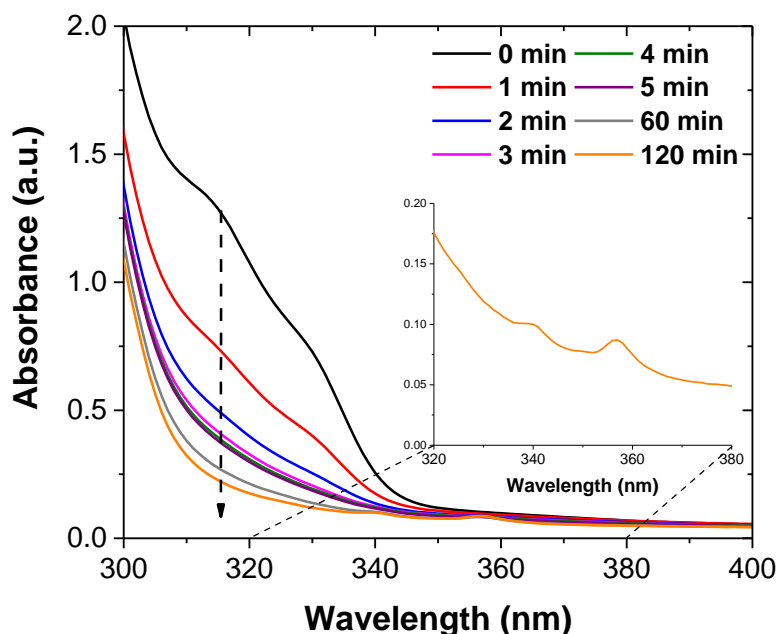


**Figure 4.6.** UV-Vis absorption spectra of the DNA-containing cubic Ia3d phase without silver added, depending on irradiation time. Inset shows the appearance of two peaks after 120 minutes of irradiation.

As a possible explanation, the above-mentioned spectral changes can be related to the chemical transformation of the monoolein. It was reported that exposure of lipids and unsaturated fatty acids to UVA light (366 nm) leads to oxidation of fatty acid producing three different reaction products of photooxidation: conjugated dienes, hydroperoxides, and malondialdehyde [117]. However, if light-induced photodegradation takes place, it does not alter cubic liquid crystalline phases. It should also be emphasized, that irradiation of the cubic Ia3d sample without DTADNA complex resulted in similar spectral changes. For a better understanding of the process occurring with monoolein upon illumination, additional measurements are required.

#### **4.4 Effect of $\text{Ag}^+$ concentration and UV irradiation time on nanoparticle formation**

In the present experiments, we have varied the concentration of the  $\text{AgNO}_3$  solution in the range of 0.01–0.04 M and extended the UV irradiation time up to 2 hours. Apart from these, a control

experiment was performed to study the impact of the radiation source on the DNA-containing cubic Ia3d phase loaded with 0.02 M AgNO<sub>3</sub> solution. The effect of Ag<sup>+</sup> concentration on the formation of silver nanoparticles in the cubic Ia3d phase has been investigated by UV-Vis spectroscopy in the region of 300–850 nm in 1 mm quartz glass cuvettes. Figure 4.7 shows absorption spectra for cubic Ia3d samples loaded with 0.01 M and 0.02 M AgNO<sub>3</sub> solutions after various irradiation times.

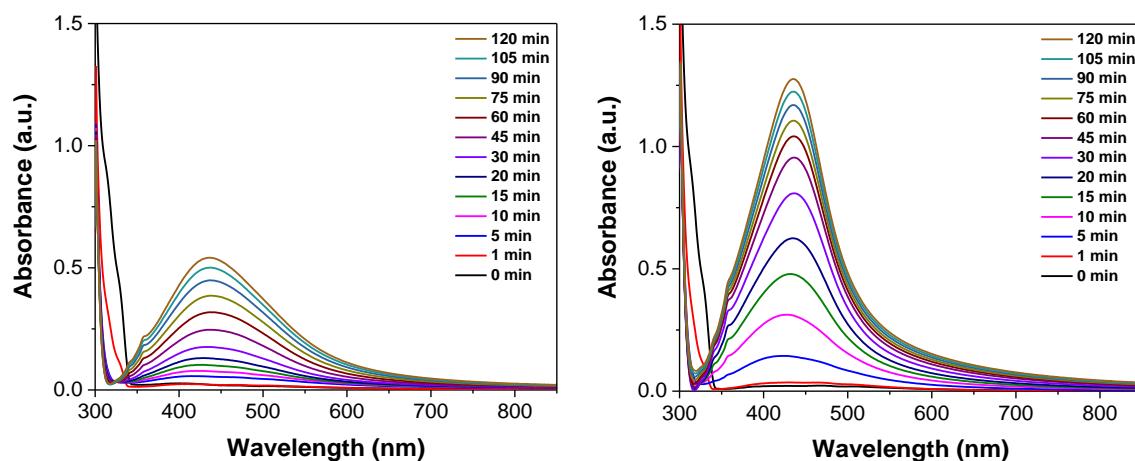


**Figure 4.7.** Absorption spectra at various irradiation times for the DNA-containing cubic Ia3d phase 1/69.5/29.5 containing (left) 0.01 M ( $[\text{Ag}^+]/[\text{DNA}_{\text{base}}] = 0.14$ ) and (right) 0.02 M ( $[\text{Ag}^+]/[\text{DNA}_{\text{base}}] = 0.28$ ) silver nitrate solution.

For this set of measurements, the cubic Ia3d phase with D<sub>2</sub>O irradiated with UV light for an appropriate time was used as a reference sample. Therefore the absorption in the region of 315–350 nm remained positive but decreased compared to the sample without exposure to UV light. As can be seen, the surface plasmon resonance band of silver nanoparticles starts to appear within the first minutes of illumination. The intensity of the SPR absorption band increases with the amount of added Ag<sup>+</sup>. After 2 hours of photolysis, the intensity for the sample with 0.02 M AgNO<sub>3</sub> solution at  $\lambda_{\text{max}}$  is approximately 2.3 times larger than for 0.01 M, indicating that more particles are formed. Peaks at 340 and 357 nm are similar to the ones shown in figure 4.5 and can result due to the incomplete subtraction of the reference spectrum as a result of small concentration variation.

If the Ag<sup>+</sup> concentration is further increased some deviations are observed in the spectra. Figure 4.8 demonstrates the evolution of the UV-Vis spectra of cubic Ia3d phase (0.04 M AgNO<sub>3</sub> solution) as a dependence on UV illumination time. Sample with 0.04 M AgNO<sub>3</sub> has a relatively high absorbance after equilibration for 1 day, suggesting that nanoparticles were already formed before irradiation. The peak shape is similar to the binary GMO/0.01 M AgNO<sub>3</sub> cubic Ia3d

sample, shown in chapter 3.4. The reason for this might be that the Ag-DNA complexation was not complete and some of the silver ions remained in the aqueous solution and were reduced by the surfactant. After exposure to UV light for 5 minutes, the absorption peak of silver nanoparticles become broader and more intense. The subsequent irradiation leads to the increase of the surface resonance band indicating an increase of the particle concentration. The shoulder appearing at ca. 750 nm (seen also in the DNA-free system) could be due to the formation of the anisotropic flat nanoparticles. During 120 minutes of irradiation, the position of the first absorption band shifts from 431 nm to 445 nm. By analogy to the two-component system, it can be attributed to the surface plasmon resonance of spherical nanoparticles and in-plane quadrupolar plasmon resonance from plate-like particles. A second peak at ca. 750 nm is assigned to the in-plane dipole resonance of flat anisotropic nanoparticles. Compared to the DNA-free cubic Ia3d phase, the peak position is shifted towards longer wavelength. An alternative explanation is a coupling of surface plasmons from nanoparticles which are close in vicinity. The second peak is also shifted towards to higher wavelength with an increase of the UV exposure time. This could indicate a growth of nanoplates in longitudinal dimensions or a decrease of the interparticle spacing of particle aggregates.

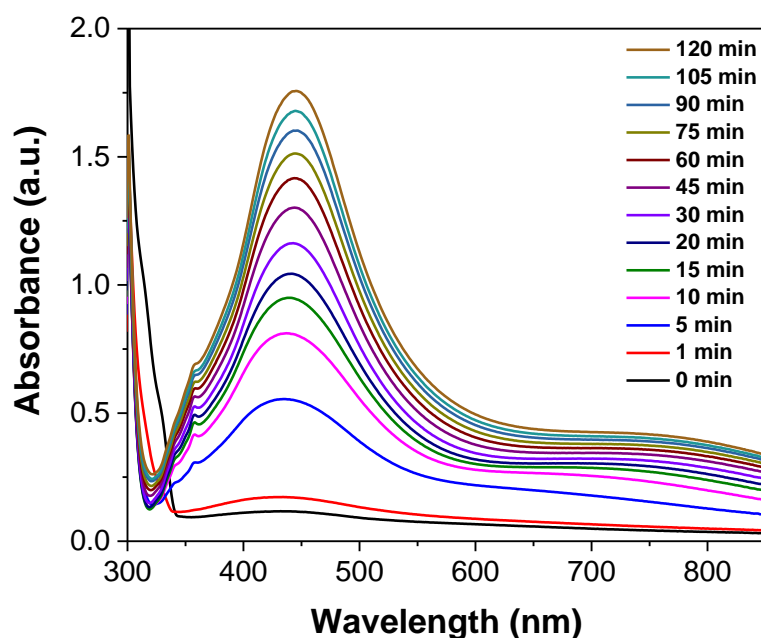


**Figure 4.8.** Absorption spectra at various irradiation times for the DNA-containing cubic Ia3d phase containing 0.04 M silver nitrate solution ( $[Ag^+]/[DNA_{base}] = 0.56$ ).

It seems that the final shape of the synthesized nanoparticles depends on the initial presence of anisotropic particles. The process occurring in the cubic Ia3d phase (0.04 M) can be explained

via a two-step reduction process. At the first stage, due to the spontaneous reduction of silver by GMO a small number of nanoparticles with variable geometries are formed. During the second (photoreduction) step silver ions are reduced in DNA as well as on the surface of the primary particles, resulting in the growth of the anisotropic nanoparticles and a red shift of the long-wavelength dipole plasmon resonance.

Figure 4.9 shows the kinetics of nanoparticle formation depending on the initial  $\text{Ag}^+$  concentration. The growth of the optical absorbance from the nanoparticles initially displays a sigmoidal behavior as shown in figure 4.9, suggesting autocatalytic surface-growth mechanism [118]. A short induction period was observed at the very early stage of the reduction-nucleation process for samples containing 0.01 M and 0.02 M  $\text{AgNO}_3$ . When small silver particles are formed, they act as nucleation centers for the remaining  $\text{Ag}^+$  ions. As it was mentioned above, for a cubic Ia3d sample with 0.04 M absorption at  $t_{\text{UV}}=0$  was larger due to the presence of spontaneously formed nanoparticles. After two hours of irradiation absorbance almost levels off, indicating a decrease of growth rate. However, after two hours the reaction was not completed. The reaction was strongly influenced by the initial silver nitrate concentration. Higher  $\text{AgNO}_3$  concentration resulted in faster formation of silver nanoparticles.

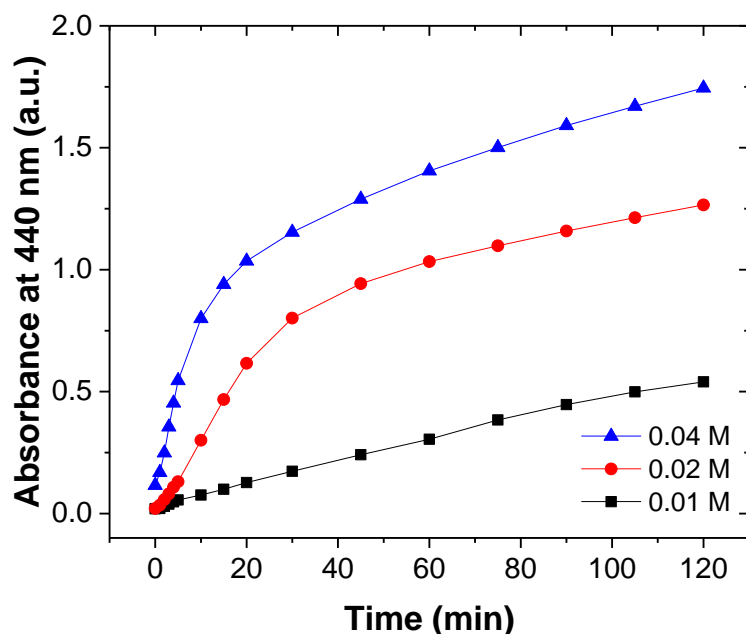


**Figure 4.9.** Kinetics of nanoparticle formation measured as absorbance at 440 nm plotted against irradiation time.

The emission spectrum of the UV lamp used for the photochemical synthesis of nanoparticles is shown in figure A.1. According to the literature, only UVC light (254 nm) promotes the

photoinduced synthesis of silver nanoparticles in DNA [69]. To study the influence of the UV light on the formation of nanoparticles and GMO photodegradation, two cubic Ia3d samples (0.02 M) were illuminated with a low-power UV lamp generating UV light with a wavelength of 254 and 366 nm. As it was found, both UVA and UVC light induce the formation of silver nanoparticles in the monoolein-based cubic Ia3d phase in the presence of DTADNA (figures A.15, A.16). However, in both cases, a decrease of absorption in the region of 300–350 nm and appearance of two peaks at 340 and 347 were observed. After irradiation was completed, lyophilized samples have been analyzed by  $^1\text{H}$  and  $^{13}\text{C}$  NMR. However, the results of NMR measurements were inconclusive, and additional experiments are required to understand the reactions occurring with the surfactant upon irradiation with UV light.

#### **4.5 Spontaneous formation of silver nanoparticles. Effect of aging**

As it was demonstrated above, two processes can be involved in the nanoparticle formation. Here, the formation of silver nanoparticles by the reduction of silver ions by monoolein as reducing agent is investigated. The spontaneous formation of silver nanoparticles in the DNA-containing cubic Ia3d phase with 0.02 M silver nitrate solution was studied by time-dependent UV-Vis spectroscopy over a period of 9 weeks after preparation. During this time, samples were stored in the dark and have not been exposed to UV light. Results are displayed in figure 4.10. The freshly prepared sample shows no plasmon absorption band, suggesting that nanoparticles did not form during the sample preparation. This fact confirms that Ag-DNA complexation was completed and silver ions were successfully embedded into the DNA double helix. After 7 days, a weak surface plasmon resonance peak can be detected at ca. 414 nm. With further increase of the aging time, the SPR position continuously shifts towards longer wavelength and intensity slowly increases, indicating an increase of both number and size of the particles. After 5 weeks, the absorption peak starts to split into a low wavelength shoulder and a long wavelength peak accompanied by an increase of intensity in the near infrared region. In addition, the spontaneous process was investigated for the sample containing 0.04 M  $\text{AgNO}_3$  (figure A.17).

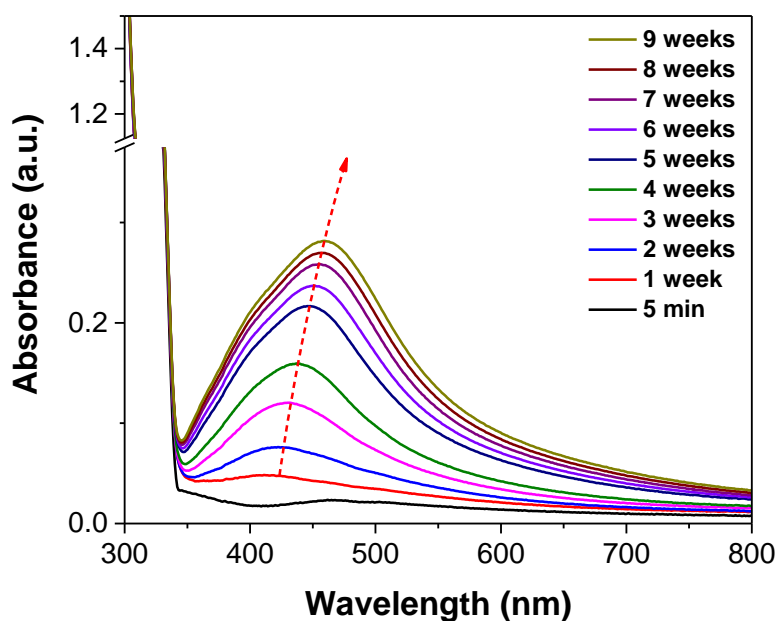


**Figure. 4.10.** Time evolution of UV-Vis spectra showing the spontaneous formation of silver nanoparticles in the DNA-containing cubic Ia3d phase (0.02 M AgNO<sub>3</sub>).

In comparison to the photoinduced synthesis, spontaneous formation of silver nanoparticles does not cause a decrease of absorption in the region of 330–360 nm. Due to this fact as well as the absence of the peaks at 340 and 357 nm, the data also suggest that during the synthesis no lipid photodegradation occurred and particles are formed only due to the Ag<sup>+</sup> reduction by GMO accompanied by oxidation of alcohol groups of monoolein.

The maximum absorbance plotted versus time follows a sigmoidal curve, as shown in figure 4.11. It is accompanied by a slow induction period (up to 2 weeks), suggesting that formation and development of silver nanoparticles occurs via an autocatalytic surface-growth mechanism in which Ag ions are adsorbed on the surface of small Ag nanoparticles and reduced [119]. The position of  $\lambda_{\text{max}}$  changes significantly over a period of 9 weeks, from 410 to almost 460 nm. Such a large shift may indicate an increase of particle size due to Oswald ripening [120] or particle aggregation.

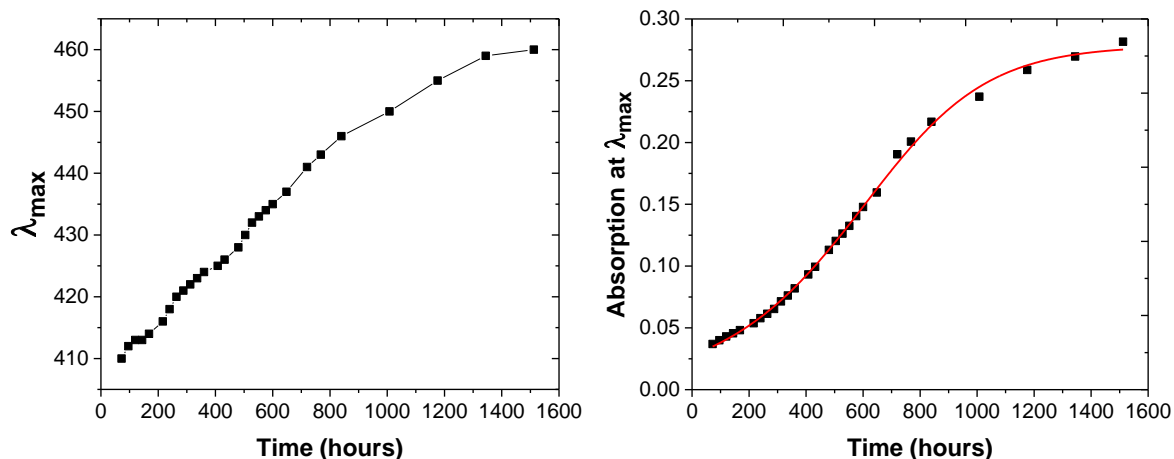


**Figure 4.11.** Change of the  $\lambda_{\max}$  position (left) and absorption maximum (right) for the DNA-containing cubic Ia3d phase during the spontaneous formation of silver nanoparticles.

After 1 month of synthesis, nanoparticles have been collected and analyzed by transmission electron microscopy. Figure 4.12 shows a TEM micrograph of the nanoparticles after 4 weeks of aging. The resulting particles prepared in the cubic Ia3d sample aged for 4 weeks are similar to the particles obtained by photoinduced formation after 1 hour of UV illumination. The size of the obtained mono- and polycrystalline particles varies widely in a range of 3–55 nm with an average of 15.2 nm.

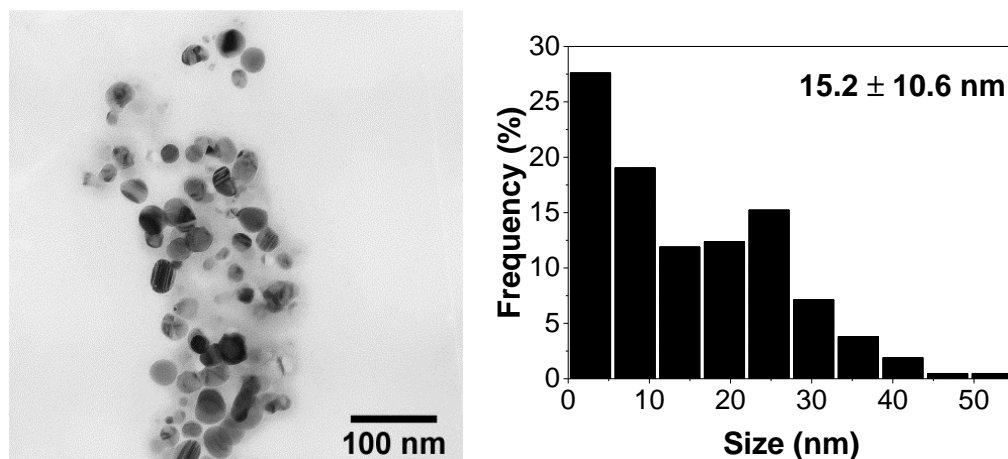


**Figure 4.12.** TEM micrograph and corresponding size distribution histogram of nanoparticles formed in the cubic Ia3d phase (0.02 M  $\text{AgNO}_3$ ) after 4 weeks of aging.

Comparison of the ternary system with DTADNA-free samples (chapter 3) reveals several important differences. At first, in the case of DNA-containing lyotropic liquid crystals, spontaneous formation of particles is much slower. This is evidence of the complexation

between silver and DNA. Due to the embedding of  $\text{Ag}^+$  ions into the DNA double helix, monoolein molecules are no longer able to interact directly with silver ions, and the reduction process is slower compared to the binary GMO/water system. Second, in the sample with 0.02 M  $\text{AgNO}_3$  aged for 1 month, anisotropic particles were not formed during the spontaneous process. It is worth to mention that for nanoparticles obtained by chemical reduction no sedimentation of nanoparticles or decrease of intensity of the SPR band was observed during 4 months of aging. On the contrary, the reduction of  $\text{Ag}^+$  by monoolein continued for a period of 4 months.

## 4.6 Summary

In the current chapter, the synthesis of silver nanoparticles in DNA-containing cubic liquid crystalline phases formed by monoolein is reported.

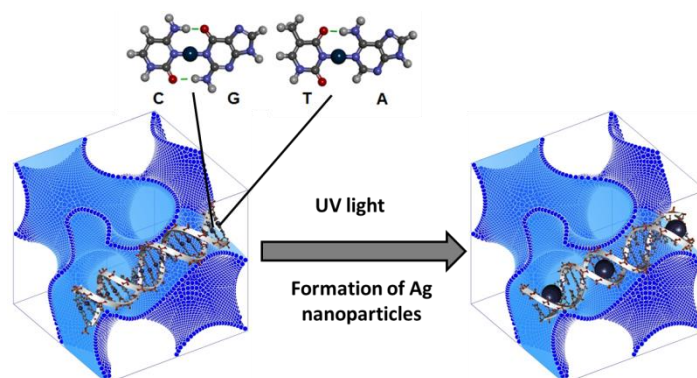


**Figure 4.13.** Schematic representation of the photoinduced formation of silver nanoparticles in the DNA-containing cubic Ia3d phase.

Two different preparative strategies have been used. Firstly, nanoparticles were obtained by exposure of the Ag-DNA complex to UV light. Secondly, similar to the DNA-free binary system, nanoparticles can be synthesized by using monoolein as a reducing agent. Due to the embedding of  $\text{Ag}^+$  inside the double-stranded DNA, the formation process is much slower, compared to the DNA-free binary system. For a low and medium silver precursor concentration, the spontaneous reduction was not noticeable during the typical time required for the sample preparation. However, an increase of the  $\text{AgNO}_3$  concentration resulted in a faster spontaneous reduction process accompanied by the formation of anisotropic particles.

From the results of the optical microscopy, small angle X-ray scattering and  $^2\text{H}$  NMR experiments, it was confirmed that the reaction medium for the particle synthesis was not influenced by the UV illumination with later formation of silver particles and maintained the initial liquid crystalline mesophase structure.

The effects of the reactant concentrations on the formation of the nanoparticles were discussed. The influence of the irradiation time on the liquid crystalline phase which possibly causes the photodegradation of monoolein should be studied in greater detail. Due to the high viscosity of the cubic phase and nanoparticle formation within DNA duplexes, the resulting particles were stable for a period of at least 3 months. During this time, no significant changes in absorption spectra or particle sedimentation have been observed.

## **5 Chemical and photochemical synthesis of silver nanoparticles in the DTADNA/lecithin/water ternary system**

### **5.1 Introduction**

In this chapter, the synthesis of silver nanoparticles in DNA-containing liquid crystals formed by aqueous lecithin dispersions is presented. One of the most abundant components present in lecithin is the zwitterionic surfactant phosphatidylcholine (PC). Phosphatidylcholine, or 1,2-diacyl-sn-glycero-3-phosphocholine (cf. figure 2.2), consists of an anionic phosphate group attached to the sn-3 position of esterified glycerol and connected to a cationic choline group, forming a neutral net charge in a wide pH range. It is the major lipid component of animal tissue and nonchloroplast plant membranes and rarely found in bacteria [121]. Phosphatidylcholine is classified as GRAS (generally recognized as safe), included in the Inactive Ingredient Guide of the U.S. Food and Drug Administration [122] and approved by the European Food Safety Authority as a food additive (E322) [123]. Due to the biocompatibility and biodegradability of phospholipids, they have been proposed as drug delivery systems [124]. Natural and synthetic cationic lipid-DNA complexes (lipoplexes) are currently the most widely used DNA transfection agents [125].

The formation of gold and silver nanoparticles in phospholipid mixtures without additional reducing agents has been reported by several research groups. D. Sharma successfully synthesized silver and gold nanoparticles in lecithin vesicles without additional reducing agents [126]. According to Meyre, the quaternary ammonium group plays an important part in the reduction process [101]. Also, the role of impurities in the reduction process was ruled out by synthesis of AgNP in pure synthetic dimeristoylphosphatidylcholine [126]. However, the detailed mechanism of metal reduction is still unknown.

Several attempts have been made to use lecithin for the shape-controlled synthesis of noble metallic nanoparticles. S. Reed et. al showed that variation of seed-mediated growth by addition of a minor component of lecithin leads to the growth of triangular prismatic nanoparticles [127]. Xiao Chen and coworkers prepared anisotropic gold nanoplates using a lamellar phase formed by lecithin and nonionic surfactants [128]. However, in both studies, an external reducing agent like sodium borohydride or nonionic surfactant was used to synthesize the nanoparticles, whereas lecithin acted as stabilizing agent. Lipoplexes also have been used for the synthesis of inorganic nanomaterials. Wong and coworkers synthesized CdS nanorods in the lamellar phase

formed by hydrated cationic phospholipid-DNA complexes. Cd ions were confined and complexed by the DNA and nanorods were formed by the reaction of Cd<sup>2+</sup> with H<sub>2</sub>S [129].

The ternary DTADNA/lecithin/water system at 25°C has been investigated by Bilalov et al. [130]. Figure 5.1 represents the phase diagram along with a schematic representation of the lamellar and inverse hexagonal liquid crystalline phases. Three regions with a single liquid crystalline phase have been found in the phase diagram. The lamellar phase of lecithin can take up water and swell to ca. 45 wt.% water. In the presence of DTADNA, the lamellar phase consists of phospholipid bilayers with DNA strands intercalated between the lecithin lamellae. The dimension of the water layer is typically above 25 Å, the thickness required to incorporate the hydrated monolayer of DNA in B-form. The addition of highly concentrated DTADNA and reduction of the water content induces a topological transition of the lamellar phase due to the change of spontaneous curvature to inverse hexagonal and normal cubic phases. In the H<sub>II</sub> phase hydrated DNA is incorporated into the aqueous cores of inverse cylindrical lecithin micelles which are arranged in a hexagonal lattice. The region of the cubic liquid crystalline phase is narrow and exists at ca. 40–70 wt.% of the DTADNA complex around a straight line characterized by a 7:1 DTA:lecithin molar ratio. The cubic phase has a normal bicontinuous type structure, and the arrangement of the phospholipid bilayers in the cubic cell corresponds to the gyroid infinite periodic minimal surface, having Ia3d space group. The water film containing DNA and surfactant headgroups drapes the resulting minimal surface.

For the synthesis of silver nanoparticles, samples from the L<sub>α</sub> and H<sub>II</sub> regions of the phase diagram have been prepared. Due to the long time required for the preparation and equilibration of cubic Ia3d samples, they have not been used. The composition of the prepared samples is shown in table 5.1.

**Table 5.1.** Composition and phase behavior of prepared samples of the ternary system DTADNA/lecithin/water (according to the phase diagram [130]).

Sample	DTADNA, wt. %	Lecithin, wt. %	Water, wt. %	Phase	[Ag <sup>+</sup> ]/[DNA <sub>base</sub> ] (0.1 M AgNO <sub>3</sub> )
C1 0/60/40	0	60	40	L <sub>α</sub>	0
C1 2/59/39	2	59	39	L <sub>α</sub>	0.98
C1 9/55/36	9	55	36	L <sub>α</sub>	0.2
C1 15/68/17	15	68	17	H <sub>II</sub>	0.057
C1 16/63/21	16	63	21	H <sub>II</sub>	0.066

The first number in the sample notation indicates the concentration of silver nitrate solution (e.g. C1 corresponds to 0.1 M AgNO<sub>3</sub>; C01 – 0.01 M, C0 – D<sub>2</sub>O only) and the following three

numbers are related to the sample composition (DTADNA/lecithin/D<sub>2</sub>O or silver nitrate solution in D<sub>2</sub>O, given as wt.%).

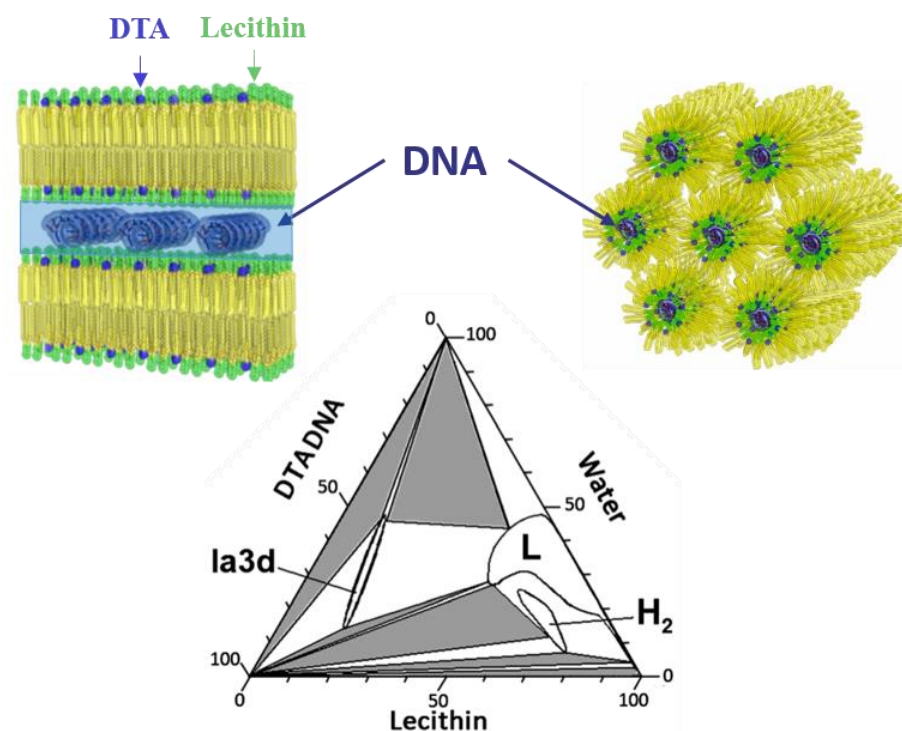


**Figure 5.1.** DTADNA/lecithin/water ternary phase diagram at 25°C and schematic representation of the lamellar and inverse hexagonal liquid crystalline mesophases, redrawn from [130]. Non-labeled white and grey areas represent two- and three-phase regions, respectively.

## 5.2 Spontaneous formation of silver nanoparticles in the DNA-free lecithin/water binary lamellar phase. Effect of Ag<sup>+</sup> concentration and aging time

As mentioned earlier, lamellar liquid crystalline phases formed by lecithin have been previously used as templates for the synthesis of noble metallic nanoparticles. In order to study the spontaneous formation of nanoparticles in the DNA-free binary system, samples containing 60 wt.% lecithin/40 wt.% D<sub>2</sub>O (or various concentration of AgNO<sub>3</sub> in D<sub>2</sub>O) have been used. After 1 week of preparation, samples have been characterized by small angle X-ray scattering, <sup>2</sup>H and <sup>31</sup>P NMR spectroscopy and polarizing optical microscopy techniques (figure 5.2).

The SAXS pattern shows Bragg peaks with a ratio of 1:2:3:4, a characteristic property of the layered structure of the lamellar phase with an interlayer distance of 52.4 Å. The  $^2\text{H}$  NMR spectrum, shown in figure 5.2 represents a superposition of two signals. A broad central peak is attributed to multilamellar vesicles, a shear-induced defect structure of the lamellar phase, whereas the Pake powder pattern originates from the planar lamellar structure [131]. The  $^{31}\text{P}$  spectrum shown in figure 5.2 confirms that a single phase is present. The vesicles leave no signature in the  $^{31}\text{P}$  spectrum because lecithin diffusion is much slower than water diffusion and because the  $^{31}\text{P}$  spectrum has a larger width than the  $^2\text{H}$  NMR spectrum and therefore is not sensitive to slow rotational diffusion. The data shown in figure 5.2 indicate that the liquid crystalline phase is maintained upon addition of 0.01 M silver nitrate solution. However, for the samples containing 0.05 M and 0.1 M  $\text{AgNO}_3$ , formation of the silver nanoparticles has a destabilizing effect on the lamellar liquid crystalline phase, as will be demonstrated later.

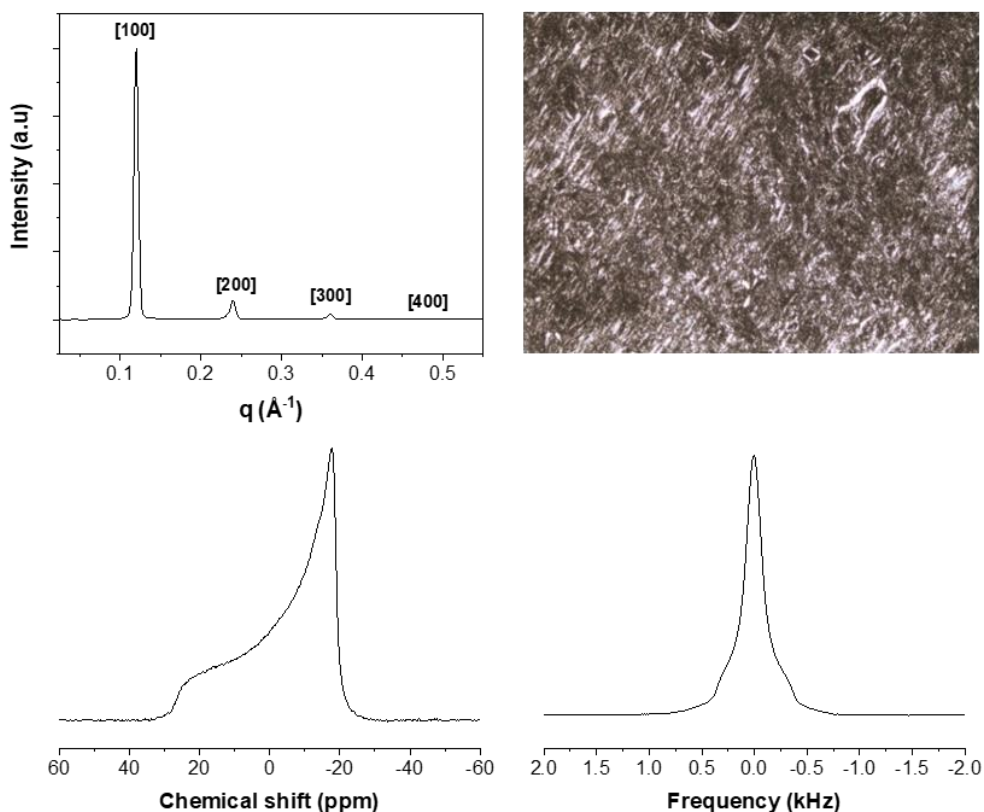


**Figure 5.2.** Top: SAXS pattern (left), polarizing optical microscopy (right); bottom:  $^{31}\text{P}$  NMR (left) and  $^2\text{H}$  NMR spectra (right) of the C01 0/60/40 after 1 week of preparation (22 °C).

In the absence of  $\text{AgNO}_3$  solution, samples of the lamellar phase are yellow, due to the presence of natural carotenoids in lecithin. Upon addition of silver nitrate solution, the color of the samples gradually changes to light brown and after several days to dark brown or green, depending on the amount of added silver salt. These color changes indicate the formation of Ag nanoparticles.



**Figure 5.3.** Samples of the lamellar phase (60/40 lecithin:water, wt.%) with various silver concentrations, 6 hours after mixing the samples.

The process of nanoparticle formation has been studied by UV-Vis spectroscopy and transmission electron microscopy. Samples have been diluted tenfold with absolute ethanol and sonicated for 1 minute to destroy possible agglomerated particles. A sample without silver added was used as a reference. Figure 5.4 shows the absorption spectra of binary lamellar samples with different  $\text{Ag}^+$  concentrations after 1 day, 3 days and 1 week.

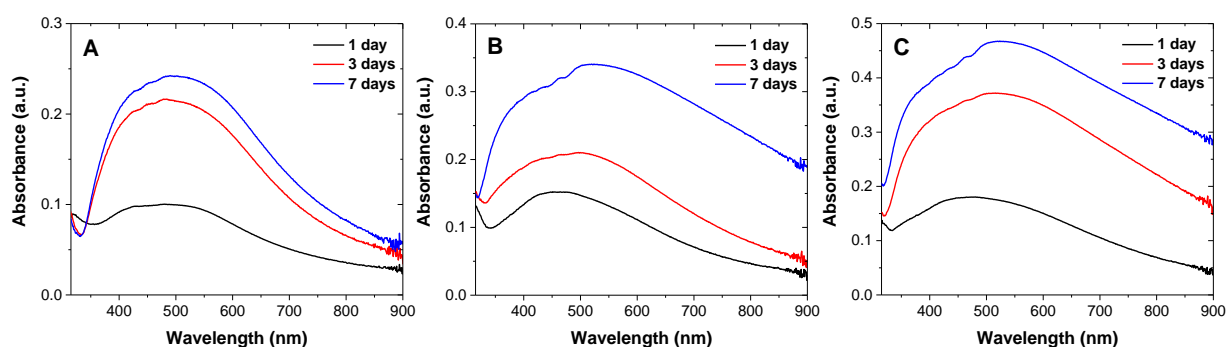


**Figure 5.4.** UV-Vis spectra of nanoparticles formed in lecithin/water lamellar samples with: A) 0.01 M, B) 0.05 M, C) 0.1 M silver nitrate solution. Reference spectra are subtracted.

At the beginning of the reaction, the results are almost identical and independent of the  $\text{Ag}^+$  concentration. A broad absorption band with a maximum at ca. 450–460 nm indicates the formation of nanoparticles due to the reaction of  $\text{Ag}^+$  with lecithin. As the  $\text{Ag}^+$  concentration is increased, the SPR band shows higher intensity, which is attributed to the larger amount of particles. The absorption peak became broader and its maximum shifts towards longer wavelength with an increase of the aging time. This change can be associated with particle aggregation. Due to the high silver content in the samples C05 and C1 0/60/40, most of the nanoparticles exist as aggregates. It should also be noted that for samples with 0.05 M and 0.1

M AgNO<sub>3</sub> aged for 1 week no plasmon resonance band was detected without sonication, indicating that nanoparticles were also agglomerated.

After 1 week of synthesis, nanoparticles have been characterized by transmission electron microscopy. One week was chosen because this time was typically required for the preparation and equilibration of the DNA-containing lamellar liquid crystalline samples. Figure 5.5 shows the results of the TEM measurements of samples loaded with 0.01 M solution. At low silver concentration, spherical nanoparticles with a size of 5–50 nm were obtained. An increase of the Ag<sup>+</sup> concentration resulted in the formation of densely packed randomly shaped aggregates with a size of 50–200 nm where primary particles are joined and partly coalesced. Figure 5.6 shows typical TEM images of the nanoparticles synthesized in a lamellar sample loaded with 0.1 M AgNO<sub>3</sub> after 1 week. The obtained TEM micrographs are in agreement with UV-Vis spectra depicting broad absorption peaks.

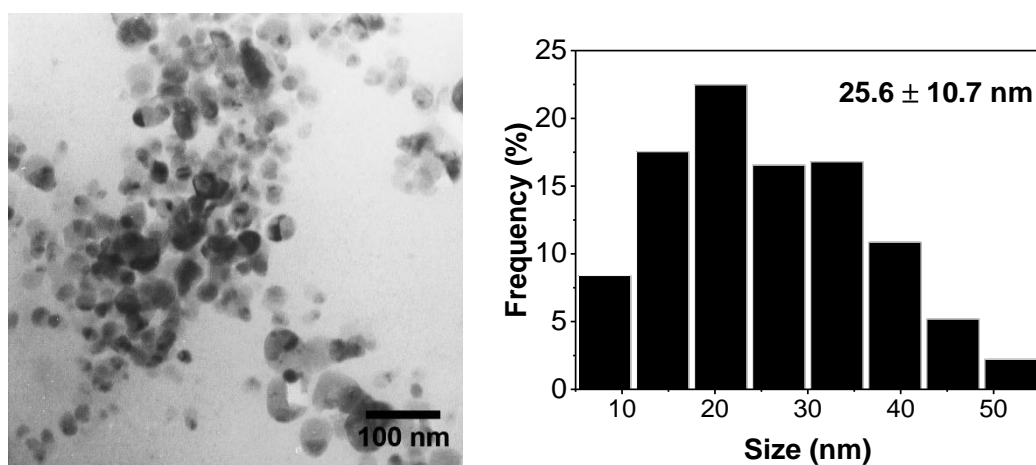


**Figure 5.5.** TEM picture and size distribution histogram of the nanoparticles formed in C01 0/60/40 aged for 1 week.

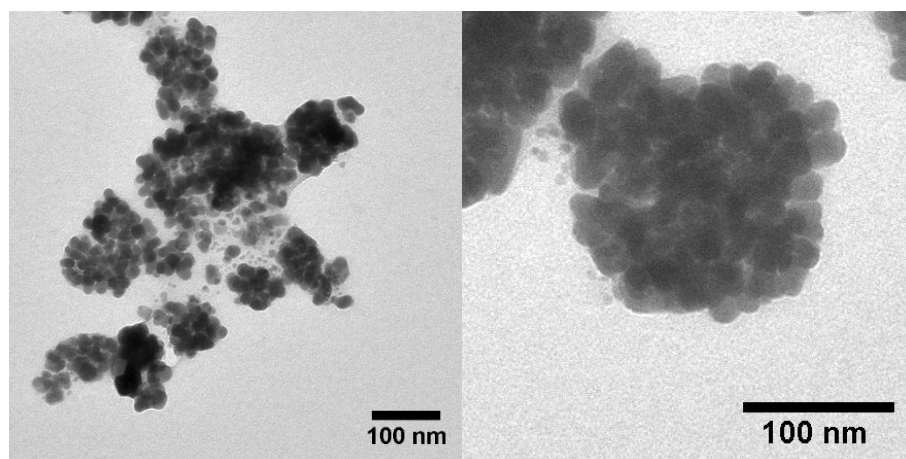


**Figure 5.6.** TEM images of nanoparticles synthesized in C1 0/60/40 aged for 1 week.

During the synthesis of the silver nanoparticles, the lamellar phase became less viscous. This was particularly noticeable for the samples with sufficiently high  $\text{Ag}^+$  concentration where phase separation was observed after 1 month. It has been previously shown that incorporation of silver nanoparticles into DPPC liposomes increase the membrane fluidity [132]. However, an effect of the formation and presence of AgNP on the long-term stability of lamellar phase had not been reported.

The stability of the two-component lamellar phase upon nanoparticle formation was monitored with  $^1\text{H}$ ,  $^{13}\text{C}$ , and  $^{31}\text{P}$  NMR spectroscopy techniques. A comparison of  $^{31}\text{P}$  solution NMR spectrum of lyophilized lecithin with and without the presence of silver nanoparticles is shown in figure 5.10.

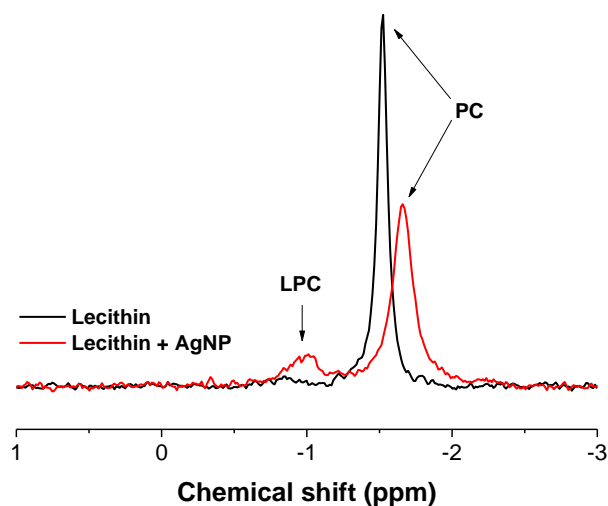


**Figure 5.10.**  $^{31}\text{P}$  NMR spectra of lyophilized C1 0/60/40 and C0 0/60/40 aged for 1 month.

For the sample containing silver nanoparticles, peaks are shifted 0.1 ppm upfield relative to the reference sample as a result of the adsorption of lecithin on the surface of silver nanoparticles. The peak at  $-1$  ppm is attributed to an increased amount of lysophosphatidylcholine (LPC) as product of the hydrolysis of phosphatidylcholine (Scheme 5.1). According to the supplier information, lecithin can contain ca. 3% of LPC. For the lamellar phase without silver added the amount of lysophosphatidylcholine was slightly increased to 4.2% (as calculated from the NMR spectrum). In comparison, for the sample loaded with 0.1 M  $\text{AgNO}_3$  the content of LPC was 19% indicating that a significant amount of lecithin was hydrolyzed.

Formation of lysophosphatidylcholine was also confirmed with  $^{13}\text{C}$  NMR. Figure 5.7 shows high-resolution solid-state  $^{13}\text{C}$  NMR spectra of the lamellar phase with and without silver added after 1 month of preparation.. The peak at 176.55 ppm seen in the enlarged group of peaks is

attributed to the C=O group of free carboxylic acid formed because of the hydrolysis of the lecithin. The intensity of the PC carbonyl group is decreased for C05 0/60/40, indicating the smaller content of phosphatidylcholine due to the hydrolysis of lecithin, compared to the reference sample (C0 0/60/40). Also, several peaks of low-intensity from the glycerol moiety of LPC were detected between 55 and 70 ppm.

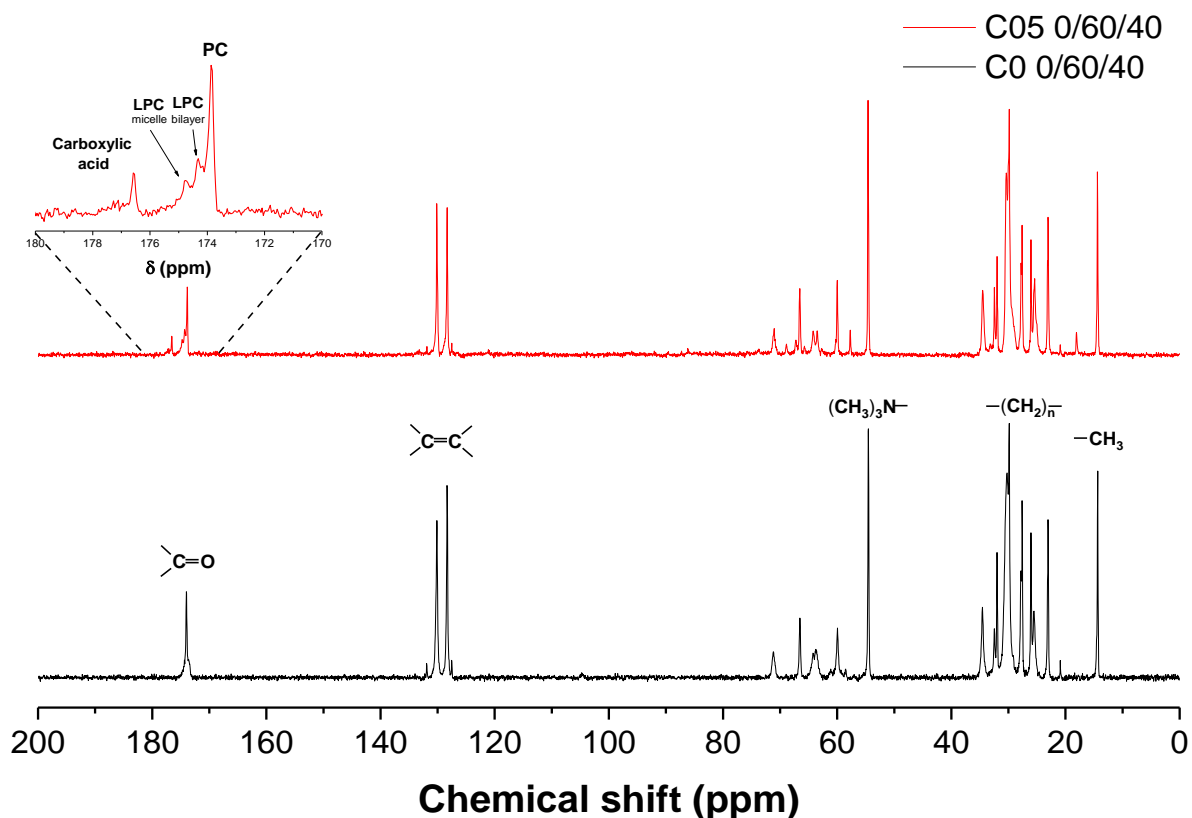
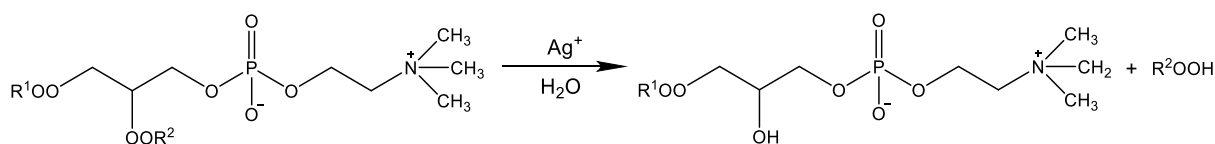


**Figure 5.7.** Comparison of  $^{13}\text{C}$  MAS NMR spectra of C0 0/60/40 ( $\text{D}_2\text{O}$ ) and C05 0/60/40 ( $0.05\text{M AgNO}_3$ ) aged for 3 months ( $\omega = 5 \text{ kHz}$ ,  $23 \text{ }^\circ\text{C}$ ).

The hydrolysis of phosphatidylcholine is shown in scheme 5.1. It should be noted that the hydrolysis of the lecithin occurred in the absence of nanoparticles. However, the hydrolysis of lecithin was considerably slower for the samples containing only  $\text{D}_2\text{O}$  (figure A.18). Hence, the presence of silver nitrate and formation of silver nanoparticles has a significant influence on the hydrolysis rate.

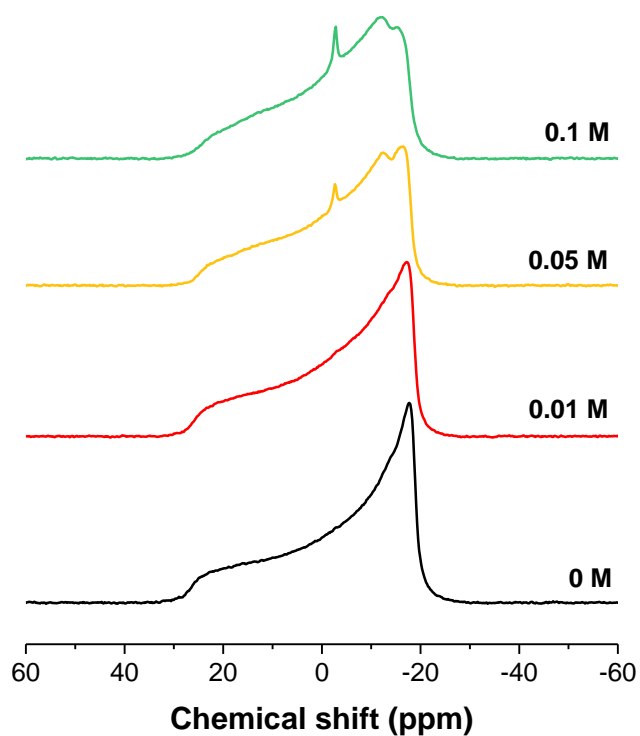


**Scheme 5.1.** Schematic representation of hydrolysis of phosphatidylcholine.

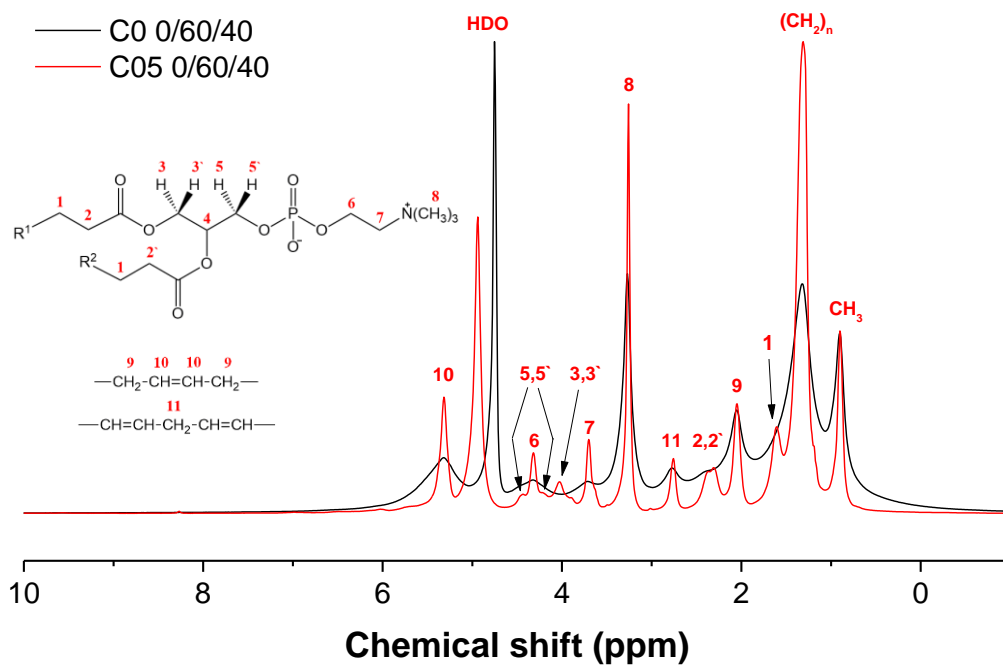
The destabilizing effect of the lysophosphatidylcholine on the PC bilayers is known [133]. Lacking one hydrocarbon chain in LPC decreases the critical packing parameter of the phospholipid and makes the molecular arrangement into micellar and hexagonal liquid crystalline phase more preferable (cf. figure 2.2).

Figure 5.9 shows static solid state  $^{31}\text{P}$  NMR spectra of C 0/60/40 with various silver concentrations after 1 month of aging. The  $^{31}\text{P}$  NMR powder pattern with the maximum at high-field peak and the shoulder at low-field is indicative for phosphatidylcholine organized in a lamellar liquid crystalline phase (cf. figure 2.11). As can be seen for the samples with high  $\text{Ag}^+$  concentrations (0.05 and 0.1 M) an appearance of additional peaks is noticeable. A narrow peak at  $-0.5$  ppm can be attributed to the presence of the isotropic micellar phase formed by lysophosphatidylcholine. A second axially symmetric powder pattern with reduced chemical shift anisotropy can be assigned to the LPC in the lamellar phase. The coexistence of LPC in the lamellar and micellar environment is also evident in the  $^{13}\text{C}$  spectrum (figure 5.7, inset). Peaks at 174.31 and 174.75 ppm are attributed to the carbonyl group of the lysophosphatidylcholine involved in bilayer and micellar organization, respectively. The signal from the lysophosphatidylcholine located in the bilayer is shifted 0.4 ppm upfield relative to the micellar LPC due to the less polar environment surrounding this group [133].

Figure 5.10 shows a comparison of the solid state  $^1\text{H}$  NMR spectra of the binary lamellar phase in the presence and absence of silver nanoparticles, aged for 3 months. Due to the presence of the micellar phase and free carboxylic acid, the C05 0/60/40 sample has a lower viscosity (and higher fluidity) than the reference sample, as well as a phase separation was observed. As a result, the  $^1\text{H}$  spectrum of the sample with silver salt exhibits sharper and more well-developed peaks. However, no signal from the free carboxylic acid could be observed in the  $^1\text{H}$  spectrum.



**Figure 5.9.**  $^{31}\text{P}$  NMR spectra of 60 wt.% lecithin/40 wt.%  $\text{AgNO}_3$  (various concentration) aged for 1 month ( $\omega = 0$  kHz,  $23^\circ\text{C}$ ).



**Figure 5.10.**  $^1\text{H}$  MAS NMR spectra of C0 0/60/40 and C05 0/60/40 after 3 months of preparation ( $\omega = 5$  kHz,  $23^\circ\text{C}$ ).

### 5.3 Photoinduced formation of silver nanoparticles in the DNA-containing lamellar phase

Analogously to the two-component lamellar phase, DNA-containing samples have been prepared with 0.01 M AgNO<sub>3</sub> solution. Upon exposure to UV light a color change indicative of nanoparticle formation was observed only in the sample with the lowest DTADNA content (C01 2/59/39). Therefore, for the nanoparticle synthesis samples were prepared in the presence of 0.1 M silver nitrate solution. For the C1 2/59/39 sample formation of a brown precipitate was observed. As it will be shown in chapter 6.2, an increase of  $[Ag^+]/[DNA_{base}] \geq 0.5$  resulted in the precipitation of the Ag-DNA complex and phase separation.

After preparation, the L<sub>α</sub> samples were exposed to UV light and the liquid crystalline phase was characterized by <sup>2</sup>H NMR, small angle X-ray scattering, and polarizing optical microscopy. The results are shown in figure 5.11.

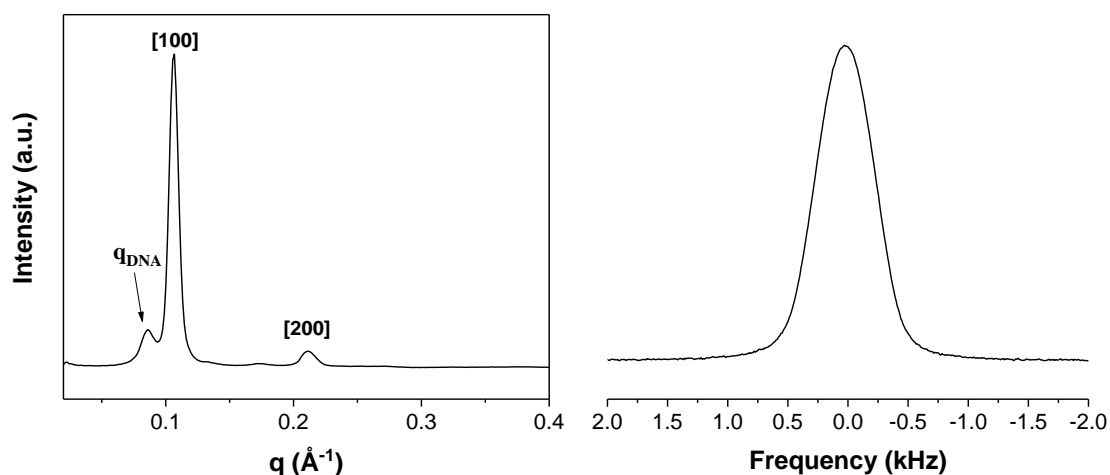


**Figure 5.11.** SAXS pattern (left) and <sup>2</sup>H NMR (left) spectrum of C1 9/55/36 at 22 °C.

Along with sharp lamellar reflections, an additional low-intensity peak is also present in the diffraction pattern. This peak corresponds to the in-plane positioning of DNA rods intercalated between lecithin bilayers [134]. Its position is dependent on the amount of DTADNA and shifts towards higher  $q$  values with an increase of DNA concentration. The DNA interhelical distance obtained from the SAXS data is 73 Å, indicating a relatively loose packing of the DNA molecules. The <sup>2</sup>H NMR spectrum of C1 9/55/36 shows a broad featureless peak attributed to multilamellar vesicular structures, rather than a planar lamellar phase [131].

Nanoparticles have been synthesized by irradiation of the liquid crystalline samples with UV light over a period of 15-120 minutes. Initially, upon irradiation with UV light the sample color changes from yellow to brown, indicating the formation of silver nanoparticles. As irradiation continues, the color of the sample continues to darken, as an indication of the appearance of more particles. The process of nanoparticle formation has been studied by UV-Vis spectroscopy and transmission electron microscopy. Figure 5.12 shows the absorption spectra of nanoparticles depending on the UV-Vis irradiation time. For UV measurements 75 mg of sample were dissolved in 0.925 ml absolute ethanol and measured in glass cuvettes with a path length of 1 cm. A sample without silver added was used as reference.

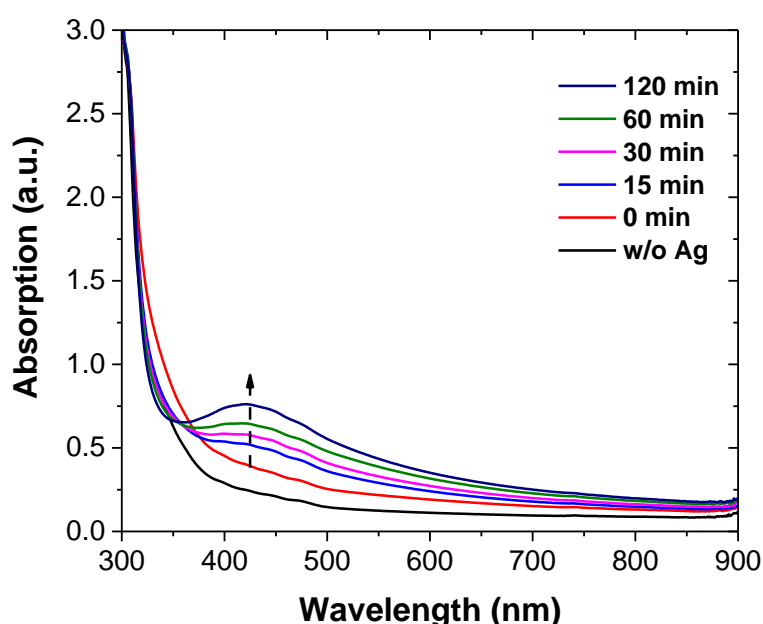


**Figure 5.12.** UV-Vis absorption spectra of C1 9/55/36 showing the dependence on the UV irradiation time.

Without illumination, the absorption spectrum is more intense compared to the reference sample due to the turbidity of the initial solution. Since no surface plasmon resonance was detected, it is assumed, that no particle formation takes place without sample exposure to UV light. After 15 minutes of irradiation, an absorption peak arises at 431 nm, indicating the formation of silver nanoparticles. Longer irradiation time resulted in a gradual increase of intensity of the absorption band with a constant  $\lambda_{\text{max}}$ , showing a concomitant increase of the number of particles with similar morphology. According to the previous UV-Vis measurements of the binary lamellar phase, nanoparticles may also aggregate and agglomerate into submicrometer particles, that show no plasmon resonance. Sonication of nanoparticle

dispersions resulted in the destruction of such agglomerated structures. However, sonication of the DNA-containing samples for 1 minute did not initiate any changes in the absorption spectra indicating that nanoparticles do not form unstable agglomerates.

Similar to the ternary DTADNA/GMO/D<sub>2</sub>O system (see section 4.3–4.4), absorption in the region of 300 – 350 nm decreases upon UV illumination, compared to the reference sample. A possible explanation is that the exposure of lecithin to UV light may lead to the photodegradation (peroxidation and oxidation) of phosphatidylcholine and other lipids or antioxidants which are present in lecithin. UV-C and UV-A were shown to induce lipid peroxidation in different systems of vesicular, micellar and lamellar structures [135]. The degradation process produces a number of products with highly different chemical nature: hydroperoxides, conjugated dienes, cyclic peroxides, malondialdehyde, alkanes [136]. Antioxidants ( $\alpha$ -tocopherol) and singlet oxygen quenchers ( $\beta$ -carotene) have been reported to improve the phospholipid resistance against photooxidation. On the contrary, D<sub>2</sub>O enhances the lifetime of the singlet oxygen and promotes the photooxidation of the phospholipids [137]. In our case, more detailed investigations would be needed for a complete understanding of the photodegradation process in the liquid crystals. However, even if any photooxidation takes place, it seems not to affect the liquid crystalline phase, as it will be demonstrated later.

Figure 5.13 displays typical TEM pictures of nanoparticles synthesized in the DNA-containing lamellar phase after exposure to UV light for 60 minutes. The majority (more than 99%) of the nanoparticles are individual ones in the range of 3–45 nm with an average size of 15 nm. Similar to the two-component lamellar phase, several agglomerates with a size of 100–200 nm were detected (not included to the size distribution histogram). They could result due to the spontaneous formation of nanoparticles caused by the reduction of silver ions by lecithin.

The influence of the UV irradiation on the template structure has been studied with <sup>13</sup>C and <sup>31</sup>P NMR spectroscopy. Figure 5.14 shows <sup>31</sup>P NMR spectra of the DNA-containing lamellar phase in dependence on the irradiation time. Since both lecithin and DNA exhibit a characteristic <sup>31</sup>P NMR chemical shift anisotropy pattern it can be used to confirm the liquid crystalline structure and incorporation of the DNA in the LC mesophase, as was demonstrated by Leal et al. [138]. They reported the reduction of the DNA chemical shift anisotropy as a result of DNA conformation change and intercalation of the DNA into the cationic phospholipid bilayer.

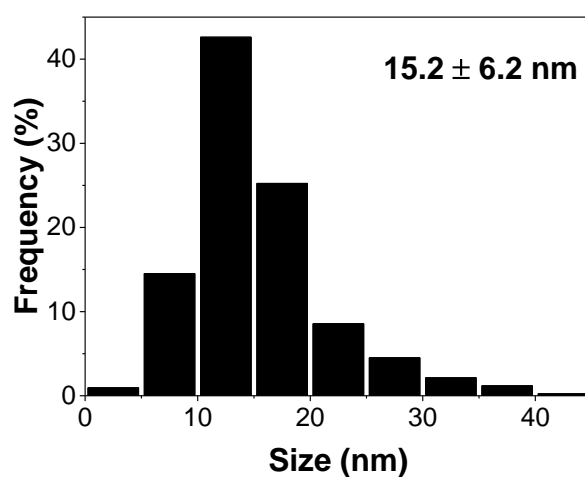
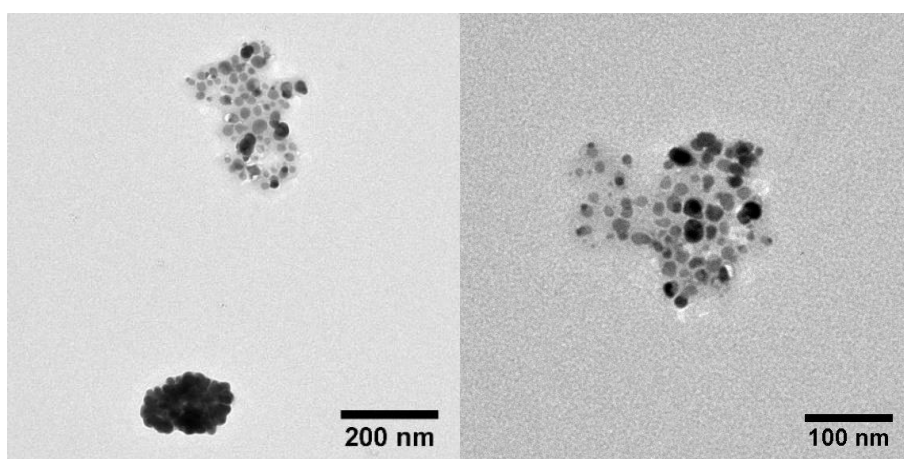


**Figure 5.13.** TEM images and size distribution histogram of nanoparticles formed in C1 9/55/36 after 60 minutes of UV irradiation.

Although the DTADNA complex had been successfully incorporated into the lamellar phase, as confirmed by SAXS, to relatively high concentrations, it had not been incorporated at the concentrations necessary to facilitate the observation of  $^{31}\text{P}$  signals originating from the DNA, over the background  $^{31}\text{P}$  signals originating from the phospholipid. The highest DTADNA complex content used in the lamellar phase was no more than 9 wt.%, corresponding to approximately 5.4 wt.% of DNA.

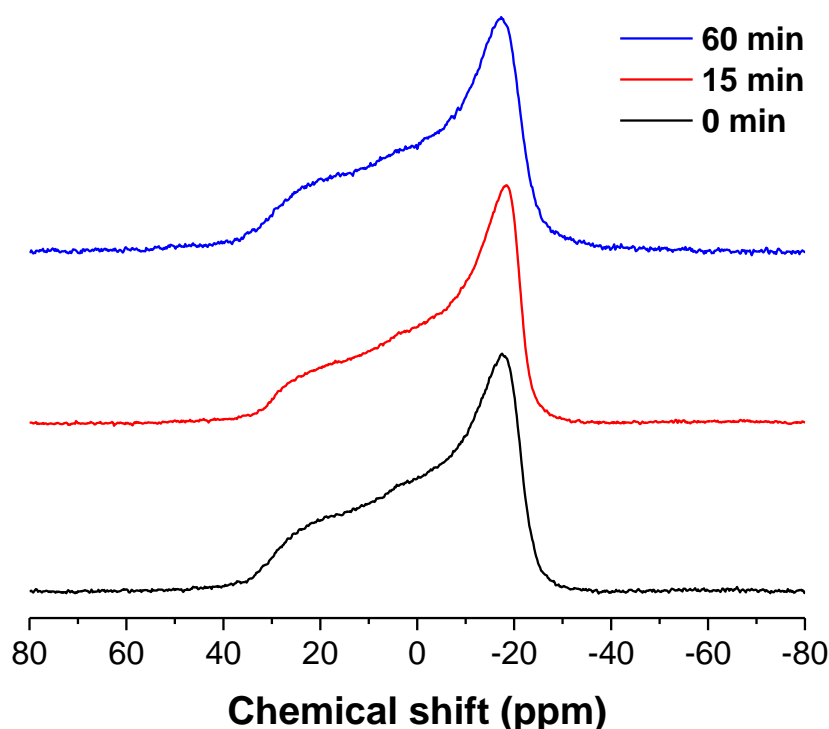


**Figure 5.14.**  $^{31}\text{P}$  solid state NMR spectra of C0 9/55/36 measured after various UV irradiation times ( $\omega=0$  kHz, 23 °C).

$^{31}\text{P}$  spectra show axially symmetric chemical shift anisotropy patterns with similar features. The small differences can be explained by a slightly different spectrum processing (in particularly baseline correction) and sample history (i.e. due to the different equilibration time, centrifugation, etc.). Results of the  $^{31}\text{P}$  NMR spectroscopy suggest that exposure of the lamellar phase to the UV light for 1 hour does not cause any significant changes in the liquid crystalline mesophase, which is in agreement with SAXS measurements.

#### **5.4 Photoinduced formation of silver nanoparticles in the DNA-containing inverse hexagonal phase**

After exposure to UV-light, samples have been characterized by SAXS,  $^2\text{H}$  and  $^{31}\text{P}$  NMR spectroscopy. Five reflections with a ratio of  $1:\sqrt{3}:2:\sqrt{7}:3$  were found in the SAXS pattern of C1 15/68/17, as shown in figure 5.15 A. These X-ray scattering data are consistent with a hexagonal structure. The absence of the DNA peak confirms a successful formation of a two-

dimensional hexagonal phase, where DNA is incorporated into the aqueous cores of cylindrical lecithin micelles. In comparison, the SAXS spectrum of C1 16/63/21 (figure 5.15 B) shows a DNA-DNA correlation peak between the first and second Bragg peaks of the lamellar structure, which yields the interhelical distance of 50.2 Å between two neighboring DNA rods. In addition, a broad peak of low intensity at  $q = 0.186 \text{ \AA}^{-1}$  can be attributed to the (110) reflection of the hexagonal phase. The data suggest that lamellar and inverse hexagonal phases coexist in this sample in contrast to the expectation of a pure hexagonal phase based on a published phase diagram (cf. figure 5.1).

The  $^{31}\text{P}$  NMR spectra of the reference samples (samples in the absence of silver nitrate solution) are in agreement with the scattering data of the corresponding samples with silver nanoparticles (figure 5.15, C, D). Both  $^{31}\text{P}$  NMR spectra are composed of the overlapping chemical shift anisotropy patterns of DNA and phospholipid. The intense axially symmetric peak in C0 15/68/17 originates from the phospholipid cylindrical micelles arranged into a hexagonal lattice. In the case of C0 16/63/21, the lecithin signal consists of two superimposed axially symmetric CSA tensors, assigned to the bilayer structure of the lamellar phase and inverse hexagonal phase (figure 5.15, C). The sign of the chemical shift anisotropy is reversed in the case of  $\text{H}_{\text{II}}$  as compared with  $\text{L}_{\alpha}$  phase. The effective  $^{31}\text{P}$  chemical shift anisotropy,  $\Delta\delta = 23.7$  ppm (C0 15/68/17), 22.3 ppm (C0 16/63/21) for the inverse hexagonal and 43.6 ppm for lamellar phase (C0 16/63/21), showing an almost twofold reduction of phospholipid linewidth, due to the lateral diffusion of lipid molecules about the cylinder axis of the phospholipid micelle. Taking into account similar composition of two samples, these results are consistent with theory. A broad low-intense axially asymmetric CSA pattern is attributed to the DNA intercalated between lecithin bilayers (C0 16/63/21) or DNA located inside the aqueous cores of the inverse hexagonal phase. The CSA pattern of DNA in the liquid crystal has a significantly reduced linewidth in comparison to the solid DTADNA complex (figure A.19), which is in agreement with previously reported data [138]. Incorporation of DNA into the aqueous medium of the lamellar or hexagonal phase induces a transition from A- to B-form due to the hydration of DNA [31].

The principal values of the DNA and phospholipid CSA tensors were obtained by fitting the  $^{31}\text{P}$  spectrum with matNMR [139]. Table 5.2 summarizes the fitting results of the  $^{31}\text{P}$  NMR spectra of the reference samples.

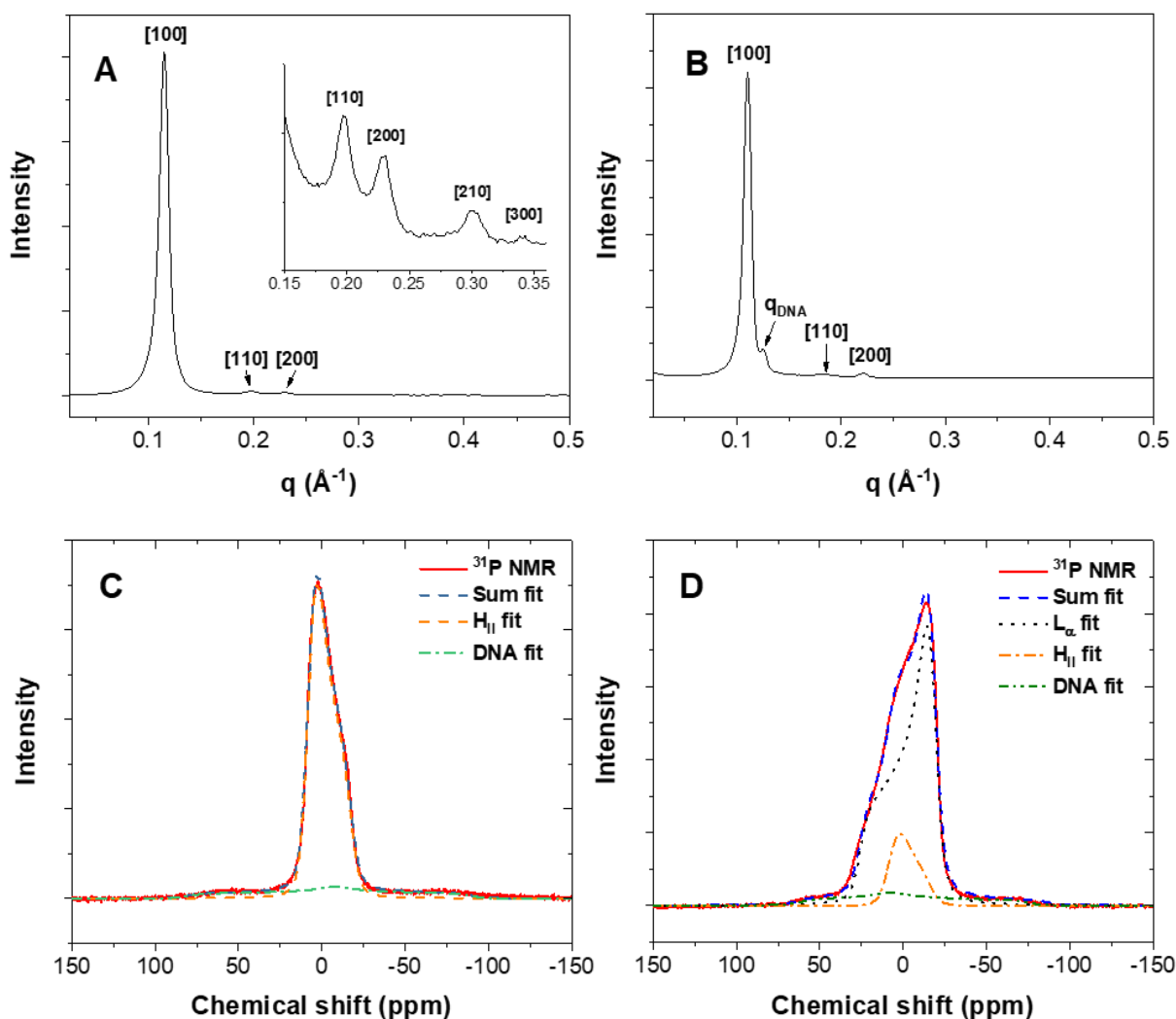


**Figure 5.15.** Top: SAXS patterns of C1 15/68/17 (A) and C1 16/63/21(B) and bottom:  $^{31}\text{P}$  NMR spectra of C0 15/68/17 (C) and C0 16/63/21 (D) ( $\omega=0$  kHz,  $23^\circ\text{C}$ ).

**Table 5.2.** Principal values of chemical shift tensor for  $^{31}\text{P}$  of DNA and lecithin of the reference samples (without silver salt).

Sample	DNA					Lecithin		
	$\delta_{11}$	$\delta_{22}$	$\delta_{33}$	$\delta_{11} - \delta_{33}$	$\eta$	$\delta_{\parallel}$	$\delta_{\perp}$	$\Delta\delta$
DTADNA	83.4	23	-107	190.4	0.56			
C0 16/63/21	62.3	7.2	-86.3	148.6	0.64	$L_{\alpha}$ : 26 $H_{II}$ : 6.3	-17.6 -16.0	43.6 22.3
C0 15/68/17	74.1	2.1	-86.6	160.7	0.83	6.4	-17.3	23.7
C0 9/55/36						26.5	-19.4	45.9
C0 0/60/40						24.5	-18	42.5

The formation of silver nanoparticles in the inverse hexagonal and lamellar phase was followed by a combination of UV-Vis spectroscopy and transmission electron microscopy. Figure 5.16 shows UV-Vis absorption spectra of C1 15/68/17 and C1 16/63/21 before and after exposure to UV light for 1 hour, in comparison with the spectra of the reference samples.

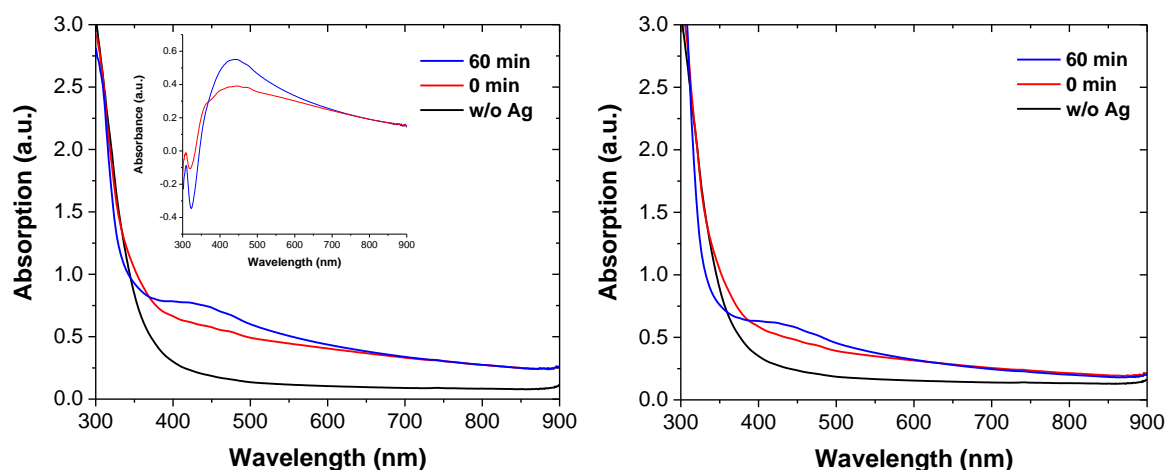


**Figure 5.16.** Dependence on the UV irradiation time for samples C1 16/63/21 (left) and C1 15/68/17 (right) before and after irradiation with UV light for 60 minutes. Inset in (left) shows absorption spectra after subtracting the reference spectrum.

Due to the higher DTADNA content resulting in higher viscosity compared to the lamellar phase, samples from the inverse hexagonal region of the phase diagram typically required 2 – 4 weeks of preparation and equilibration time. As a result, nanoparticles are already present in the samples, due to the reduction of  $\text{Ag}^+$  ions by lecithin without exposure to UV light. The spontaneous formation of nanoparticles in liquid crystals with DNA is generally slower than in the DNA-free samples, as was already shown in chapter 4.5. A broad absorption band arises at ca. 430 nm (figure 5.16, inset). After exposure to UV-light for 1 hour, the intensity of the surface plasmon resonance band is increased, indicating that silver was only partly reduced by the spontaneous process. The position of the absorption band maxima of silver nanoparticles was red-shifted to 438 nm after 1 hour of irradiation.

After samples were exposed to UV light for 1 hour, nanoparticles have been collected from the liquid crystalline mesophase and measured with transmission electron microscopy. TEM measurements of particles synthesized in C1 15/68/17 (inverse hexagonal phase), presented in figure 5.17, show small nanoparticles with a size of 3–45 nm and spherical aggregates consisting of the densely-packed almost spherical particles with dimensions of 80–200 nm.

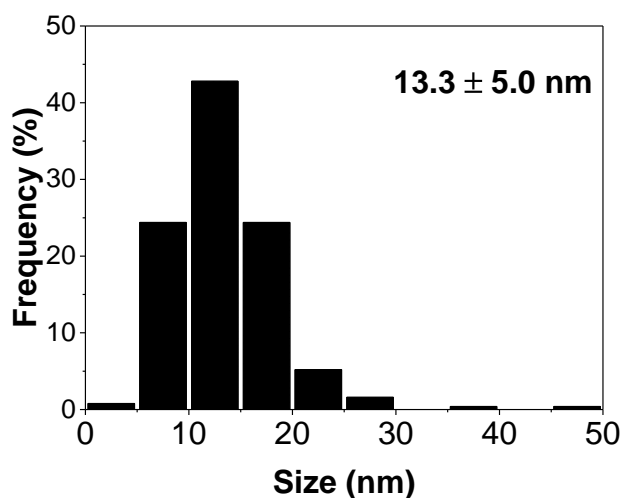
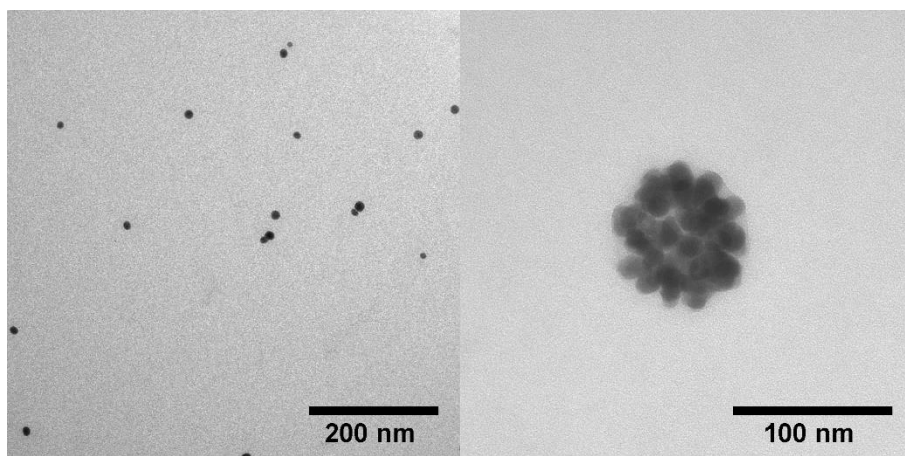


**Figure 5.17.** Top: TEM images of isolated particles (left) and particle aggregate (right). Bottom: size distribution histogram of nanoparticles synthesized in C1 15/68/17 after 60 minutes of irradiation.

When nanoparticles formed in C1 16/63/21 were analyzed via TEM, two different types of nanostructures have been found, as can be seen in figure 5.18. Approximately 99% of the nanoparticles are spherical and ellipsoidal with a dimension of 4–45 nm. A second type consists of submicrometer-sized fractal aggregates. In addition, several linear AgNP chains were observed, containing between 3-12 ellipsoidal nanoparticles. However, it is not entirely clear, whether the growth of the fractal aggregates is an experimental artifact due to agglomeration (aggregation) and coalescence of particles on the microscope grid or whether it occurs in the liquid crystalline phase already. It was reported that for a fractal dendrite growth a 2D interface is required, like Langmuir monolayer [140] or thermally evaporated film [141]. A formation of fractal aggregates within sheared lecithin containing vesicles has been reported by Meyre et al. [142].

As it was previously shown, in our case particle aggregates formed in the lamellar phase (with and without DNA) and in the inverse hexagonal phase resulted in dense, partly coalesced spherical aggregates.

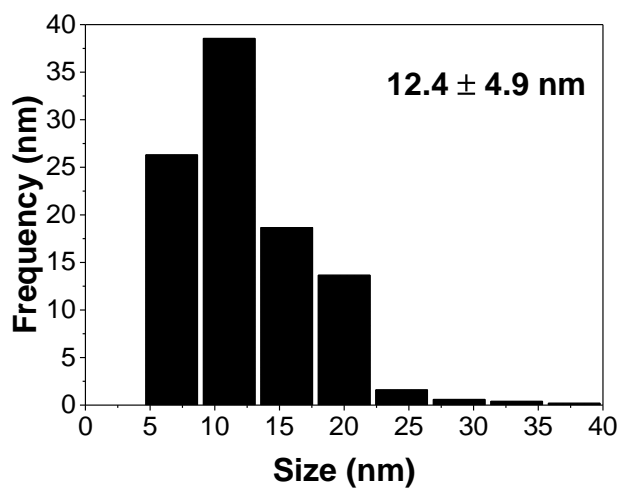
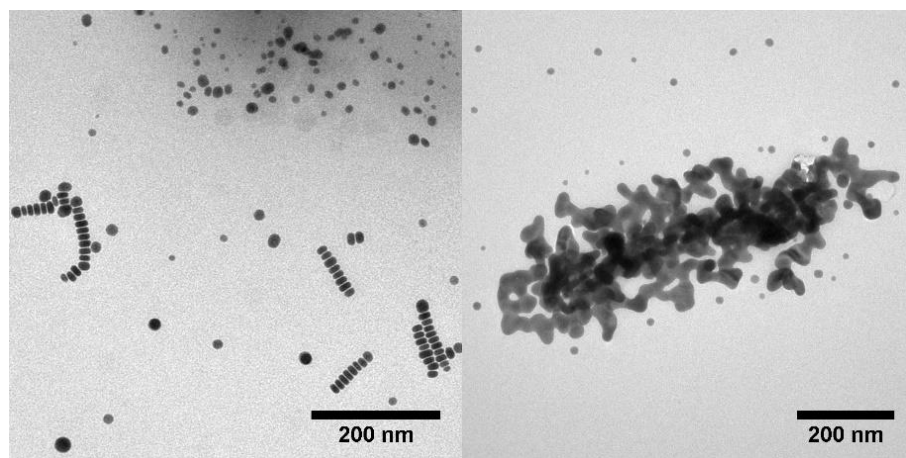


**Figure 5.18.** Top: TEM images of isolated particles (left) and fractal dendrite aggregate (right). Bottom: size distribution histogram of nanoparticles synthesized in C1 16/63/21 after 60 minutes of irradiation.

## 5.5 Summary

In the present chapter, the synthesis of silver nanoparticles in DNA-containing liquid crystals is presented with double-stranded DNA incorporated into the lamellar and inverse hexagonal phase formed by lecithin. Nanoparticles have been synthesized by the chemical and photoreduction of the Ag-DNA complex, where silver ions are embedded into the double helix. The reported synthetic method does not require any additional reducing agent for the silver precursor since DNA can act as a photoreduction and stabilizing agent.

Most of the synthesized AgNP are isolated spherical and ellipsoidal particles; but aggregated nanoparticles were found as well. It is not yet clear, however, whether the formation of the observed fractal dendrite aggregates takes place on the TEM grid as an artifact of the specific sample preparation, or whether it occurs in the liquid crystalline phase.

Due to the long time required for preparation and equilibration of the samples with a high DNA amount, nanoparticles were already formed while preparing the inverse hexagonal samples. Similar to the binary lecithin/water system lecithin can act as a reduction agent for the silver ions. However, due to the embedding of Ag<sup>+</sup> ions into the DNA double helix, the reported process was slower in comparison to the DNA-free analogues.

An exposure of liquid crystalline samples to UV may lead to photooxidation of lecithin but has no or little effect on the liquid crystalline structure. Further investigations are necessary to obtain detailed information of the UV-induced phospholipid degradation. It was found, that formation of silver nanoparticles affects the long-term stability of the liquid crystals, by facilitating the hydrolysis of lecithin and inducing a transition from lamellar to the isotropic phase.

## 6 Photoinduced formation of silver nanoparticles in the DTADNA/2-hydroxypropyl- $\beta$ -cyclodextrin/water system

### 6.1 Introduction

In previous chapters, the particle formation processes in systems which can form liquid crystalline phases without DTADNA complex were investigated. An addition of DTADNA at low concentration causes DNA intercalation into the aqueous channels between lipid bilayers. A high concentration of DTADNA usually transforms the original bicontinuous cubic or lamellar phase into an inverse hexagonal one. As demonstrated in Chapters 4 and 5, the synthesis of Ag-NPs was possible by exposure of the Ag-DNA complex to UV-light without additional reducing agents. As an alternative method (see chapter 3 and 5), nanoparticles could be synthesized by the Ag<sup>+</sup> reduction by the surfactant aggregates which act as both template and reducing agents. In comparison to the previous systems, in the following chapter we report the formation of Ag nanoparticles in a system where the presence of DTADNA is required for both the formation of liquid crystalline phases as well as for the successful synthesis of silver nanoparticles.

The aqueous phase behavior of the dodecyl trimethyl ammonium DNA complex (DTADNA) in the presence of 2-hydroxypropyl- $\beta$ -cyclodextrin (HP $\beta$ CD) or  $\beta$ -cyclodextrin ( $\beta$ CD) has been studied by Bilalov et al. [143]. The phase diagram and schematic representation of the hexagonal and tetragonal phases are shown in figure 6.1. 2-hydroxypropyl- $\beta$ -cyclodextrin is a cyclic oligosaccharide which consists of seven glucopyranose units bound through  $\alpha$ -1,4-glycosidic linkages with one 2-hydroxypropyl group per each sugar unit. The HP $\beta$ CD molecule is rigid and has toroidal shape, with a hydrophilic exterior and a hydrophobic inner cavity with a diameter of the narrow and wide side of 6.0 and 6.5 Å, respectively [144]. Cyclodextrins and their derivatives can form host-guest inclusion complexes of different stoichiometry with a variety of hydrophobic and amphiphilic molecules of appropriate size by incorporating them, fully or partially, in the cavity in aqueous solution. Due to the high affinity of such inclusion complexes, DNA-cationic surfactant aggregates are disassembled, and DNA is released into solution.

Three different phases have been identified in the phase diagram of DTADNA/HP $\beta$ CD/water shown in figure 6.1: an isotropic phase and two liquid crystalline ones: a normal hexagonal and a tetragonal phase [143]. The structure of the liquid crystalline phase can be controlled by

adjusting the  $[DTADNA]/[HP\beta CD]$  molar ratio. Due to the high solubility of  $HP\beta CD$ , a small amount of DNA can be solubilized in the isotropic phase when the  $[DTA]/[HP\beta CD] \leq 1$ , where the charge of the phosphate group is neutralized by the CD-DTA inclusion complexes. The hexagonal phase is formed when the DTADNA concentration is increased to 10 wt.% while the  $[DTA]/[HP\beta CD]$  ratio is kept less than 1. At a ratio of 1, all surfactant molecules are involved in the formation of the inclusion complex. The normal hexagonal phase consists of DNA molecules which are packed into the two-dimensional hexagonal lattice and the charge of the phosphate group is neutralized by the CD-DTA inclusion complexes.

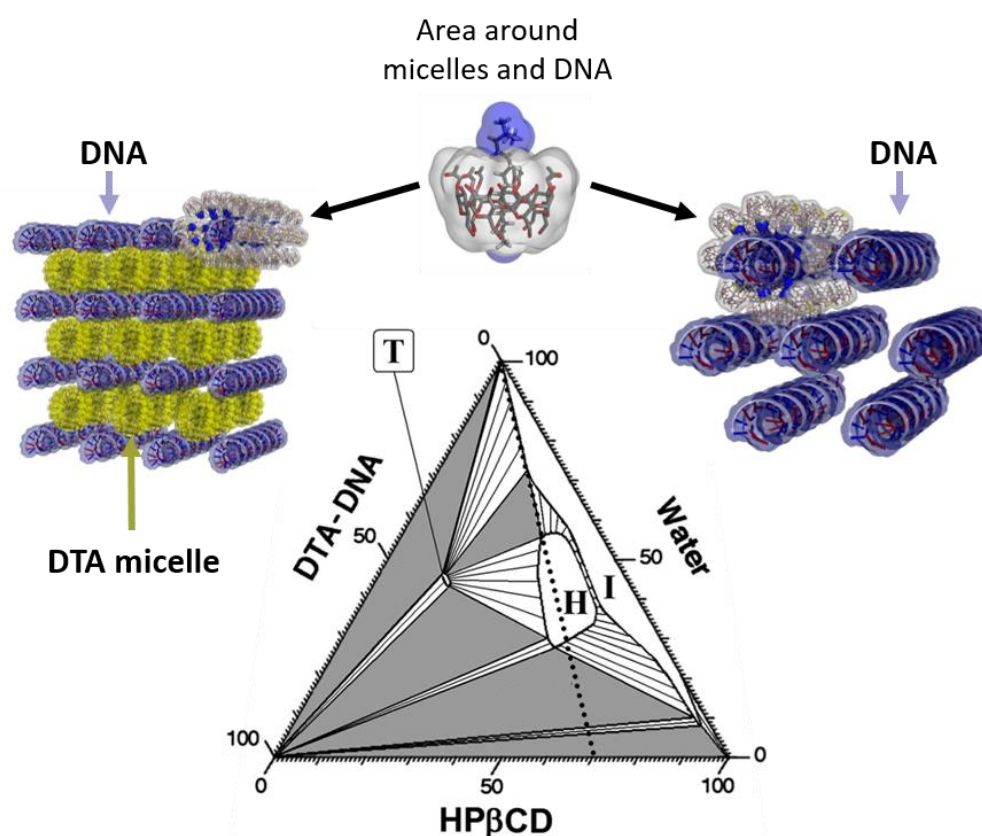


**Figure 6.1.** DTADNA/ $HP\beta CD$ /water ternary phase diagram at 25°C and schematic representation of liquid crystalline phases, redrawn from [143]. White areas without labels – two phase regions, gray – three phase regions. The dotted line shows  $[DTA]/[HP\beta CD] = 1$  (H – hexagonal, T – tetragonal and I – isotropic phases).

An increase of the DTADNA concentration to a  $[DTA]/[HP\beta CD]$  ratio of 1.5–2 leads to the formation of the tetragonal phase. It occurs in a very narrow area of the phase diagram, being a unique stoichiometric compound. In this phase, DNA rods are incorporated into the square lattice and the charge of the DNA is neutralized by the mixture of the monovalent CD-DTA inclusion complexes and spherical surfactant micelles. Because of the high local charge

micelles are associated with more than one DNA molecule and helices of neighboring DNA double strands are in phase.

Samples of both types of liquid crystalline phases as well as the isotropic phase have been prepared. For particle synthesis silver nitrate solution in D<sub>2</sub>O was used. The composition of the prepared samples is shown in table 6.1. Moreover, several samples from isotropic and hexagonal phases of the ternary DTADNA/βCD/water system have been prepared. However, upon addition of silver nitrate, a precipitation of the DTADNA complex occurred making this system not suitable for the nanoparticle synthesis.

**Table 6.1.** Composition of samples of DTADNA/HPβCD/water ternary system.

Sample	DTADNA, wt. %	HPβCD, wt. %	D <sub>2</sub> O, wt. %	DTA/HPβCD molar ratio	[Ag <sup>+</sup> ]/[DNA <sub>base</sub> ] (0.1 M AgNO <sub>3</sub> )	Phase
A 2/48/50	2	48	50	0.115	0.075 (0.005 M) – 1.51 (0.1 M)	I
A1 10/40/50	10	40	50	0.69	0.252	H + I
A1 15/35/50	15	35	50	1.18	0.168	H
A1 18/41/41	18	41	41	1.21	0.115	H
A1 17.5/25/57.5	17.5	25	57.5	1.93	0.165	T
A1 25/25/50	25	25	50	2.76	0.1	T

For all experiments in this chapter, two different sets of samples were prepared, with D<sub>2</sub>O and with AgNO<sub>3</sub> solution in D<sub>2</sub>O (0.01–0.1 M). The first number in the sample notation indicates the concentration of silver nitrate solution (e.g. A1 – 0.1 M AgNO<sub>3</sub> solution in D<sub>2</sub>O, A01 – 0.01 M, A0 – D<sub>2</sub>O only) and the additional three numbers are related to the sample composition (DTADNA/HPβCD/D<sub>2</sub>O or silver nitrate solution in D<sub>2</sub>O, wt.%).

The stability of the liquid crystalline phases upon silver addition and nanoparticle formation was measured by small angle X-ray scattering, <sup>2</sup>H and <sup>31</sup>P NMR spectroscopy.

## **6.2 Synthesis of silver nanoparticles in isotropic DTADNA/HPβCD solution. Effect of Ag<sup>+</sup> concentration and UV irradiation time on the nanoparticle formation**

For the study of the influence of the silver concentration on nanoparticle formation in the isotropic phase, a series of samples with the same basic composition but with various Ag<sup>+</sup> concentration in the range of 0.01–0.1 M has been prepared. Experiments were conducted by varying the concentration of the silver solution and the UV exposure time. The samples are

colorless, transparent and highly viscous solutions. The viscosity of the solution gradually decreases with the increase of  $\text{Ag}^+$  concentration. For  $[\text{Ag}]/[\text{DNA}_{\text{base}}] \geq 0.6$  a precipitate was found without illumination, so those samples have not been used for the nanoparticle synthesis. Irradiation of the samples with UV light leads to the formation of silver nanoparticles and causes a change in the color of the solution from colorless to yellow or brown, depending on the initial  $\text{Ag}^+$  concentration, as shown in figure 6.2.

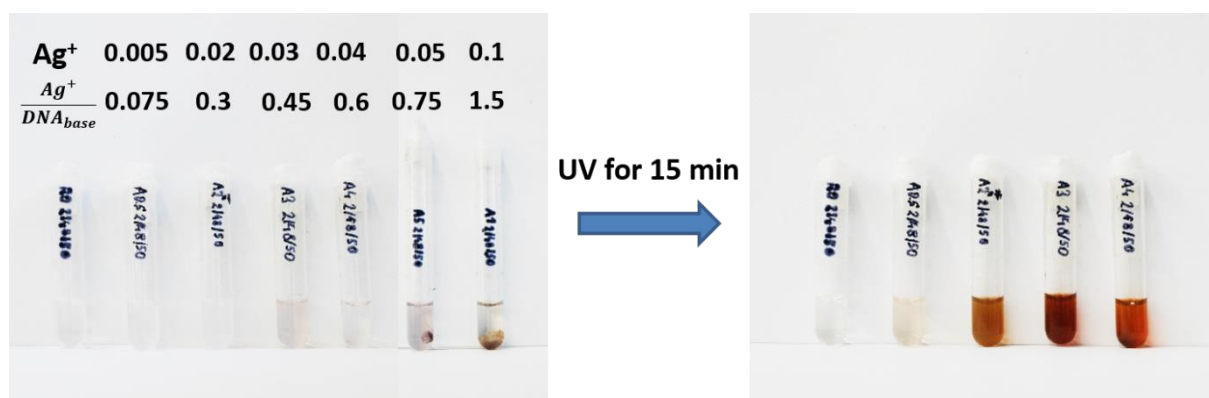


**Figure 6.2.** Samples of the A 2/48/50 with different  $\text{Ag}^+$  concentration before and after exposure to UV light for 15 minutes.

Both the  $^2\text{H}$  and  $^{31}\text{P}$  NMR spectra, shown in figure 6.3, display only a single peak, typical for the isotropic phase where DNA molecules are randomly distributed, without any degree of ordering. The isotropic motion of DNA in this solution averages the CSA tensor to the isotropic value resulting in a single narrow peak.

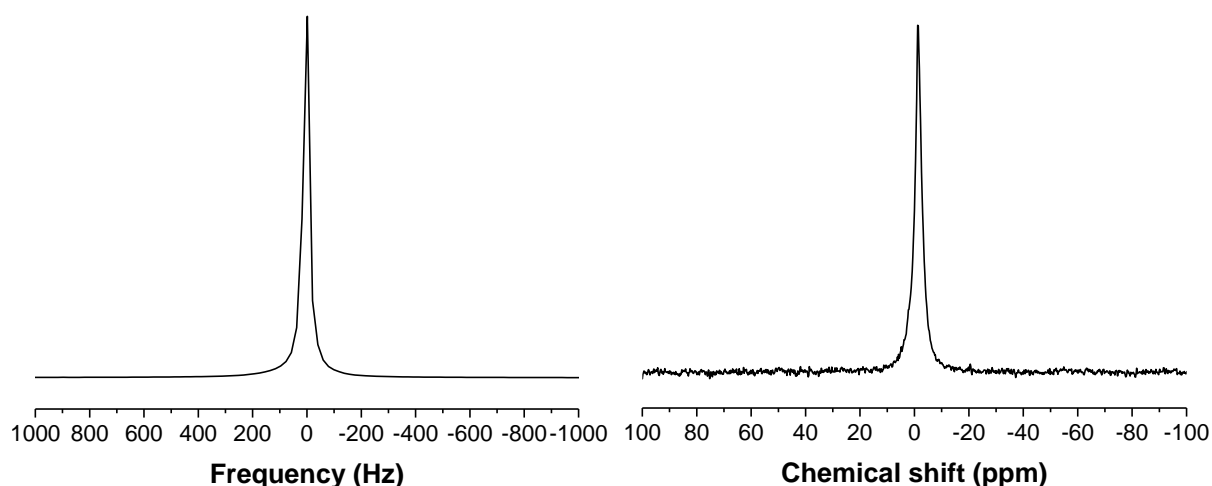


**Figure 6.3.**  $^2\text{H}$  (left) and  $^{31}\text{P}$  NMR (right) spectra of A0 2/48/50 at 23 °C.

In order to investigate an influence of the UV irradiation time on the nanoparticle formation, samples were illuminated by UV light. Figure 6.4 represents UV-Vis absorption spectra

showing an effect of the irradiation time on the nanoparticle formation rate in the isotropic A 2/48/50 sample with 0.01 M and 0.03 M  $\text{AgNO}_3$ .

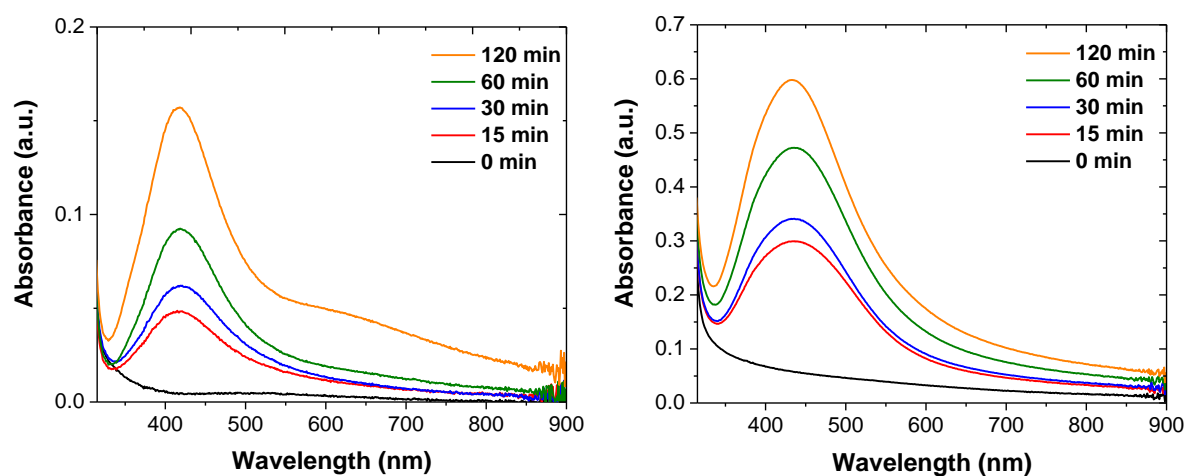


**Figure 6.4.** UV-Vis absorption spectra showing the dependence on the UV irradiation time of A01 2/48/50 (left) and A03 2/48/50 (right).

No absorption band of silver nanoparticles was detectable in the samples prior to their exposure to UV light. After UV illumination for 15 minutes, an absorption peak appears at ca. 414–440 nm, depending on the  $\text{AgNO}_3$  concentration. With increase of the exposure time, a continuous increase of the surface plasmon resonance band intensity is observed. During the photolysis, the position and shape of the plasmon resonance peak remain almost constant suggesting that average size, size distribution, and shape of the nanoparticles remain the same during the synthesis. The shoulder around 600 nm for A01 2/48/50 (figure 6.4 left) after 120 minutes of UV irradiation was observed only for this sample and is most likely an experimental artefact.

The maximum absorption as a function of the  $[\text{Ag}^+]/[\text{DNA}_{\text{base}}]$  ratio from 0.075 to 0.45 follows a Lambert-Beer law showing a linear increase of absorption at  $\lambda_{\text{max}}$  with an increase of  $\text{Ag}^+$  concentration in the range of 0.005–0.03 M (figure 6.5). Such a behavior suggests a linear dependence of the nanoparticle concentration on the amount of precursor. On the contrary, upon increasing the  $\text{Ag}^+$  concentration from 0.01 to 0.03 M the SPR position shifts towards longer wavelength (from 414 nm for 0.01 M to 434 nm for 0.03 M  $\text{AgNO}_3$ ) which can be attributed to an increase of the nanoparticle size (while keeping the assumption that the refractive index remains constant) or to a coupling of the surface plasmon resonance from neighboring particles. The SPR is red-shifted due to the electromagnetic interaction between nanoparticles, in particular due to the coupling of the surface plasmons from closely located particles [145]. The

absorption peak does not show a splitting into a short- and long-wavelength peak because the mean interparticle distance is still high, forming a red-shifted and broadened peak upon the increase of  $[Ag^+]/[DNA_{base}]$  (figure 6.6).

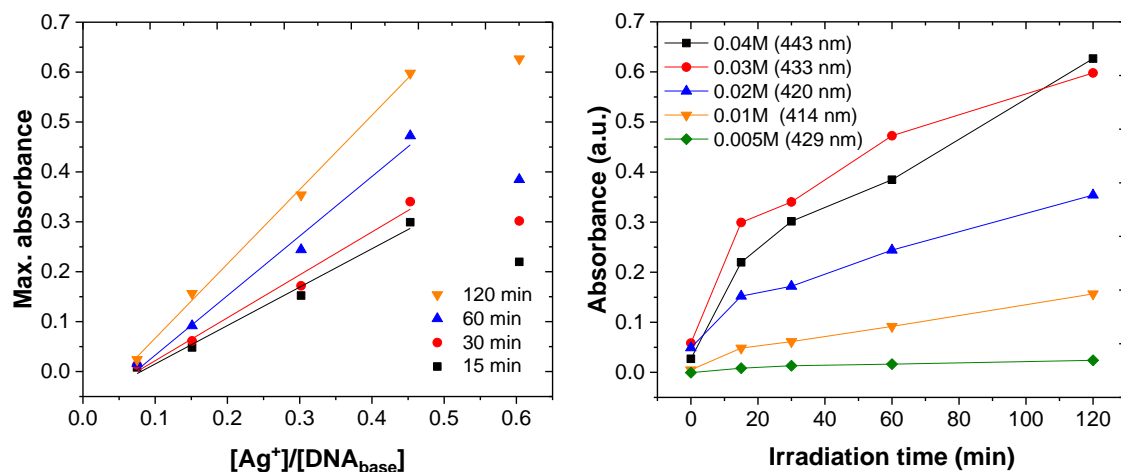


**Figure 6.5.** Left: absorbance at  $\lambda_{max}$  plotted against  $[Ag^+]/[DNA_{base}]$  ratio for various irradiation times. Because of precipitation the sample with 0.04 M  $AgNO_3$  ( $[Ag^+]/[DNA_{base}] = 0.6$ ) was excluded from the fitting. Right: time evolution of the surface plasmon resonance peak intensity as a function of irradiation in the presence of different  $Ag^+$  concentrations. The peak position of the surface plasmon resonance is shown in brackets.

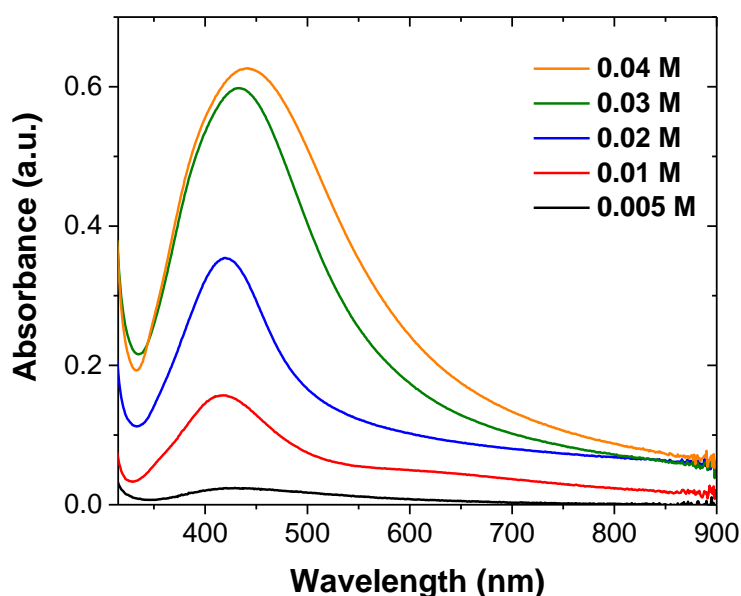


**Figure 6.6.** UV-Vis spectra of A 2/48/50 samples with various silver concentration. Samples were exposed to UV light for 120 minutes prior the measurement.

After exposure to UV light for 60 minutes, nanoparticles were collected and measured with transmission electron microscopy. Figure 6.7 shows TEM micrographs and size distribution histograms of particles synthesized in solution loaded with 0.01 and 0.03 M AgNO<sub>3</sub>. Nanoparticles synthesized in A01 2/48/50 are in the range of 3–45 nm with an average size of  $11.8 \pm 5.6$  nm. Several large particles with a size of approximately 100 nm were found in TEM pictures of A01 2/48/50. These particles are not included in the size distribution histogram, since they may result due to the aggregation of small particles. It is not yet clear, whether such aggregated structures are an artifact due to the specific sample preparation for TEM measurements or whether they are indeed formed in the DTADNA/cyclodextrin solution. The average size of particles obtained in A03 2/48/50 after 60 minutes of illumination was slightly bigger,  $14.9 \pm 6.3$  nm. Nevertheless, such a small difference in the particles size cannot result in a substantial red shift of the surface resonance band. The red shift and broadening of the surface plasmon resonance band result due to a coupling of the SPR from particles in close vicinity and aggregated particles.

As it was mentioned above, for  $[\text{Ag}^+]/[\text{DNA}_{\text{base}}] \geq 0.6$  precipitate was found without illumination. The amount of precipitate gradually increased with an increase of the  $[\text{Ag}^+]/[\text{DNA}_{\text{base}}]$  ratio. Our findings are in agreement with studies of the interaction of silver with calf thymus DNA. Jensen and Davidson reported a formation of precipitate pH = 7 and below for a type III complex where  $[\text{Ag}^+]/[\text{DNA}_{\text{base}}]$  ratio  $\geq 0.5$  [47]. Based on that, we can assume that  $[\text{Ag}^+]/[\text{DNA}_{\text{base}}]=0.5$  is the maximal ratio which can be used for the nanoparticle synthesis in the solution.  $[\text{Ag}^+]/[\text{DNA}_{\text{base}}]=0.05$  was found to be the minimum concentration required to initiate nanoparticle formation. Below this value, no surface plasmon resonance band of silver nanoparticles was detected (data not shown).

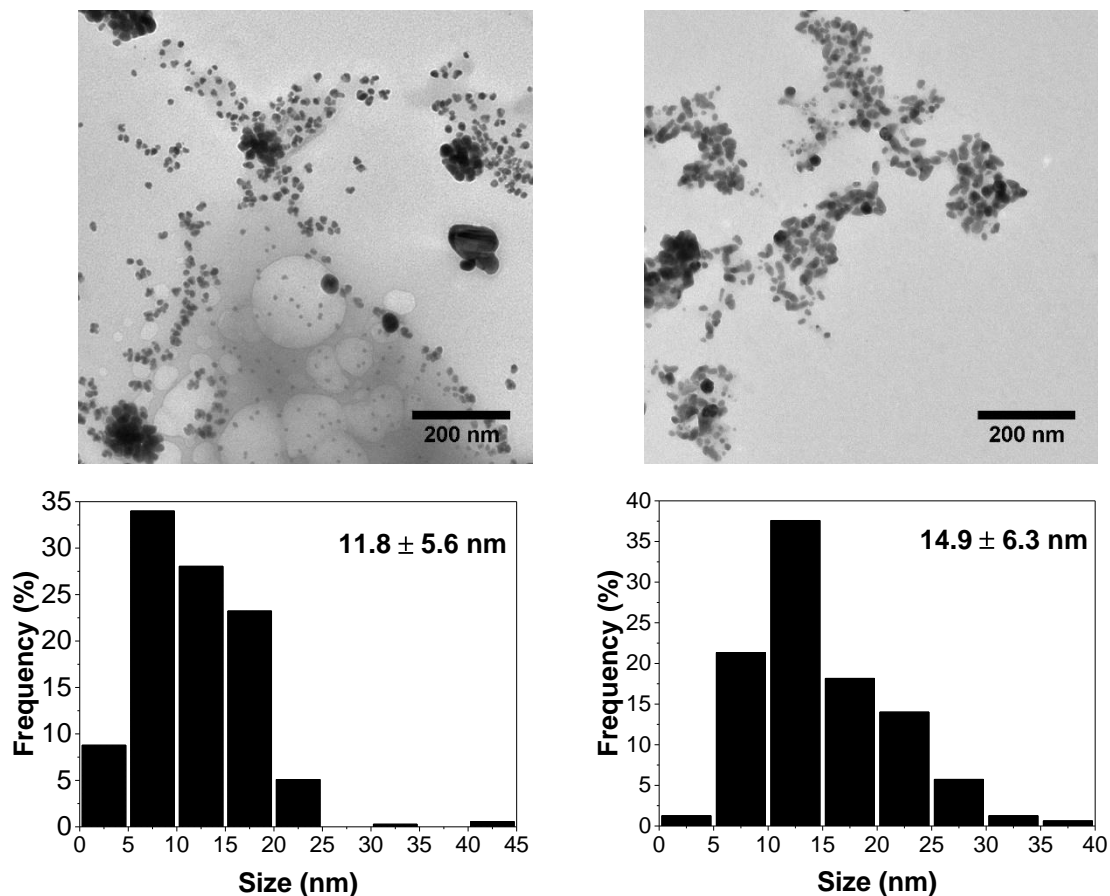


**Figure 6.7.** TEM images (top) and size distribution of nanoparticles (bottom) prepared in A001 2/48/50 (left) and A003 2/48/50 (right) irradiated for 60 minutes.

In order to verify that the presence of DNA is indeed responsible for the *nanoparticle* formation, two DNA-free samples with a composition of 50 wt.% HP $\beta$ CD/50 wt.% AgNO<sub>3</sub> solution (0.02 and 0.1 M) were prepared. After preparation and equilibration for 2 days, samples were exposed to UV light for 15 minutes and measured by UV-VIS spectroscopy. UV-Vis spectra of samples before and after irradiation are shown in figures A.20 and A.21. Freshly prepared samples were colorless and turbid, resulting in higher absorbance in the visible region of the spectrum. Only after 2 days of equilibration, the sample with 0.1 M AgNO<sub>3</sub> had turned slightly yellow, and a low-intense absorption band at 470 nm was detected, attributed to the spontaneous formation of a very small amount of nanoparticles. (The synthesis of silver nanoparticles in the presence of cyclodextrin has been demonstrated by Gopalan and coworkers [146]. However, in contrary to our protocol, in this work a slightly basic pH and elevated temperature were used for the successful particle synthesis). On the other hand, when our samples were exposed to UV light for 15 minutes, the color of samples turned to violet-black, and particle aggregates could be observed by the naked eye. UV-Vis spectra of irradiated samples displayed broad absorption bands in the visible and near-infrared region in the absorption spectrum, characteristic of large

particles and aggregates. Moreover, the synthesized particles showed fast sedimentation due to the absence of a stabilization agent. All these observations show that there are aggregates, but no individual nanoparticles. This control experiment indicates that the role of DNA is critical for the photoinduced formation of silver *nanoparticles* in the DTADNA/HP $\beta$ CD/water system.

### 6.3 Photochemical formation of silver nanoparticles in the hexagonal phase. Effect of composition and irradiation time

One week after sample preparation, samples were exposed to UV light for 1 hour to generate nanoparticles. The template structure has been analyzed with small angle X-ray scattering,  $^2\text{H}$  and  $^{31}\text{P}$  NMR spectroscopy, and polarizing optical microscopy. Results for the A1 18/41/41 are shown in figure 6.8. The SAXS pattern displays three distinctive Bragg reflections with a ratio of  $1:\sqrt{3}:2$ , typical for the hexagonal phase. The distance between neighboring DNA rods varied in the range 50–68 Å depending on the sample composition.

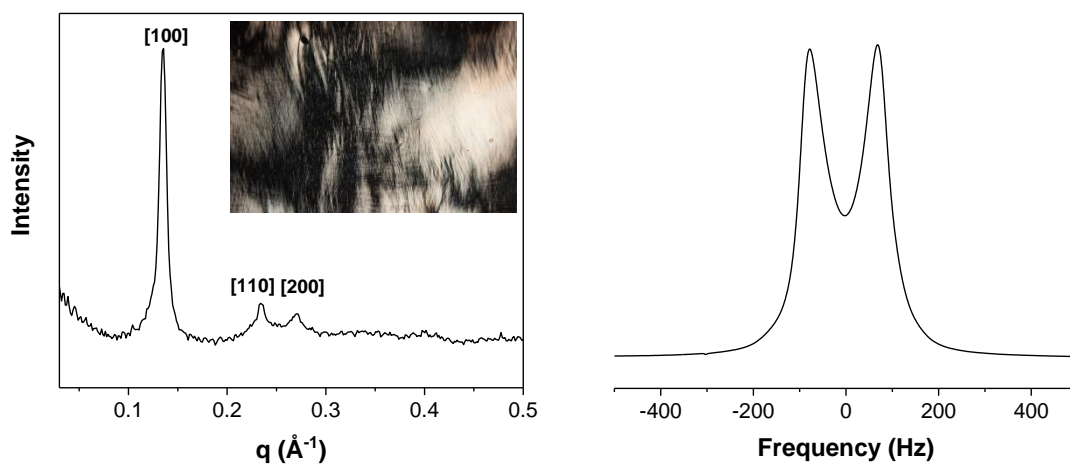


**Figure 6.8.** Small angle X-ray patterns (left) and  $^2\text{H}$  NMR spectra (right) of A1 18/41/41 at  $23^\circ\text{C}$  after 1 week. Inset – polarizing optical microscopy image of a hexagonal phase.

The right side of figure 6.8 displays the typical deuterium NMR spectrum of the hexagonal phase with a quadrupole splitting of 147 Hz. It should be noted, that a  $^2\text{H}$  spectrum with a quadrupole splitting can be recorded when samples were equilibrated for sufficiently long time (more than 1 week). Often only a single peak without splitting was observed for the  $^2\text{H}$  spectrum of samples from hexagonal and tetragonal liquid crystalline phases. The  $^{31}\text{P}$  NMR spectrum (figure A.22) shows a broad axially asymmetric chemical shift anisotropy pattern of DNA with

a smaller linewidth compared to the solid DTADNA. As it was already mentioned in chapter 5.4, the hydration of DNA leads to the transition from A- to B-form, accompanied by the reduction of the CSA tensor [31]. In addition, a narrow peak was detected in the NMR spectrum. It could be due to the presence of isotropic phase or low molecular weight or single-stranded DNA (or insufficient equilibration time).

DNA acts not only as a photosensitizing but also as a templating agent [69]. Formation of the nanoparticles within DNA molecules was also confirmed with AFM microscopy. DNA has been extracted from diluted liquid crystals by a modified ethanol precipitation protocol using low-speed centrifugation and subsequently immobilized onto mica surface. Figure 6.9 shows an AFM picture of the extracted DNA with synthesized nanoparticles.

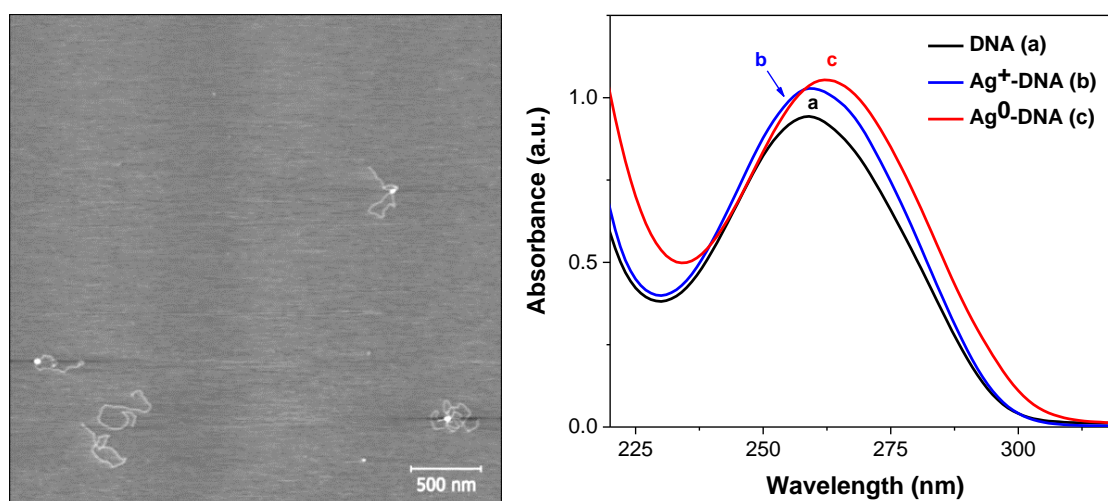


**Figure 6.9.** Left: tapping mode AFM picture of the DNA molecules with nanoparticles extracted from A1 10/40/50 after exposure to UV light for 15 minutes. Right: UV-Vis absorption spectra of DNA for the different stages of the synthesis process: (a) bare dsDNA, (b)  $\text{Ag}^+$ -DNA complex, (c)  $\text{Ag}^+$ -DNA complex irradiated with UV light for 15 minutes.

Interestingly, only rather long DNA molecules were seen in the AFM image. The measured contour length of DNA was found to be 1–1.2  $\mu\text{m}$ , corresponding to approximately 2.9–3.5 kbp. Some free AgNP were detected as a result of nonspecific silver deposition or sedimentation of particles from DNA duplexes due to centrifugation used for the sample preparation.

A comparison of UV-Vis spectra of DNA shows two important differences. Firstly, when silver salt is added (spectrum b), the DNA absorption peak at 260 nm has higher absorption intensity than the reference sample. Secondly, if the sample with Ag-DNA complex is irradiated with UV light (spectrum c), a bathochromic and hyperchromic shift of the DNA peak is observed.

Changes in the DNA absorption spectrum are usually related to complexation between  $\text{Ag}^+$  and DNA [147]. The addition of silver ions leads to the redistribution of the electron density in the nucleobases which is accompanied by corresponding spectral differences. Embedding of silver between two complementary bases leads to destabilization of the hydrogen bonds. Increased number of complexation sites can cause base stacking disorder followed by a partial denaturation upon exposure to UV-light, and thus a hyperchromic shift of the DNA absorption peak is observed. Also, no noticeable changes in the DNA spectrum in the absence of  $\text{Ag}^+$  were observed when the sample was exposed to UV.

The synthesized nanoparticles have been characterized by UV-Vis spectroscopy and transmission electron microscopy. For the typical UV spectroscopy measurements, 0.075 g of the sample have been diluted in 0.925 ml of 70% ethanol. The resulting viscous solution was measured in 1 cm quartz glass cuvettes. A sample without silver added was used as a reference. Due to a significant amount of the soft matter (DTADNA complex and  $\text{HP}\beta\text{CD}$ ), samples from the hexagonal and tetragonal liquid crystalline phases could not be measured by conventional TEM, even highly diluted. Therefore, for the TEM measurements nanoparticles must be separated from the residual soft matter. Figure 6.10 displays the absorption spectrum and TEM picture of nanoparticles, obtained in A1 10/40/50 after exposure to UV light for 60 minutes. A1 10/40/50 showed a coexistence of hexagonal and isotropic phase as confirmed by SAXS and  $^{31}\text{P}$  NMR measurements. No macroscopic phase separation was observed. The phase fractions were estimated by fitting the  $^{31}\text{P}$  NMR spectrum and was 57% for the hexagonal liquid crystalline and 43% for the isotropic phase (figure A.23).

Samples were slightly turbid due to the incomplete solubility of the DTADNA and Ag-DNA in ethanol which resulted in higher absorption compared to the reference sample. The broad SPR band is due to the coupling of surface plasmons between neighboring particles and large particles with a size of ca. 100 nm. However, such particles were not observed in the TEM micrographs (figure 6.10). The absorption band is split into a lower wavelength peak with a  $\lambda_{\text{max}} = 400$  nm attributed to isolated AgNP and a higher wavelength peak with  $\lambda_{\text{max}} = 448$  nm arising from the coupling of surface plasmons between neighboring particles and within particle aggregates indicating small interparticle distances. The absorption band at longer wavelength dominates over the shorter wavelength peak of isolated particles. According to TEM, the nanoparticles were in the range of 2–30 nm with an average size of  $9 \pm 3.7$  nm.

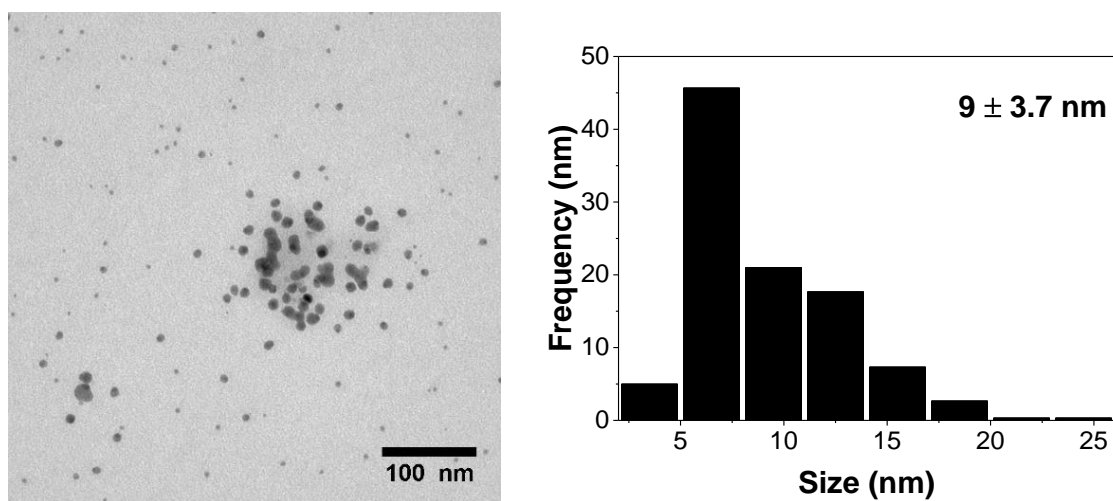
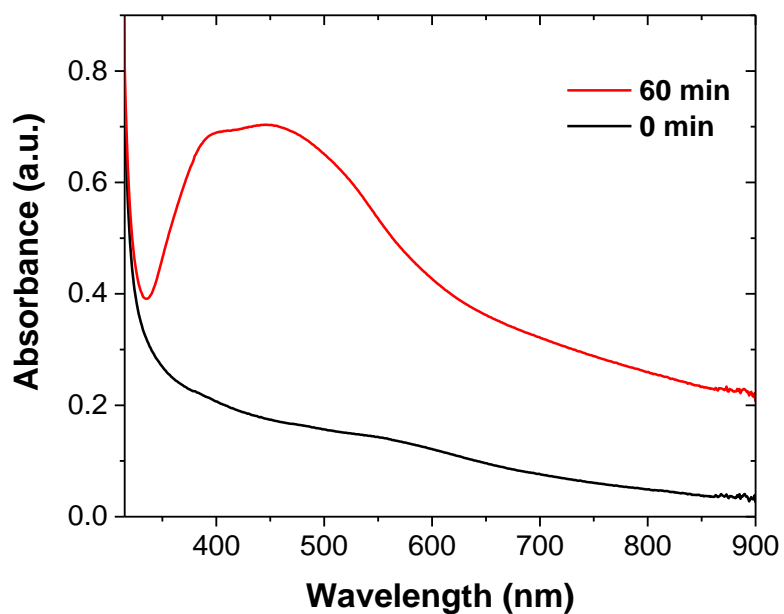


**Figure 6.10.** Top: UV-Vis absorption spectra of A1 10/40/50 before and after exposure to UV light for 60 minutes ( $[\text{Ag}^+]/[\text{DNA}_{\text{base}}]=0.252$ ). A sample without silver added was used as a reference. Bottom: TEM image (left) and size distribution histogram (right) of nanoparticles synthesized after exposure to UV light for 60 min.

Nanoparticles have been prepared in two additional samples from the hexagonal phase region of the phase diagram. Figure 6.11 presents the absorption spectra of silver nanoparticles synthesized in A1 15/35/50 and A1 18/41/41 after various irradiation times.

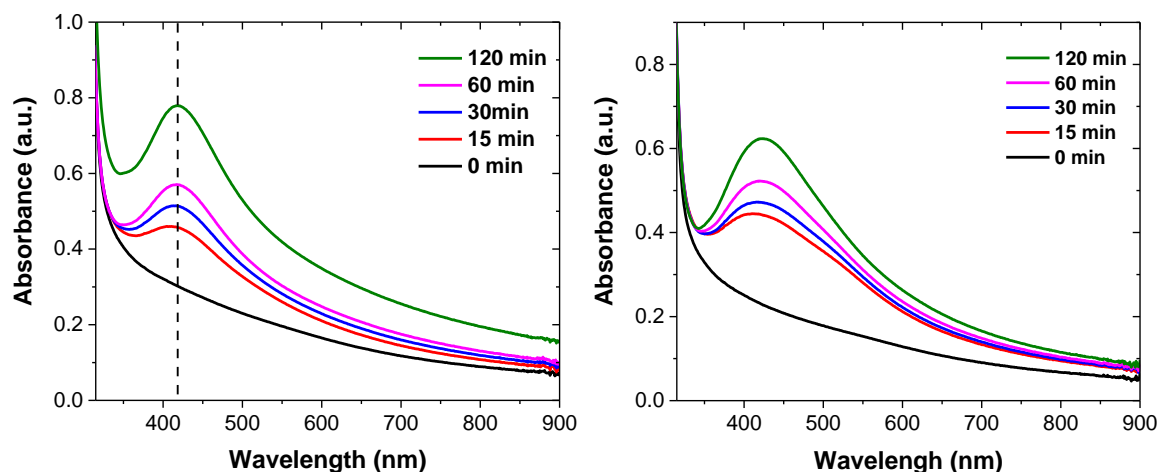


**Figure 6.11.** Dependence on the UV irradiation time A1 18/41/41 ( $[\text{Ag}^+]/[\text{DNA}_{\text{base}}]=0.115$ ) (left) and A1 15/35/50 ( $[\text{Ag}^+]/[\text{DNA}_{\text{base}}]=0.168$ ) (right). Reference spectra are subtracted.

Without UV irradiation samples did not show any surface plasmon resonance of silver nanoparticles. After 15 minutes of illumination, a broad peak appears with an absorption maximum at 418 or 424 nm for the samples with  $[\text{Ag}^+]/[\text{DNA}_{\text{base}}]=0.115$  and 0.168, respectively. The subsequent irradiation leads to an increase of intensity of the absorption band, which is attributed to an increase of the number of particles. The position of the absorption maximum was independent of the irradiation time, indicating that the morphology of nanoparticles remains unchanged throughout photoreduction synthesis. Because of the lower  $[\text{Ag}^+]/[\text{DNA}_{\text{base}}]$  ratio and bigger particle size, compared to A1 10/40/50 (cf. figure 6.10) a larger interparticle spacing and concomitant shift of the  $\lambda_{\text{max}}$  position is expected. This is indeed observed.

Figure 6.12. shows a typical TEM picture of nanoparticles obtained in A1 18/41/41 after 60 minutes of irradiation which are rather homogeneous in shape with a size in the range of 3–45 nm. Synthesis in A01 15/35/50 yields particles in the range of 2–40 nm (11.8 nm average), as shown in figure A.25. In addition to the isolated nanoparticles, nanoparticle chain assemblies on the DNA duplexes (figure A.25), which may explain the shift of the SPR position towards a slightly longer wavelength and peak broadening in comparison to A1 18/41/41. Due to the lower DNA concentration and higher  $[\text{Ag}^+]/[\text{DNA}_{\text{base}}]$  ratio, compared to A1 18/18/41 the absorption peak is red-shifted, despite the smaller particle size. The obtained dependence of the optical properties of the resulting nanoparticles on the  $[\text{Ag}^+]/[\text{DNA}_{\text{base}}]$  ratio is in good agreement with previously reported data presented in chapter 6.2.

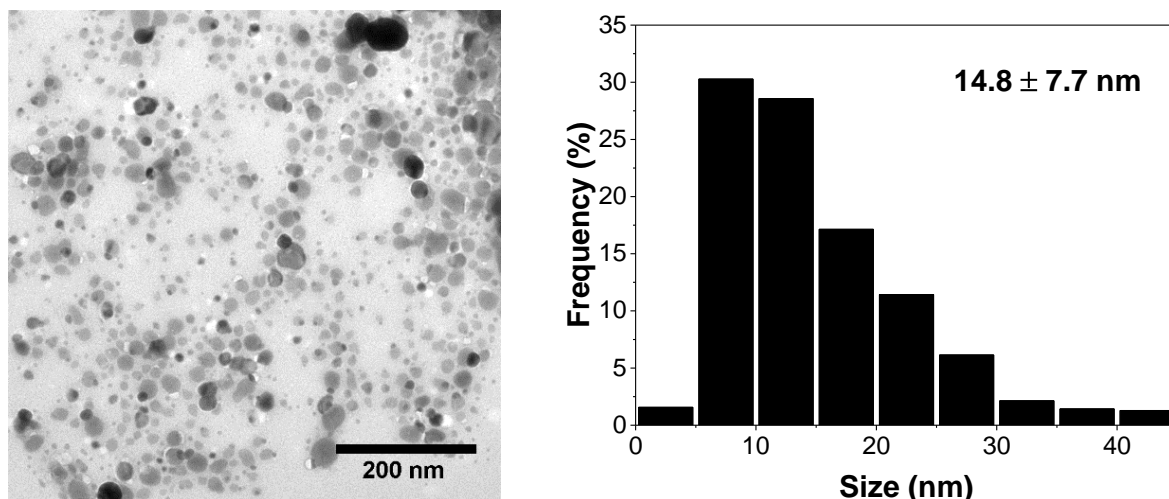


**Figure 6.12.** TEM image and corresponding size distribution of nanoparticles formed in the A1 18/41/41 (0.1M AgNO<sub>3</sub>) after 60 minutes of irradiation.

#### 6.4 Photoinduced formation of silver nanoparticles in the tetragonal phase

Samples of the tetragonal phase are viscous and turbid due to two coexisting phases. However, no macroscopic phase separation was observed. The SAXS pattern displays five Bragg peaks with a ratio of  $1:\sqrt{2}:\sqrt{3}:2:\sqrt{5}$ , attributed to the reflections from (100), (001), (110), (111) and (210) planes, respectively (figure 6.13). The peak positions in the SAXS diffractograms are almost independent of sample composition, which is in agreement with original data from Bilalov et al. [143]. The presence of an additional diffuse peak at  $q = 0.1\text{--}0.14 \text{ \AA}^{-1}$  suggests that samples consist of a mixture of two phases. The DNA interhelical spacing calculated from X-ray spectra is  $\sim 36 \text{ \AA}$  revealing a closer DNA packing compared to the hexagonal phase. Similar to the hexagonal phase, the tetragonal one shows a superposition of axially asymmetric <sup>31</sup>P CSA pattern of DNA and a narrow isotropic peak, indicating a coexistence of two phases in the sample. The content of the tetragonal phase was estimated by fitting <sup>31</sup>P NMR data and found to be approximately 87% for A 25/25/50 (figure A.24). The <sup>2</sup>H NMR spectrum of the tetragonal shown in figure 6.13 (right) is a Pake powder pattern with a splitting of 52.4 Hz.

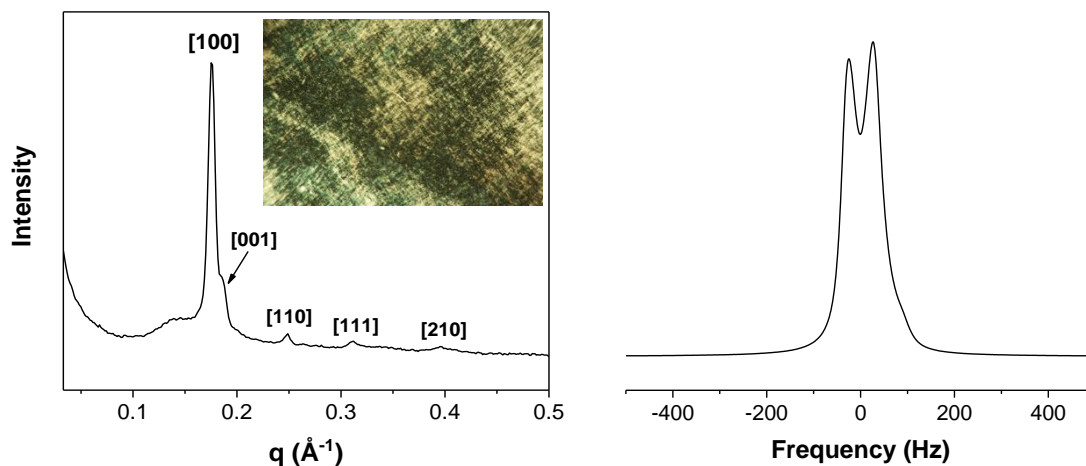


**Figure 6.13.** SAXS pattern (left) and  $^2\text{H}$  NMR spectrum (right) of A1 25/25/50 at 23°C. The inset shows a polarizing optical microscopy image of the tetragonal phase.

Formation of silver nanoparticles has been studied by transmission electron microscopy and UV-Vis spectroscopy. Figure 6.14 shows absorption spectra of samples before and after exposure to UV light for 1 hour and TEM pictures of nanoparticles synthesized in the tetragonal phase.

The UV-Vis spectra of nanoparticles obtained in the tetragonal phase show a broad absorption peak with a shoulder in the region of 350–650 nm. The first peak, located at 404 nm, is attributed to the small spherical nanoparticles with a size in the range of 2–15 nm (figure 6.14). The shoulder at 515 nm probably arises from chains of nanoparticles, resulting in the coupling of the surface plasmon resonance due to the small interparticle spacing [148]. However, since most nanoparticles are individual, the short-wavelength maximum is higher than the intensity of the long-wavelength absorption peak. Alternative reasons for the long-wavelength shoulder could be the presence of particles with a size of 60–100 nm or anisotropic nanoparticles.

Low contrast rod-like objects with different aspect ratio in the TEM pictures (figure 6.14) are DNA molecules. Since for the TEM analysis the liquid crystal was dissolved in ethanol and repeatedly sonicated, the remaining DNA could be fragmented. Taking into account that the diameter of dsDNA in its native B-form is  $\sim 20$  Å, and the objects in the TEM micrographs are much larger, it is reasonable to assume that most of the DNA exists in the form of supramolecular aggregates [149]. Due to the close packing of the DNA duplexes in the tetragonal phase, the growth of particles can exceed the dimension of the single DNA chain. The resulting silver nanoparticles self-assemble in the DNA molecules in the chain-like morphology, as shown in figure 6.14 (bottom row). The small DNA interhelical distance in the

tetragonal liquid crystalline samples resulted in the smaller nanoparticle spacing which is accompanied by broadening and splitting of the surface plasmon resonance. The chain formation of silver nanoparticles within DNA bundles is also in agreement with AFM measurements from chapter 6.3. A similar photoinduced formation of particle chain structures and metallic nanowires within DNA rods have been previously reported for Ag [150], Pd[70], Au [151], Cu [152], CdS [153].

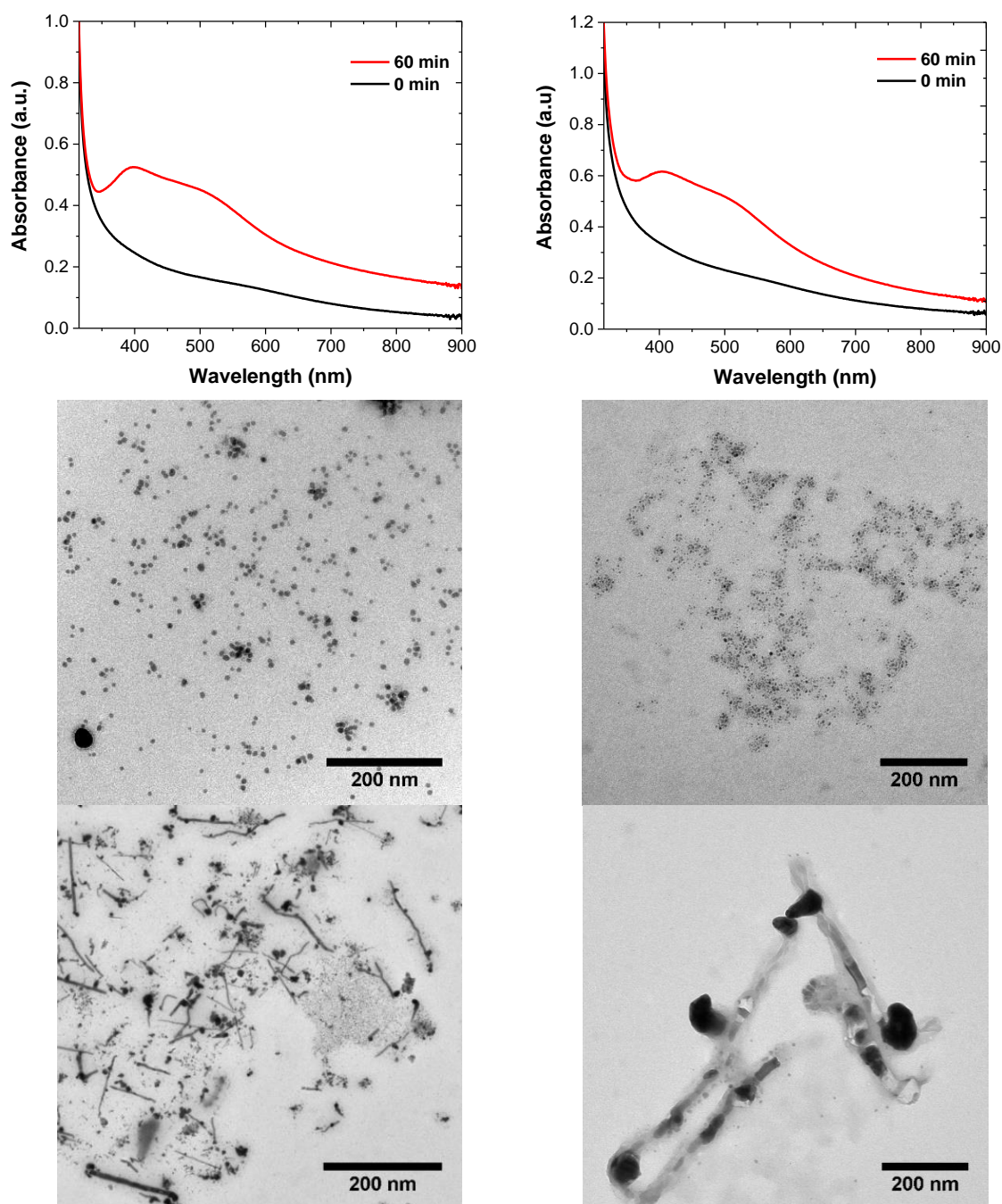


**Figure 6.14.** (Top) UV-Vis spectra of A1 17.5/25/57.5 (left) and A1 25/25/50 (right) before and after exposure to UV light for 1 hour. Reference spectra are subtracted. (Bottom) TEM micrographs showing individual particles and chain structures.

It should be noted that most of the soft matter was removed during sample centrifugation and purification required for the TEM sample preparation so the results of the TEM measurement may not represent the real-life situation. Nevertheless, the obtained TEM pictures are in good agreement with UV-Vis spectra depicting broad absorption peaks.

## 6.5 Summary

In the present chapter, we report the photochemical synthesis of silver nanoparticles in various lyotropic liquid crystalline phases formed by the dodecyltrimethylammonium-DNA complex in the presence of an aqueous solution of 2-hydroxypropyl- $\beta$ -cyclodextrin. Nanoparticles have been synthesized by UV irradiation of the liquid crystalline samples.

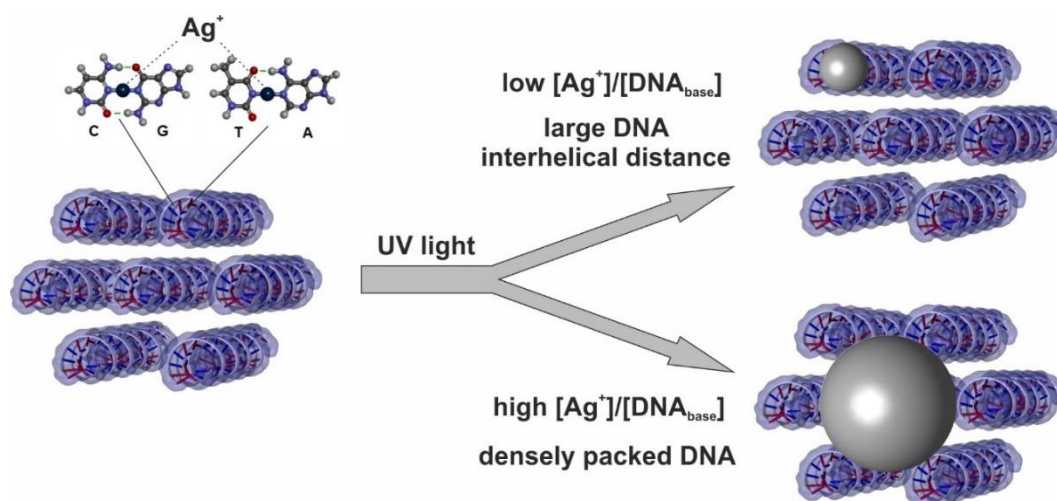


**Figure 6.15.** Schematic representation of photoinduced formation of two types of silver nanoparticles in DTADNA/HP $\beta$ CD/water system.

By studying the formation of particles in the isotropic solution the range of  $\text{Ag}^+$  concentration needed for the synthesis of nanoparticles was found. Only if the  $\text{Ag}^+$  concentration exceeds the critical ratio of  $[\text{Ag}^+]/[\text{DNA}_{\text{base}}]=0.05$  ratio is the nanoparticle formation initiated. Below this value, no surface plasmon resonance of silver nanoparticles was detected. The highest  $\text{Ag}^+$  concentration was limited to  $[\text{Ag}^+]/[\text{DNA}_{\text{base}}]=0.5$ . If the precursor concentration exceeds this ratio, phase separation occurs due to the precipitation of the Ag-DNA complex. When both conditions were satisfied, then neither an exposure of liquid crystals to UV light nor a formation of particles induced a phase transition or any significant changes in the liquid crystalline structure. In comparison with previously reported systems (chapter 3–5), no spontaneous

formation of silver nanoparticles was observed. Results of the control experiment demonstrate that in the absence of DNA or UV light no nanoparticles were formed.

Formation of silver nanoparticles in DNA duplexes was confirmed by AFM and TEM techniques. Depending on the liquid crystalline mesophase, different nanoparticle morphologies have been observed. A synthesis in isotropic and hexagonal phase at low ratio of  $[\text{Ag}^+]/[\text{DNA}_{\text{base}}]$  resulted mostly in the formation of spherical particles with a size of 2–50 nm. An increase of the  $[\text{Ag}^+]/[\text{DNA}_{\text{base}}]$  ratio in the hexagonal phase or use of the tetragonal phase lead to the synthesis of AgNP chains in DNA due to the close packing of the DNA in the liquid crystalline phase.

Due to the high viscosity of the liquid crystalline mesophases and formation of particles within DNA rods, the resulting nanoparticles obtained in hexagonal and tetragonal phases were stable over a period of at least 3 months. During this time neither a change of intensity or maximum position of the surface plasmon resonance nor a sedimentation was observed. A small amount of precipitated particles was found only in the isotropic phase after several months of storage.

## 7 Conclusion and outlook

In the final chapter of this thesis, we review the main results of our experiments and discuss the direction of future work in the synthesis of silver nanoparticles and, in particular, in DNA-containing liquid crystals and their use as templates for synthesis of metallic nanoparticles.

We report the chemical and photochemical synthesis of silver nanoparticles in various lyotropic liquid crystalline phases formed by biologically-friendly surfactants like monoolein and lecithin with and without dodecyltrimethylammonium-DNA complex. Also, nanoparticles were obtained in liquid crystalline mesophases formed by the DTADNA complex in the presence of an aqueous solution of 2-hydroxypropyl- $\beta$ -cyclodextrin. In all cases, silver ions were reduced by components contained in the system, no additional reductants were employed. In total, four different systems have been investigated as potential templates for the nanoparticle preparation. Composition, phase behavior and preparative methods are summarized in table 7.1.

**Table 7.1.** Overview of the systems used for the synthesis of silver nanoparticles (I – isotropic phase, Q – bicontinuous cubic,  $L_\alpha$  – lamellar, H – hexagonal,  $H_{II}$  – inverse hexagonal, T – tetragonal liquid crystalline phases).

Composition	Method of synthesis	Liquid crystalline phase					
		I	Q	$L_\alpha$	H	$H_{II}$	T
GMO/TAG/water	Chemical		+	+		+	
DTADNA/GMO/water	Chemical		+			+	
	Photochemical						
DTADNA/Lecithin/water	Chemical			+		+	
	Photochemical						
DTADNA/HP $\beta$ CD/water	Photochemical	+			+		+

Two different protocols have been utilized for the nanoparticle preparation. At first, nanoparticles have been synthesized by reduction of silver ions with either lecithin or monoolein. It was shown that monoolein and lecithin act both as a reducing agent as well as a template for the particle formation. Monoolein can take part in the polyol-type redox reaction, where alcohol groups of the GMO are oxidized upon silver ion reduction. The obtained particles consist of two sets of AgNP with different morphologies, mono- and polycrystalline spherical particles with a size of 3–40 nm, and plate-like particles with various shapes. The average size of the resulting nanoparticles was approximately 4–5 times larger than the dimensions of the aqueous domains of the liquid crystalline phase. Interestingly, the average size of nanoparticles was almost independent of the  $Ag^+$  concentration and the template structure. Despite the similar

particle size, the optical properties of the resulting reaction mixtures were strongly affected by the presence of platelets and particle aggregates.

In the case of lecithin, the detailed mechanism of synthesis is still unknown, and further investigation is necessary. The size of the obtained nanoparticles varied in the range of 5–55 nm. The increase of the AgNO<sub>3</sub> concentration and aging time resulted in the formation of spherical aggregates with the dimensions of 80–200 nm.

Preparation of particles in the monoolein-based liquid crystals does not have a significant effect on the liquid crystalline mesophase, as was demonstrated with small angle X-ray scattering. However, the formation of particles may affect the long-term stability of the liquid crystals. It was shown, that formation and presence of AgNP may facilitate the hydrolysis of the lipid, inducing the cubic to inverse hexagonal phase transition. In the case of the lecithin/water binary system, the metal-assisted hydrolysis of phosphatidylcholine leads to lysophosphatidylcholine and free carboxylic acid, which induces the phase transition from the lamellar to an isotropic micellar phase, as demonstrated by <sup>31</sup>P NMR spectroscopy.

Secondly, nanoparticles have been synthesized by UV irradiation of DNA-containing liquid crystals where DNA acts as templating and a photosensitizing agent. At the first stage, a Ag-DNA complex is formed by embedding of silver ions into the double helix. Due to the specific Ag–nucleotide interaction silver binds exclusively to the nucleobases. Illumination of this complex with UV light that is absorbed by the nucleobases induced the formation of nanoparticles within the DNA double helix. The photoinduced synthesis typically resulted in spherical particles with a size in the range of 3–55 nm, similar to the particles produced in the binary system. Besides isolated particles, two different particle aggregates were observed in the DTADNA/lecithin/water system: quasispherical aggregates with the dimensions of 80–200 nm and submicrometer-sized dendrite fractal aggregates.

The spontaneous formation of silver nanoparticles was also observed in DNA-containing liquid crystals. However, due to the embedding of the silver ions in the dsDNA, this process was considerably slower than for the samples without DNA. In comparison to the DTADNA-free system, no formation of plate-like particles was observed in DNA-containing monoolein-based cubic phases at low Ag<sup>+</sup> concentration. The initial liquid crystalline phase was maintained upon nanoparticle formation for at least six months after particle preparation.

It was also shown that in the inverse hexagonal and lamellar phases of the DTADNA/lecithin/water system spontaneous formation of nanoparticles was observed due the

long time required for the preparation and equilibration of the samples. Analogously to the DNA-free system, nanoparticle preparation resulted in the partial hydrolysis of lecithin, leading to the formation of the second phase. Only one sample has been studied so far, and this process should be investigated in more detail.

In comparison to the other systems, the synthesis of nanoparticles in the DTADNA/HP $\beta$ CD/D<sub>2</sub>O system does not result in the spontaneous formation of AgNP, at least on the time scale of the sample preparation and experiment. By controlling the liquid crystalline phase and the  $[\text{Ag}^+]/[\text{DNA}_{\text{base}}]$  ratio, two nanoparticle structures can be obtained. An increase of the  $\text{Ag}^+$  concentration and DNA packing leads to the formation of silver nanochains within DNA molecules. On the other hand, relatively small  $\text{Ag}^+$  and DNA concentrations result in small isolated nanospheres with a size in the range of 2–50 nm. Beyond the ratio of  $[\text{Ag}^+]/[\text{DNA}_{\text{base}}] = 0.05$  no absorption band of silver nanoparticles has been detected. An increase of the  $[\text{Ag}^+]/[\text{DNA}_{\text{base}}]$  ratio to 0.5 and more resulted in precipitation of the Ag-DNA complex from the solution. The photoinduced formation of silver nanoparticles in DTADNA/HP $\beta$ CD/water did not have a significant effect on the liquid crystalline mesophase.

Illumination of the DNA-containing liquid crystalline phases to UV light does not affect the DNA structure. It was shown that irradiation of the samples containing monoolein or lecithin might cause photodegradation of the surfactant molecules. However, it seems to have little or no effect on the liquid crystalline mesophase. The possible photo- and peroxidation processes are not yet fully understood and require some additional measurements.

The stability of the resulting colloids strongly depends on the initial viscosity and the structure of the liquid crystalline phase. For the nanoparticles synthesized in DNA-containing liquid crystals, no significant shift or intensity change of the surface resonance band was detected after 2–4 months. In the case of nanoparticles formed in aqueous monoolein and lecithin systems, particle sedimentation was observed after 4–6 weeks.

As a possible continuation of this project, the reported chemical and photoinduced formation of metallic nanoparticles can be applied to the synthesis of different metals, in particular, gold and copper. It has been previously shown, that Au-DNA interaction results in the specific binding of gold atoms to the phosphate moiety. In comparison, complexation between copper and DNA occurs due to the binding of  $\text{Cu}^{2+}$  with a phosphate group and nucleobases (at high  $\text{Cu}^{2+}$  concentration). Moreover, by optimizing the  $[\text{Ag}^+]/[\text{DNA}_{\text{base}}]$  ratio or by using DNA with

a well-defined base sequence, the complete DNA metallization can be obtained resulting in the formation of silver nanorods and nanowires.

Preparation of the nanoparticles in GMO/water binary system can be reproduced at different temperatures to obtain insights of the kinetics and mechanism of nanoparticle formation, in particular of the anisotropic particles. Also, other surfactant systems can be studied as potential templates for the nanoparticle synthesis. Finally, it would also be interesting to test lyotropic liquid crystals not only as templates but also as matrixes for the alignment of metallic nanoparticles.

## **Appendix**

### **A1 Experimental procedures**

#### **Sample preparation**

##### **Preparation of the DTA-DNA complex**

DNA–surfactant aggregates were prepared by mixing equal molar amounts of negative charges of DNA and positive charges of DTA, as reported by Bilalov [143]. An appropriate amount of the DNA was dissolved in 0.01 M NaBr (pH=7) and mixed using a magnetic stirrer at 4°C for 24 hours. Then a water solution of DTAB (0.05 M) was added and the complex was mixed with a magnetic stirrer for 48 hours. The resulting precipitate was filtered through a Büchner funnel, washed extensively with Millipore water, frozen with liquid nitrogen and freeze-dried for 5 days. Until needed, the complex was stored at 4°C.

##### **Preparation of the GMO/D<sub>2</sub>O, GMO/TAG/D<sub>2</sub>O, GMO/DTADNA/D<sub>2</sub>O samples**

The samples of the binary monoolein/water system were prepared by the procedure described in [103]. A syringe-based lipid mixer was loaded with melted GMO and silver nitrate solution in D<sub>2</sub>O (or in pure D<sub>2</sub>O). Samples containing the DTADNA complex have been incubated with water or silver nitrate solution for 12–48 hours prior to the mixing with GMO. Typically, 100–250 cycles were performed to obtain a homogeneous sample. After preparation samples were kept in the dark.

##### **Preparation of the DTADNA/HPβCD/water and DTADNA/lecithin/water systems**

The desired amount of the DTADNA and D<sub>2</sub>O (or silver nitrate solution in D<sub>2</sub>O) were weighed in to the sample tubes (5 or 8 mm outer diameter) and mixed overnight. After incubation for 12–48 hours, 2-hydroxypropyl-β-cyclodextrin (or lecithin) was added and tubes were immediately flame-sealed. After sealing, samples were mixed with a vortex mixer and centrifuged back and forth at 7000 rpm at room temperature for one week. The samples were finally left to equilibrate in the dark at room temperature for 2–7 days prior to the analysis.

## Techniques

### Nuclear Magnetic Resonance

$^1\text{H}$ ,  $^2\text{H}$ ,  $^{13}\text{C}$  and  $^{31}\text{P}$  solid state NMR measurements were performed on a Tecmag Apollo spectrometer operated at 299.809 MHz, 75.348 MHz, 42.022 MHz, and 121.384 MHz respectively. A standard temperature control unit was used (accuracy of  $\pm 0.5$  °C). The samples were thermally equilibrated for at least 1 day at the desired temperature prior to the measurements. For temperature-dependent measurements the samples were equilibrated for 25 minutes for a given temperature. A heating rate of 0.2 °C/min was typically chosen.

$^{31}\text{P}$  NMR spectra were measured using a spin echo pulse sequence with inverse gated proton decoupling. Typical spectra were acquired from 512–8096 repetitions with a recycle delay of 5 seconds at static conditions. Chemical shift was adjusted by calcium hydroxyapatite (2.3 ppm relative to orthophosphoric acid).  $^{13}\text{C}$  NMR measurements were acquired using an inverse gated 90° pulse sequence. Chemical shift was calibrated using the secondary carbon atom of adamantane (38 ppm). Typically, 2048–4096 spectra with a recycle delay of 5 seconds were averaged.  $^2\text{H}$  spectra were measured with a quadrupole echo pulse sequence. Usually, 64–256 scans were averaged.

$^1\text{H}$ ,  $^{13}\text{C}$  and  $^{31}\text{P}$  solution NMR measurements were carried out on a Bruker Avance 500 MHz spectrometer, operated at 500.13, 125.76, and 202.46 MHz, respectively. A standard Bruker ZG 30 pulse sequence was used.

### Polarizing optical microscopy

Polarizing optical microscopy was performed using a Leitz Ortholux II microscope equipped with a Linkam CSS 450 shear cell and a Leica microscope equipped with a temperature cell. The resulting pictures of the liquid crystalline phases were later compared with typical LC patterns.

### Small angle X-ray scattering

Small angle X-ray scattering was measured with a Xenocs Xeuss SAXS instrument operated at 50 kV and 0.6 A. Cu  $K_\alpha$  radiation of wavelength 1.54 Å was provided by an X-ray generator PANalytical, PW 3830A. To minimize scattering from air, the camera volume was kept under vacuum during the measurements. The 2D patterns were recorded with a Dectris Pilatus 300K detector and processed using Fit2D software provided by Dr. A. Hammersley

(<http://www.esrf.fr/computing/scientific/FIT2D>). Silver behenate ( $\text{CH}_3\text{-(CH}_2\text{)}_{20}\text{-CH}_2\text{-COOAg}$ ) with a  $d$  spacing of 58.38 Å was used for the  $q$  space calibration. Samples were measured in 1 mm glass capillaries (Hilgenberg) or in home-built stainless-steel sample holders closed to the environment by a thin Kapton polyimide film at room temperature (22 °C). Scattering patterns were typically recorded for 600–1200 s.

### **Atomic force microscopy**

AFM imaging was performed in air using a JPK Nanowizard III AFM operating in the tapping mode and HQ:NSC15/Al BS cantilevers from MikroMasch. DNA was extracted from the liquid crystal by using a modified ethanol precipitation method [154]. 0.01 g of sample was dissolved in 1 ml of 70% ethanol and mixed on a vortex mixer for 3 minutes. Then, 0.2 ml of 3 M sodium acetate (pH=5.2) was added and samples were placed for 1 hour in the freezer. After cooling, samples were centrifuged for 3 minutes at 1000 rpm and the supernatant was discarded. The procedure was repeated twice using 70% and absolute ethanol. After the last removal of ethanol, the precipitate was dried in air for 15 minutes and dissolved in 10 mM 4-(2-hydroxyethyl)piperazine-1-ethanesulfonic acid (HEPES) buffer. The concentration of the extracted DNA was determined by UV-Vis spectroscopy. For AFM imaging, samples were diluted to a concentration of 1-5 µg/ml with buffer containing 20 mM HEPES and 5 mM  $\text{NiCl}_2$ . DNA was immobilized on freshly cleaved mica by putting 30 µl of the solution on the mica surface and incubating for 5 minutes. The buffer solution was removed by washing with 2 ml of distilled water and drying with nitrogen.

### **Transmission electron microscopy**

Transmission Electron Microscopy images were taken with a Philips CM200 STEM at the Paderborn University and a Philips CM100 TEM at the Bielefeld University. Photomicrographs were obtained at 200 kV or 80 kV and various magnifications. For a typical sample preparation, a small amount of liquid crystal was diluted in an appropriate type of solvent and particles were collected via centrifugation and redispersed in ethanol or water. The procedure was repeated several times to remove surfactant and unreduced silver solutions. Then, 5 µl of the final solution were placed onto a carbon coated copper TEM grid (300 mesh, Microscopy Science) and dried at room temperature. Nanoparticle size and size distribution were calculated by image analysis of 200–1000 particles using ImageJ software (National Institute of Health, USA). Due to the variety of shapes, the size of the plate-like particles was measured by height or diameter for nanodisks and nanoprisms, respectively.

### **Freeze-fracture electron microscopy**

A replica of the cubic Ia3d phase (70 wt. % GMO/30 wt.% 0.01 M AgNO<sub>3</sub>) was prepared using the Freeze Fracture and Etching System EM BAF060 from Leica at the Stuttgart University. A small amount of the cubic phase was sandwiched between two copper plates, frozen with liquid ethane and fractured in liquid N<sub>2</sub>. Specimen was shadowed with platinum–carbon (~2 nm) at 45° and subsequently covered by a layer of pure carbon (~20 nm) at 90°. Liquid crystal and silver nanoparticles were removed from the replica by washing it with ethanol and chloroform. After the replica preparation, it was placed on a copper grid and inspected with a transmission electron microscope Techai G2 Sphera (Fei) operated at 200 kV.

### **Scanning electron microscopy**

A Zeiss Neon 40 scanning electron microscope (AK Bremser, Technical chemistry department, Paderborn University) was used for the imaging of the silver carboxylate crystals. Samples were prepared by the drop casting of the silver carboxylate/AgNP dispersion in ethanol on carbon tape and drying overnight in vacuum at 30 °C.

### **Fourier transform infrared spectroscopy**

A Bruker Vertex 80 spectrometer, equipped with a single reflection ATR sampling module was used to record FTIR spectra. The spectra were recorded with 16 scans, with a spectral resolution of 2 cm<sup>-1</sup>, at room temperature (22 °C).

### **UV-VIS spectroscopy**

Ultraviolet-visible spectroscopy measurements were performed on a Perkin Elmer Lambda 19 double-beam spectrometer operating in the 190-4000 nm wavelength range at room temperature (22 °C). Depending on the experiment, quartz or optical glass cuvettes with a pathway of 0.1–10 mm were used.

### **Photoinduced formation of silver nanoparticles**

For the photoinduced synthesis of nanoparticles, samples were placed 20 cm apart from the UV lamp (Dr. Hönle UVASPOT 400F, 400 W input power) resulting in irradiance of 20 mW/cm<sup>2</sup> (UVA). Air cooling was used to prevent samples from heating. The exposure time was controlled from several minutes to several hours. The emission spectrum of the UV lamp is shown in figure A.1. As alternative lamp, a low power Desaga minUVIS lamp (8 W, 254 and

366 nm) was used to study the influence of the irradiation wavelength for the DNA-containing monoolein-based samples (chapter 4.4).

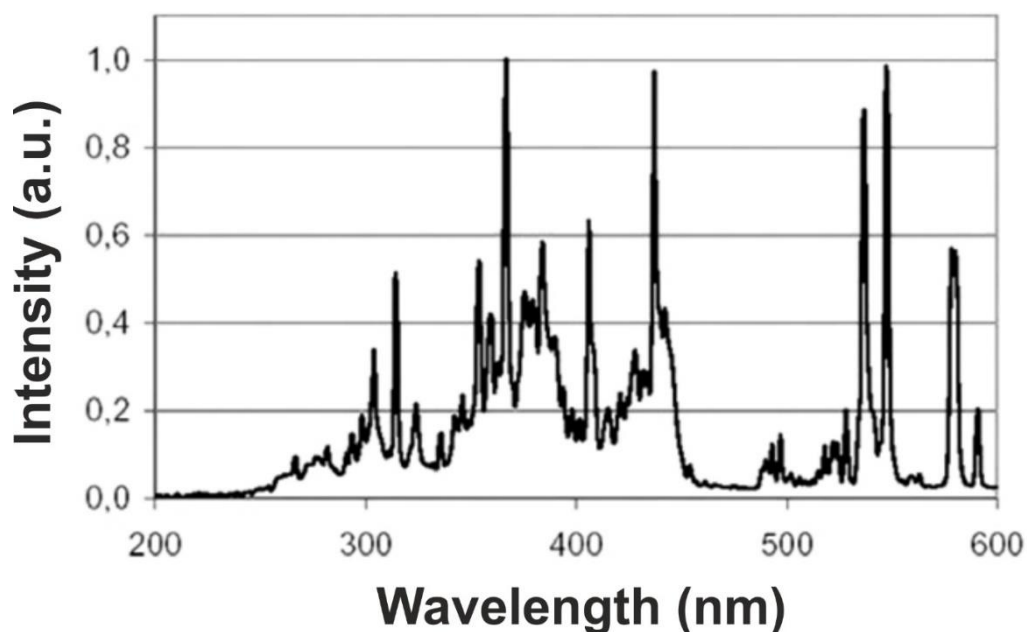


**Figure. A.1.** Standard spectrum of the Dr. Hönle UVASPOT 400F lamp [155].

Simulation of the UV-Vis spectra of the silver nanoparticles was performed using the Boundary Element Method (BEM), developed by Garcia de Abajo [156]. The MNPBEM software package written for Matlab was used [157]. The dielectric function of silver was taken from the Handbook of Optical Constants of Solids [158].

## Chemicals

Dodecyltrimethylammonium bromide ( $\geq 98\%$ ), hydroxypropyl- $\beta$ -cyclodextrin (molar suaverage molecular weight 1540 g/mol, 1 hydroxypropyl group per glucose unit),  $\beta$ -cyclodextrin ( $\geq 97\%$ ), ethanol ( $\geq 99.8\%$ ), glycerol tricaprylate ( $\geq 99\%$ ), octanoic acid ( $\geq 99\%$ ), sodium octanoate ( $\geq 99\%$ ), HEPES ( $\geq 99.5\%$ ), nickel (II) chloride (98%), and decanol ( $\geq 99\%$ ) were purchased from Sigma-Aldrich.

Deuterium oxide (99%) was obtained from Cambridge Isotope Lab.  $\text{CDCl}_3$  (99.8%) was purchased from Deutero GmbH.

Monoolein (Rylo MG19 Pharma) was kindly provided by Danisco. It has the following composition according to the certificate of analysis: 96% monoglyceride, 4% diglyceride, 0.1%

free glycerin, fatty acid composition: 0.2% C<sub>16</sub>, 2.7% C<sub>18</sub>, 90% C<sub>18:1</sub>, 4.3% C<sub>18:2</sub>, 0.7% C<sub>18:3</sub>, 0% C<sub>20</sub>, 1.5% C<sub>20:1</sub>.

Soybean lecithin (Epikuron 200, average molecular mass 772 g/mol) was purchased from Cargill Deutschland GmbH. According to the supplier information, it contains a minimum of 92% phosphatidylcholine (PC, 1,2-diacyl-sn-glycero-3-phosphocholine) and a maximum of 3% lysophosphatidylcholine, 2% other phospholipids, 2% triglycerides. The fatty acid composition is 75-81% polyunsaturated, of which 68-72% are C<sub>18:2</sub> (n-6), 7-9% C<sub>18:3</sub> (n-3), 6-8% mono-unsaturated, and 13-17% saturated. It is stabilized with 0.2%  $\alpha$ -tocopherol.

Deoxyribonucleic acid sodium salt was purchased from Sigma-Aldrich. Earlier batches were examined by Bilalov et al. [159]. The results show that it is a polydispersed mixture of dsDNA with an average molecular mass of 700 bp, estimated by electrophoresis. The A<sub>260</sub>/A<sub>280</sub> ratio was measured with UV-Vis spectroscopy and was found to be 1.8, suggesting that DNA is free of proteins [160].

Unless indicated, all chemicals were used as received, without further purification.

## A2 Synthesis of silver nanoparticles in the ternary systems sodium octanoate/octanoic acid/water and sodium octanoate/decanol/water

As a possible photoreduction matrix the ternary systems containing sodium octanoate ( $\text{NaC}_8$ ) as a surfactant,  $\text{D}_2\text{O}$  and either octanoic acid ( $\text{HC}_8$ ) as cosurfactant or decanol as an oil component were chosen. For the synthesis of silver nanoparticles,  $\text{AgNO}_3$  solution in  $\text{D}_2\text{O}$  was used. The ternary phase diagrams have been established by some of the pioneers in the chemistry of lyotropic liquid crystals, Per Ekwall and Leo Mandell [161] and are shown in figure A.2. The system  $\text{NaC}_8/\text{HC}_8/\text{H}_2\text{O}$  shows a phase sequence par excellence. It has two isotropic solution regions,  $L_1$  and  $L_2$ , two liquid crystalline phases with two-dimensional hexagonal structure (E and F), and in the center of the diagram a large lamellar liquid crystalline region (D). Samples from all liquid crystalline phases were prepared. For the synthesis of silver nanoparticles  $\text{D}_2\text{O}$  was replaced by  $\text{AgNO}_3$  solution.

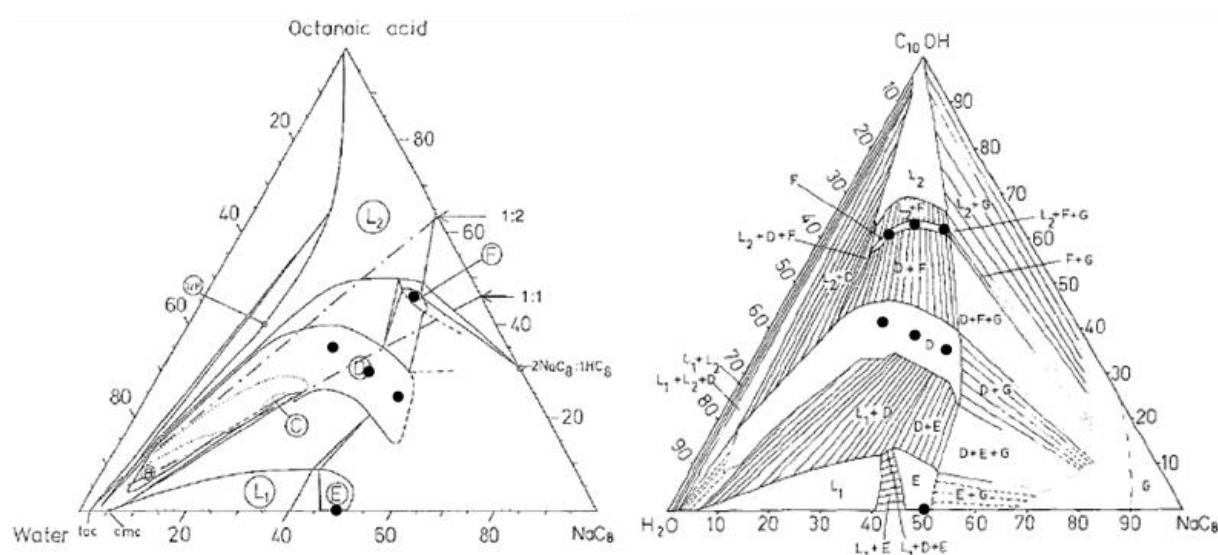


**Figure A.2.** Ternary phase diagrams of sodium octanoate/octanoic acid/water (left) and sodium octanoate/decanol/water (right) at 20 °C [161].  $L_1$  and  $L_2$ : isotropic solution regions, micellar and inverse micellar, respectively. E and F: liquid crystalline two-dimensional hexagonal phase regions, normal and inverse, respectively. B, C and D: sub-regions of the liquid crystalline one-dimensional lamellar phase. The black dots represent prepared samples.

The prepared samples are viscous with a glassy appearance. The liquid crystalline phase was investigated by polarizing microscopy and by  $^2\text{H}$  NMR at 20 °C. As can be seen in figure A.3, samples show birefringence when examined between crossed polarizers, and exhibit an ordered fanlike texture (A) or nongeometric striated texture (B) which is characteristic of a hexagonal

phase (inverse and normal) as previously shown by Rosevear [104]. The  $^2\text{H}$  NMR spectra show Pake powder patterns, characteristic of the hexagonal phases. In the case of the  $\text{H}_{\text{II}}$  phase, the powder pattern is superimposed by a doublet, which has a splitting corresponding to the full width of the powder pattern. This is due to a partial alignment of the sample with its hexagonal axis parallel to the magnetic field [162].

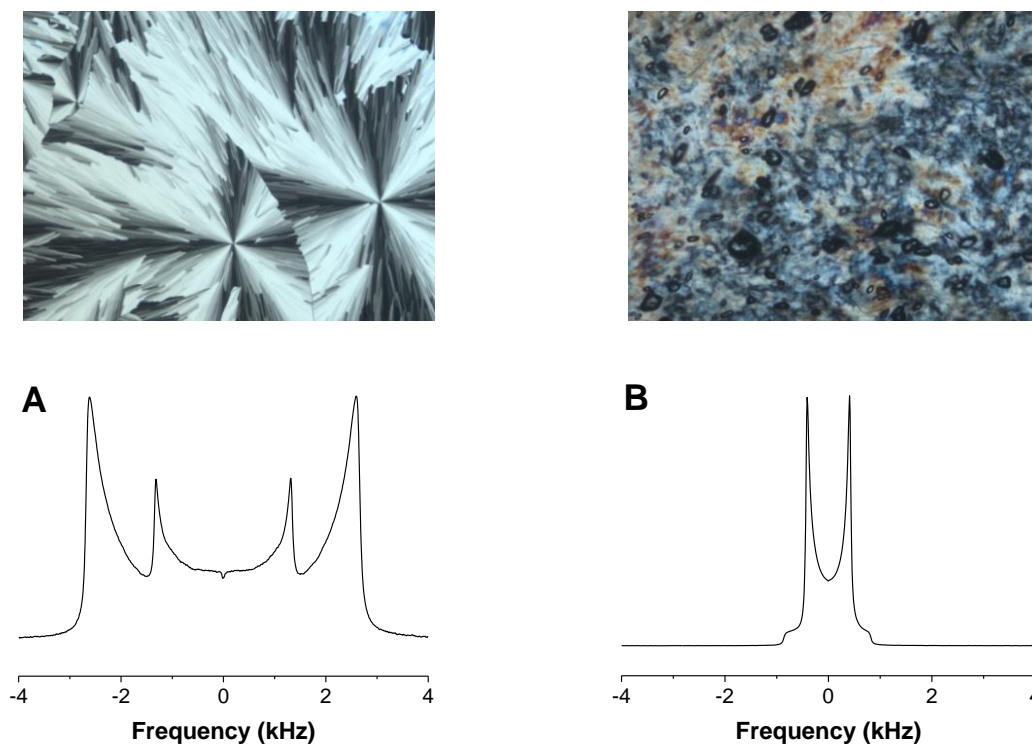


**Figure A.3.** Polarizing optical microscopy images (top) and  $^2\text{H}$  NMR spectra (bottom) of (A) 39.6 wt.%  $\text{NaC}_8$ /46.9 wt.%  $\text{HC}_8$ /13.5 wt.% 0,01 M  $\text{AgNO}_3$  ( $\text{H}_{\text{II}}$  phase), (B) 50 wt.%  $\text{NaC}_8$ /50 wt.% 0,01 M  $\text{AgNO}_3$  ( $\text{H}_{\text{I}}$  phase).

To generate nanoparticles, liquid crystalline samples were exposed to UV light using a high-pressure mercury lamp for 1–30 min. Figure A.4 shows the dependence of UV-Vis spectra of  $\text{NaC}_8/\text{HC}_8/0.01$  M  $\text{AgNO}_3$  on irradiation time in the range of 300–800 nm. After the samples were illuminated for 1 minute, a broad absorption band appears in the region of 350–600 nm, indicating the formation of nanosized particles. Further irradiation of the samples shows dramatic changes in the UV-Vis spectra. The possible explanation will be discussed later.

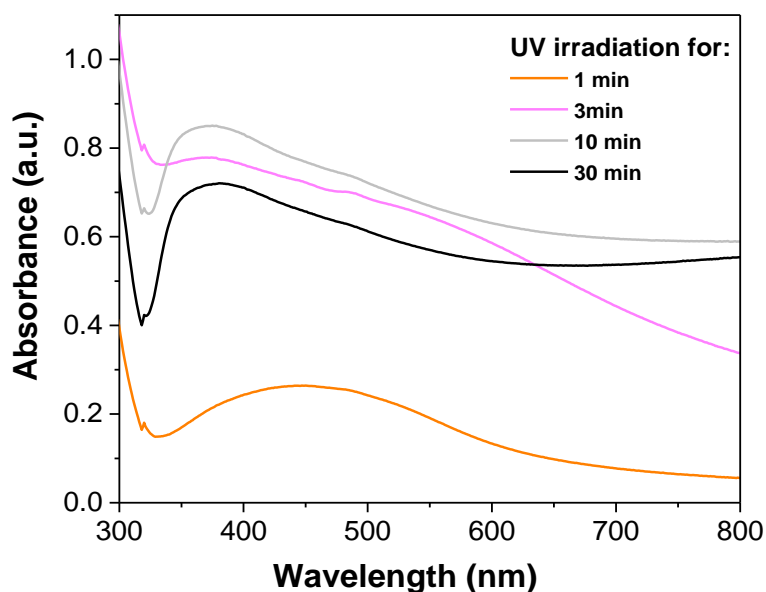


**Figure A.4.** UV-vis spectra of NaC<sub>8</sub>/decanol/0,01M AgNO<sub>3</sub> after UV irradiation.

Also, for samples containing silver solution the formation of needle-like crystals was observed, even without UV irradiation, as can be seen in figure A.5. This is the result of a metathesis reaction between sodium octanoate and silver nitrate, which leads to the formation of the silver salt of carboxylic acid as reported in several publications [163].

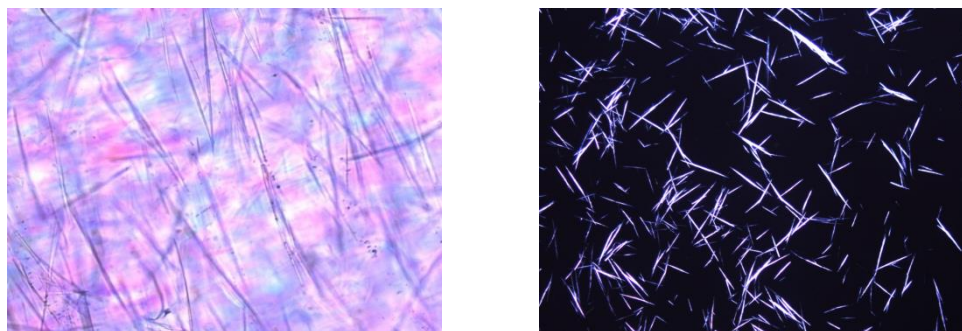
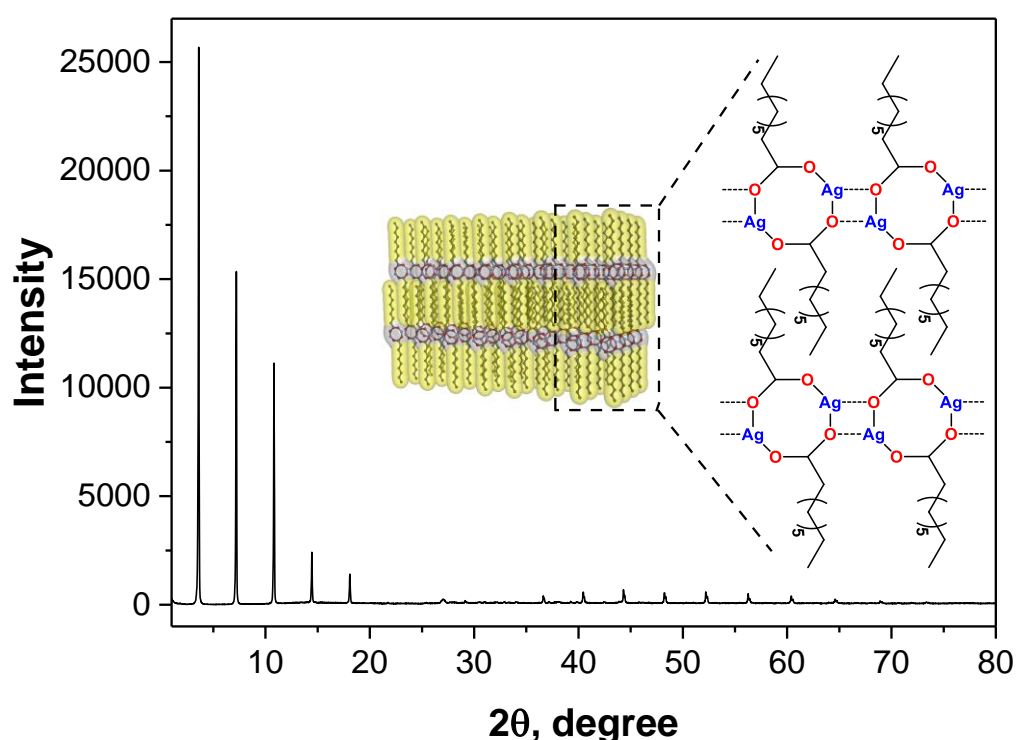


**Figure A.5.** Polarizing optical microscopy images of silver octanoate (crossed polarizers): in the liquid crystalline state (left), dispersed in methanol (right).

Silver carboxylates, so-called silver soap, have been used in the photography industry and are known to have a unique solid-state arrangement of the silver atoms in a layer, as shown in figure A.6. Tolochko et al. refined the structure of silver carboxylates by using EXAFS data unit cell parameters obtained from X-ray powder data [164]. They found that in the solid-state the silver atoms are connected by the bridging carboxylates in the form of eight-membered rings, which are linked to each other by long Ag-O bonds generating a polymeric chain.

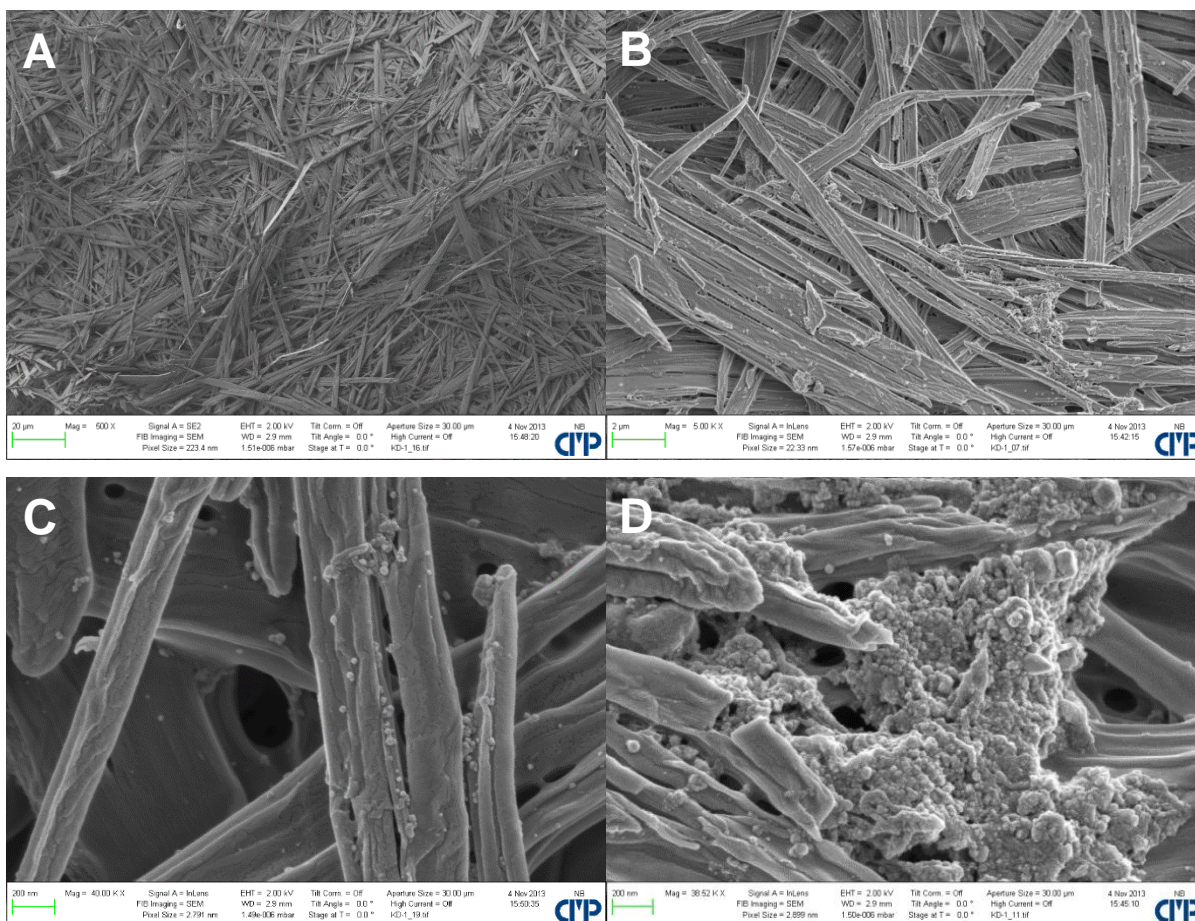
The solid product was collected, purified and investigated with X-ray diffraction and scanning electron microscopy. The X-ray diffraction pattern of silver octanoate shows well-developed intense (00 $l$ ) reflection peaks attributable to the regularly stacked Ag(I) carboxylate layers. The interlayer spacing calculated from the Bragg equation is 2.45 nm, which is slightly smaller than twice the length of the carboxylate chain.

The crystalline domain size calculated from the Scherrer formula is 114.2 nm, indicating that silver octanoate has crystalline domains much larger than the unit cell. These values are in good agreement with the data reported in the literature [165].



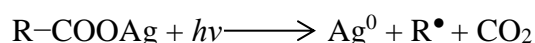
**Figure A.6.** X-ray diffraction pattern of silver octanoate. Inset shows the schematic representation of crystalline structure of silver octanoate, redrawn according to ref [165].

Figure A.7 shows scanning electron micrographs of the silver octanoate obtained. As can be seen in figure A.7 (A, B) the crystals are plate- or needle-shaped with a length of 10-60  $\mu\text{m}$  and a width of 0.2-3  $\mu\text{m}$ . However, at higher magnification (figure A.7 C, D) some spherical particles were observed. They may be the result of a partial photodecomposition of silver carboxylate during the sample preparation and UV-irradiation.



**Figure A.7.** Scanning electron microscopy images of silver octanoate at different magnification.

The thermal and photochemical decomposition of silver carboxylates has been studied by Bokhonov et al. [166]. The photochemical decomposition occurs according to



The obtained silver atoms aggregate into metallic particles, and hydrocarbon radicals mainly recombine resulting in formation of alkane. The partial decomposition of silver octanoate may explain the appearance of the absorption band in figure A.4. Further irradiation increases the degree of decomposition and leads to formation of sub-micrometer particles, which aggregate into bigger clusters of micrometer size. After 30 minutes of irradiation, no more needle-like crystals were observed.

The described systems were not further investigated because of their inability to act as photoreduction matrix for the synthesis of silver nanoparticles.

### A3 Additional data

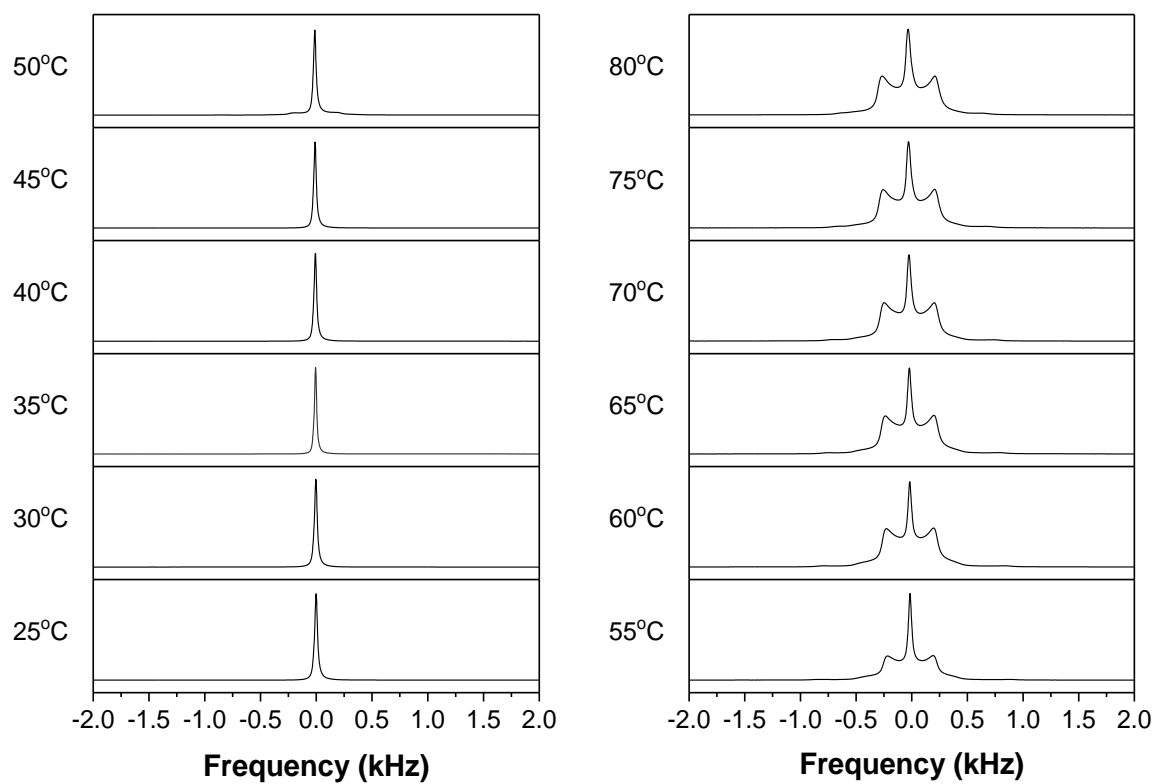


**Figure A.8.** Temperature dependence of the 70 wt.% GMO/30 wt.%  $\text{D}_2\text{O}$  (cubic  $\text{Ia}3\text{d}$  phase), measured with  $^2\text{H}$  NMR spectroscopy.

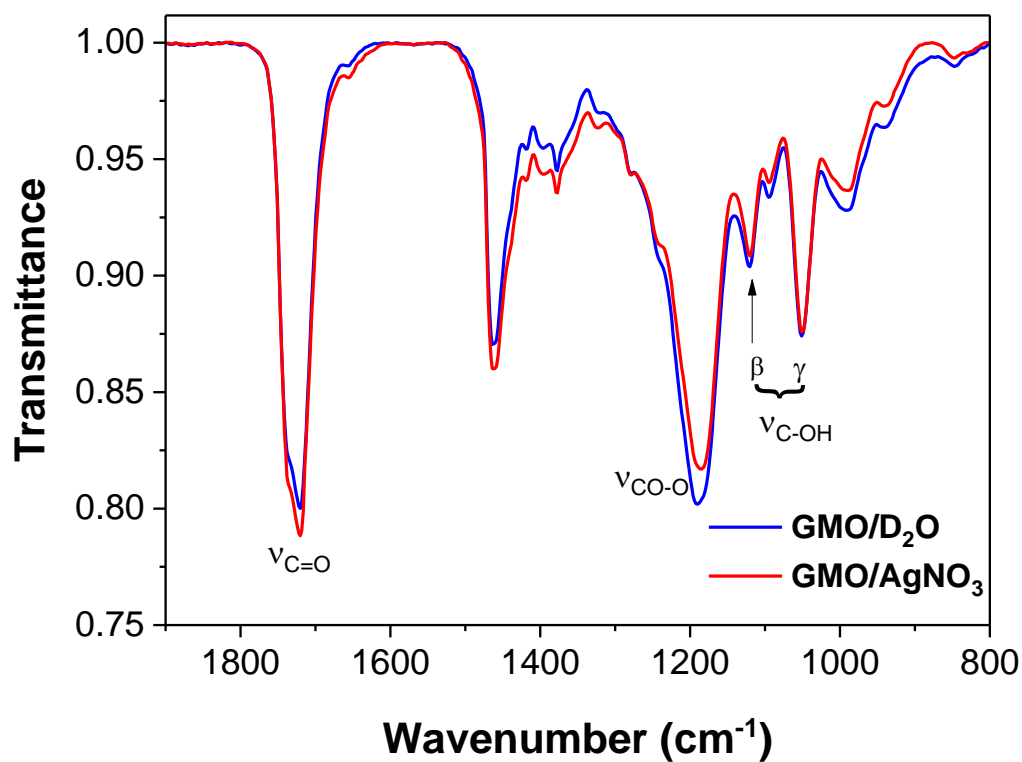


**Figure A.9.** Infrared spectra of the cubic phase with and without silver added at 25 °C. Decrease of intensity of the  $\beta$  and  $\gamma$  C–OH stretching vibrations as well as increase of C=O stretching vibrations are attributed to the formation of aldehyde due to the oxidation of monoolein.

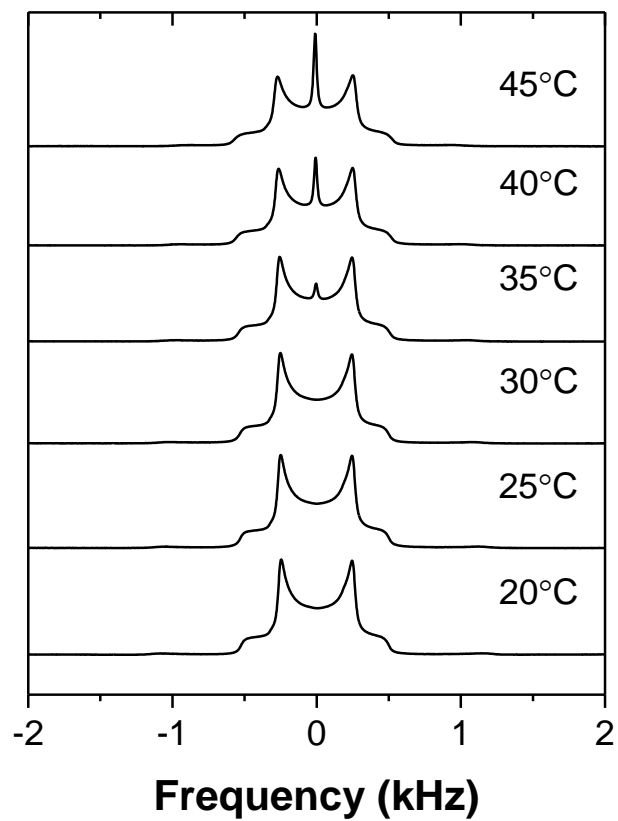


**Figure A.10.**  $^2\text{H}$  NMR spectra of 70 wt.% GMO/5 wt.% TAG/25 wt.% 0.01 M  $\text{AgNO}_3$  ( $\text{H}_{\text{II}}$  phase) at varying temperatures.

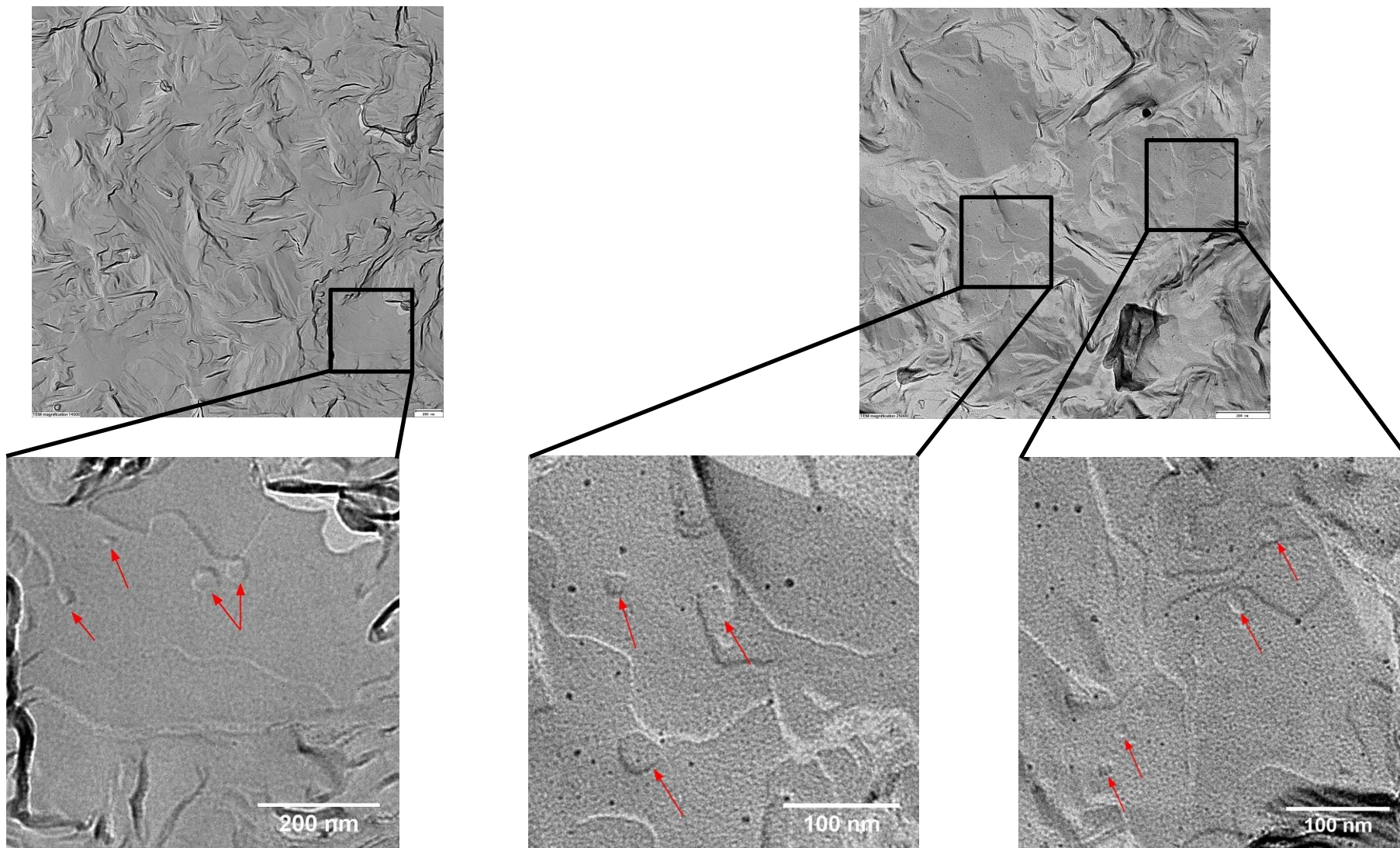


**Figure A.11.** FFEM micrograph of cubic Ia3d phase (70 wt.% GMO/30 wt.% 0.01 M AgNO<sub>3</sub>), 1 week after preparation. Arrows indicate possible nanoparticle location. The black dots are nanoparticles which have not been washed away from the replica during the soft matter removal procedure.

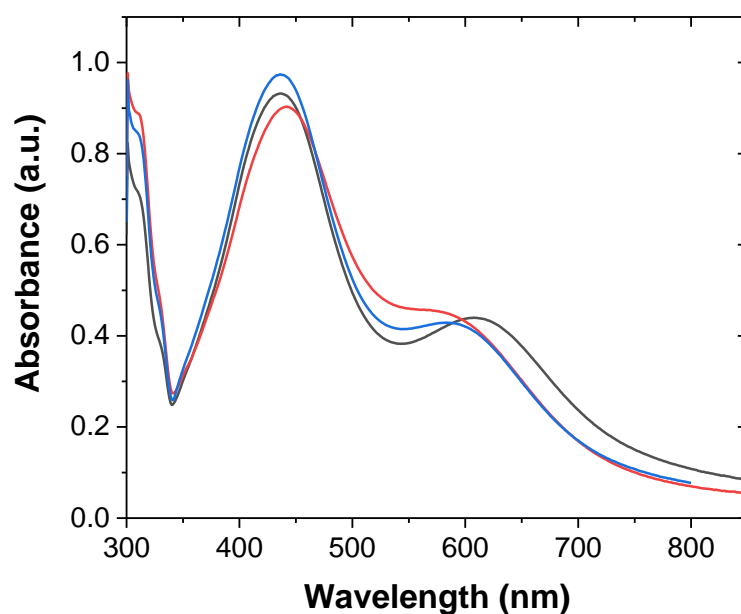


**Figure A.12.** UV-Vis absorption spectra of nanoparticles synthesized in cubic Ia3d phase (70 wt. % GMO/30 wt.% 0.02 M AgNO<sub>3</sub>) after 1 week in three independent samples.

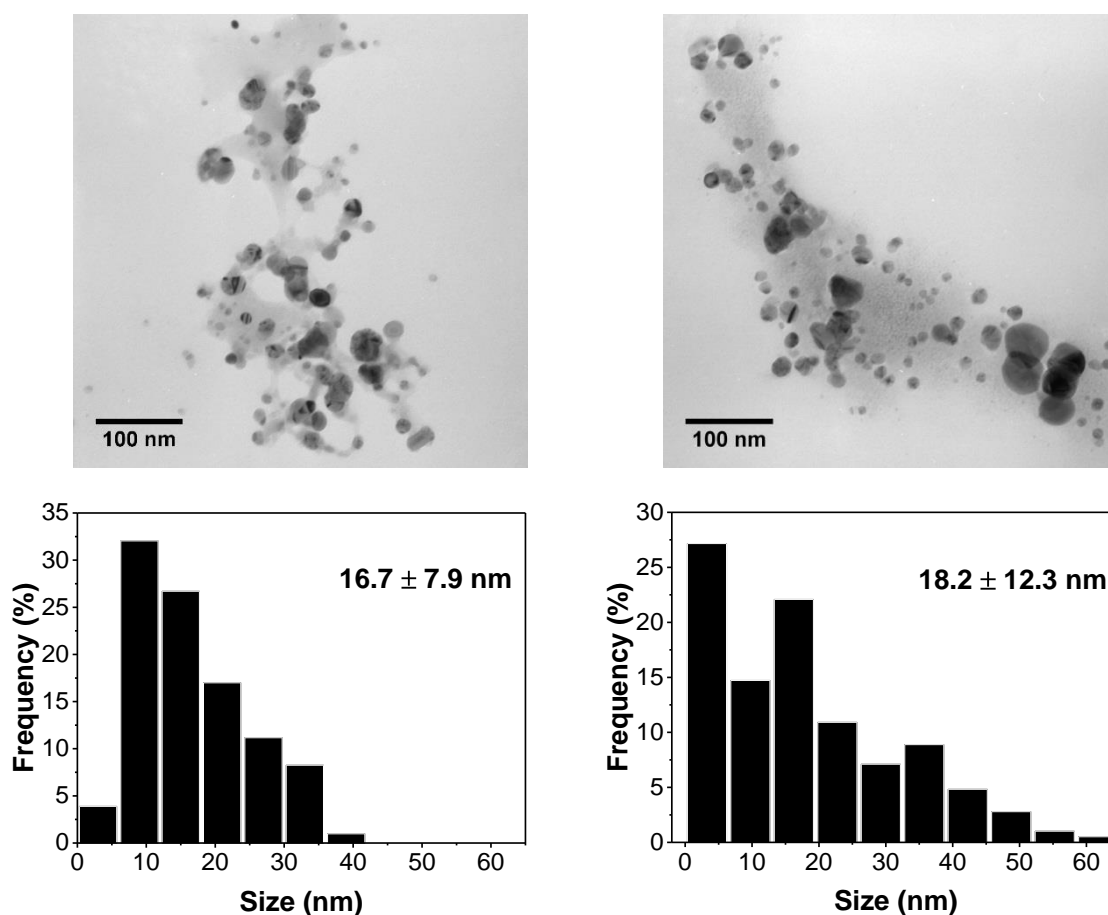


**Figure A.13.** TEM images and size distribution of nanoparticles formed in Pn3m cubic phase (63 wt.% GMO/30 wt.% 0.02 M AgNO<sub>3</sub>) after 12 hours (left) and 1 month (right).

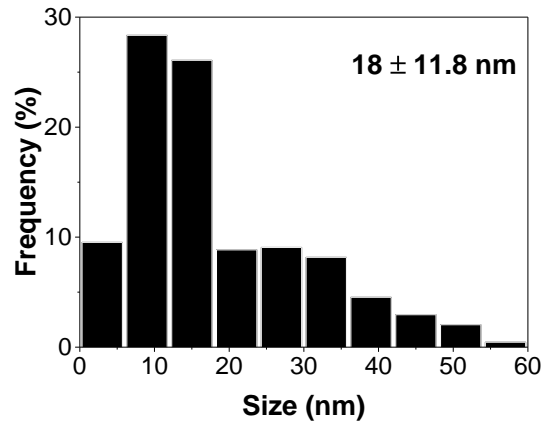
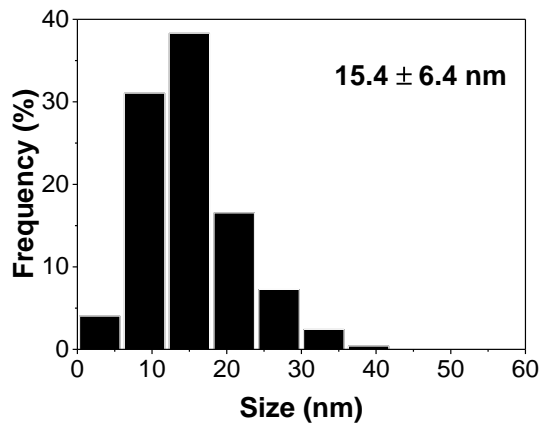
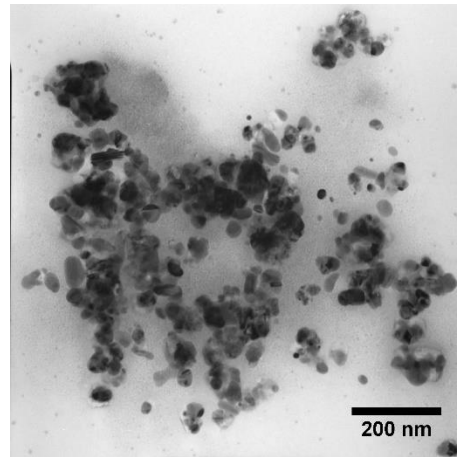
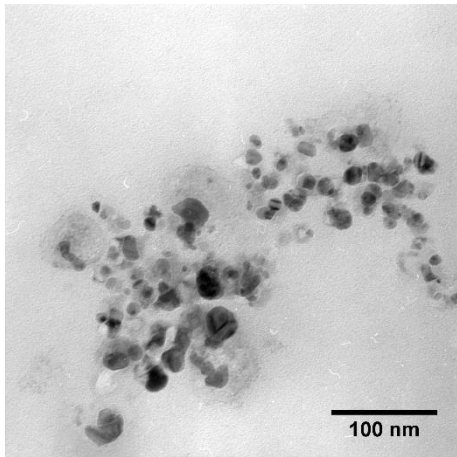


**Figure A.14.** TEM images and size distribution of nanoparticles formed in Pn3m cubic phase (63 wt.% GMO/30 wt.% 0.05 M AgNO<sub>3</sub>) after 12 hours (left) and 1 month (right).

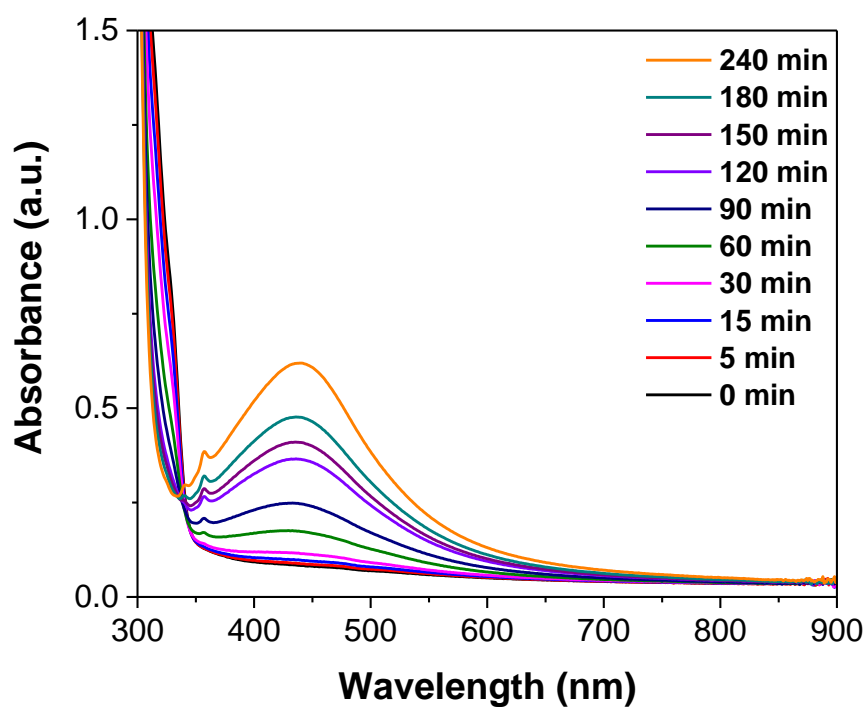


**Figure A.15.** UV-Vis absorption spectra of DNA-containing cubic Ia3d phase (0.02 M AgNO<sub>3</sub>) showing the dependence on 254 nm irradiation wavelength.

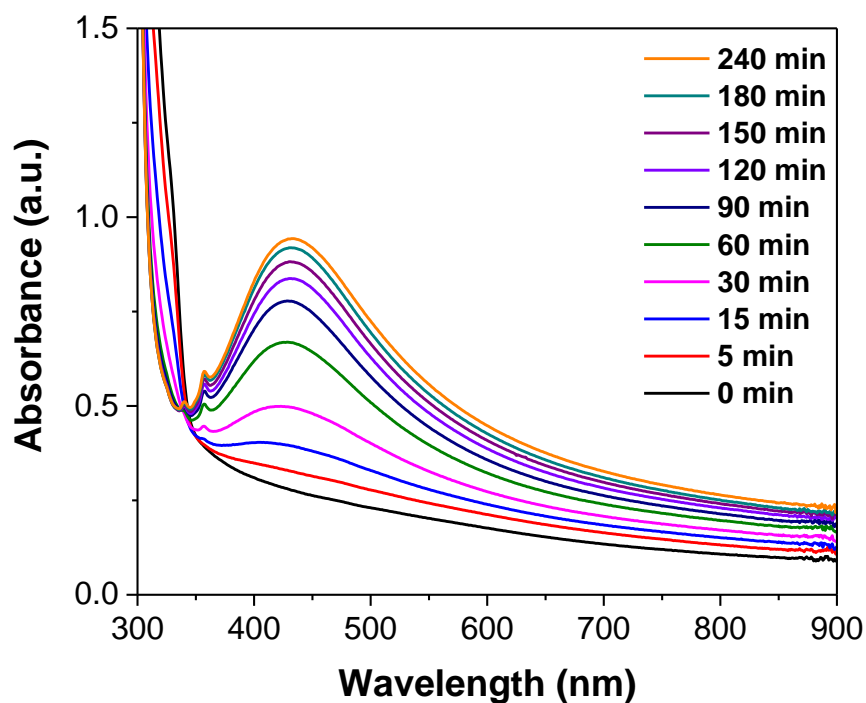


**Figure A.16.** UV-Vis absorption spectra of DNA-containing cubic Ia3d phase (0.02 M AgNO<sub>3</sub>) showing the dependence on 366 nm irradiation wavelength.

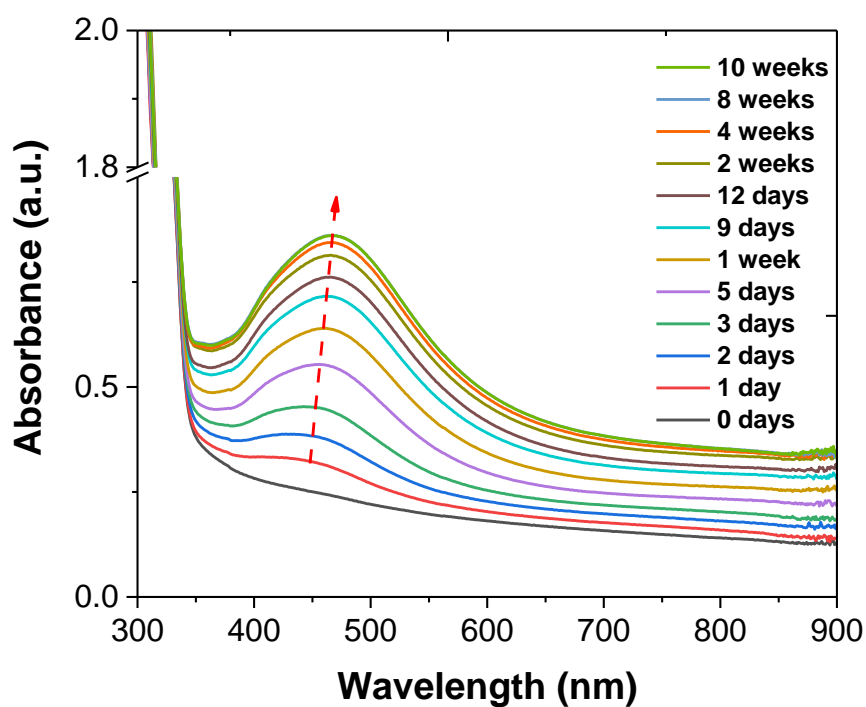


**Figure A.17.** Time evolution UV-Vis spectra showing the spontaneous formation of the silver nanoparticle in DNA-containing cubic Ia3d phase (0.04 M AgNO<sub>3</sub>).

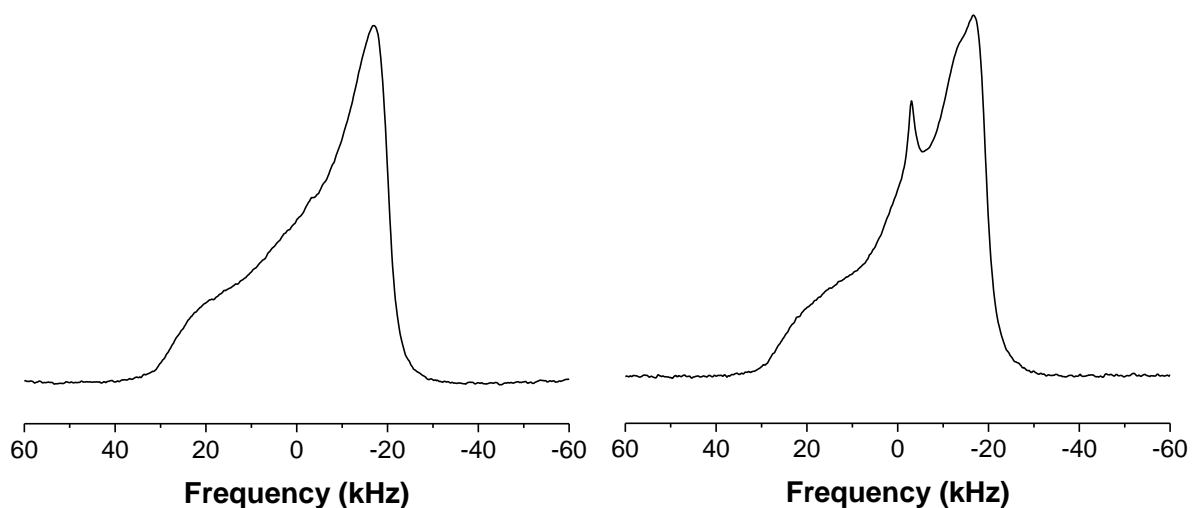


**Figure A.18.** <sup>31</sup>P NMR spectrum of C0 5/57/38 after 1 month (left) and 1 year (right) of preparation at 25 °C.

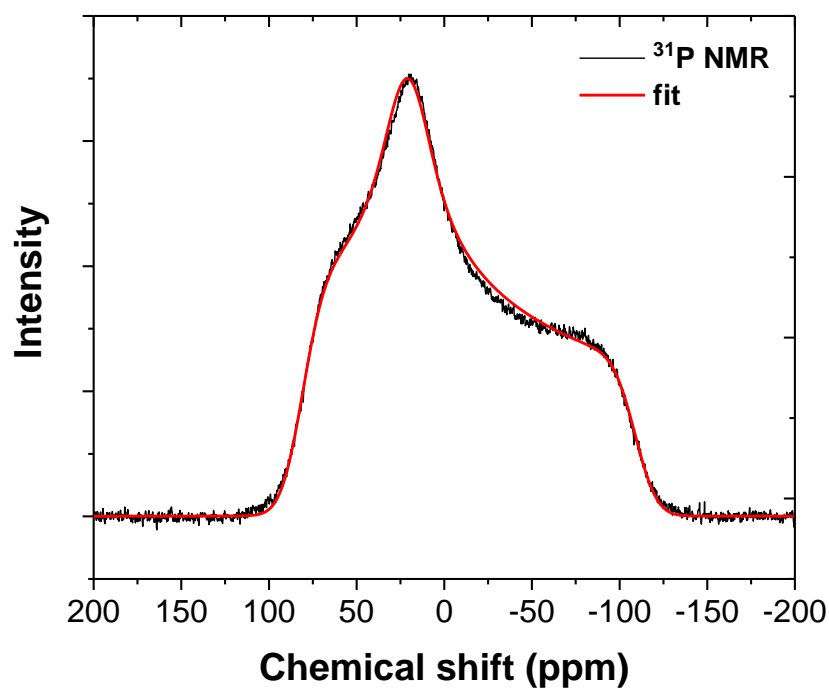


**Figure A.19.** Static  $^{31}\text{P}$  NMR spectrum of solid DTADNA complex at 23 °C.

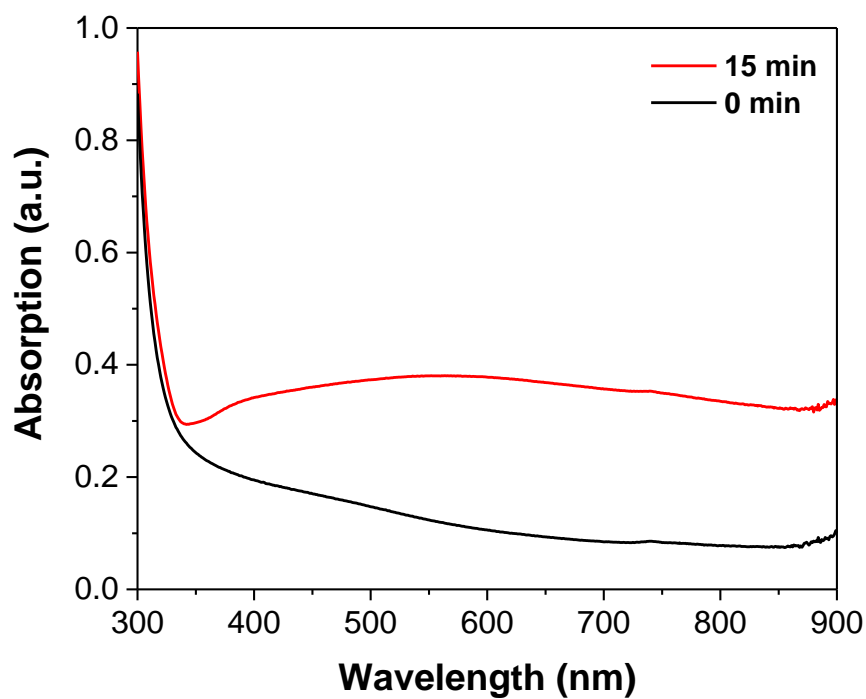


**Figure A.20.** UV-Vis absorption spectra of 50 wt.% HP $\beta$ CD/50 wt.% 0.1 M AgNO<sub>3</sub> before and after irradiation for 15 minutes.

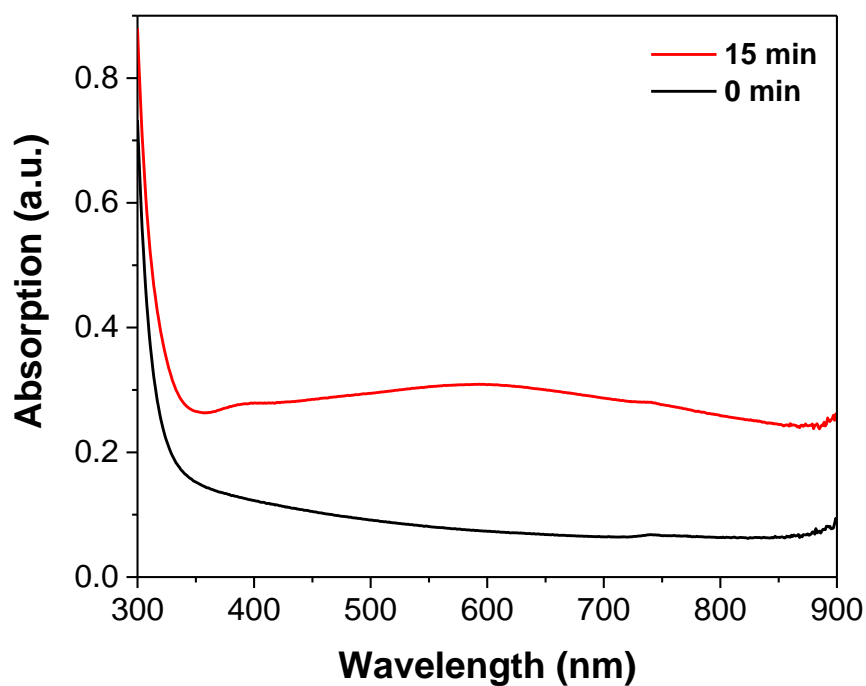


**Figure A.21.** UV-Vis absorption spectra of 50 wt.% HP $\beta$ CD/50 wt.% 0.02 M AgNO<sub>3</sub> before and after irradiation for 15 minutes.

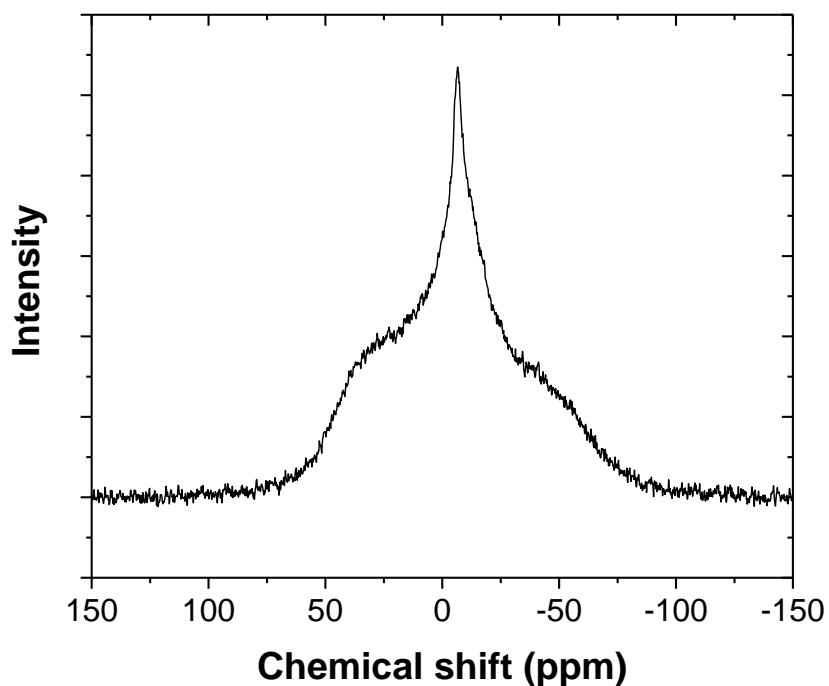


**Figure A.22.** Static <sup>31</sup>P NMR spectrum of A1 18/41/41 at 23 °C.

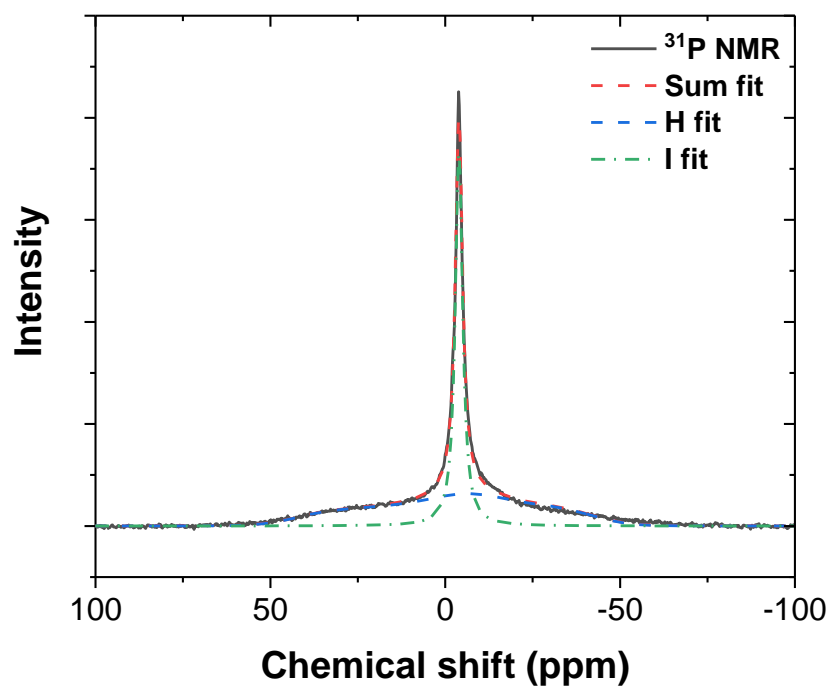


**Figure A.23.** Static  $^{31}\text{P}$  NMR spectrum of A0 10/40/50 at 23 °C.

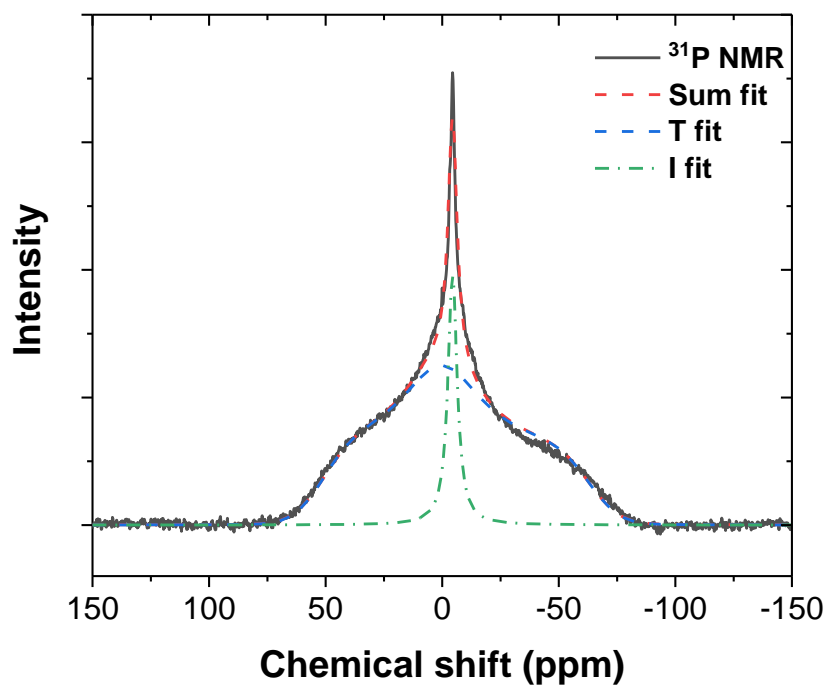


**Figure A.24.** Static  $^{31}\text{P}$  NMR spectrum of A0 25/25/50 at 23 °C.

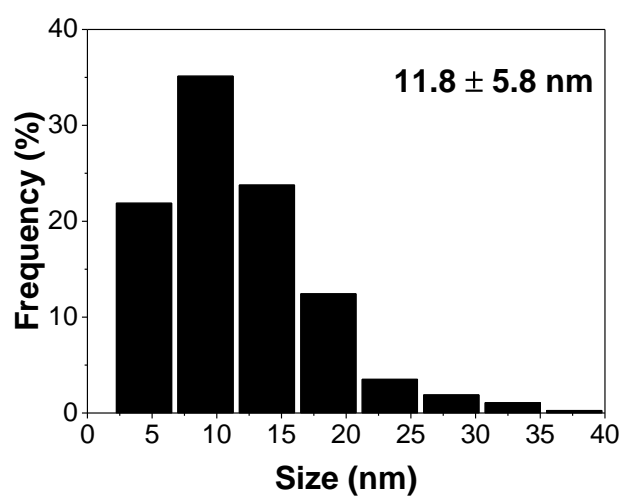
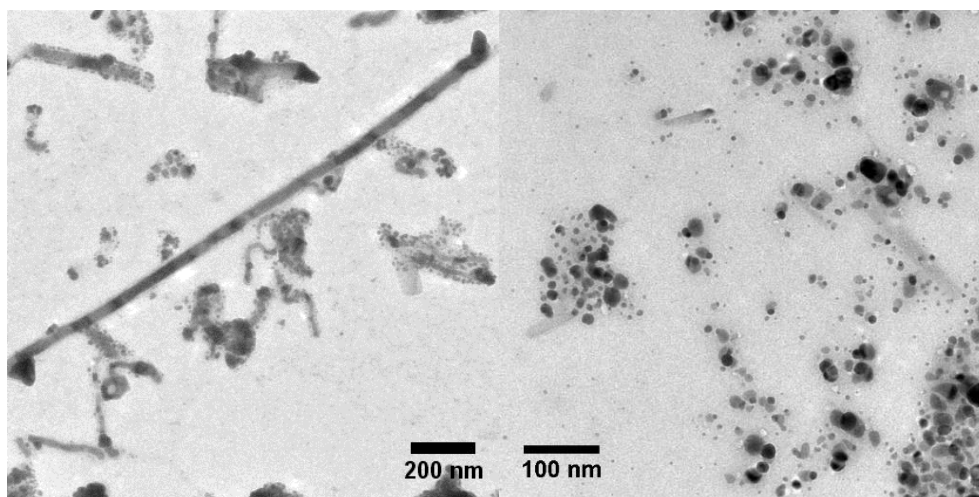


**Figure A.25.** TEM images and size distribution histogram of nanoparticles synthesized in A1 15/35/50 irradiated for 60 minutes.

## Abbreviations and symbols:

$a$	Lattice parameter
AFM	Atomic force microscopy
ATR	Attenuated total reflectance
BEM	Boundary element method
bp	Base pair
CSA	Chemical shift anisotropy
CSDNA	Cationic surfactant-DNA complex
DDA	Discrete dipole approximation
DNA	Deoxyribonucleic acid
dsDNA	double stranded DNA
DTAB	Dodecyltrimethylammonium bromide
DTADNA	Dodecyltrimethylammonium – DNA complex
EELS	Electron energy loss spectroscopy
FDTD	Finite difference time domain
FFEM	Freeze fracture electron microscopy
GMO	Monoolein
H <sub>II</sub>	Inverse hexagonal liquid crystalline phase
HP $\beta$ CD	2-Hydroxypropyl- $\beta$ -cyclodextrin
IPMS	Infinite periodic minimal surface
IR	Infrared
LLC	Lyotropic liquid crystal
LPC	Lysophosphatidylcholine

$L_{\alpha}$	Lamellar liquid crystalline phase
MAS	Magic angle spinning
NMR	Nuclear magnetic resonance
PC	Phosphatidylcholine
POM	Polarizing optical microscopy
ppm	Parts per million
$r_w$	Radius of aqueous channels
SAXS	Small angle X-ray scattering
SEM	Scanning electron microscopy
SERS	Surface enhanced Raman spectroscopy
SPR	Surface plasmon resonance
TAG	Triacyl glycerol (Tricaprylin)
TEM	Transmission electron microscopy
UV-Vis	Ultraviolet-Visible
WAXS	Wide angle X-ray scattering
$\beta$ CD	$\beta$ -Cyclodextrin
$\lambda_{\max}$	Position of the absorption peak

## References

- [1] C. Burda, X. B. Chen, R. Narayanan, M. A. El-Sayed, *Chem. Rev.*, **2005**, 105, 1025
- [2] S. Bhattacharrya, S. K. Saha, D. Chakravorty, D, *Appl. Phys. Lett.*, **2000**, 76, 3896–3898
- [3] M. Zhang, L. Liu, C. Wu, G. Fu, H. Zhao, B. He, *Polymer*, **2007**, 48, 1989
- [4] A. Fukuoka, Y. Sakamoto, S. Guan, S. Inagaki, N. Sugimoto, Y. Fukushima, K. Hirahara, S. Iijima, M. Ichikawa, *J. Am. Chem. Soc.*, **2001**, 123, 3373–3374
- [5] E. Braun, Y. Eichen, U. Sivan, G. Ben-Yoseph, *Nature*, **1998**, 391, 775–778
- [6] J. Sloan, D. M. Wright, H. G. Woo, S. Bailey, G. Brown, A. P. E. York, K. S. Coleman, J. L. Hutchison, M. L. H. Green, *Chem. Commun.*, **1999**, 8, 699–700
- [7] M. Andersson, J. Pedersen, A. E. C. Palmqvist, *Langmuir*, **2005**, 21, 11387–11396
- [8] T. M. Dellinger, P. V. Braun, *Chem. Mater.*, **2004**, 16, 2201–2207, C. Wang. D. Chen, X. Jiao, *Sci. Technol. Adv. Mater.*, **2009**, 10, 1–11, V. T. Liveri, *Controlled Synthesis of Nanoparticles in Microheterogeneous Systems*, Springer, **2006**, 115–164
- [9] V. Luzzati, in *Biological Membranes*, D. Chapman (ed.), Academic Press, **1968**, 71–123
- [10] T. Hahn, H. Klapper, *International Tables for Crystallography*, Springer, **2006**, 762–803
- [11] J.N. Israelachvili, D.J. Mitchell, B.W. Ninham, *J. Chem. Soc. Faraday Trans.*, **1976**, 72, 1525–1568
- [12] S. A. Safran, *Statistical thermodynamics of surfaces, interfaces, and membranes*, Addison-Wesley Reading, **1994**, 284
- [13] K. Fontell, *Colloid Polym. Sci.*, **1990**, 268, 264–285
- [14] P. Alexandridis, U. Olsson, B. Lindman, *Langmuir*, **1998**, 14, 2627–2638
- [15] A. M. Figueiredo Neto, S. R. A. Salinas, *The physics of lyotropic liquid crystals*, Oxford University press, **2005**, 304
- [16] V. Luzatti, R. Vargas, P. Mariani, A. Gulik, H. Delacroix, *J. Mol. Biol.*, **1993**, 229, 540–551
- [17] G. C. Shearman, A. I. I. Tyler, N. J. Brooks, R. H. Templer, O. Ces, R. V. Law, J. M. Seddon, *Liquid Crystals*, **2010**, 37, 679–694
- [18] J. M Seddon, R.H. Templer, in *Handbook of Biological Physics: Structure and Dynamics of Membranes*, A. J. Hoff, R. Lipowsky, E. Sackmann (ed.), Elsevier Science **1995**, 97–160
- [19] J. Lendermann, R. Winter, *Phys. Chem. Chem. Phys.*, **2003**, 5, 1440–1450

- [20] P. Kekicheff, B. Cabane, *J. Phys.*, **1987**, 48, 1571–1583
- [21] A. Tardieu, V. Luzzati, F.C. Reman, *J. Mol. Biol.*, **1973**, 75, 711–733
- [22] M. C. Holmes, M. S. Leaver, in *Bicontinuous Liquid Crystals*, M. L. Lynch, P. T. Spicer (ed.), CRC Press, **2005**, 15–39
- [23] R. Strey, R. Schomäcker, D. Roux, F. Nallet, U. Olsson, *J. Chem. Soc. Faraday Trans.*, **1990**, 86, 2253–2261
- [24] M. Duer, *Solid-State NMR Spectroscopy Principles and Applications*, Blackwell Science, **2002**, 567
- [25] M. C. Holmes, in *Nanostructured soft matter*, A. V. Zvelindovsky (ed.), Springer, **2007**, 99–127
- [26] G. E. Pake, *J. Chem. Phys.*, **1948**, 16, 327
- [27] M. Baciú, U. Olsson, M. S. Leaver, M. C. Holmes, *J. Phys. Chem. B*, **2006**, 110, 8184–8187
- [28] J. Mason, *Solid State Nucl. Mag.*, **1993**, 2, 285–288
- [29] H. Saito, I. Ando, A. Naito, *Solid state NMR Spectroscopy for Biopolymers: Principles and Applications*, Springer, **2006**, 59–88
- [30] I. C. P. Smith, I. H. Ekiel, in *Phosphorus-31 NMR Principles and Applications*, David G. Gorenstein (ed.), Academic Press, **1984**, 447–475
- [31] L. van Dam, M. H. Levitt, *J. Mol. Biol.*, **2000**, 304, 541–561, M. T. Mai, D. E. Wemmer, O. Jardetzky, *J. Am. Chem. Soc.*, **1983**, 105, 7149–7152
- [32] A. I. I. Tyler, R. V. Law, and J. M. Seddon, in *Methods in Membrane Lipids*, Dylan M. Owen (ed.), **2015**, Humana press, 199–225
- [33] W. P. Williams, B. A. Cunningham, D. H. Wolfe, G. E. Derbyshire, G. R. Mant, W. Bras, *Biochimica et Biophysica Acta*, **1996**, 1284, 86–96
- [34] S. Murgia, S. Lampis, R. Angius, D. Berti, M. Monduzzi, *J. Phys. Chem. B*, **2009**, 113, 9205–9215, V. Cherezov, J. Clogston, Y. Misquitta, W. Abdel-Gawad, M. Caffrey, *Biophys. J.*, **2002**, 83, 3393–3407
- [35] D. M. Anderson, S. M. Gruner, S. Leibler, *Proc. Natl. Acad. Sci. USA*, **1988**, 85, 5364–5368
- [36] C. Frontali, E. Dore, A. Ferrauto, E. Gratton, A. Bettini, M. R. Pozzan, E. Valdevit, *Biopolymers*, **1979**, 18, 1353–1373, Z. Kam, N. Borochev, H. Eisenberg, *Biopolymers*, **1981**, 20, 2671–2690
- [37] F. M. Pohl, T. M. Jovin, *J. Mol. Biol.*, **1972**, 67, 375
- [38] W. Zacharias, A. Jaworski, R.D. Wells, *J. Bacteriol.*, **1990**, 172, 3278

- [39] R. Dias, B. Lindman, *DNA interaction with polymers and surfactants*, John Wiley and Sons, **2008**, 407
- [40] K. Hayakawa, J. P. Santerre, J. C. T. Kwak, *Biophys. Chem.*, **1983**, 17, 175–181
- [41] A. Bilalov, U. Olsson, B. Lindman, *Soft Matter*, **2012**, 8, 11022–11033
- [42] C. Leal, L. Wadsö, G. Olofsson, M. Miguel, Håkan Wennerström, *J. Phys. Chem. B*, **2004**, 108, 3044–3050
- [43] A. Kriptsov, A. Bilalov, U. Olsson, B. Lindman, *Langmuir*, **2012**, 28, 13698–13704
- [44] R. M. Izatt, J. J. Christensen, J. H. Rytting, *Chem. Rev.*, **1971**, 71, 439–481
- [45] N. Dattagupta, D. M. Crothers, *Nucleic Acid Res.*, **1981**, 9, 2971–2985
- [46] H. Arakawa, J. F. Neault, H. A. Tajmir-Riahi, *Biophysical Journal*, **2001**, 81, 1580–1587
- [47] R. H. Jensen, A. Davidson, *Biopolymers*, **1966**, 4, 17–32
- [48] M. P. Zach, K. H. Ng, R. M. Penner, *Science*, **2000**, 290, 2120–2123, N. R. Jana, L. Gearheart, C. J. Murphy, *Chem. Commun.*, **2001**, 7, 617–618, J. Hu, T. W. Odom, C. M. Lieber, *Acc. Chem. Res.*, **1999**, 32, 435–445
- [49] M. Faraday, *Phil. Trans. Roy. Soc.*, **1857**, 147, 145, J. Turkevich, P. C. Stevenson, J. Hillier, *Discuss. Faraday Soc.*, **1951**, 11, 55
- [50] C. R. Martin, *Science*, **1994**, 266, 1961, C. R. Martin, *Chem. Mater.*, **1996**, 8, 1739, Y. Yu, S. Chang, C. Lee, C. R. Wang, *J. Phys. Chem. B*, **1997**, 101, 661, S. Chang, C. Shin, C. Chen, W. Lai, C. R. Wang, *Langmuir*, **1999**, 15, 701
- [51] K. R. Brown, M. J. Natan, *Langmuir*, **1998**, 14, 726, C. J. Murphy, N. R. Jana, *Adv. Mater.*, **2002**, 14, 80
- [52] L. J. Sherry, S. H. Chang, G. C. Schatz, R. P. Van Duyne, B. J. Wiley, Y. Xia, *Nano Lett.*, **2005**, 5, 2034, T. K. Sau, C. J. Murphy, *Philos. Mag.*, **2007**, 87, 2143
- [53] B. J. Wiley, S. H. Im, Z. Y. Li, J. McLellan, A. Siekkinen, Y. Xia, *J. Phys. Chem. B*, **2006**, 110, 15666
- [54] M. Yamamoto, Y. Kashiwagi, T. Sakata, H. Mori, M. Nakamoto, *Chem. Mater.*, **2005**, 17, 5391, J. Xie, J. Lee, D. I. Wang, *J. Phys. Chem. C*, **2007**, 111, 10226
- [55] N. Zhao, Y. Wei, N. Sun, Q. Chen, J. Bai, L. Zhou, Y. Qin, M. Li, L. Qi, *Langmuir*, **2008**, 24, 991, T. Huang, T. Cheng, Y. Ming, H. Wei, S. Lung, R. Fu, J. Ji, Y. Chi, T. Hsin, *Langmuir*, **2007**, 23, 5722
- [56] M. Pelton, J. Aizpurua, G. Bryant, *Laser Photonics Rev.*, **2008**, 2, 136–159
- [57] D. P. Fromm, A. Sundaramurthy, P. J. Schuck, G. Kino, and W. E. Moerner, *Nano Lett.*, **2004**, 4, 957, A. A. Tseng, *J. Micromech. Eng.*, **2004**, 14, R15

- [58] R. Zamiri, A. Zakaria, A. R. Sadrolhosseini, H. A. Ahangar, G. P. C. Drummen, *Sci. Adv. Mater.*, **2013**, 5, 748–757
- [59] T. Tsuzuki, P. G. McCormick, *J. Mater. Sci.*, **2004**, 39, 5143–5146
- [60] T. M. Tolaymat, A. M. El Badawy, A. Genaidy, K. G. Scheckel, T. P. Luxton, M. Suidan, *Sci. Total. Environ.*, **2010**, 408, 999
- [61] X. Lu, M. Rycenga, S. Skrabalak, B. Wiley, Y. Xia, *Annu. Rev. Phys. Chem.*, **2009**, 60, 167–192
- [62] N. Jana, L. Gearheart, C. Murphy, *J. Phys. Chem. B*, **2001**, 105, 4065–4067
- [63] W. Niu, L. Zhang, G. Xu, *Nanoscale*, **2013**, 5, 3172–3181
- [64] W. X. Niu, Z. Y. Li, L. H. Shi, X. Q. Liu, H. J. Li, S. Han, G. B. Xu, *Cryst. Growth Des.*, **2008**, 8, 4440–4444, W. X. Niu, L. Zhang, G. B. Xu, *ACS Nano*, **2010**, 4, 1987–1996
- [65] L. Qi, Y. Gao, J. Ma, *Colloids Surf. A*, **1999**, 157, 285–294
- [66] D. Zhao, Q. Huo, J. Feng, B. Chmelka, G. Stucky, *J. Am. Chem. Soc.*, **1998**, 120, 6024–6036.
- [67] M. Andersson, V. Alfredsson, P. Kjellin, A. Palmqvist, *Nano Lett.*, **2002**, 2, 1403–1407
- [68] C. T. Wirges, J. Timper, M. Fischler, A. S. Sologubenko, J. Mayer, U. Simon, T. Carell, *Angew. Chem. Int. Ed.*, **2009**, 48, 219–223, L. Berti, G. A. Burley, *Nat. Nanotechnology*, **2008**, 3, 81–87
- [69] L. Berti, A. Alessandrini, P. Facci, *J. Am. Chem. Soc.*, **2005**, 127, 11216–11217
- [70] S. Kundu, K. Wang, D. Huitink, H. Liang, *Langmuir*, **2009**, 25, 10146–10152
- [71] S. Kundu, *Phys. Chem. Chem. Phys.*, **2013**, 15, 14107–14119
- [72] J. Liu, X. Zhang, M. Yu, S. i Li, J. Zhang, *Small*, **2012**, 8, 310–316
- [73] N. Toshima, T. Takahashi, *B. Chem. Soc. Jpn.*, **1992**, 65, 400–409
- [74] S. H. Yu, H. Colfen, Y. Mastai, *J. Nanosci. Nanotechnol.*, **2004**, 4, 291–298
- [75] K. Esumi, K. Matsuhisa, K. Torigoe, *Langmuir*, **1995**, 11, 3285–3287
- [76] R. Jin, Y. Charles Cao, E. Hao, G. S. Metraux, G. C. Schatz, C. A. Mirkin, *Nature*, **2003**, 425, 487, J. Zhang, S. Li, J. Wu, G. Schatz, C. Mirkin, *Angew. Chem., Int. Ed.*, **2009**, 48, 7787
- [77] K. Huber, T. Witte, J. Hollmann, S. Keuker-Baumann, *J. Am. Chem. Soc.*, **2007**, 129, 1089–1094, A. Ezhova, *Specific interaction of Ag<sup>+</sup> ions with linear polyacrylate chains and spherical polyacrylate brushes and Ag nanoparticle formation therein*, Dissertation, Paderborn University, **2015**

- [78] K. L. Kelly, E. Coronado, L. L. Zhao, G. C. Schatz, *J. Phys. Chem. B*, **2003**, 107, 668–677
- [79] G. Mie, *Ann. Physik*, **1908**, 25, 377
- [80] V. Myroshnychenko, J. Rodríguez-Fernández, I. Pastoriza-Santos, A. M. Funston, C. Novo, P. Mulvaney, L. M. Liz-Marzán, F. J. Garcia de Abajo, *Chem. Soc. Rev.*, **2008**, 37, 1792–1805.
- [81] L. M. Liz-Marzan, *Materials today*, **2004**, 7, 26–31
- [82] D. D. Evanoff, G. Chumanov, *J. Phys. Chem. B*, **2004**, 108, 13957–13962
- [83] H. Jing, L. Zhang, H. Wang in *UV-Vis and Photoluminescence spectroscopy for Nanoparticle Characterisation*, C. S. S. R. Kumar (ed.), Springer-Verlag, **2013**, 1–60
- [84] E. A. Coronado, E. R. Encina, F. D. Stefani, *Nanoscale*, **2011**, 3, 4042–4059
- [85] B. Nikoobakht, M. A. El-Sayed, *Chem. Mater.*, **2003**, 15, 1957–1962
- [86] R. Gans, *Ann. Phys.*, **1912**, 37, 881
- [87] I. Pastoriza-Santos, L. M. Liz-Marzan, *J. Mater. Chem.*, **2008**, 18, 1724–1737
- [88] C. Sönnichsen, B. M. Reinhard, J. Liphardt, P. Alivisatos, *Nat. Biotechnol.*, **2005**, 23, 741–745
- [89] J. P. Camden, J. A. Dieringer, Y. Wang, D. J. Masiello, L. D. Marks, G. C. Schatz, R. P. Van Duyne, *J. Am. Chem. Soc.*, **2008**, 130, 12616, S. Nie, S. R. Emory, *Science*, **1997**, 275, 1102
- [90] S. Schlücker, *Angew. Chem. Int. Ed.*, **2014**, 53, 4756–4795
- [91] J. Briggs, H. Chung, M. Caffrey, *J. Phys. II France*, **1996**, 6, 723–751, H. Qiu, M. Caffrey, *Biomaterials*, **2000**, 223–234
- [92] *Code of Federal Regulations*, **2016**, 3, 21, 184.1323
- [93] *Official Journal of the European Communities*, **1995**, 38, L61/8
- [94] P. T. Spicer, *Curr. Opin. Colloid Interface Sci.*, **2005**, 10, 274–279
- [95] A. Ganem-Quintanar, D. Quintanar-Guerrero, P. Buri, *Drug Dev. Ind. Pharm.*, 2000, 26, 809–820
- [96] I. Amar-Yuli, N. Garti, *Colloid. Surf. B*, **2005**, 43, 72–82
- [97] P. Barnickel, A. Wokaun, *Mol. Phys.*, **1990**, 69, 1–8
- [98] K. Esumi, T. Hosoya, K. Torigoe, *Langmuir*, **2000**, 16, 2978–2980
- [99] S. Puvvada, S. Baral, M. Chow, S. E. Qadri, E. R. Ratna, *J. Am. Chem. Soc.*, **1994**, 116, 2135–2136
- [100] O. Regev, R. Backov, C. Faure, *Chem. Mater.*, **2004**, 16, 5280–5285
- [101] M.-E. Meyre, O. Lambert, B. Desbat, C. Faure, *Nanotechnology*, **2006**, 17, 1193–1201

- [102] G. Popescu, J. Barauskas, T. Nylander, F. Tiberg, *Langmuir*, **2007**, 23, 496–503
- [103] A. Cheng, B. Hummel, H. Qiu, M. Caffrey, *Chem. Phys. Lipids*, **1998**, 95, 11–21
- [104] F. B. Rosevear, *J. Am. Oil Chem. Soc.*, **1954**, 31, 628–639
- [105] L. J. Sherry, R. Jin, C. A. Mirkin, G. C. Schatz, R. P. Van Duyne, *Nano Lett.*, **2006**, 6, 2060–2065
- [106] Y. Yu, S. Handa, T. Yajima, M. Futamata, *Chem. Phys. Lett.*, **2013**, 560, 49–54
- [107] F. K Guedje, M. Giloan, M. Potara, M. N. Hounkonnou, S. Astilean, *Phys. Scr.*, **2012**, 86, 055702
- [108] S. T. Gentry, M. W. Bezpalko, *J. Phys. Chem. C*, **2010**, 114, 6989–6993, S. T. Gentry, S. F. Kendra, M. W. Bezpalko, *J. Phys. Chem. C*, **2011**, 115, 12736–12741
- [109] J. Nelayah, M. Kociak, O. Stephan, F. J. Garcia De Abajo, M. Tence, L. Henrard, D. Taverna, I. Pastoriza-Santos, L. M. Liz-Marzan, C. Colliex, *Nat. Phys.*, **2007**, 3, 348–353
- [110] L. M. Liz-Marzan, I. Lado-Tourino, *Langmuir*, **1996**, 12, 3585
- [111] L. Sun, Y. Song, L. Wang, C. Guo, Y. Sun, Z. Liu, Z. Li, *J. Phys. Chem. C*, **2008**, 112, 1415–1422
- [112] B. Tang, S. Xu, X. Hou, J. Li, L. Sun, W. Xu, X. Wang, *ACS Appl. Mater. Inter.*, **2013**, 5, 646–653
- [113] P. Pitzalis, M. Monduzzi, N. Krog, H. Larsson, H. Ljusberg-Wahren, T. Nylander, *Langmuir*, **2000**, 16, 6358–6365,
- [114] J. Borne, T. Nylander, A. Khan, *Langmuir*, **2001**, 17, 7742–7751
- [115] A. Bilalov, J. Elsing, E. Haas, C. Schmidt, U. Olsson, *J. Colloid Interface Sci.*, **2013**, 394, 360–367
- [116] C. Leal, K. K. Ewert, N. F. Bouxsein, R. S. Shirazi, Y. Li, C. R. Safinya, *Soft Matter*, **2013**, 9, 795
- [117] A. W. Girott, *J. Lipid Res.*, **1998**, 39, 1529–1542, B. Bose, S. N. Chatterjee, *Radiat. Res.*, **1993**, 133, 340–344
- [118] S. Kundu, *Phys. Chem. Chem. Phys.*, **2013**, 15, 14107
- [119] M. Harada, E. Katagiri, *Langmuir*, **2010**, 26, 17896–17905
- [120] M. Harada, K. Saijo, N. Sakamoto, K. Ito, *J. Colloid Interf. Sci.*, **2010**, 343, 423–432
- [121] F. D. Gunstone, J. L. Harwood, A. J. Dijkstra, *The Lipid Handbook*, **2007**, CRC Press, 781
- [122] *Code of Federal Regulations*, **2016**, 3, 21, 184.1400
- [123] *Official Journal of the European Communities*, **1995**, 38, L61/8

- [124] L. Zema, G. Melocchi, A. Maroni, A.J. Gazzaniga, *J. Control Release*, **2012**, 159, 324
- [125] P. L. Felgner, G. M. Ringold, *Nature*, **1989**, 337, 387–388
- [126] D. Sharma, *Colloid. Surf. B*, **2011**, 88, 610–613, D. Sharma, *Colloid. Surf. B*, **2013**, 107, 262–266
- [127] Benjamin R. Ayres, Scott M. Reed, *Environ. Sci. Nano*, **2014**, 1, 37–44
- [128] L. Wang, X. Chen, Z. Sun, Y. Chai, *Can. J. Chem. Eng.*, **2007**, 85, 598
- [129] H. Liang, T. E. Angelini, P. V. Braun, G. C. L. Wong, *J. Am. Chem. Soc.*, **2004**, 126, 14157–14165
- [130] A. Bilalov, U. Olsson, B. Lindman, *Soft Matter*, **2011**, 7, 730–742
- [131] B. Medronho, S. Shafaei, R. Szopko, M. G. Miguel, U. Olsson, C. Schmidt, *Langmuir*, **2008**, 24, 6480–6486
- [132] S-H. Park, S-G. Oh, J-Y. Mun, S-S. Han, *Colloid. Surf. B*, **2005**, 44, 117–122
- [133] S. P. Bhamidipati, J. A. Hamilton, *Biochemistry*, **1995**, 34, 5666–5677
- [134] J. O. Radler, I. Koltover, T. Salditt, C. R. Safinya, *Science*, **1997**, 275, 810–814.
- [135] B. Bose, S. Agarwal, S.N. Chatterjee, *Radiat. Environ. Biophys.*, **1989**, 28, 59–65
- [136] A. Kamal-Eldin, J. Pokorny, *Analysis of Lipid Oxidation*, AOCS press, **2005**, 293
- [137] P. B. Merkel, D. R. Kearns, *J. Am. Chem. Soc.*, **1972**, 94, 7244–7253
- [138] C. Leal, D. Sandström, P. Nevsten, D. Topgaard, *Biochim. Biophys. Acta*, **2008**, 1778, 214–228
- [139] J. D. van Beek, *J. Magn. Res.*, **2007**, 187, 19–26
- [140] A. Swami, A. Kumar, P. R. Selvakannan, S. Mandal, R. Pasricha, M. Sastry, *Chem. Mater.*, **2003**, 15, 17–19
- [141] S. Mandal, S. Datare, P. R. Selvakannan, R. Pasricha, M. Sastry, *Nanotechnology*, **2003**, 14, 878–881
- [142] M.-E. Meyre, O. Lambert, C. Faure, *J. Mater. Chem.*, **2006**, 16, 3552–3557
- [143] A. Bilalov, J. Carlstedt, E. Krivtsova, B. Lindman, U. Olsson, *Soft Matter*, **2012**, 8, 4988
- [144] E. M. M. Del Valle, *Process Biochem.*, 2004, 39, 1033–1046
- [145] B. Khlebtsov, A. Melnikov, V. Zharov, N. Khlebtsov, *Nanotechnology*, **2006**, 17, 1437–1445
- [146] P. R. Gopalan, A. G. Annaselvi, P. Subramaniam, *Int. J. Nanomat. Biostruct.*, **2013**, 3, 26–30
- [147] T. Yamane, N. Davidson, *Biochimica et Biophysica Acta*, **1962**, 55, 609–621
- [148] A. O. Pinchuk, G. C. Schatz, *Mat. Sci. Eng. B*, **2008**, 149, 251–258

- [149] D. McLoughlin, M. Delsanti, C. Tribet, D. Langevin, *Europhys. Lett.*, **2005**, 69, 461–467
- [150] J. Lu, L. Yang, A. Xie, Y. Shen, *Biophys. Chem.*, **2009**, 145, 91–97
- [151] S. Kundu, M. Jayachandran, *RSC Adv.*, **2013**, 3, 16486–16498
- [152] C. F. Monson, A. T. Woolley, *Nano Lett.*, **2003**, 3, 259–363
- [153] S. Kundu, H. Liang, *Adv. Mater.*, **2008**, 20, 826–831
- [154] M. R. Green, J. Sambrook, *Molecular Cloning: A Laboratory Manual*, Cold Spring Harbor Laboratory Press, **1982**, 1–80
- [155] <http://www.hoenle.de/pdfs/produktbroschueren/en/uvaspot-e.pdf>
- [156] F. J. Garcia de Abajo, A. Howie, *Phys. Rev. Lett.*, **1998**, 80, 5180–5183.
- [157] U. Hohenester, A. Trügler, *Comp. Phys. Commun.*, **2012**, 183, 370
- [158] E. D. Palik, *Handbook of Optical Constants of Solids*, Academic Press, **1985**
- [159] A. Bilalov, C. Leal, B. Lindman, *J. Phys. Chem. B*, **2004**, 108, 15408–15414
- [160] W. Saenger, *Principles of Nucleic Acid Structure*, Springer-Verlag, **1984**
- [161] L. Mandell, *Finska Kemistsamf. Med.*, **1963**, 72, L. Mandell, K. Fontell, A. Lehtinen, P. Ekwall, *Acta Polytech. Scand.*, **1968**, 74
- [162] S. Müller, P. Fischer, C. Schmidt, *J. Phys. II France*, **1997**, 7, 421–432
- [163] F. W. Matthews, G. G. Warren, J. H. Mitchell, *Anal. Chem.*, **1950**, 22, 515, V. Vand, A. Altiken, R. K. Campbell, *Acta Cryst.*, **1949**, 2, 388
- [164] B. P. Tolochko, S. V. Chernov, S. G. Nikitenko, D. R. Whitcomb, *Nucl. Instrum. Meth. A*, **1998**, 405, 428–434
- [165] K. Binnemans, R. V. Deun, B. Thijs, I. Vanwelkenhuysen, I. Geuens, *Chem Mater.* **2004**, 16, 2021–2027, E. Aret, V. Volochaev, S. Verhaegen, H. Meekes, E. Vlieg, *Cryst. Grow. Des.*, **2006**, 4, 1027–1032
- [166] B. B. Bokhonov, O. I. Lomovskiy, V. M. Andreev, V. V. Boldyrev, *J. Solid State Chem.*, **1985**, 58, 170–175, B. B. Bokhonov, L. P. Burleva, D. R. Whitcomb, *J. Imaging Sci. Technol.*, **1999**, 43, 505–508